SYNTHESIS AND CHARACTERIZATION OF ZIRCONIUM BASED BULK AMORPHOUS ALLOYS

A THESIS SUBMITTED TO
THE GRADUATE SCHOOL OF NATURAL AND APPLIED SCIENCES
OF
THE MIDDLE EAST TECHNICAL UNIVERSITY

BY

İLKAY SALTOĞLU

IN PARTIAL FULFILLMENT OF THE REQUIREMENTS FOR THE DEGREE OF
MASTER OF SCIENCE
IN
THE DEPARTMENT OF METALLURGICAL AND MATERIALS ENGINEERING

JANUARY 2004

Approval of the Graduate School of Natural and Applied Sciences

_____

Prof. Dr. Canan öZGEN

Director

I certify that this thesis satisfies all the requirements as a thesis for the degree of Master of Science.

_____

Prof. Dr. Bilgehan ÖGEL

Head of Department

This is to certify that we have read this thesis and that in our opinion it is fully adequate, in scope and quality, as a thesis for the degree of Master of Science.

_____	_____
Prof. Dr. Amdulla O. MEKHRABOV	Prof. Dr. M. Vedat AKDENİZ
Co-Supervisor	Supervisor

Examining Committee Members

Prof. Dr. Tayfur ÖZTÜRK	_____
Prof. Dr. Nizami HASANLI	_____
Prof. Dr. Amdulla O. MEKHRABOV	_____
Prof. Dr. M. Vedat AKDENİZ	_____
Assoc. Prof. Dr. C. Hakan GÜR	_____

ABSTRACT

SYNTHESIS AND CHARACTERIZATION OF ZIRCONIUM BASED BULK AMORPHOUS ALLOYS

Saltoğlu, İlkay
M. Sc., Department of Metallurgical and Materials Engineering
Supervisor: Prof. Dr. M. Vedat AKDENİZ
Co-Supervisor: Prof. Dr. Amdulla O. MEKHRABOV

January 2004, 191 pages

In recent years, bulk amorphous alloys and nanocrystalline materials have been synthesized in a number of ferrous and non-ferrous based alloys systems, which have gained some applications due to their unique physico-chemical and mechanical properties. In the last decade, Zr-based alloys with a wide supercooled liquid region and excellent glass forming ability have been discovered. These systems have promising application fields due to their mechanical properties; high tensile strength, high fracture toughness, high corrosion resistance and good machinability.

In this study, the aim is to model, synthesize and characterize the Zr-based bulk amorphous alloys. Initially, theoretical study on the basis of the semi-empirical rules

well known in literature and the electronic theory of alloys in pseudopotential approximation has been provided in order to predict the potential impurity elements that would lead to an increase in the GFA of the selected Zr-Ni, Zr-Fe, Zr-Co and Zr-Al based binary systems. Furthermore, thermodynamic and structural parameters were calculated for mentioned binary and their ternary systems.

According to the theoretical study, $Zr_{67}Ni_{33}$ binary system was selected and its multicomponent alloys were formed by adding its potential impurity elements; Mo, W and Al. Centrifugal casting method was used to produce alloy systems. Structural characterizations were performed by DSC, XRD, SEM and EDS methods.

In the near-surface regions of $Zr_{60}Ni_{25}Mo_{10}W_5$ and $Zr_{50}Ni_{20}Al_{15}Mo_{10}W_5$ alloys, amorphous structure has been observed. Experimental studies have shown that Zr-Ni based systems with impurity elements Mo, W and Al, not widely used in literature, might be good candidates for obtaining high GFA.

Keywords: Bulk Metallic Amorphous Alloys, Zirconium and Zirconium Based Alloy Systems, Glass Forming Ability, Thermodynamic and Kinetic Approaches, Atomistic Approaches, Semi-empirical Approaches, Centrifugal Casting Technique.

ÖZ

ZİRKON ESASLI İRİ VE HACİMLİ CAMSI ALAŞIMLARIN ÜRETİMİ VE NİTELENDİRİLMESİ

Saltoğlu, İlkay
Yüksek Lisans, Metalurji ve Mazeme Mühendisliği Bölümü
Tez Yöneticisi: Prof. Dr. M. Vedat AKDENİZ
Ortak Tez Yöneticisi: Prof. Dr. Amdulla O. MEKHRABOV

Ocak 2004, 191 sayfa

Son yıllarda, önemli fiziko-kimyasal ve mekanik özelliklerinden bazı uygulamalar kazanmış olan iri ve hacimli camsı alaşımlar ve nanokristal malzemeler, birçok demir esaslı ve demirdışı alaşım sistemlerinde üretilmektedir. Son on yılda, geniş aşırı soğutulmuş sıvı bölgeli ve mükemmel cam oluşturabilme yetenekli Zr-esaslı alaşım serileri bulunmuştur. Bu sistemler, mekanik özelliklerinden dolayı, örneğin; yüksek gerilme direnci, yüksek kırılma tokluğu, yüksek darbe kırılma enerjisi, yüksek korozyon dayanıklılığı, iyi işlenebilirlik, için umut verici uygulama alanlarına sahiptir.

Bu çalışmada, amaç Zr-bazlı iri ve hacimli camsı alaşımların üretilmesi ve nitelendirilmesidir. Başlangıç olarak, literatürden iyice bilinen yarı-deneysel kurallara ve psödo-potansiyel tahminlerdeki alaşımların elektronik teorisine dayanan teorik çalışma, seçilen Zr-Ni, Zr-Fe, Zr-Co ve Zr-Al esaslı ikili sistemlerin cam oluşturabilme yeteneklerinde artışı sağlayan, muhtemel alaşım elementlerini önermesi için yapılmıştır. Buna ek olarak, belirtilen ikili sistemler ve bunların üçlü sistemleri için termodinamik ve yapısal değerlerin hesaplanmıştır.

Teorik çalışmaya bağlı olarak, $Zr_{67}Ni_{33}$ ikili sistemi seçilmiş ve daha sonra teorik çalışmaların değerlendirilmesi ile belirlenen olası alaşım elementlerinin, Mo, W ve Al, eklenmesiyle çok bileşenli alaşımları oluşturulmuştur. Sistemlerin üretilmesi için savurmalı döküm yöntemi kullanılmıştır. Yapısal nitelendirilme, DSC, XRD, SEM ve EDS metodları ile yapılmıştır.

$Zr_{60}Ni_{25}Mo_{10}W_5$ ve $Zr_{50}Ni_{20}Al_{15}Mo_{10}W_5$ alaşımlarının yüzeye yakın bölgelerinde camsı yapı gözlenmiştir. Deneysel çalışmalar, literatürde çok fazla kullanılmayan, Mo, W ve Al alaşım elementli Zr-Ni sistemlerinin, yüksek cam oluşturabilme yeteneği elde etmek için aday sistemleri olabileceğini göstermektedir.

Anahtar Kelimeler: İri ve Hacimli Metalik Camsı Alaşımlar, Zirkon ve Zirkon Bazlı Alaşım Sistemleri, Cam Oluşturabilme Yeteneği, Termodinamik ve Kinetik Yaklaşımlar, Atomistik Yaklaşımlar, Yarı-deneysel Alaşımlar, Savurmalı Döküm Yöntemi.

To Sevim & Hamit SALTOĞLU

ACKNOWLEDGEMENTS

I am sincerely appreciation to my supervisor Prof. Dr. M. Vedat Akdeniz and co-supervisor Prof. Dr. Amdulla O. Mekhrabov for their guidance, patience and full support throughout the entire period of my thesis.

I would like to thank to my friends; Hülya Arslan, Selen Gürbüz, Ali Abdelal, Emrah Salim Erdiller and Can Ayas for their advices and moral support. Also, my thanks go to the technicians of the Department of Metallurgical and Materials Engineering.

I am profoundly grateful to my family; my mother, Sevim Saltoğlu, my father, Hamit Saltoğlu and my brother, Koray Saltoğlu, for their never ending love, support and trust in me. I would like to send my special thanks to my love, Yunus Eren Kalay, for his endless patience, motivation, moral support and presence in my life. I would not do anything and this study would not be completed without him.

TABLE OF CONTENTS

LIST OF SYMBOLS

SYMBOL	MEANING
T_m	Melting temperature
T_g	Glass transition temperature
R_c	Critical cooling rate
T_l	Liquidus temperature
T_x	Crystallization temperature
ΔT_x	Supercooled liquid region
η	Viscosity
t_{max}	Maximum thickness for glass formation
T_g/T_m	Reduced glass transition temperature
R*	Solute atom radius divided by the solvent atom radius
ΔG_f	Formation Gibbs free energy

ΔH_f	Molar enthalpy of fusion
ΔS_f	Molar entropy of fusion
ΔT_r	Reduced undercooling
I_v	Homogeneous nucleation frequency
T_r	Reduced temperature
σ	Solid/liquid interfacial energy
α	Dimensionless parameter related to the σ
β	Dimensionless parameter related to the σ
N	Avagadro's number
V	Molar volume of crystal
u_c	Crystal growth velocity
R	Ideal gas constant
$S_{cc}(0)$	Long wavelength limit
$V_{ij}(r)$	Effective interatomic interaction potential
$W_{ord}(r)$	Interaction energy of ordered structure

w	Interchange energy
α_1	Chemical short-range order parameter
P_{AB}	Probability of A atom exists as a nearest neighbour of B atom
ΔH_{mixing}	Heat of mixing
c_i	Composition of i^{th} component of the alloy
N_i	Number of i atoms
k_B	Boltzmann constant
ΔS_{mixing}	Entropy of mixing
ΔG_{mixing}	Free energy of mixing
G^l	Gibbs Free energy of liquid
G^s	Gibbs Free energy of solid
ΔS^{ideal}	Ideal configurational entropy
ΔS_σ	Mismatch term of entropy
d_i	Atomic diameter
η_0	Pre-exponential term for viscosity

B	Constant corresponding to the activation energy
f_1	Temperature dependent parameter for critical cooling rate
f_2	Temperature dependent parameter for critical cooling rate
D_m	Diffusion coefficient for liquid alloys
σ_i	Parameter depends on size and shape of the diffusing particle
ϕ	Parameter obtained from S_{cc}
Z	Coordination number
ψ_i	Individual electron wave function
Σ_{str}	Total structural energy
U_0	Volume-dependent electronic contributions to total energy of crystal
U_{bs}	Structure-dependent electronic contributions to total energy of crystal
$U_{lattice}$	Coulomb repulsion between the ion cores
E_F^0	Fermi energy level of a free electron gas
Ω	Atomic volume

Ω_0	Volume per ion
$F_p(q)$	Characteristic function of partial ordering energy
z	Effective valancy of atom
$\varepsilon(q)$	Dielectric constant in the Hartree approximation
λ	Ewald parameter
$\varepsilon^*(q)$	Modified dielectric constant on the basis of the correlation and exchange effects
$\overline{\Omega}$	Average atomic volume of the alloy
Q	Configurational partition function

CHAPTER 1

INTRODUCTION

The atomic structure is the most striking characteristic of the amorphous alloy as it fundamentally differentiates amorphous alloy from ordinary metals. The atomic structure of ordinary or conventional metals and alloys is periodic, where the layout of atomic elements shows repeating patterns over an extended range. This atomic structure, called crystalline, limits the overall performance of conventional metals.

Amorphous metallic alloys are metals and metal alloys with no long range atomic order. They have also been called glassy alloys or non-crystalline alloys. They are made of a variety of techniques involving the rapid solidification of the alloying constituents from the gas or liquid phases. The solidification occurs so rapidly that the atoms frozen in their liquid configuration. There are clear structural indications and indications from their various properties that nearest neighbour, or local, order does exist in most amorphous metallic alloys, but no long range atomic order [1].

Bulk metallic amorphous alloys constitute a new and exciting class of metallic materials due to their unique physico-chemical and mechanical properties for structural and functional use. For the formation of an amorphous phase, it is required to solidify from liquid phase to suppress the nucleation and growth reaction of a crystalline phase in the supercooled liquid region between melting temperature (T_m) and glass transition temperaure (T_g). More recently, some exceptions have been reported because of the findings of new multicomponent

amorphous alloys with much lower critical cooling rate (R_c) ranging from 0.100 K/s to several hundreds K/s [2].

The unique physico-chemical and mechanical properties of bulk metallic amorphous alloys explain the strong interest in the development of these materials in view of possible special applications. These bulk metallic amorphous alloys are manufactured by some companies for sporting goods, cases for electronic products, cell phone cases, high performance springs and medical devices [3]. Being a new and interesting subject and due to the present developments, further major applications of bulk metallic amorphous alloys are expected in the near future.

In this study, the work has two main parts; theoretical and experimental. In the theoretical part, literature survey has been done based on bulk amorphous alloys and Zr-based bulk amorphous alloys. Theoretical study on the basis of the semi-empirical rules are well known in literature and the electronic theory of alloys in pseudopotential approximation has been provided in order to predict the right impurity elements that will lead to an increase in the glass forming ability (GFA) of Zr-based multicomponent systems.

Furthermore, theoretical study includes the calculations of the thermodynamic and structural parameters for selected Zr-based binary and multicomponent systems for which an atomistic approach through electronic theory in the pseudopotential approximation were applied. In the experimental part, by using the centrifugal casting method, the production of selected Zr-based binary and multicomponent systems on the basis of theoretical calculations were carried out. The structural characterization of the these systems were done by some characterization tests.

The historical development of bulk amorphous metallic alloys, Zr-based bulk amorphous alloys and their properties, production methods, application fields and theory of glass formation of bulk amorphous alloys will be explained in Chapter Two. In Chapter Three, the informations will be given about the theoretical and

experimental studies. The materials preparation and production technique and structural characterization tests will also be explained. The results of the theoretical and experimental studies and discussion of these results will be given in Chapter Four. In Chapter Five, the conclusions of this study will be summarized. In the last chapter, Chapter Six, in the light of Chapters Four and Five, suggestions for future studies will be given.

CHAPTER 2

THEORY

2. 1. Introduction

The metastable amorphous (or glassy) state of metals is characterized by the lacking of the ordered atomic configuration of crystals resulting in the non-existence of defects such as grain boundaries or dislocations. Due to this structure, amorphous alloys show excellent physico-chemical and mechanical properties.

The advent of metallic glasses has been one of the most exciting events in the annals of materials science and engineering. No other class of materials has, in recent times, so a captured the imagination of scientists, technologists, and engineers alike, or has exhibited such a remarkable and widespread development and growth [4].

In this Chapter, initial part include the sections of historical development of bulk amorphous alloys, properties of bulk amorphous alloys and Zr-based bulk amorphous alloys, their production processes and solidification structures. The following sections will explain some approaches to determine theory of glass formation. These approaches are named as semi-empirical approaches, thermodynamic and kinetic approaches, atomistic approach, and pseudopotential theory. This chapter also gives the ways of calculations of some thermodynamic and structural formulas, required to determine the glass forming ability and used in calculations in following chapters.

2. 2. Historical Development of Bulk Amorphous Alloys

Amorphous materials have been employed for thousands of years, e.g. in the glass making industry. The preparation of metallic amorphous alloys was first reported shortly after the Second World War when Brenner and Riddell (1946) reported on electrolytically deposited amorphous Ni-P films. Since the first synthesis of an amorphous phase in the Au-Si system by a rapid solidification technique in 1960 [5], a great number of amorphous alloys have been produced for the last three decades. In the early 1960's, Duwez and his group (Klement, Willens and Duwez, 1960) began extensive research on metastable alloys prepared by rapid solidification of liquid alloys. First ferromagnetic amorphous alloys were reported by Mader and Nowik (1965) and the attractive soft magnetic properties were observed soon after (Tsuei and Duwez, 1966). The technological potential of these metastable materials then became appreciated in conjunction with the more basic scientific interest in the alloys.

The search for other alloy compositions that could be produced as bulk amorphous alloys began and resulted a few years later in a series of new alloy compositions. More recently, since 1988, it has been succeeded in finding new multi-component alloy systems with much lower critical cooling rates in the Mg, Ln, Zr, Fe, Pd-Cu-, Pd-Fe-, Ti- and Ni-based alloy systems [6]. The Mg-based (Inoue, Ohtera, Kito and Masumoto, 1988), lanthanide-based (Inoue, Zhang and Masumoto, 1989), Zr- and Hf-based (Inoue, Zhang and Masumoto, 1993), Ti-based (Inoue, Nishiyama, Amiya, Zhang and Masumoto, 1994) and Ni-based (Yi, Park and Kim, 2000) are among the alloy systems that so far have been developed and investigated.

Bulk amorphous alloys and nanocrystalline materials have been synthesized in a number of ferrous and non-ferrous based alloys systems, which have gained some applications due to their unique physico-chemical and mechanical properties. Table 2.1 summarizes the alloy systems of the bulk amorphous alloys, calender years when their alloy systems were found, and the maximum sample thickness

(t_{max}) for glass formation [2]. The first alloy systems developed were nonferrous alloy systems, and then followed by ferrous alloy systems.

Table 2.1. New multicomponent alloy systems with large glass-forming ability, when their alloy systems' found years, and the maximum sample thickness for glass formation [2].

I. Nonferrous Metal Base	**Years**	**t_{max}(mm)**
Mg-Ln-M (Ln = Lanthanide metal, M = Ni, Cu or Zn)	1988	
Ln-Al-TM (TM = VI-VIII transition metal)	1989	10
Ln-Ga-TM	1989	
Zr-Al-TM	1990	30
Zr-Ti-Al-TM	1990	
Ti-Zr-TM	1993	
Zr-Ti-TM-Be	1993	25
Zr-(Nb,Pd)-Al-TM	1995	
Pd-Cu-Ni-P	1996	72
Pd-Ni-Fe-P	1996	
Pd-Cu-B-Si	1997	
Ti-Ni-Cu-Sn	1998	
II. Ferrous Group Metal Base	**Years**	**t_{max}(mm)**
Fe-(Al, Ga)-(P, C, B, Si, Ge)	1995	3
Fe-(Nb, Mo)-(Al, Ga)-(P, B, Si)	1995	
Co-(Al, Ga)-(P, B, Si)	1996	
Fe-(Zr, Hf, Nb)-B	1996	
Co-Fe-(Zr,Hf,Nb)-B	1996	
Ni-(Zr, Hf, Nb)-(Cr-Mo)-B	1996	
Co-(Zr, Hf, Nb)-B	1997	
Ni-(Zr, Hf, Nb)-B	1997	
Fe-(Co, Ni)-(Zr, Hf,Nb)-B	1997	6
Fe-Co-Ln-B	1998	
Fe-(Nb, Cr, Mo)-(P, C, B)	1999	
Ni-(Nb, Cr, Mo)-(P, B)	1999	

2. 3. Bulk Metallic Amorphous Alloys

Bulk metallic amorphous alloys (bulk metallic glasses) are currently a subject of numerous investigations because of their interest for both fundamental science and engineering applications [7]. They possesses some of the characteristics of ordinary oxide glasses in that they exhibit random, non-crystalline arrangements of atoms, a glass transition temperature, generally live up to the description of supercooled liquid. Bulk metallic amorphous alloys are primarily composed of metallic elements and the interatomic bonding between them is essentially metallic in character. These features have enabled the appearance of various kinds of characteristics such as good mechanical properties, useful physical properties and unique chemical properties, which have not been obtained for conventional crystalline alloys [4]. The differences between traditional metals, traditional (oxide) glasses, and metallic glasses are summarized in a simple and effective manner by the data in Table 2.2 [4].

Table 2.2. Comparison of the characteristics of traditional metals, traditional glasses, and metallic glasses [4].

Property	**Traditional metal**	**Traditional glass**	**Metallic glass**
Structure	Crystalline	Amorphous	Amorphous
Bonding	Metallic	Covalent	Metallic
Strength	Non-ideal	Almost ideal	Almost ideal
Workability	Good, ductile	Poor, brittle	Good, ductile
Hardness	Low to high	Very high	Very high
Corrosion resistance	Poor to good	Very good	Very good

More recently, amorphous alloys have also attracted increasing interest as a precursor to produce nanocrystalline alloys containing a remaining amorphous phase by partial crystallization because of the appearance of good mechanical properties, soft magnetism, hard magnetism, high magnetostriction in low applied

fields, and high catalytic properties that have not been obtained for amorphous or crystalline single-phase alloys. [2].

During the last decade, much attention has been devoted to the development of bulk metallic glasses. The critical cooling rate for solidification of these alloys is less than 10^3 °C/s, and amorphous products with thicknesses of 1 mm and greater can be produced by a conventional casting process. Bulk metallic glass alloys have been obtained in Zr, Ti, Ni, Cu, and Mg based systems [8, 9], and more recently in Ca–Mg–Cu and Ca–Mg–Ag–Cu systems [10, 11]. Based on these research results, scientific and engineering importance of the amorphous and nanocrystalline alloys has increased significantly for the last three decades.

2. 3. 1. Zirconium Based Bulk Amorphous Alloys

In the late 1980s, Inoue [12], Zhang [13] and Peker and Johnson [14] developed a series of Zr- and La-based amorphous alloys that have a very low critical cooling rate and a large supercooled region. Recently, several families of Zr-based multicomponent amorphous alloys have been reported to exhibit excellent glass-forming ability. These include Zr-Ni-Cu-Al [15], Zr-Ni-Ti-Cu-Be [13], Zr-Ti-Cu-Ni [16], and Zr-Ti(Nb)-Cu-Ni-A [17] with the critical cooling rate for glass formation in 1-100 Ks^{-1} range. Zr-based alloys exhibit the best combination of good mechanical properties, excellent corrosion resistance and low thermal expansion coefficient [18-21].

Zirconium-based alloys show many interesting phase transformations. One of these is the ability to form metallic glasses [22]. The reasons for extensive work carried out in the field of non-crystalline zirconium-based alloys are:

(i) Ability to form metal–metal metallic glasses,
(ii) Ability to form glass in wide composition ranges,
(iii) Specific glass to crystal transformation modes shown by these amorphous alloys [23].

Many of the Zr-based glasses crystallise to crystalline phases of the same composition. These alloys provide opportunities for examining the effect of atomic arrangement alone on properties, without any interference from change in chemistry of the phase [24].

In the Zr–Fe, Zr–Co, Zr–Ni, Zr–Be, Zr–Cu and Zr–Cr systems which have many common features, rapid solidification has yielded amorphous phase over very large composition ranges [25–27]. In some of these systems the as-solidified microstructure has been examined in detail [28–32]. The microstructures resulting from rapid solidification of these alloys have been found to be fully amorphous or partially crystalline depending upon the cooling rate and the glass forming ability of the alloys. Zr-based alloys have also acquired considerable significance because of the fact that these can form bulk metallic glasses [17].

Table 2.3 shows some of the thermal properties of Zr-based bulk amorphous alloys, obtained from the literature survey. These properties, taken from the DSC tests, include heating rate, the glass transition temperature, T_g, crystallization temperature, T_x, supercooled liquid region, ΔT_x, melting temperature, T_m, liquidifying temperature, T_l, T_g/T_m, T_g/T_l and enthalpy of crystallization, ΔH values.

Table 2.3. Thermal properties of some of the Zr-based bulk metallic amorphous alloys.

Alloy Systems	Heating rate (K/min)	T_g (K)	T_x (K)	ΔT_x (K)	T_m (K)	T_l (K)	T_g/T_m	T_g/T_l	ΔH (J/g)
$Zr_{65.5}Al_{5.6}Ni_{6.5}Cu_{22.4}$ [33]	40.2	636	733	97	1090	1211	0.584	0.525	
$Zr_{65.3}Al_{6.5}Ni_{8.2}Cu_{20}$ [33]	40.2	640	745	105	1090	1188	0.588	0.539	
$Zr_{65}Al_{17.5}Ni_{10}Cu_{17.5}$ [33]	40.2	650	750	100	1094	1153	0.594	0.564	
$Zr_{64.8}Al_{8.3}Ni_{11.4}Cu_{15.5}$ [33]	40.2	653	752	99	1086	1143	0.602	0.572	
$Zr_{64.5}Al_{9.2}Ni_{13.2}Cu_{13.1}$ [33]	40.2	658	757	99	1090	1138	0.604	0.578	
$Zr_{63.8}Al_{11.4}Ni_{17.2}Cu_{7.6}$ [33]	40.2	671	758	87	1100	1153	0.610	0.582	
$Zr_{65}Al_{7.5}Ni_{10}Cu_{17.5}$ [33]	20	374	461	87					60
$Zr_{50}Al_{10}Ni_{17}Cu_{18}Ti_5$ [34]	20	399	445	46					49
$Zr_{65}Al_{7.5}Ni_{10}Cu_{17.5}$ [35]	40	651	764	113					
$Zr_{60}Al_{10}Ni_9Cu_{18}Co_3$ [35]	40	668	766	98					
$Zr_{60}Al_{10}Ni_9Cu_{18}B_3$ [35]	40	655	753	98					
$Zr_{52.5}Al_{10}Ni_{14.6}Cu_{17.9}Ti_5$ [36]	10.2	686	647	39	1075		0,638		
$Zr_{35}Hf_{17.5}Al_{10}Ni_{14.6}Cu_{17.9}Ti_5$ [36]	10.2	708	663	45	1126		0,629		
$Zr_{60}Al_{10}Cu_{30}$ [37]	40.2	676	748	72					
$Zr_{60}Al_{10}Cu_{20}Pd_{10}$ [37]	40.2	699	761	62					

2. 3. 2. Fundamental Characteristics and Application Fields

Based on a large number of experimental data on the bulk amorphous alloys for the last ten years, it is confirmed that the bulk amorphous alloys, exhibit various useful characteristics, are produced in the diameter range of 1 to 100 nm. These characteristics are much superior to those for the corresponding crystalline alloys and excellent enough to be used as practical materials. Table 2.4 summarizes the fundamental characteristics and application fields of bulk amorphous alloys [38].

Table 2.4. Fundamental characteristics and application fields of bulk metallic amorphous alloys [38].

Fundamental Characteristics	Application Fields
High strength	Machinery structural materials
High hardness	Optical precision materials
High impact fracture energy	Tool materials
High elastic energy	Electrode materials
High corrosion resistance	Corrosion resistant materials
High wear resistance	Hydrogen storage materials
High viscous flowability	Ornament materials
Good soft magnetism	Writing applicance materials
High magnetostriction	Bonding materials
High frequency permeability	Sporting goods materials
High hydrogen storage	High magnetostrictive materials

The bulk amorphous alloys in Zr-Al-Ni-Cu, Zr-Ti-Al-Ni-Cu and Zr-Nb-Al-Ni-Cu systems have already been commercialized as various kinds of golf clubs, i.e., putter-, iron- and wood-type clubs. The bulk amorphous alloys in Zr-Ti-Be-Ni-Cu system have also been used in the face parts of putter- and iron-type golf clubs [39]. The bulk amorphous alloys have important and useful characteristics, therefore the application fields of the bulk amorphous alloys are seemed to be extended in the future.

2. 3. 3. Production Methods of Bulk Metallic Amorphous Alloys

Bulk metallic amorphous alloys can be produced by various methods. These methods can be summarized as follows:

1. **High-Pressure Die Casting Method:** By choosing the Mg-Ln-TM and Ln-Al-TM ternary alloys with the wide supercooled liquid region and the high glass forming ability, bulk amorphous alloys have been produced in a thickness range up to about 10 mm in cylindrical and sheet shapes by the high pressure die casting method [2].

2. **Water Quenching Method:** The further multiplication of alloy components from ternary to quaternary and penternary systems causes a further decrease in R_c to 1 to 10 K/s which are almost comparable to those for oxide glasses. The quaternary Pd-Cu-Ni-P and Zr-Al-Ni-Cu alloys have been amorphized into a bulk form with 72 mm (ϕ) x 75 mm and 16 mm (ϕ) x 150 mm, respectively, by quenching their molten alloys in a quartz tube into water [2].

3. **Copper Mold Casting Method:** Zr-based bulk amorphous alloys have been vitrified by ejection of the melt into copper molds [2].

4. **Arc Melting Method:** By choosing the quaternary or penternary alloys in Zr-Al-TM (TM = Co, Ni, Cu) system, bulk amorphous alloys can be produced by arc melting on a copper hearth. However, in this method, it is very difficult to suppress completely the precipitation of the Zr_2TM crystalline phase because of the ease of the heterogeneous nucleation by incomplete melting at the bottom side contacted with copper heart. It is to be noticed that, an amorphous phase is formed in the inner region where the heat of flux reinforced from copper hearth disappears and the cooling capacity is reduced. That is, the low cooling rate obtained by arc melting is high enough to cause an amorphous phase in Zr-Al-Co-Ni-Cu system [2].

5. **Unidirectional Zone Melting Method:** A continuous bulk amorphous alloy is produced by the this method using an arc-type heat source. This method is useful for the production of a continuous bulk amorphous alloy with a homogeneously mixed alloy composition, when an alloy with R_c much lower than about 10^3 K/s is used. The successs of producing the bulk amorphous alloy by this method also implies the significant relaxation of the shape and dimension of amorphous alloys which have been limited to thin sheet, fine wire and small powder shapes [2].

6. **Suction Casting Method:** The suction casting method is used for the elimination of cavity and hole because of the solidification under a sucking

force and the rapid solidification resulting from the fast movement of the sucked metal [2].

2. 4. Formation of Bulk Metallic Amorphous Alloys

2. 4. 1. Undercooling of the Melt and Glass Formation

A non-crystalline solid phase represents the ultimate state of solid metastability and may be formed by a number of different routes, including solidification from the liquid or vapor states, deposition from a chemical solution or an electrolyte and by high-energy ion or neutron-bombardment of crystalline materials. A non-crystalline solid formed by continuous cooling from the liquid state is known as a glass in the original sense of the word. The vitrification of a melt requires that it be cooled at a rate sufficiently high to avoid a significant degree of crystallization, so that the disordered atomic configuration of the liquid state is frozen-in, or at least largely so.

When a metal or alloy melts, the three dimensional lattice arrangement of atoms, the long range order, is destroyed. During melting, the crystal and liquid phases are in equilibrium and for pure metals, the volume, enthalpy and entropy undergo discontinuous change; the enthalpy and entropy increase, and the volume usually does also. A liquid, at temperatures above the melting point, is in a state of internal equilibrium and its structure and properties are independent of its thermal history. Metallic liquids have high fluidity because of the non-directional nature of the metallic bond while, in contrast, molten silicates, borates and similar substances, in which the atomic bonding is strongly covalent, are characterized by very low fluidity or, conversely, high viscosity.

When a liquid is cooled down below its melting temperature, T_m, either crystallization or undercooling may occur. During the latter process, homogeneous nucleation of crystalline phases is suppressed for an extended period of time. If the cooling rate is sufficiently high, homogeneous nucleation of crystalline phases can be completely avoided. Then, with decreasing temperature,

the undercooled liquid becomes more and more viscous and finally falls out of equilibrium into the structurally arrested glassy state. Microscopically, the glassy state is characterized by a lack of long-range atomic order and is very similar to a frozen-in liquid.

Upon cooling, a liquid must undercool below the equilibrium crystallization temperature before crystallization can begin because of the existence of an energy barrier to the formation of nuclei. The degree of undercooling that occurs depends on several factors. Viscosity is the key parameter to describe the kinetic slowdown when a melt is undercooled below its liquidus temperature. The increase of initial viscosity of the liquid with undercooling reflects the increasingly longer time scale for structural rearrangements in the supercooled liquid state. Non-glass-forming liquids usually have $\eta = 10^{-3}$ Pa s at the equilibrium melting point, whereas, for metallic glass-formers, η is of the order of $\sim 10^{-1}$ Pa s at T_m and increases up to $\sim 10^{12}$ Pa s in correspondence of T_g [40]. As a consequence, mobility is progressively reduced, nucleation is retarded and the system can be vitrified before its crystallization. From the Figure 2.1, viscosity (η) – temperature (T) relationship corresponding to crystallization and vitrification of a metallic melt is seen.

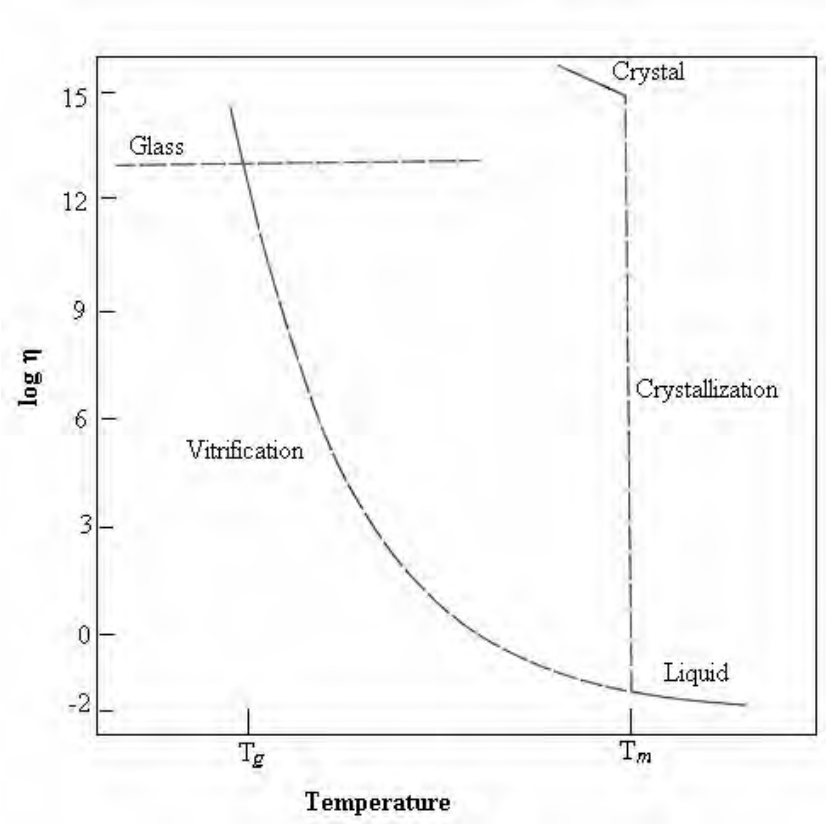

Figure 2.1. Viscosity (η) – temperature (T) behavior corresponding to crystallization and vitrification of a metallic melt.

Furthermore, the temperature dependence of the free energy difference between the undercooled liquid and the crystal phase, the interfacial energy between melt and the crystal, the volume density and the efficacy of heterogeneous nucleating particles and the imposed cooling rate are the factors that effect the degree of undercooling. When the cooling rate is sufficiently high, crystallization is suppressed because of insufficient time for significant growth or, in extreme, for nucleation. Then, the atomic configuration of the liquid departs from equilibrium and shortly thereafter becomes homogeneously frozen, at the so-called glass transition temperature T_g.

Glass formation occurs easily in some familiar classes of non-metallic material such as silicates and organic polymers. In these, the nature of the bonding places severe limits on the rate at which the atomic or molecular rearrangements, necessary for maintaining thermodynamic equilibrium during cooling, can occur; thus the melt

solidifies to a glass, even at low rates of cooling often less than 10^{-2} K/s. Metallic melts, in contrast, have non-directional bonding, so that atomic rearrangements occur very rapidly, even at high degrees of undercooling below their equilibrium freezing temperatures. The difference between phase transitions of conventional and bulk amorphous metallic alloys can be seen from the Figure 2.2.

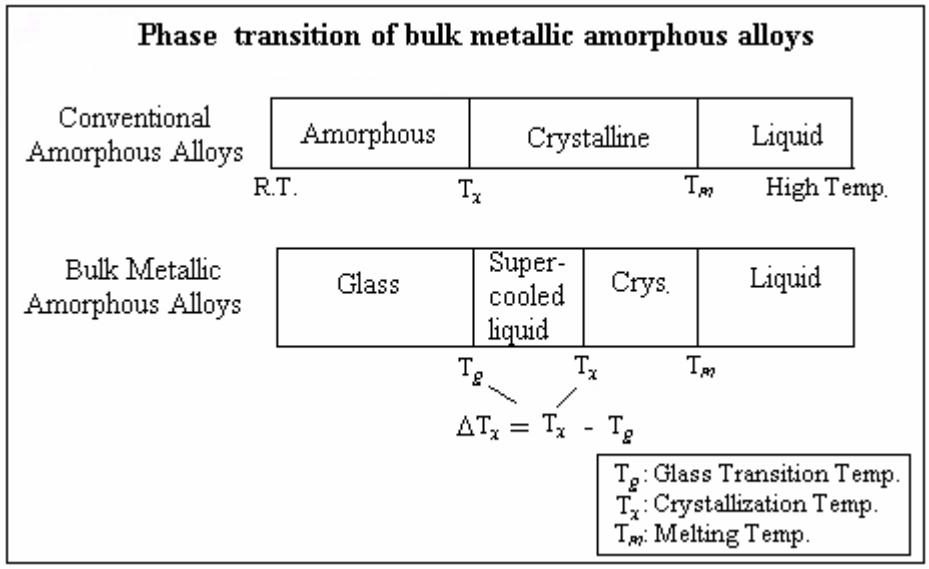

Figure 2.2. The feature of the phase transition of bulk metallic amorphous alloys by continuous heating in comparison with that for conventional amorphous alloys which require high cooling rates above 10^4 K/s for glass formation [2].

2. 5. Theory of Glass Formation

In order to understand the metallic glass formation phenomena, there exist some approaches. These approaches are named as; semi-empirical approach, thermodynamic and kinetic approaches and atomistic approach. Following sections give explanations of these approaches.

2. 5. 1. Semi-empirical Approach

It is essential for the formation of an amorphous phase by solidification from liquid phase to supress the nucleation and growth reaction of a crystalline phase in the supercooled liquid region between melting temperature (T_m) and glass transition temperaure (T_g). More recently, new multicomponent amorphous alloys were produced with much lower critical cooling (R_c) ranging from 0.100 K/s to several hundreds K/s, as shown in Figure 2.3. Simultaneously, the maximum thickness for glass formation (t_{max}) increases drastically from several milimeters to about one hundred milimeters.

It can be proposed that the lowest R_c and the largest t_{max} are almost comparable to those for ordinary oxide and fluoride glasses. Figure 2.3 shows the relationship between the critical cooling rates (R_c), maximum sample thickness (t_{max}) and reduced glass transition temperature (T_g/T_m) for amorphous alloys reported to date. The new amorphous alloys have higher (T_g/T_m) above 0.60 and the highest (T_g/T_m) value reaches 0.73.

Furthermore, one important parameter that effect the glass forming ability of alloys is the temperature difference between the crystallization temperature (T_x) and T_g, $\Delta T_x(=T_x-T_g)$. The glass formation will be easier, if ΔT_x, supercooled liquid region, becomes higher. The new multicomponent amorphous alloys have a much wider supercooled liquid region before crystallization which is defined by the difference, as shown in Figure 2.4. From the empirical strong relations between R_c, t_{max} and T_g/T_m or ΔT_x shown in Figure 2.3 and Figure 2.4, it can be proposed that the high glass-forming ability is obtained in the satisfaction of the following two factors [2];

(i) High T_g/T_m
(ii) Large ΔT_x

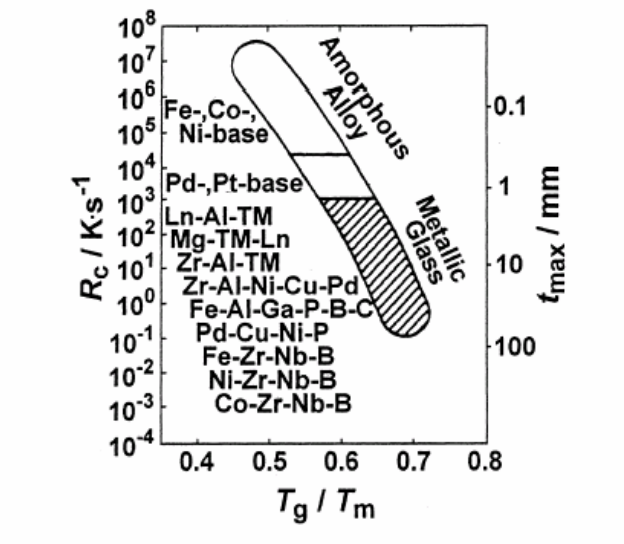

Figure 2.3. Relationship between the R_c, t_{max} and (T_g/T_m) for bulk amorphous alloys [2].

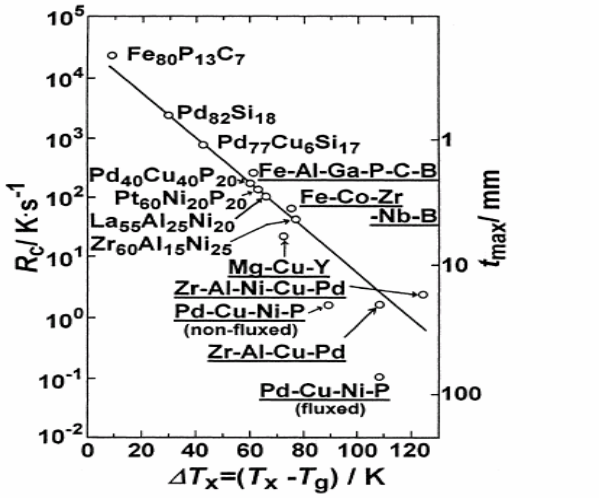

Figure 2.4. Relationship among R_c, t_{max} and ($\Delta T_x = T_x - T_g$) bulk amorphous alloys [2].

As summarized in Table 2.1, the bulk amorphous alloys consist of multicomponent systems containing Mg, Ln, Zr, Pd, Fe or Co as a main constituent element. Based on the multicomponent systems for the amorphous alloys with high glass forming ability, it has been noticed the existence of simple three emprical rules for the achievement of high glass forming ability for bulk amorphous alloys as follows:

1. The multicomponent system consisting of more than three elements.
2. Significant difference in atomic size ratios above about 12% among the main constituent elements.
3. Negative heats of mixing among their elements.

Table 2.4 summarizes the reasons for the achievement of the high glass forming ability of some multicomponent amorphous alloys in Ln-, Mg-, Zr-, Pd-, Fe- and Co- based systems.

Table 2.4. Summary of the reasons for the achievement of the high glass forming ability for some ternary alloy systems such as Zr-Al-TM, Ln-Al-TM and Mg-Ln-TM, etc. (Ln = Lanthanide metal, TM = Transition metal) [2].

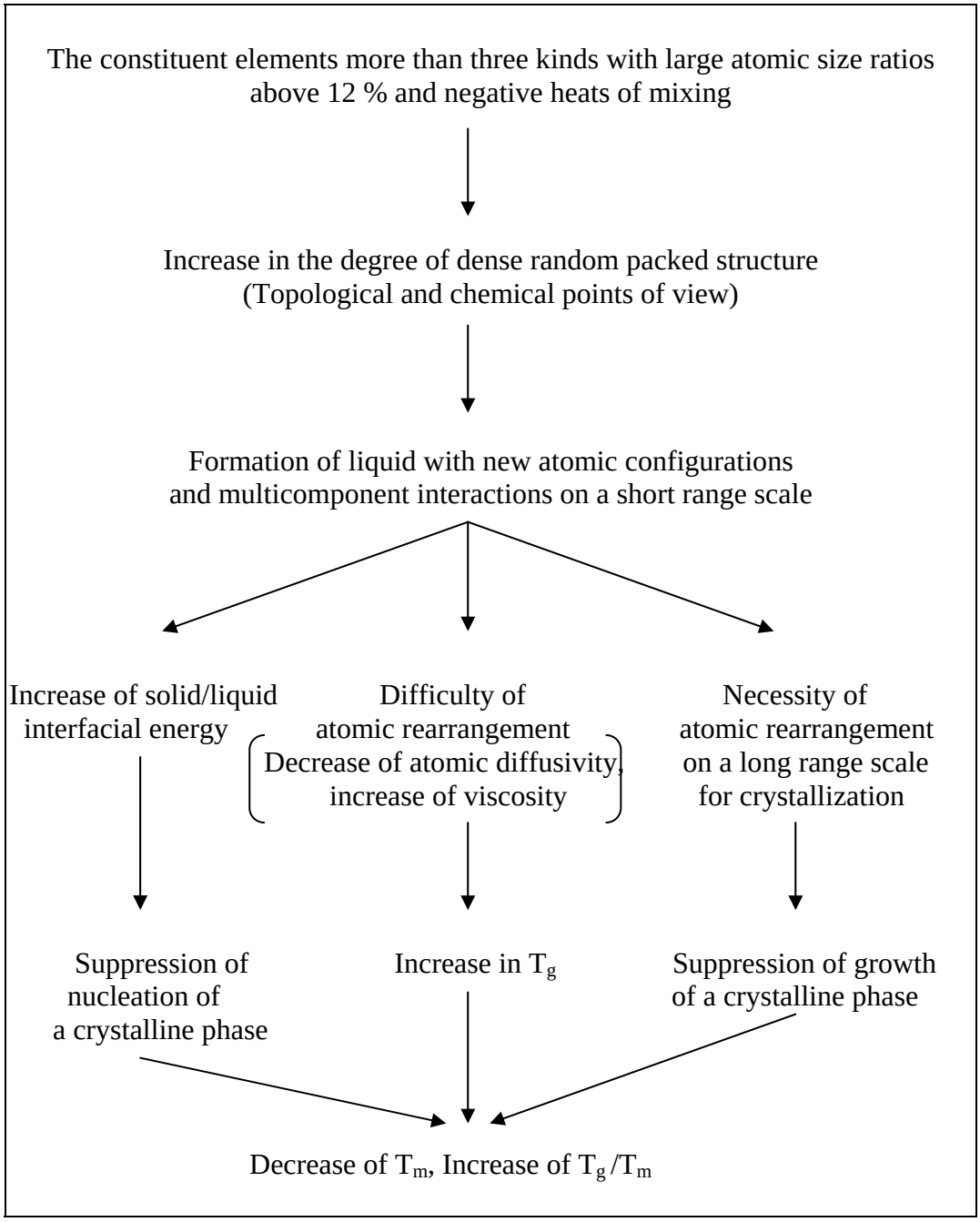

It is confirmed that high glass forming ability is attributed to the formation of a new kind of supercooled liquid with a higher degree of dense random packing density, new short range atomic configurations and long range atomic

interactions. That is, the peculiar liquid structure can have a higher liquid/solid interfacial energy leading to the suppression of nucleation of a crystalline phase, a higher viscosity, and a lower atomic diffusivity leading to the increase in T_g, and the necessity of long-range atomic rearrangements leading to the degradation of growth reaction of a crystalline phase [2].

The multicomponent alloys with the low nucleation and growth reactions and low atomic diffusivity can have a deep valley in melting temperature such as a deep eutectic point, leading to the high-reduced glass transition temperature (T_g/T_m) values, in addition to the large ΔT_x. Furthermore, the high thermal stability of the supercooled liquid against crystallization also implies the appearance of the large ΔT_x values [2].

Recently, additional and more specific criteria for easy glass forming alloy systems have been developed [41–44] which narrow selection of the alloying elements and their concentrations based on the relative atomic sizes R* of these elements. (R* is defined as the radius of the solute atom divided by the radius of the solvent atom.) It was found that most of the bulk amorphous alloys have a characteristic dependence of the atomic concentrations of the alloying elements on their R* [41, 42]. The solvent element generally has the largest atom size in these systems. Atomic concentrations of other alloying elements decrease, or show a minimum at an intermediate atomic size and then increase with decreasing atomic size, so that the smallest element often has the second highest concentration.

This concave upward shape of the so-called atomic size distribution plot (ASDP) typical for many bulk amorphous alloys is completely different from the concave downward shape for marginal amorphous alloys, in which the main element (solvent) has an intermediate size [41, 42]. These characteristic atomic size distributions correlate with low molar volume and high packing efficiency of atoms in bulk metallic glasses [44–46]. Topological [42] and thermodynamic [43] models have recently been developed to explain such a behavior. The latter model also predicts an increase in the glass forming ability with an increase in the atom

size of the solvent element. This prediction agrees with the experimental observation that amorphization of alloys based on elements with large atomic radii, such as zirconium or rare earth metals, occurs much easier than alloys based on elements with smaller atomic radii, such as aluminum. It also agrees with an earlier prediction of Davies [1] that the rate of crystallization decreases with an increase in the size of the solvent.

An analysis of the influence of the efficient atomic packing on the constitution of metallic glasses has recently been conducted [44]. This analysis has shown that critical values of R*, such as 0.62, 0.71, 0.80, 0.88, 0.90, etc., are preferred in the constitution of metallic glasses. Based on these recent developments [41–44], new criteria for selection of bulk metallic glass compositions can be formulated as follows:

1. A solvent (main) element is selected with an atom radius of 0.15 nm or larger. The larger is the radius of the solvent element, the better can be expected the glass forming ability of the corresponding alloy.

2. Two or more solute elements are selected with atom radii that correspond to critical values of R*, relative to the selected solvent element. Because of some uncertainties in the determination of the atomic radii, R can deviate from the critical R* values by up to 3% [43].

3. The number of the solute elements with R of ~0.62, 0.71 and 0.80 is further narrowed by leaving only elements that form binary eutectics with the solvent and each other.

4. The concentrations of the selected elements for a certain alloy are chosen in such a way that, the atomic concentration of the solvent element is selected in the range of 40–70%, the concentrations of the solute elements with R of ~0.62 and/or ~0.71 are in the range of 15–35% and are higher than the concentrations of the elements with R of ~0.8, 0.88, and/or 0.90.

2. 5. 2. Thermodynamic and Kinetic Approaches

Bulk amorphous alloys are obtained by rapidly quenching of the melt at a quenching rate, which is high enough to prevent crystallisation. In order to consider glass forming ability, nucleation and growth kinetics should be considered. It is generally known that the high glass-forming ability is obtained in the condition of low free energy, ΔG_f, for the transformation of liquid to crystalline phase. Thermodynamically glass formation is favoured in certain composition ranges of some systems where the free energy difference between the supercooled liquid and the metastable and stable phases competing with glass formation is as little as possible [2]. In the following relation for Gibbs free energy, the low ΔG_f value is obtained in the cases of low ΔH_f and large ΔS_f. Here, ΔH_f and ΔS_f are molar enthalpy of fusion and molar entropy of fusion, respectively.

$$\Delta G_f = \Delta H_f + T\Delta S_f \quad (1)$$

Based on the thermodynamic aspects, it is concluded that the multiplication of alloy components leading to the increase in ΔS_f causes an increase in the degree of dense random packing, which is favourable for decreasing ΔH_f and increasing solid/liquid interface energy. The interpretation is consistent with the result that the high glass-forming ability has been obtained for multi-component systems containing more than three elements. ΔG_f can be given by the below equation [2]

$$\Delta G_f = \Delta H_f \Delta T_r \quad (2)$$

where ΔT_r, is the reduced undercooling, $(T_l\text{-}T)/T_l$.

From the point of kinetic view, the homogeneous nucleation frequency, I_v, of a crystalline phase with a spherical morphology from supercooled liquid, can be expressed by the following relation;

$$I_v = \frac{k_n}{\eta(\mathrm{T})} \exp\left[-16\pi\alpha^3\beta / 3T_r\Delta T_r^2\right] \quad (3)$$

where, T_r is the reduced temperature T/T_l, k_n is a kinetic constant, $\eta(T)$ is the shear viscosity at temperature T (which is inversely related to the atomic diffusivity, D), α and β dimensionless parameters related to the liquid/solid interface energy (σ), ΔH_f and ΔS_f can be expressed as;

$$\beta = \Delta S_f / R \quad (4)$$

$$\alpha = \left(N\overline{V}^2\right)^{1/3} \sigma / \Delta H_f \quad (5)$$

N is the Avagadro's number and V is the molar volume of crystal. It is evident from the homogeneous nucleation frequency equation that, as the magnitude of $\alpha\beta^{1/3}$ increases, I_v decreases very steeply, for a given temperature and viscosity of the melt.

The isothermal crystallization kinetics of amorphous alloys is normally modelled by the Johnson-Mehl-Avrami (JMA) following equation

$$x \approx I_v u_c^3 t^4 \quad (6)$$

where t is the time, I_v is the nucleation frequency and u_c, the crystal growth velocity, can be expressed as:

$$u_c = \frac{k_B T_f}{3\pi a_0^2 \eta}\left[1 - \exp(-\Delta T_r \Delta H_f / RT\right] \quad (7)$$

In this equation, k_B is Boltzmann's constant, f is the fraction of sites at the crystal surfaces where the atomic attachment can occur (f will be equal to one for closed

packed crystals and $0.2\Delta T_r$ for facetted crystals) and a_0 is the mean atomic diameter [2].

In faceted materials, such as intermetallic compounds or minerals, substances exhibit complex crystal structures, and directional bonding from crystals having planar, angular surfaces (facets). The inherently rough, high index planes accept added atoms readily and grow quickly. As a result, these planes disappear and the crystal remains bounded by the more slowly growing facets.

During a solidification of a non-faceted material, such as a metal, it can be assumed that the kinetics of transfer of atoms from the liquid to the crystal is so rapid that they can be neglected. Metals and a special class of molecular compounds (plastic crystals), usually solidify with macroscopically smooth solid/liquid interfaces and exhibit no facets, despite their crystalline nature. In non-faceted material, atoms can be added easily to any point of the surface.

The classes of non-faceted and faceted crystals can be distinguished on the basis of the higher entropy of fusion of the latter. This is due to the greater difference in structure between the solid and liquid phases as compared to metals, which exhibit only very small differences between the two phases. The melting entropy is a convenient criterion for predicting this aspect of the crystallization behavior. Values of β ($=\Delta S_f / R$) which are less than ~2 can be taken to imply a tendency to non-faceted crystal growth, while higher α-values imply that faceted growth forms will produced [47].

2. 5. 3. Atomistic Approach

2. 5. 3. 1. Atomic Ordering in Liquid Alloys

From the interatomic interactions' point of view of a binary alloy can be either:

(i) An ordered alloy, where unlike atoms are preferred as nearest neighbours over like atoms, or

(ii) A segregated alloy, where like atoms are preferred to pairs as nearest neighbours over unlike atoms.

Unfortunately, there is no direct way to distinguish the constituent atoms and hence the identification of a nearest-neighbour pair of atoms is problematic. In this case either the structural data or the observed thermodynamic functions (such as chemical activity, heat of mixing, excess Gibbs energy of mixing, excess heat capacity, etc) or other thermo physical data (such as viscosity, diffusivity, density, surface tension, electrical resistivity, etc) are considered to extract information associated with interatomic interactions. Some of the empirical criteria as well as microscopic parameters, used to identify ordered alloy, are summarizing as [48]:

(a) Alloys exhibiting negative deviations from Raoult's law,
(b) The heat of formation and the excess Gibbs energy of mixing are negative,
(c) The concentration fluctuation in the long wavelength limit ($S_{cc}(0)$) is less than the ideal value,
(d) If $V_{ij}(r)(i, j = A, B)$ is the effective interatomic interaction potential, then one can define the radial form of the order potential, i.e.,

$$W_{ord}(r) = 2V_{AB}(r) - \left(V_{AA}(r) + V_{BB}(r)\right) \tag{8}$$

For ordered alloys, $W_{ord}(r) < 0$ around the nearest-neighbour distances is required.

(e) In the framework of regular solution theory, the interchange energy should be $w < 0$.

(f) The Warren–Cowley short-range order parameter, α, $\alpha < 0 (-1 \leq \alpha \leq 0)$.

2. 5. 3. 2. Atomistic Approach to Binary Ordered Liquid Alloys

Consider that two liquid metals, say A and B, at standard state are mixed together to form an alloy. On mixing, if A and B atoms prefer to remain self-coordinated

(i.e. A–A pair or B–B pair) over the hetero-coordinated (i.e. A–B pair), then it is called segregating alloy. Phase separation is an extreme condition of segregation. In order to quantify it, let consider the Warren–Cowley (Warren 1969, Cowley 1950) short-range order parameter, α_1, for the first-neighbour shell which is defined in terms of the conditional probability, P_{AB};

$$P_{AB} = c_A(1-\alpha_1) \tag{9}$$

where P_{AB} defines the probability that an A atom exists at one site as a nearest neighbour of a given B atom at other site. Equation provides an immediate insight into the local arrangement of atoms in the mixture. For a random distribution of atoms, $P_{AB} = c_A$, then $\alpha_1=0$. If $\alpha_1 > 0$, then A–A or B–B pairs of atoms are preferred over A–B pairs as nearest neighbours. By taking a probabilistic approach one can easily show that the limiting values of α_1 lie in the range

$$-\frac{c_A}{c_B} \le \alpha_1 \le 1 \qquad \text{for} \quad c_A \le 1/2 \tag{10}$$

$$-\frac{c_B}{c_A} \le \alpha_1 \le 1 \qquad \text{for} \quad c_A \ge 1/2 \tag{11}$$

For $c_A = c_B = 1/2$, one has

$$-1 \le \alpha_1 \le 1 \tag{12}$$

The minimum possible value, $\alpha_1^{min} = -1$, means complete ordering of A–B pairs in the melt, whereas the maximum value, $\alpha_1^{max} = 1$, suggests that A–A and B–B pairs in the melt are totally segregated. For ordering statement, α_1 varies from –1 to 0 [48].

2. 5. 3. 3. Importance of Ordering Energy on Glass Forming Ability

In this study, the glass forming ability of alloys were tried to determine by semi-empirical approaches, thermodynamic and kinetic approaches, atomistic approach, and pseudopotential theory. In the previous sections, factors effecting the glass forming ability and the reasons of their influence on the glass forming ability were determined. In the following sections, the calculation ways of these factors will be given. As mentioned in the previous section, negative heat of mixing is very effective factor in order to obtain high glass forming ability. During the calculation of ΔH_{mixing}, ordering energy values, obtained from the computer program based on the pseudopotential theory, were used. Therefore, high negative ordering energy values are required to satisfy high negative heat of mixing. Due to the given dependence, ordering energy values underlie the factors effecting the glass forming ability.

2. 5. 4. Approaches for Thermodynamic and Structural Parameters Calculations

Thermodynamic and structural parameters are very important in order to understand the glass forming ability of alloys. In this study, two approaches were used, for simplicity these approaches can be named as; Inoue's and Singh and Sommer's approaches. By these two approaches, thermodynamic and structural parameters were calculated for both binary and ternary alloy systems. Singh and Sommer's approach can be used only for binary alloys, whereas Inoue's for both binary and ternary alloys. Following sections will give detailed explanations and the ways of calculations of the parameters for these approaches.

2. 5. 4. 1. Heat of Mixing and Entropy of Mixing for Binary and Ternary Alloy Systems

2. 5. 4. 1. 1. Singh and Sommer's Approach for Binary Alloy Systems

Thermodynamic data and phase diagrams of alloys play an important role in understanding the properties of these materials and in developing their production processes. Miedema [49-53] have described such a model to calculate the enthalpy of formation of solid and liquid alloys. This model is simple and has the great advantage that the ethalpy of formation can be calculated for alloys where no experimental information is available.

The quasi-lattice theory (QLT) of mixtures is based on the ideas underlying Guggenheim's theory of mixture of polymers [54]. He showed systematically that the statical theory based on the partition function approach and the quasi-lattice theory lead to similar results.

The consideration of the energetic effect of the binary mixture, QLT provides an explicit expression for heat of mixing for liquid alloy, ΔH_{mixing}. Let N_A be the number of A atoms, i.e., N_A occupy a group of γ_1-lattice sites and N_B occupy γ_2-lattice sites. The heat of mixing for liquid alloy can be expressed as:

$$\Delta H_{mixing} = N \frac{2c_A c_B q_A q_B}{(h+1)(c_A q_A + c_B q_B)} w \tag{13}$$

where N is the number of atoms, c_i is the composition of the i^{th} component of the alloy.

In the following equation, h can be defined as:

$$h = \left(1 + \frac{4c_A c_B q_A q_B}{(c_A q_A + c_B q_B)^2}(k^2 - 1)\right)^{1/2} \tag{14}$$

with

$$k = \exp\left(\frac{w}{2k_B T}\right) \tag{15}$$

where k_B is the Boltzmann constant, T is the absolute temperature and w is the interchange energy, found as:

$$\frac{2w}{Z} = (2V_{AB} - (V_{AA} + V_{BB})) \tag{16}$$

For all possible arrangements of atoms (if there is no enegetic effect, $\Delta H_{mixing}=0$), the entropy of mixing can be expressed by the following equations [54]:

$$\frac{\Delta S_{mixing}}{Nk_B} = -\frac{\Delta G_{mixing}}{Nk_B T} \tag{17}$$

$$\begin{aligned}\frac{\Delta S_{mixing}}{Nk_B} &= -c_A \ln\left(\frac{c_A}{c_A + \gamma c_B}\right) - c_B \ln\left(\frac{\gamma c_B}{c_A + \gamma c_B}\right) \\ &- \frac{1}{2} Z q_A c_A \ln\left(\frac{c_A + \gamma c_B}{c_A + q c_B}\right) - \frac{1}{2} Z q_B c_B \ln\left(\frac{c_B + \frac{c_A}{\gamma}}{c_B + \frac{c_A}{q}}\right)\end{aligned} \tag{18}$$

where

$$\gamma = \frac{\gamma_B}{\gamma_A} \tag{19}$$

and

$$q = \frac{q_A}{q_B} \tag{20}$$

q_i is related to Z (the coordination number of liquid alloy) and γ_{ij} by

$$\frac{1}{2}Z(\gamma_i - q_i) = \gamma_i - 1, \quad \text{i = A, B} \tag{21}$$

$$\frac{1}{2}Z(\gamma_A - q_A) = \gamma_A - 1 \quad ; \quad \frac{1}{2}Z(\gamma_B - q_B) = \gamma_B - 1 \tag{22}$$

For all practical purposes;

$$\gamma = \frac{\gamma_B}{\gamma_A} = \frac{\Omega_A}{\Omega_B} \qquad (\Omega_B > \Omega_A, \Omega \text{ is atomic volume}) \tag{23}$$

2. 5. 4. 1. 2. Inoue's Approach for Binary and Ternary Alloy Systems

For the analysis of solidification, the difference in energy between solid and liquid state, G^l-G^s, is generally required [55]. For multicomponent systems, however, it is impossible to estimate the energies accurately as a function of composition and temperature. It was proposed that the difference G^l-G^s at any composition can be proportional to the free energy of mixing, ΔG_{mixing} of the liquid phase.

ΔG_{mixing} is defined in terms of its enthalpy of mixing, ΔH_{mixing} and entropy of mixing, ΔS_{mixing} as expressed in the following relation when consisting pure states are standard states:

$$\Delta G_{mixing} = \Delta H_{mixing} - T\Delta S_{mixing} \tag{24}$$

According to the regular solution model, for binary and ternary systems with N elements, ΔH_{mixing} can be defined as:

$$\Delta H_{mixing} = \sum_{i=1, i\neq j}^{N} w_{ij} c_i c_j \tag{25}$$

where w_{ij} is the regular solution interaction parameter between i and j elements, and R the gas constant. w_{ij} is assumed independent of both the composition and temperature and can be determined as:

$$w_{ij} = \frac{ZW_{ij}^{R}}{2} = \frac{Z}{2}\left(2V_{ij} - (V_{ii} + V_{jj})\right) \tag{26}$$

ΔH_{mixing} can be defined interms of W_{ij}^{R} as:

$$\Delta H_{mixing} = \frac{Z}{2}\sum_{i=1, i\neq j}^{N} W_{ij}^{R} c_i c_j \tag{27}$$

Ideal configurational entropy ΔS^{ideal} and mismatch term of entropy ΔS_{σ} resulting from atomic size were put into the following equation:

$$\Delta S_{mixing} = \Delta S^{ideal} + \Delta S_{\sigma} \tag{28}$$

For the mulicomponent systems with N elements, ΔS^{ideal} can be defined according to the regular solution model in the as:

$$\Delta S^{ideal} = -R\sum_{i=1}^{N}(c_i \ln c_i) \tag{29}$$

It was proposed that for the mixture of hard spheres, an equation of state was used over the two results of the solution of the Percus-Yevik integral equation [56]. As a result, the mixing entropies consisting of four terms were derived: ideal gas-, concentration-, packing- and misfit-term. In the present study, only misfit term S_{σ} was taken into account to describe the entropy of mixing concerning the differences in atomic radii and S_{σ} can be expressed as [57]:

$$\Delta S_{\sigma} = k_B \left[\frac{3}{2}\left(\zeta^2 - 1\right) y_1 + \frac{3}{2}\left(\zeta - 1\right)^2 y_2 \left[\frac{1}{2}(\zeta - 1)(\zeta - 3) + \ln \zeta \right] (1 - y_3) \right] \quad (30)$$

where ζ is defined as in terms of packing fraction, ξ:

$$\zeta = \frac{1}{(1-\xi)} \quad (31)$$

In above Eq. (30), y_1, y_2 and y_3 parameters having a following relation [56]:

$$y_1 + y_2 + y_3 = 1 \quad (32)$$

where

$$y_1 = \frac{1}{\sigma^3} \sum_{j \rangle i=1}^{n} (d_i + d_j)(d_i - d_j)^2 c_i c_j \quad (33)$$

$$y_2 = \frac{\sigma^2}{(\sigma^3)^2} \sum_{j \rangle i=1}^{n} d_i d_j (d_i - d_j)^2 c_i c_j \quad (34)$$

$$y_3 = \frac{(\sigma^2)^3}{(\sigma^3)^2} \quad (35)$$

with

$$\sigma^k = \sum_{i=1}^{n} c_i {d_i}^k \quad (36)$$

where d_i is the atomic diameter of ith element. By Eqs. (30)-(36), mismatch entropy of mixing of the multicomponent system consisting of N elements is calculated as a function of atomic diameter, composition and packing fraction. These above equations were derived by transforming original formulae [56].

2. 5. 4. 2. Critical Cooling Rate for Binary and Ternary Alloy Systems

In the calculations of critical cooling rate for both approaches, nearly same formulas were used, but Inoue modified the formulae that Singh and Sommer used for binary alloys.

2. 5. 4. 2. 1. Singh and Sommer's Approach for Binary Alloy Systems

Since a dimensional unit of R_c is K/s, it is reasonable to assume that R_c is proportional to the melting temperature and inversely proportional to the incubation time to crystallize τ. Under this assumption, R_c for oxide glasses can be expressed by the below equation [58]:

$$R_c = A_1 \frac{T_m}{\tau} = A_1 f T_m \tag{37}$$

where R_c is the critical cooling rate, A_1 is the constant of $2x10^{-6}$ which is determined by the analysis of R_c for NaCl. The term f, associated to the diffusion or viscosity, is the rate constant in jumps/s unit. The rate constant f is expressed by the following equation:

$$f = A_1 \frac{k_B T}{a^3 \eta} \tag{38}$$

where a is the interatomic distance and η is the viscosity [58].

Substitution of Eq. (38) at T_m in Eq. (37) leads to following equation:

$$R_c = A_1 \frac{k_B T_m^{\ 2}}{a^3 \eta_{T=T_m}} \tag{39}$$

Vogel-Fulcher-Tanmann (VFT) equation was proposed for estimation of viscosity at melting temperature for glass-forming alloys [58]:

$$\eta = \eta_0 \exp\left(\frac{B}{T - T_0}\right) \tag{40}$$

where η_0 is the pre-exponential term, B the constant corresponding to the activation energy, T_0 the temperature at which excess configurational entropy or the free volume is zero, being usually lower than T_g. The values of η_0, B and T_0 were examined for the glass-forming alloys [59]. Also $\eta(T_m)$ can be estimated by the modified Andrade's equation [60] as:

$$\eta(T_m) = A_2 \frac{\sqrt{AT_m}}{V^{2/3}} \tag{41}$$

where A_2 is a constant, A the atomic weight, and V the molar volume. The constant $A_2 = 1.85 \times 10^{-7}$ $(J/Kmol^{1/3})^{1/2}$ is adopted for glass-forming systems [61].

The evaluation of R_c based on Eq. (39) was first carried out for typical metallic glasses. The calculated R_c values [62] were compared with the values calculated by Davies [59]. The difference between these values was over 10^5 and the decrease in R_c is only achieved by modification of constant A_1 in Eq. (39). Consequently, a modified probability A_3 in addition to A_1 was assumed as:

$$A_3 = \exp\left(\frac{\Delta G_{mixing}}{RT}\right) \tag{42}$$

The sign in the exponential term is defined to be plus, so that the system with a large negative value of ΔG_{mixing} has a large tendency to decrease R_c. ΔG_{mixing} of pure elements is zero; therefore, the modification is only adopted for the systems with two or more elements. Eqs. (39) and (42) are combined, eventually, and

taken into account the effect of decrease in R_c on alloying; following equation was obtained for the evaluation of R_c:

$$R_c = A_1 \frac{k_B T_m^2}{a^3 \eta_{T=T_m}} \exp\left(\frac{\Delta G_{mixing}}{RT}\right) \tag{43}$$

In order to evaluate R_c for binary alloys on the basis of Eq. (43), ΔH_{mixing} should be first determined from the Eq. (13). By using the Eq. (24), ΔG_{mixing} can be determined after the determination of ΔS_{mixing} from the Eq. (18).

2. 5. 4. 2. 2. Inoue's Approach for Binary and Ternary Alloy Systems

In order to evaluate R_c for multi-component alloys, the calculated R_c values were subjected to fit with that of Davies [59] or that experimentally [62] determined. Because ΔG_{mixing} consists of two terms, regular solution model term and misfit excess entropy term, fitting parameters related above were put as f_1 and f_2 as:

$$R_c = A_1 \frac{k_B T_m^2}{a^3 \eta_{T=T_m}} \exp\left[f_1\left(\frac{\Delta H_{mixing} - T_m \Delta S^{ideal}}{T_m R}\right) - f_2\left(\frac{S_\sigma}{R}\right)\right] \tag{44}$$

In the Eq. (44) to calculate R_c for multi-component alloys, the ΔH_{mixing} term should be determined from the Eq. (27). ΔS_{mixing} term can be found from the Eq. (28). By using the method of least squares, f_1 and f_2 were calculated to be 0.75 and 1.2, respectively [62].

Eq. (44) was used for binary and ternary alloy systems as Inoue's approach for critical cooling rate in this study.

2. 5. 4. 3. Viscosity for Binary and Ternary Alloy Systems

For the calculations of viscosity, similar formulas were used for Sing and Sommer's and Inoue's approaches. Only, the way of calculations of parameters in these formulas are different for these two approaches.

2. 5. 4. 3. 1. Singh and Sommer's Approach for Binary Alloy Systems

Viscosity of liquid alloys is very important in the understanding of the atomic level structure and interactions. Singh and Sommer have proposed extensive thermodynamic information (both theoretical and experimental) on phase separating systems. They showed that it is possible to derive an expression relating the viscosity and diffusion coefficient D_m for liquid alloys as [63]:

$$\eta = \frac{k_B T}{D_m}\left(\frac{C_A}{\sigma_B} + \frac{C_B}{\sigma_A}\right)\phi \tag{45}$$

where, k_B is the Boltzmann constant, T is the temperature. σ_i depends on size and shape of the diffusing particle, η is the coefficient of viscosity. The thermodynamic parameter of viscosity can be defined as:

$$\phi = \frac{C_A C_B}{Scc(0)} \tag{46}$$

It may be pointed out that D_m in Eq. (45) is not the measured (D_m^{exp}) interdiffusion coefficient but stands for $D_m^{exp} = D_m\phi$. More conveniently η can be expressed as:

$$\eta = \eta_0\phi \tag{47}$$

with

$$\eta_0 = \frac{k_B T}{D_m}\left(\frac{C_A}{\sigma_B} + \frac{C_B}{\sigma_A}\right) \tag{48}$$

Ideally, it can be expected that η_0 should be linear in c_A, because the deviation of η - c_A isotherm from the additive rule of mixing, i.e. $\eta = \Sigma_i c_i \eta_i$ can be ascribed to the factor, ϕ. This factor has been extensively studied in the literature [48, 64] for a large number of binary liquid alloys. The important inference that can be drawn is that

$$\Phi = \begin{cases} \approx 1 & \text{for simple liquid alloys} \\ >> & \text{for compound-forming alloys} \\ << & \text{for segregating and immiscible alloys} \end{cases} \tag{49}$$

Thermodynamic investigation of ϕ have been carried out for the more general case, in which can be incorporated the enthalpy effects (via the interchange energy W) and the entropic effects (through the size ratio $\gamma = \Omega_B/\Omega_A$, $\Omega_B > \Omega_A$, Ω being the atomic volume). ϕ has a derived expression as [65]:

$$\phi = 1 - C_A C_B g(\gamma, W) \tag{50}$$

where

$$g(\gamma, W) = \frac{2\gamma^2 w - (\gamma - 1)^2 \{C_A + \gamma C_B\}}{(C_A + \gamma C_B)^3} \tag{51}$$

with

$$w = \Omega_A\left(\frac{W}{k_B T}\right) \tag{52}$$

w being the interchange energy. V_{AB}, V_{AA} and V_{BB} are the interaction energies for A-B, A-A and B-B pairs or atoms, respectively, and Z is the coordination number of the liquid alloy. Using Eq.(47) and Eqs.(50)-(52), $\Delta\eta/\eta_0$ can be expressed as:

$$\frac{\eta - \eta_0}{\eta_0} = \frac{\Delta\eta}{\eta_0} = -C_A C_B g(\gamma, W) \tag{53}$$

The factor g(γ,W) which incorporates both energetic and size effects is responsible for the characteristic behavior of Δη for a given liquid binary alloy. Due to the above solution results, following relation can be [63]:

$$\frac{\Delta\eta}{\eta_0} = -\frac{\Delta H_{mixing}}{RT} \tag{54}$$

where R is the ideal gas constant.

2. 5. 4. 3. 2. Inoue's Approach for Binary and Ternary Alloy Systems

As mentioned before, same equation was used for Singh and Sommer's and Inoue's approaches in order to calculate viscosity term. Eq. (54) was used for Inoue's approach for both binary and ternary alloy systems.

2. 5. 4. 4. Short-range Order and Long Wavelength Limit for Binary Alloy Systems

Short-range order and long wavelength limit parameters were calculated only for binary systems. These parameters were determined only by Singh and Sommer's approach.

2. 5. 4. 4. 1. Singh and Sommer's Approach for Binary Alloy Systems

By the virtue of the basic thermodynamic relations, $S_{cc}(0)$ (long wavelength limit) and α_l (chemical short-range order (SRO) parameter) are directly related [48]. The long wavelength limit of the number-concentration structure factor has useful physical meaning in terms of fluctuations in composition and in the number of particles.

The concentration fluctuation at the long wavelength limit, $S_{cc}(0)$, due to entropic effect can be shown as:

$$Scc(0) = \frac{C_A C_B}{\left(1 + C_A C_B \left(\frac{\gamma - 1}{(C_A + \gamma C_B)}\right)^2\right)} \tag{55}$$

For a mixture where size effects are negligible, there exists an exact relation between $S_{cc}(0)$ and α_l for different coordination shells [48],

$$\frac{Scc(0)}{c_A c_B} = 1 + \sum_l Z_l \alpha_l \tag{56}$$

where Z_l and α_l are the coordination number and SRO parameter for the l_th shell, (l varies from first-neighbour shells to higher shells). Later, lattice model theory was used to obtain expressions for α_l and $S_{cc}(0)$:

$$\alpha_1 = \frac{s - 1}{s + 1} \tag{57}$$

and

$$Scc(0) = \frac{c_A c_B}{1 + \frac{1}{2} Z (\frac{1}{s} - 1)} \tag{58}$$

with

$$s = \left[1 + 4 c_A c_B (e^{\frac{2w}{k_B T}} - 1)\right]^{1/2} \tag{59}$$

It is obvious that;

a) If $w/k_BT \to 0$, $\alpha_1 = 0$ which shows a completely random distribution of atoms in the alloy.

b) If $w/k_BT \rangle 0$, α_1 is positive which shows a preference for like atoms (A-A or B-B) to pair as nearest neighbours.

c) If $w/k_BT \langle 0$, α_1 is negative which shows a preference for unlike atoms (A-B) to pair in the alloy.

Eqs. (57) and (58) are taken together, so an explicit relation between $S_{cc}(0)$ and α_l can be obtained for the first-neighbour shell:

$$\frac{Scc(0)}{c_A c_B} = \frac{1+\alpha_1}{1-(Z-1)\alpha_1} \tag{60}$$

Eq. (60) can be expressed in expanded form as in the following equation:

$$\frac{Scc(0)}{c_A c_B} = 1 + Z\alpha_1 + Z\alpha_1\left[(Z-1)\alpha_1\right] + Z\alpha_1\left[(Z-1)\alpha_1\right]^2 + ... \tag{61}$$

Eqs. (56) and (61), agree if $Z_1\alpha_1$ rapidly tends to zero for higher shells. Therefore, in the nearest-neighbour shell (l = 1), Eq. (61) can be used to determine α_1 from $S_{cc}(0)$ as:

$$\alpha_1 = \frac{(S^* - 1)}{S^*(Z-1)+1} \tag{62}$$

$$S^* = \frac{Scc(0)}{c_A c_B} \tag{63}$$

As $T \rightarrow T_c$, $S_{cc}(0) \rightarrow \infty$, therefore Eq. (63) implies that;

$$\alpha_1 = \frac{1}{Z - 1} \qquad \text{at } T = T_c \tag{64}$$

2. 5. 5. Pseudopotential Theory

2. 5. 5. 1. Principles of the One-electron Theory

In principle, it is possible to find out everything about a crystal structure by solving Schrödinger's equation for a system of interacting nuclei and electrons that form the crystal structure. This problem, however, is too hard to solve and some simplifications are therefore unavoidable. The assumptions of the one-electron free theory are given as follows [66]:

i. First, it is generally assumed that the nuclei are too massive to follow the rapidly changing spatial distribution of the electrons (the adiabatic approximation). For this reason, two Schrödinger's equations will be considered, one for the electrons and the other for the nuclei. In the following, the one with the behavior of electrons will be concerned.

ii. It is further assumed that instead of treating the electronic subsystem as a whole, it is possible to consider separately the motions of individual electrons. Each of them is then thought of as moving in the effective field of the (stationary) nuclei and all the other electrons (hence the name – the effective field approximation). Accordingly, the total electron wave function is expressed in terms of individual electron wave functions, ψ_i.

iii. Further approximations are made in the actual evaluation of the total function and in the consequent determination of the effective potential as seen by a

single electron (Pauli-exclusion principle). It is customary to use Slater's determinant which automatically incorporates the Pauli exclusion principle. This leads to a system of one-electron Schrödinger equation in the Hartree-Fock approximation including both Coulomb and exchange interactions between the electrons.

The one electron theory is the primitive or basis. It has been worked detail by several times, however it will be surveyed in some detail through, first of all, nearly-free electron model.

2. 5. 5. 2. Nearly-Free Electron Model (NFE)

In this model, a structure is viewed as a spatial lattice of ions embedded in an electron gas. While in linear combination of atomic orbital the perturbation in the eigen-value problem is the departure of the true potential from the atomic potential, in an NFE model it is the departure from zero. For a zero potential (in i.e. vacuum) an electron wave function is a plane wave normalized to all space. In a structure, the normalization integral may be conveniently presented as the sum of contributions from all the structural sites. In the following, more complicated effective potentials (pseudopotentials) will be introduced with form factors dependent both on $\vec{q}$, any vector and $\vec{K}$ wave vector. These form factors and potentials are called non-local. Moreover, a perturbation theory must be introduced here. It is assumed that the flat-bottomed potential well of free electron theory is a good approximation to the real potential in a metal.

Additionally, in the Fermi free-electron gas model, the structure formation process is as follows: N neutral isolated atoms are each stripped of z outer (valance) electrons. The resulting ions are then brought together to form a structural lattice, with a volume of Ω_0 per ion. An electron gas is then allowed into the lattice, its spatial distribution being assumed uniform, so that its density is z / Ω_0. If the fact that the lattice potential is not constant is ignored, the electron dispersion law is simply $E = K^2$. The energy

levels occupied by the electrons range from zero to a maximum, which is known as the Fermi level of a free electron gas:

$$E_F^0 = \left(\frac{3\pi^2 z}{\Omega_0}\right)^{2/3} = K_F^2 \tag{65}$$

To calculate the total structure energy in the NFE model, the dispersion laws are summed over all the occupied states. This is performed by integrating the perturbation theory expansion in the Rayleigh-Schrödinger form over all the wave vectors within the Fermi sphere. As a result, the total structure energy, Σ_{str}, takes the form of following equation:

$$\sum_{str} = U_0 + U_{bs} + U_{lattice} \tag{66}$$

where $U_{lattice}$ takes account the Coulomb repulsion between the ion cores; U_0 and U_{bs} are respectively the volume and structure-dependent electronic contributions to the total energy:

$$U_0 = -2 * \frac{\Omega}{(2\pi)^3} * \int_{\substack{inside\\ the\\ Fermi\\ sphere}} \left(K^2 + \left\langle \vec{K} \middle| V \middle| \vec{K} \right\rangle \right) d^3K \tag{67}$$

$$U_{bs} = -2 * \frac{\Omega}{(2\pi)^3} * \sum_q \left| S\left(\vec{q}\right) \right|^2 \int_{\substack{inside\\ the\\ Fermi\\ sphere}} \frac{\left| \left\langle \vec{K} + \vec{q} \middle| V \middle| \vec{K} \right\rangle \right|^2}{\left(\vec{K} + \vec{q}\right)^2 - K^2} d^3K - U_{el}^{\text{int}} \tag{68}$$

where the g_n are replaced, for generality, by the ordinary position vectors $\vec{q}$. The U_0 term describes a "free" electron gas with the inclusion of electron-electron interaction; U_{bs} is associated with band characteristics and is therefore called the band-structure energy. If a potential V is local, its form-factor is $\vec{K}$-independent and

can be taken out of the $\vec{K}$ integral that appears then in U_{bs} is known as Lindhard's function [67]:

$$X\left(\vec{q}\right) = -2 * \frac{\Omega}{(2\pi)^3} * \frac{1}{N} * \int_{\substack{inside\ the\\ Fermi\\ sphere}} \frac{d^3K}{\left(\vec{K}+\vec{q}\right)^2 - \vec{K}^2} \tag{69}$$

The structure potential is composed of the ionic potentials (that is, about the screening mechanism). X(q) is a function arising from perturbation theory whereas $\alpha(\vec{q})$ is the ratio of the original potential of the ions to the crystal potential. A frequently used characteristic function $\Phi_{bs}(q)$ is defined as

$$\Phi_{bs}(q) = \left|V(q)\right|^2 X(q)\alpha(q) \tag{70}$$

The interatomic interaction potential takes the form:

$$\Phi_{(r)} = \frac{z^2e^2}{r} + \frac{2\Omega}{(2\pi)^3} * \sum_q \int_{\substack{inside\ the\\ Fermi\\ sphere}} \frac{\left|\left\langle \vec{K}+\vec{q}\left|V\right|\vec{K}\right\rangle\right|^2}{\left(\vec{K}+\vec{q}\right)^2 - K^2} d^3K - U_{el}^{\text{int}}$$

$$= \frac{z^2e^2}{r} + \frac{2\Omega}{(2\pi)^3}\int\left[W^{str}(q)\right]^2 X(q)\varepsilon^*(q)e^{i\vec{q}\vec{r}}d^3q \tag{71}$$

It is considered that the simplest pseudopotential, namely the Coulomb potential ($-ze^2 / r$) with a form factor, can be shown as:

$$V(q) = -\frac{4\pi ze^2}{\Omega_0}\frac{1}{q^2} \tag{72}$$

2. 5. 5. 3. Ordering Energy Calculations and Pairwise Interatomic Interactions for Ternary Alloys

According to the electronic theory of ternary alloys in the pseudopotential approximation, the partial ordering potential, $W_{AB}(R_i)$, as a function of interatomic distance, R_i, can be written as [68-72]:

$$W_{AB}(R_i) = V_{AA}(R_i) + V_{BB}(R_i) - 2V_{AB}(R_i) \tag{73}$$

and

$$W_{AB}(R_i) = \frac{2}{N}\sum_{q}^{\iota} F_p(q) e^{i\vec{q}\vec{R}_i} \tag{74}$$

or

$$W_{AB}(R_i) = \frac{\overline{\Omega}}{\pi^2}\int dq * q^2 F_p(q) \frac{\sin qR_i}{qR_i} \tag{75}$$

where

$$\begin{aligned} F_p(q) &= \frac{\overline{\Omega}}{8\pi}\left|\Delta W^b(q)\right|^2 q^2 \frac{1-\varepsilon(q)}{\varepsilon^*(q)} \\ &+ \frac{2\pi}{\overline{\Omega}}(\Delta z)^2 \frac{1}{q^2}\exp\left(-q^2 \diagup 4\lambda\right) \\ &= F_{bs}(q) + F_{es}(q) \end{aligned} \tag{76}$$

$F_p(q)$ is the characteristic function of partial ordering energy.

In the above equations, $\varepsilon(q)$ is the dielectric constant in the Hartree approximation; $\varepsilon^*(q)$ is the modified dielectric constant on the basis of the correlation and

exchange effects; λ is the Ewald parameter; z is the effective valancy of atoms; $\overline{\Omega}$ is the average atomic volume of the alloy, and can be written as:

$$\overline{\Omega} = c_A \Omega_A + c_B \Omega_B + c_C \Omega_C \tag{77}$$

Placing the Eq. (76) into the Eq. (75), $W_{AB}(R_i)$ can be obtained as:

$$W_{AB}(R_i) = \frac{\overline{\Omega}}{\pi^2} \int dq * q^2 \frac{\sin qR_i}{qR_i} *$$

$$\left\{ \frac{\overline{\Omega}}{8\pi} q^2 \frac{1-\varepsilon(q)}{\varepsilon^*(q)} \left| W_B^b(q) \right|^2 + \frac{2\pi}{q^2} \left(z_B^* \right)^2 \exp\left(-q^2 / 4\lambda \right) \right\}$$

$$- \frac{2\overline{\Omega}}{\pi^2} \int dq * q^2 \frac{\sin qR_i}{qR_i} \left\{ \frac{\overline{\Omega}}{8\pi} q^2 \frac{1-\varepsilon(q)}{\varepsilon^*(q)} W_A^b(q) W_B^b(q) + \frac{2\pi}{q^2} z_A^* z_B^* \exp\left(-q^2 / 4\lambda \right) \right\}$$

$$- \frac{\overline{\Omega}}{\pi^2} \int dq * q^2 \frac{\sin qR_i}{qR_i} \left\{ \frac{\overline{\Omega}}{8\pi} q^2 \frac{1-\varepsilon(q)}{\varepsilon^*(q)} \left| W_A^b(q) \right|^2 + \frac{2\pi}{q^2} \left(z^* \right)^2 \exp\left(-q^2 / 4\lambda \right) \right\} \tag{78}$$

where, z_A^*, z_B^* are the effective valences of the component atoms, A and B, respectively.

In Eq. (78), integrals corresponds to the total effective interatomic interaction potential and depend on the interatomic separation in a quasi-oscillatory manner. Interatomic interaction potentials between different ionic pairs in the alloys can be calculated in a similar way,

$$V_{AB}(R_i) = \frac{\overline{\Omega}}{\pi^2} \int_0^\infty F^1{}_{AB}(q) \frac{\sin qR_i}{qR_i} q^2 dq \tag{79}$$

where

$$F^{1}{}_{AB}(q) = -\frac{\overline{\Omega}}{8\pi}\left|W^{\circ}{}_{A}(q)W^{\circ}{}_{B}(q)\right|q^{2}\,\frac{\varepsilon(q)-1}{\varepsilon^{*}(q)}$$
$$+\frac{2\pi}{\overline{\Omega}}\left|z_{A}^{*}z_{B}^{*}\right|\frac{1}{q^{2}}\exp\left(-q^{2}\Big/4\lambda\right) \qquad (80)$$

In the above equations, $W^{\circ}{}_{A}(q)$ and $W^{\circ}{}_{B}(q)$ are the form factor of an unsecreened pseudopotential of A and B ions, respectively.

CHAPTER 3

EXPERIMENTAL PROCEDURE

3. 1. Introduction

Bulk amorphous alloys are new class of metallic materials with their interesting properties as mentioned in the previous sections. Bulk amorphous materials generally composed of three or more elements. Among various types of bulk amorphous alloys, Zr-based bulk amorphous alloys have an important position due to their physico-chemical and mechanical properties. These properties and the glass forming ability of the bulk amorphous alloys are effected by the additional elements.

In this chapter, the two main study parts; theoretical and experimental, will be explained. In the theoretical part, the study on the basis of the semi-empirical rules well known in literature and the electronic theory of alloys in pseudo potential approximation has been provided in order to predict the right impurity elements that will lead to an increase in the glass forming ability of Zr-based multicomponent systems. In addition, it includes the way of calculation of thermodynamic and structural parameters of the selected Zr-based alloys. The results of these theoretical parts will be given and discussed in Chapter 4.

Production methods, crucible design and development, casting method and structural characterization methods of the casting alloys will be explained in this chapter.

3. 2. Theory of Glass Formation

The objective of this thesis is to synthesize and characterize of the zirconium-based bulk amorphous alloys are synthesized and characterized as signified before. In this thesis, the study has been achieved in two main parts such as theoretical and experimental. In order to achieve high glass-forming ability, Zr-based binary systems that have large atomic size mismatch and a composition close to a deep eutectic and intermetallics, which have growth problems during solidification, were selected for this study. These binary systems are tabulated in Table 3.1.

Table 3.1. Zr-based binary systems used in this study.

Binary Systems	**Intermetallics/ Eutectics**
Zr-Ni	**$Zr_{50}Ni_{50}$** **$Zr_{64}Ni_{36}$** **$Zr_{67}Ni_{33}$** **$Zr_{70}Ni_{30}$** **$Zr_{75}Ni_{25}$**
Zr-Fe	**$Zr_{75}Fe_{25}$**
Zr-Co	**$Zr_{75}Co_{25}$**
Zr-Al	**$Zr_{60}Al_{40}$** **$Zr_{75}Al_{25}$**

After the selection of binary systems, theoretical part was studied. In the theoretical study, as explained in the introduction of this chapter, based on the semi-empirical rules well known in literature and the electronic theory of alloys in

pseudopotential approximation has been provided in order to predict the right impurity elements that will lead to an increase in the glass forming ability of Zr-based multicomponent systems. For this reason, for each studied Zr-based binary systems, various candidate elements as an impurity elements were selected from the periodic table. The binary systems and impurity elements used in this study in ordering energy calculations are indicated on the periodic table, Figure 3-1.

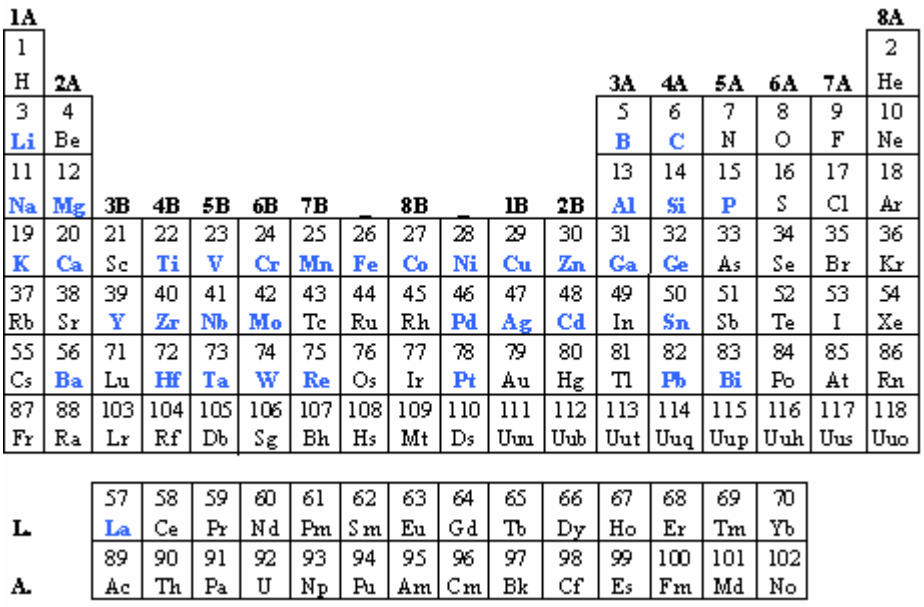

Figure 3.1. The periodic table indicates the elements of binary systems and impurity elements studied in theoretical part in finding the ordering energy calculations.

As mentioned in Chapter 2, the differences between the radius values of the constituent elements were very important. Figure 3.2 indicates the radius differences between the Zr and the studied impurity elements (M) in the calculations.

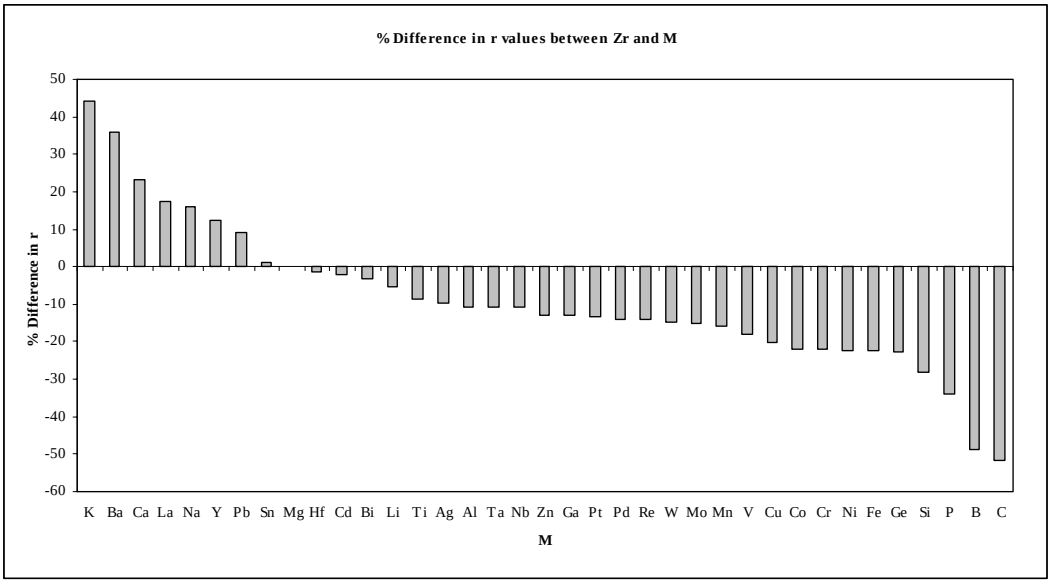

Figure 3.1. The radius differences between the Zr and the studied impurity elements (M) in the calculations.

In addition to the factor of radius differences between the main and constituent elements, the new factor related to the atomic radius of the constituent elements was found, as explained in Chapter 2. this new factor, named as R* is defined as the radius of the solute atom divided by the radius of the solvent atom and the analysis has shown that critical values of R*, such as 0.62, 0.71, 0.80, 0.88, 0.90, etc., are preferred in the constitution of metallic glasses. Figure 3.2 indicates the R* values, calculated for this study for the main element, Zr, and studied impurity elements (M).

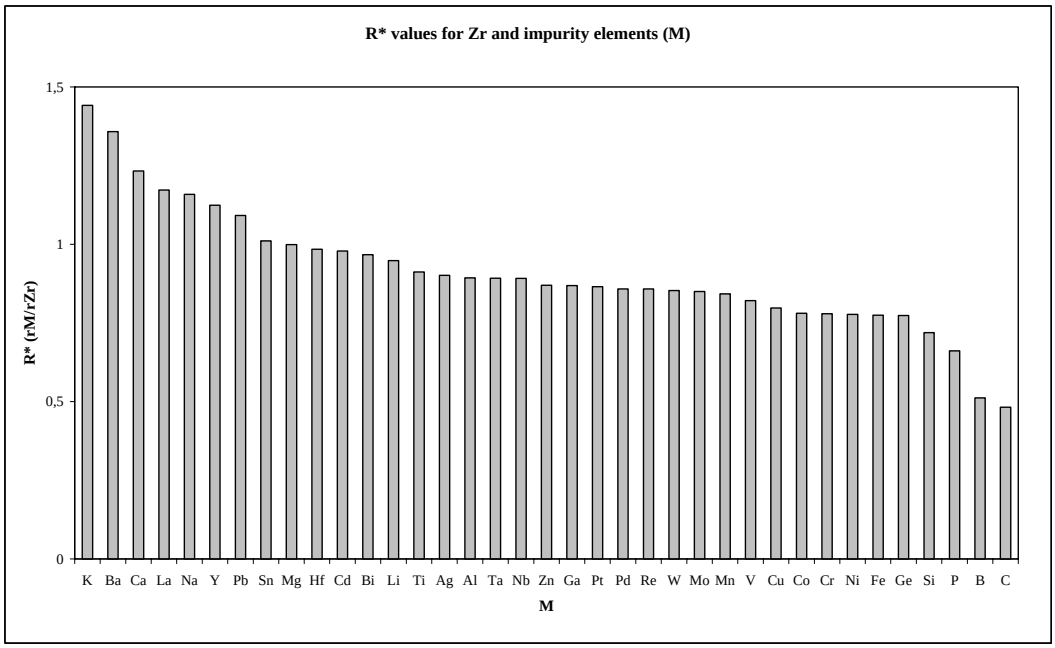

Figure 3.2. The R* values, calculated for this study for the main element, Zr, and studied impurity elements (M).

3. 2. 1. Calculations of Thermodynamic and Structural Parameters for Binary and Multicomponent Systems

The computer program based on pseudopotential theory, were practiced for Zr-based intermetallic systems to calculate the ordering energy of the binary systems and of multicomponent systems between the constituent atoms. By this way, the effects of the addition of impurity elements at 1 at % on the calculated ordering energy data of the binary systems were synthesized. Then the graphs were drawn for binary systems in two cases, as impurity element (M) is taken either from the Zr or from the second element.

By using the results of ordering energy between the first and the second elements (1^{st} Fortran Program), ordering energy between the first and the impurity elements (2^{nd} Fortran Program), ordering energy between the second and the impurity elements (3^{rd} Fortran Program), some of the thermodynamical and structural

parameters, the way of calculations and formulas were explained in the theory part, were calculated. These calculations were done for the binary systems, given in Table 3.1.

It has been known that thermodynamic data and phase diagrams of alloys play an important role in understanding the properties of these materials and in developing their production processes. During the calculations of thermodynamic and structural parameters, two approaches were used. These approaches were explained in Chapter 2. For simplicity in the calculations, these two approaches were named as Approach 1 (Singh's and Sommer's approach) and Approach 2 (Inoue's approach). For binary systems, thermodynamic and structural parameters were calculated from both approaches. For multicomponent systems, only Approach 2 was used.

During the calculation of thermodynamic and structural parameters for binary systems from Approach 1, some equations, given in the Chapter 2, were used. The equations, used in the calculations of thermodynamic and structural parameters from Approach 1 and Approach 2, are given in Table 3.2.

Table 3.2. The equations were used in the calculations of thermodynamic and structural parameters from Approach 1 and Approach 2.

Parameters	**Approach 1**	**Approach 2**
ΔH_{mixing}	Equation (13)	Equation (25)
ΔS_{mixing}	Equation (18)	Equation (28)
ΔG_{mixing}	Equation (24)	Equation (24)
R_c	Equation (43)	Equation (43)
$\Delta\eta/\eta_0$	Equation (54)	Equation (54)
α	Equation (57)	-

The results and comparison of thermodynamic and structural parameters for selected binary systems, calculated from both Approach 1 and Approach 2, will be given in the Chapter 4.

3. 2. 2. Comparison and Selection of Alloy Systems

Numerous factors have been found to influence glass forming ability (GFA). The thermodynamic and structural parameters, required to estimate the GFA and to determine the suitable binary system for casting, and their formulas were given in previous sections. The results of these calculations for each binary systems will be given in Chapter 4.

For the experimental part of the study, $Zr_{67}Ni_{33}$ binary system was selected as an initial casting system. The results of its thermodynamic and structural parameters, its position in Zr-Ni phase diagram and its high glass forming ability, known from literature, largely effect the decision to select it as a casting binary system. These comparison and evaluation will be given in Chapter 4 in detail. After selecting the $Zr_{67}Ni_{33}$ intermetallic system, the suitable impurity elements were decided from the theoretical results, given in Chapter 4, for $Zr_{67}Ni_{33}$ intermetallic system. After some elimination, possible impurity elements, predicted to increase the GFA of the $Zr_{67}Ni_{33}$ binary system, were added into the binary alloy with decided proportions. The cast alloy systems and their casting order number were given in Table 3.3.

Table 3.3. The casting order number and compositions cast alloy systems.

Cast number	Cast Alloy Systems
1	$Zr_{67}Ni_{33}$
2	$Zr_{60}Ni_{25}Mo_{15}$
3	$Zr_{60}Ni_{25}Mo_{10}W_5$
4	$Zr_{50}Ni_{20}Al_{15}Mo_{10}W_5$

The casting process were started with binary $Zr_{67}Ni_{33}$ system. This binary $Zr_{67}Ni_{33}$ system and then $Zr_{60}Ni_{25}Mo_{15}$ system were cast into the cylindrical shaped copper mould by centrifugal casting method. Subsequently, $Zr_{60}Ni_{25}Mo_{10}W_5$ and $Zr_{50}Ni_{20}Al_{15}Mo_{10}W_5$ alloy systems were cast into the wedge shaped copper mould by centrifugal casting method. The explanations of the comparison and selection of alloy systems will be given in detail in Chapter 4.

3. 3. Materials Preparation and Production Technique

Due to the calculations explained above and the results of the theoretical study, cast systems were selected as explained in the previous section. These selected alloys had been prepared as explained in following sections.

3. 3. 1. Constituent Materials

After selecting the $Zr_{67}Ni_{33}$ binary system, the theoretical calculations were again evaluated and due to this evaluation, suitable impurity elements were determined. The form and purity of constituent elements of alloy systems, cast during experiments, are listed in Table 3.4.

Table 3.4. Form and purity of constituent elements used in experiments.

Elements	Form	Purity (%)
Aluminum (Al)	Flakes obtained from hammered shots	99.9
Molybdenum (Mo)	Pieces obtained by hammered pellets	99.7
Nickel (Ni)	Chips obtained by drilling large pieces	99.9+
Tungsten (W)	Pieces obtained from a wire	99.9+
Zirconium (Zr)	Pieces cut from a 2.0 mm diameter wire	99.2

The selected alloy systems were prepared from the above form and purity of the constituent elements, and then the melting and casting process of the alloy were carried out.

3. 3. 2. Production Processes

During this study, centrifugal casting method had been used for melting and casting of selected alloy systems.

3. 3. 2. 1. Centrifugal Casting Method

Centrifugal casting method was used for melting and casting in this study and centrifugal casting machine (Manfredi Neutromag Digital) was used for melting and casting of selected alloys. Centrifugal Casting Method is the well-known, conventional casting method. The maintenance and operation of this method are easy, quick and economic.

As mentioned before, alumina crucibles were used and the prepared alloy mixture placed into these crucibles and then the melting was carried out by induction heating of these alloys. By induction melting, the melt is cast into molds of desired geometry under vacuum or controlled atmosphere. The crucible filled with molten alloy is held at the end of a rotating arm in a portable coil for induction melting and this alloy cast into the copper mould by the action of centrifugal force created by rotation of the arm together with the mold at the same end of the arm to transfer the melt into the mold cavity of desired shape. The melting and casting chamber was airproof and the temperature was controlled through a pyrometer installed on the centrifugal casting machine. The pyrometer accuracy was controlled by comparing with chromel-alumel thermocouples. In order to prevent the oxidation and contamination of the prepared alloy during melting and casting, protective atmosphere of argon gases or vacuum were used. The spectroscopic analysis of these two argon gases given by the supplier is shown in Table 3.5.

Table 3.5. Spectroscopic analysis of argon gases used to form protective atmosphere.

Content	Amount
Ar	99.999 (%)
O_2	1.2 (vpm)
Vapor	0.8 (vpm)
N_2	2.7 (vpm)

3. 3. 2. 2. Crucible Design and Development

The Zr-based amorphous alloys are widely investigated because of their high glass forming ability and lower critical cooling rates have been developed in the last 10 years [43]. Zr-based bulk amorphous alloys will be synthesized and characterized in the experimental part of this thesis. The conventional method of casting the Zr-based bulk amorphous alloys is centrifugal casting method, as explained in previous section. Melting is done in an crucibles by induction melting and the melt is cast into Cu-mould under vacuum. Elemental mixture put into the cast alumina crucibles with conic geometry, as shown in Figure 3.3.

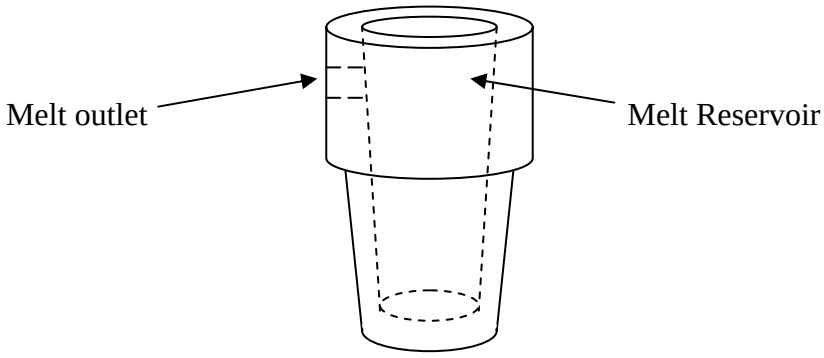

Figure 3.3. The castable alumina crucibles's view used in centrifugal casting machine.

The castable alumina is chosed as a raw material in the production of crucibles because it will eliminate the contaminations that may be resulted from the reactions of the alloy and the crucible. The size distribution is very important for alumina crucibles, because big alumina particles have binding effect and small size particles increase the thermal shock resistance of the castable alumina. Therefore, big attention shoud be paid to the preserve the size distribution. Table 3.6 shows the elemental analysis of the castable alumina.

Table 3.6. Elemental analysis of the castable alumina used as a raw material in the production of crucibles.

Elements	**Weight (% (±2))**
Al_2O_3	97.0 (app.)
SiO_2	0.2 (max.)
Fe_2O_3	0.1 (max.)
CaO	1.6 (max.)

The raw material should be prepared as ceramic mud by water and can be cast into desired crucible geometry. After casting, air drying should be applied for 24 hours. In order to obtain high trength, high thermal shock resistant alumina crucible, thermal treatments should be conducted. Heat treatment procedure of the crucibles are shown in Table 3.7.

Table 3.7. Heat treatment procedure; heat treatment temperatures and corresponding times of the crucibles.

Temperature	Time
~ 100˚ C	24 hours
~200˚ C	1-2 hours
~300˚ C	1-2 hours
~400˚ C	1-2 hours
~500˚ C	1-2 hours
~600˚ C	12 hours
~700˚ C	1-2 hours
~800˚ C	1-2 hours
~900˚ C	1-2 hours
~1000˚ C	1-2 hours

3. 3. 2. 3. Moulds

Centrifugal casting method was used for melting and casting operations in this study. As mentioned before, there are several of parameters that affect the glass forming ability of the alloys, and beside those parameters the mould used in the casting stage is very important. The parameters of shape, dimension, cavity and material of the mould are very important for obtaining amorphous structure.

The mould surface is the first place that the molten metal alloys first contact with the mould during casting. Therefore, the amorphous phase is predicted to take place on the surface contacted with the mould. In this study, the mould material was selected as copper. This copper selection as mould material was done because of its relatively high heat removal capacity in order to transfer heat easily and also due to the literature scanning which gives the result that the most convenient mould material is copper.

During this study, casting process was carried out with two types of mould; cylindrical and wedge-shaped copper moulds. The cylindrical moulds were used for initial part of the casting operation, especially for binary and ternary alloy systems. For multicomponent alloy systems, the wedge-shaped copper moulds were used. These casting experiments give the result that the wedge-shaped copper moulds are the best shaped moulds. The wedge shaped moulds have higher surface area to volume ratio than the cylindrical shaped moulds; and so this provides an efficient cooling rate and heat transfer from the sample to the mould to produce amorphous structure. The view of the wedge-shaped copper mould used in the casting process and the dimensions of the cast sample are shown in the Figure 3.4.

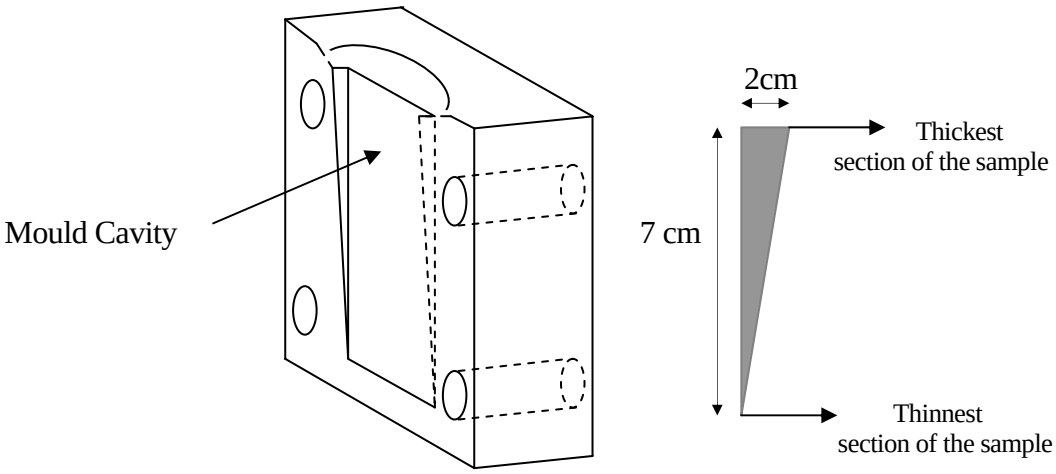

Figure 3.4. Schematic view of the half of the wedge-shaped copper mould and the dimensions of the cast sample.

3. 4. Structural Characterization

After casting operation, cast alloys were analysed in order to determine the existence of amorphous phases and structure. For structural characterization, X-Ray Diffraction (XRD), Optic Microscope (OM), Scanning Electron Microscope (SEM), Energy Dispersive X-Ray Spectroscopy (EDS) and Differential Scanning

Calorimetry (DSC) techniques were used. The results of these characterization tests for cast samples will be given in Chapter 4.

3. 4. 1. Metallography

As an initial step, the cast alloys were metallographically prepared (mounted, grinded, polished and etched) for structural characterization. Cast samples were initially mounted onto bakalits and then grinded. All samples were mechanically polished and etched by an etchant 15 grams FCl_3, 15 ml H_2O and 120 ml Alcohol solution to reveal the microstructures. The optic micrograph of these cast alloys were taken before the SEM analysis.

3. 4. 2. X-Ray Diffraction (XRD)

In order to determine whether the amorphous phase took place or not and to investigate the crystallization kinetics, X-Ray Diffraction tests were performed. The samples were characterized by X-Ray Diffraction with a Phillips PW 1352/20 (model 1967) X-Ray Diffractometer using the Co-K_α radiation, at an operating voltage of 30 kV.

3. 4. 3. Scanning Electron Microscopy (SEM)

Microscopic examination had been carried out by using scanning electron microscope (SEM) ina Jeol JSM 6400 Scanning Electron Microscope. SEM was used in order to investigate the microstructural features of the cast alloys and the existence of amorphous phase by the help of two modes; secondary electron and back scatter electron image modes.

3. 4. 4. Energy Dispersive X-Ray Spectroscopy (EDS)

Energy Dispersive X-Ray Spectroscopy (EDS) was carried out in order to analyze the composition of the constituent elements of the phases shown in the scanning

electron micrograph views. EDS analysis were performed in Noran Series II Energy Dispersive X-Ray Analyzer.

3. 4. 5. Differential Scanning Calorimetry (DSC)

Differential Scanning Calorimetry (DSC) tests were performed with Setaram and Setsys DSC 131 Differential Scanning Calorimeter in order to determine the existence of the amorphous phase and to determine the T_g, T_x and T_l of the cast alloys. The analyzed samples were especially taken from the thinnest part of cast alloys where the amorphous structure were predicted mostly. These samples had a mass range from 20 mg to 45 mg. The experiments were carried out under argon gas in calorimeters and at 40 °C/min heating rate.

CHAPTER 4

RESULTS AND DISCUSSION

4. 1. Introduction

Bulk amorphous and nanocrystalline alloys have been an important research area for last 10 years. Since the discovery of amorphous alloys, a number of attempts have been made to understand the mechanism of amorphization in order to predict alloy compositions with better glass forming ability (GFA) [73].

In this thesis, the study has been achieved in two main parts such as theoretical and experimental.

In the theoretical part of the study, based on the semi-empirical rules well known in literature and the electronic theory of alloys in pseudopotential approximation has been provided in order to predict the right impurity elements that will lead to an increase in the glass forming ability of Zr-based multicomponent systems. For this reason, for each studied Zr-based binary systems, various candidate elements as an impurity elements were selected from the periodic table.

The computer program based on pseudopotential theory, were practiced for Zr-based intermetallic systems to calculate the ordering energy of the binary systems and of multicomponent systems between the constituent atoms. By using the results of ordering energy data, some of the thermodynamical and structural parameters, the way of calculations and formulas were explained in the theory part, were calculated.

During the calculations of thermodynamic and structural parameters, two approaches were used. These approaches were described in Chapter 2. For simplicity, these two approaches were named as Approach 1 (Singh's and Sommer's approach) and Approach 2 (Inoue's approach). These calculations were done for the binary systems given in Table 3.1. The results of the calculations for each system will be given in Section 4. 2. The selected binary system and the reasons of its selection will be discussed in Section 4.3. The theoretical results including the calculations of ordering energy, thermodynamic and structural factors for selected binary system will be explained in Section 4.4. Theoretical calculations of other systems will be given in Appendix B. Potential impurity elements for each studied binary systems, determined according to the theoretical studies, will be given in Section 4. 5.

In the experimental part of this study, the selected Zr-based alloy systems, given in Table 3.3, were cast by centrifugal casting method in order to produce bulk amorphous alloys. The cast samples were characterized by using some of the structural characterization techniques, explained in Section 3. 4, Chapter 3. The results of these structural characterization tests will be given in Section 4. 6.

4. 2. Results of Thermodynamic and Structural Parameters for Binary and Multicomponent Systems

As mentioned in the Chapter 2, glass forming ability (GFA) of alloys depend on various factors. To obtain information about the GFA of alloys, as explained before in Chapter 3 and Section 4.1, initially computer programs, Fortran, based on pseudo potential theory, were operated for binary systems, given in Table 3.1 and their multicomponent systems.

The ordering energy values for binary systems were calculated as: ordering energies between the first and the second elements (1^{st} Fortran Program), ordering energies between the first and the impurity elements (2^{nd} Fortran Program), ordering energies between the second and the impurity elements (3^{rd} Fortran

Program). By this way, the effects of the impurity elements for their 1 at % addition on the calculated ordering energy data of the binary systems were synthesized. The studies were carried out in two cases: as impurity element (M) was taken from the Zr element or taken from the second element of binary systems. After the calculation of ordering energy of the binary systems and the effects of the impurity elements on the ordering energy of the binary systems, the ordering energy for multicomponent systems and the effects of impurity elements on the ordering energy for the multicomponent systems were determined.

By using the results of computer programs, gave the data of ordering energies, some of the thermodynamical and structural parameters, required for gaining information about GFA of systems, were calculated. The way of calculations and formulas of these parameters were explained in Chapter 2. Those calculations were done for the binary systems given in Table 3.1.

4. 2. 1. Results of Calculations of Two Approaches for Binary Systems

During the calculations of thermodynamic and structural parameters, two approaches were used. Those approaches were described in Chapter 2 and for simplicity; those two approaches were named as Approach 1 (Singh's and Sommer's approach) and Approach 2 (Inoue's approach).

For binary systems, thermodynamic and structural parameters were calculated by using both Approach 1 and Approach 2. However, for multicomponent systems, only Approach 2 was used. By using the results of those two approaches, the comparison had been done between those two approaches and between selected systems. The results of Approach 1 and Approach 2 for the selected binary systems are given in Table 4.1.

Table 4.1. Thermodynamic and structural parameters of intermetallic and/or eutectic systems were calculated from Approach 1 and Approach 2.

Intermetallics and/or eutectics	Approach	ΔH_{mixing} (J/mol)	ΔS_{mixing} (J/K.mol)	ΔG_{mixing} (J/mol)	R_c (J/s)	$\Delta\eta/\eta_0$
$Zr_{50}Ni_{50}$	**Approach 1**	-3,70E+04	4,528	-4,39E+04	2,59E+07	2,903
	Approach 2	-3,66E+04	8,531	-4,96E+04	3,78E+07	2,868
$Zr_{64}Ni_{36}$	**Approach 1**	-3,10E+04	3,996	-3,61E+04	2,18E+07	2,906
	Approach 2	-2,83E+04	7,739	-3,824E+04	3,87E+07	2,654
$Zr_{67}Ni_{33}$	**Approach 1**	-2,84E+04	3,809	-3,37E+04	3,99E+10	2,454
	Approach 2	-3,6E+04	7,441	-4,68E+04	3,16E+07	3,146
$Zr_{70}Ni_{30}$	**Approach 1**	-2,60E+04	3,596	-3,08E+04	4,41E+10	2,333
	Approach 2	-3,46E+04	7,097	-4,42E+04	3,24E+07	3,102
$Zr_{75}Ni_{25}$	**Approach 1**	-2,10E+04	3,088	-2,49E+04	5,87E+07	2,018
	Approach 2	-3,55E+04	6,42	-4,36E+04	2,529E+07	3,41
$Zr_{75}Fe_{25}$	**Approach 1**	-7,50E+03	3,188	-1,16E+04	1,70E+11	0,695
	Approach 2	-2,02E+04	6,466	-2,86E+04	6,23E+07	1,87
$Zr_{75}Co_{25}$	**Approach 1**	-1,91E+04	3,18	-2,33E+04	7,24E+10	1,701
	Approach 2	-1,11E+04	6,371	-1,97E+04	1,42E+08	0,988
$Zr_{60}Al_{40}$	**Approach 1**	-2,38E+04	2,51	-2,82E+04	1,57E+11	1,613
	Approach 2	-3,66E+04	6,137	-4,75E+04	9,24E+07	2,481
$Zr_{75}Al_{25}$	**Approach 1**	-1,60E+04	1,925	-1,94E+04	2,60E+11	1,109
	Approach 2	-2,82E+04	5,078	-3,71E+04	1,42E+08	1,954

As can be seen from the Table 4.1, thermodynamic and structural parameters, calculated from these two approaches, are closed to each other for each system. However, among the studied binary systems, calculated parameters are much more closed to each other for Zr-Ni based binary systems. Generally, for all binary systems, Approach 2 gives reasonable values according to Approach 1. As mentioned before, for multicomponent systems, Approach 2 was used to calculate thermodynamic and structural parameters. During the chosen of binary system as an initial point of casting operation, Approach 2 was taken into account.

4. 3. Selection of Zr-Based Binary System for Experimental Study

For experimental part of the study, theoretical results were used and evaluated for each studied Zr-based binary systems. These systems, as mentioned previously, were selected for their positions in their phase diagrams and for their glass forming ability obtained from the literature. After the determination of the Zr-based binary systems, theoretical study was carried out and required thermodynamic and structural parameters for understanding the GFA of these systems were calculated. These calculations and requirements, mentioned in Chapter 2, were used for determining the potential impurity elements for each system. These elements were satisfy all the requirements to obtain high GFA in their binary alloys.

After the theoretical part, the study was continued with the experimental part. For experimental study, one of the given intermetallic and/or eutectic Zr-based systems was selected for casting. During the study to decide the casting system, initially Table 4.1 was taken into consideration. This table was made to compare the results of parameters for both binary systems and two approaches.

For comparison, critical cooling rate values were taken as a dominating factor because of the economical view of point, low R_c values were preferred and it was clearly seen from Table 4.1 that R_c values for Zr-Ni binary systems were the lowest ones among the others.

Furthermore, as mentioned in Chapter 2, the one important parameter in the determination of GFA is the radius difference between the constituent elements. The graphical indication of radius differences between Zr and other studied elements were in Figure 3.1. As can be seen from this graph, Zr-Ni has very high radius difference with the value of 22.25%. This big difference is very important advantage for obtaining high glass forming ability, as explained previously. In Chapter 2, the new factor R* was explained and Figure 3.2 was drawn for these values for Zr and other elements. From this graph, R* value for Zr and Ni is read as 0.78 which is much closed to the critical value of R*, preferred in the constitution of metallic glasses. For the selection of Zr-Ni binary systems, in addition to the evaluation of Table 4.1, above statements were also considered.

After deciding the Zr-Ni binary system for casting process, then the comparison were done for the selection of one of those systems. From Table 4.1, the lowest R_c values for Zr-Ni based binary systems are seen for $Zr_{67}Ni_{33}$ and $Zr_{75}Ni_{25}$ binary systems. Considering the advantage of low R_c values, these two systems were taken as candidate for casting operation. The high negative heat of mixing was also preferred as mentioned previously. From Table 4.1, the highest negative ΔH_{mixing} value, between these two systems, is seen for $Zr_{67}Ni_{33}$ binary system and that gives an important advantage for this system. In Chapter 2, it was mentioned that the higher ΔS_{mixing} satisfy the higher degree of dense random packing. It is seen from the Table 4.1 that the highest value of ΔS_{mixing}, between these two binary systems, is obtained for $Zr_{67}Ni_{33}$ binary system. The high negative ΔH_{mixing} and high ΔS_{mixing} values are two important advantages for $Zr_{67}Ni_{33}$ binary system. In addition to the R_c, ΔH_{mixing} and ΔS_{mixing} , other factors were considered, also.

In order to give a right decision for the selection of Zr-Ni based binary system for casting operation, literature survey was also taken into account. From the literature survey, two important parameters were investigated; changing of crystallization temperature (T_x) for Zr-Ni binary systems and the stability of glassy phase during solidification phenomena.

For most metallic glasses T_x is between 0.4 and $0.6T_m$; in absolute terms, therefore it can vary from as little as 100°C for some simple metallic glasses [74]. In many binary metal-metalloid glasses, T_x is a maximum near the equilibrium eutectic composition, [75]. The same does not appear to be the case in all metal glasses, such as Ni-Zr, Figure 4.1, which show a monotonic decrease of T_x with increasing zirconium content despite the existence in the equilibrium diagram of two eutectics and an intermetallic compound [1].

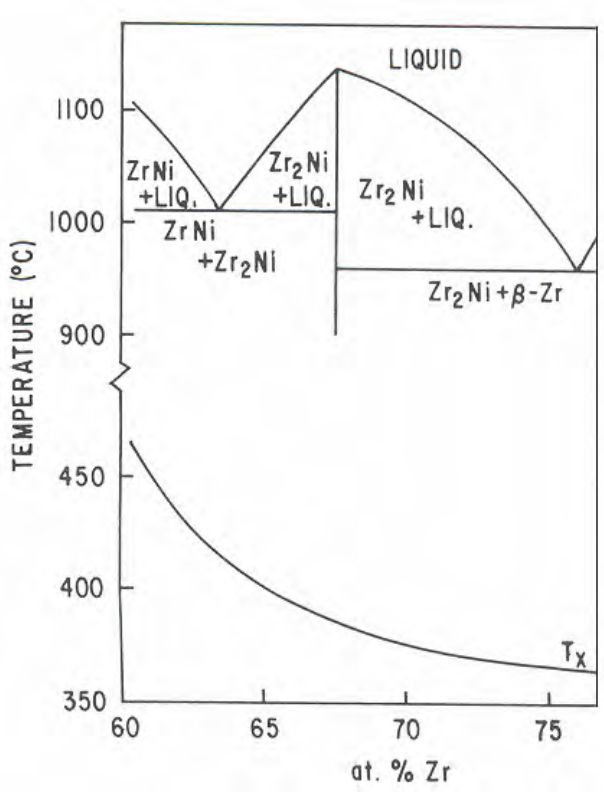

Figure 4.1. Variation of T_x as a function of composition of Zr-Ni [1].

As can be seen from the Figure 4.1, T_x values are lower for $Zr_{75}Ni_{25}$ binary system than that of the $Zr_{67}Ni_{33}$ binary intermetallic system. As mentioned in Chapter 2, the glass formation will be easier, if ΔT_x ($=T_x-T_g$), supercooled liquid region, becomes higher, and therefore high values of T_x are preferred for high glass

forming ability. Figure 4.1 gives a reason for the selection of Zr_2Ni intermetallic systems with higher T_x in place of Zr_3Ni system.

Recently, a number of bulk glassy alloys with extremely high glass-forming ability (GFA) were found in Zr-based multicomponent alloy systems [76–78]. They have attracted much attention for scientific interest in a high-stability glassy state, as well as for industrial applications [79]. It is well known that high GFA is attributed to a high stability of the supercooled liquid state [2]. Based on the previously reported experimental data for Zr-based glassy alloys, it has been clarified that the glassy alloys can have

i. A higher degree of dense randomly packed atomic configurations,
ii. New local atomic configurations, which are different from those of the corresponding final crystalline phases, and
iii. Homogeneous atomic configurations with attractive interaction on a long-range scale.

The existence of a local icosahedral order satisfies the above-described criteria. The nanoicosahedral phase formation in Zr-based glassy alloys suggests that a local structural correlation exists between the icosahedral phase and the glassy phase. Among the Zr-based multicomponent alloys, the $Zr_{65}Al_{7.5}Ni_{10}Cu_{17.5}$ glassy alloy has an extremely high GFA [80], where the primary phase from the glassy state is the metastable fcc Zr_2Ni phase with a large unit cell [81]. Considering that the metastable Zr_2Ni phase contains an icosahedron in the unit cell [82,83], it is suggested that an icosahedral short- or medium-range order exists in the Zr–Al–Ni–Cu glassy alloy, which can grow as an icosahedral quasicrystalline phase with a nano-grain size as a result of the high nucleation rate.

It is concluded that the icosahedral short- or medium-range order stabilizes the glassy state by restraining the long range atomic rearrangements that are required to form crystalline phases. Since the fcc Zr_2Ni phase has an icosahedron in the unit cell [82,83], it is recognized that icosahedral medium-range order exists in the

Zr-based multicomponent alloy and stabilizes the glassy state. It is known from the literature that the Zr_2Ni alloy exhibits polymorphic crystallization which results in the formation of Zr_2Ni crystals [4], increasing the possibility of founding of Zr_2Ni phase. Also the growth problems existing for intermetallics during solidification and high glass forming ability of Zr_2Ni intermetallic system, known from the literature, supported the selection of Zr_2Ni binary intermetallic system as an initial casting system.

4. 4. Results of Calculations for Zr-Based Binary Systems

4. 4. 1. Results of Calculations for Zr-Ni Binary Systems

The equilibrium phase diagram for Zr-Ni binary alloys contains four well-defined eutectics at 8.8, 36.3, 63.5 and 76 at % Zr, as seen in Figure A.1 in Appendix A. As mentioned previously in Chapter 2, glasses are generally formed at compositions which corresponds to these eutectics, and also at compositions corresponding to the equilibrium phases, Zr_7Ni_{10} and Zr_2Ni [4]. By considering this statement, for Zr-Ni binary systems, $Zr_{50}Ni_{50}$ (ZrNi), $Zr_{64}Ni_{36}$ ($Zr_{16}Ni_9$), $Zr_{67}Ni_{33}$ (Zr_2Ni), $Zr_{70}Ni_{30}$ (Zr_7Ni_3) and $Zr_{75}Ni_{25}$ (Zr_3Ni) intermetallic and/or eutectic systems were studied. These systems were selected for their properties and position in the Zr-Ni phase diagram.

4. 4. 1. 1. $Zr_{67}Ni_{33}$ Binary System

Ordering energy of the $Zr_{67}Ni_{33}$ (Zr_2Ni) intermetallic system and the effects of the impurity elements on the ordering energy of the binary systems had been carried out. During the calculations, the coordination numbers for each system were required. The values of the coordination number for binary systems were obtained from the literture. The coordination number of the amorphous Zr_2Ni binary alloy, required for thermodynamic and structural calculations, was taken as 7.5 [84]. The melting temperature was taken as 1393 K from Figure A.1 in Appendix A.

Initially, the ordering energy values were taken from the computer program and using these values, thermodynamic and structural parameters were calculated for the Zr_2Ni intermetallic system. The ordering energy values, taken from the Fortran Programs for $Zr_{2-x}NiM_x$ system for the addition of impurity elements (M) up to 1 at %, are given in Table 4.2.

Thermodynamic and structural parameters of $Zr_{2-x}NiM_x$ system, calculated for the addition of impurity elements up to 1 at %, are tabulated in Table 4.3. The ordering energy values taken from the Fortran Programs for $Zr_2Ni_{1-x}M_x$ system for the addition of impurity elements (M) up to 1 at % are tabulated in Table 4.4. Thermodynamic and structural parameters for $Zr_2Ni_{1-x}M_x$ system are given in Table 4.5.

By using the above calculated data for binary and ternary systems of Zr_2Ni based intermetallic, the comparison was done between the binary sytems and its ternary systems. According to these data, the graphs were drawn to make comparisons. Figures 4.2 and 4.3 indicate the % change in ordering energy for the addition of impurity elements up to 1 at % , for $Zr_{2-x}NiM_x$ and $Zr_2Ni_{1-x}M_x$ systems, respectively. Figures 4.4 and 4.5 indicate the % change in ΔH_{mixing} and the % change in R_c for the addition of impurity elements up to 1 at % for $Zr_{2-x}NiM_x$ system. Figures 4.6 and 4.7 indicate the % change in ΔH_{mixing} and the % change in R_c for the addition of impurity elements up to 1 at % for $Zr_2Ni_{1-x}M_x$ system.

Table 4.2. The ordering energy values for $Zr_{67}Ni_{33}$ and $Zr_{0,66}Ni_{0,33}M_{0,01}$ systems.

M	W_{Zr-Ni} (J/mol)	w_{Zr-Ni} (J/mol)	W_{Zr-M} (J/mol)	w_{Zr-M} (J/mol)	W_{Ni-M} (J/mol)	w_{Ni-M} (J/mol)
$Zr_{67}Ni_{33}$	-2,197E+04	-1,648E+05				
Ag	-2,193E+04	-1,645E+05	1,171E+04	8,783E+04	3,215E+03	2,411E+04
Al	-2,198E+04	-1,649E+05	-2,246E+04	-1,684E+05	3,755E+03	2,816E+04
B	-2,199E+04	-1,649E+05	-9,556E+04	-7,167E+05	-2,255E+04	-1,691E+05
Ba	-2,198E+04	-1,649E+05	-4,098E+05	-3,074E+06	-4,655E+05	-3,491E+06
Bi	-2,199E+04	-1,649E+05	-4,236E+02	-3,177E+03	-5,452E+04	-4,089E+05
C	-2,201E+04	-1,651E+05	-6,027E+04	-4,520E+05	-7,212E+03	-5,409E+04
Ca	-2,198E+04	-1,648E+05	-1,067E+05	-8,000E+05	-1,054E+05	-7,905E+05
Cd	-2,195E+04	-1,646E+05	-2,515E+04	-1,886E+05	9,874E+02	7,405E+03
Co	-2,196E+04	-1,647E+05	-2,182E+04	-1,637E+05	0	0
Cr	-2,197E+04	-1,648E+05	-1,561E+04	-1,171E+05	5,611E+02	4,208E+03
Cu	-2,195E+04	-1,646E+05	-6,536E+03	-4,902E+04	2,098E+03	1,573E+04
Fe	-2,196E+04	-1,647E+05	-1,175E+04	-8,816E+04	-3,891E+02	-2,918E+03
Ga	-2,198E+04	-1,648E+05	-2,781E+04	-2,086E+05	1,247E+03	9,350E+03
Ge	-2,200E+04	-1,650E+05	-1,773E+04	-1,330E+05	1,917E+03	1,437E+04
Hf	-2,197E+04	-1,648E+05	-1,918E+02	-1,438E+03	-2,093E+04	-1,570E+05
K	-2,202E+04	-1,652E+05	-7,540E+04	-5,655E+05	-6,118E+04	-4,588E+05
La	-2,195E+04	-1,646E+05	-1,342E+03	-1,007E+04	-1,165E+04	-8,734E+04
Li	-2,197E+04	-1,648E+05	-5,059E+04	-3,794E+05	2,042E+03	1,531E+04
Mg	-2,197E+04	-1,648E+05	-2,575E+04	-1,931E+05	-5,452E+04	-4,089E+05
Mn	-2,195E+04	-1,646E+05	-1,283E+04	-9,625E+04	-6,361E+02	-4,771E+03
Mo	-2,198E+04	-1,648E+05	6,822E+02	5,116E+03	-2,759E+04	-2,069E+05
Na	-2,198E+04	-1,648E+05	-3,993E+04	-2,995E+05	-1,317E+04	-9,880E+04
Nb	-2,198E+04	-1,649E+05	1,830E+03	1,372E+04	-1,818E+04	-1,364E+05
P	-2,201E+04	-1,651E+05	-3,227E+04	-2,420E+05	4,246E+03	3,184E+04
Pb	-2,197E+04	-1,648E+05	1,467E+04	1,100E+05	-4,122E+04	-3,092E+05
Pd	-2,196E+04	-1,647E+05	7,119E+03	5,339E+04	-8,955E+03	-6,716E+04
Pt	-2,196E+04	-1,647E+05	-5,252E+04	-3,939E+05	-5,085E+03	-3,814E+04
Re	-2,201E+04	-1,651E+05	6,719E+03	5,039E+04	-1,874E+04	-1,406E+05
Si	-2,200E+04	-1,650E+05	-2,356E+04	-1,767E+05	7,314E+03	5,485E+04
Sn	-2,198E+04	-1,648E+05	-1,577E+03	-1,183E+04	-8,880E+03	-6,660E+04
Ta	-2,198E+04	-1,649E+05	1,785E+03	1,338E+04	-1,561E+04	-1,171E+05
Ti	-2,198E+04	-1,648E+05	-2,574E+04	-1,930E+05	1,158E+03	8,682E+03
V	-2,199E+04	-1,649E+05	-1,163E+04	-8,726E+04	7,848E+03	5,886E+04
W	-2,199E+04	-1,650E+05	2,694E+02	2,021E+03	-3,307E+04	-2,480E+05
Y	-2,196E+04	-1,647E+05	-2,363E+03	-1,772E+04	-7,964E+03	-5,973E+04
Zn	-2,196E+04	-1,647E+05	-3,073E+04	-2,305E+05	-2,775E+02	-2,081E+03

Table 4.3. Thermodynamic and structural data of $Zr_{67}Ni_{33}$ and $Zr_{0,66}Ni_{0,33}M_{0,01}$.

M	ΔH_{mixing} (J/mol)	S^{σ} (J/K.mol)	ΔS^{ideal} (J/K.mol)	ΔS_{mixing} (J/K.mol)	ΔG_{mixing} (J/mol)	R_c (J/s)	$\Delta\eta/\eta_o$	α_1
$Zr_{67}Ni_{33}$	-3,643E+04	2,168	5,273	7,441	-4,680E+04	3,155E+07	3,146	-0,493
Ag	-3,517E+04	2,156	5,705	7,861	-4,612E+04	3,300E+07	3,036	
Al	-3,692E+04	2,159	5,705	7,864	-4,788E+04	2,944E+07	3,188	
B	-4,121E+04	2,414	5,705	8,119	-5,252E+04	2,149E+07	3,558	
Ba	-6,771E+04	2,294	5,705	7,999	-7,886E+04	3,931E+06	5,846	
Bi	-3,729E+04	2,137	5,705	7,842	-4,821E+04	2,884E+07	3,220	
C	-3,911E+04	2,439	5,705	8,144	-5,046E+04	2,454E+07	3,377	
Ca	-4,379E+04	2,187	5,705	7,892	-5,478E+04	1,880E+07	3,780	
Cd	-3,707E+04	2,135	5,705	7,840	-4,799E+04	2,926E+07	3,201	
Co	-3,695E+04	2,213	5,705	7,918	-4,798E+04	2,915E+07	3,190	
Cr	-3,665E+04	2,214	5,705	7,919	-4,768E+04	2,973E+07	3,164	
Cu	-3,612E+04	2,204	5,705	7,909	-4,714E+04	3,080E+07	3,119	
Fe	-3,646E+04	2,217	5,705	7,922	-4,749E+04	3,009E+07	3,148	
Ga	-3,725E+04	2,169	5,705	7,874	-4,822E+04	2,878E+07	3,216	
Ge	-3,676E+04	2,217	5,705	7,922	-4,780E+04	2,950E+07	3,174	
Hf	-3,642E+04	2,134	5,705	7,839	-4,734E+04	3,053E+07	3,144	
K	-4,122E+04	2,402	5,705	8,107	-5,251E+04	2,153E+07	3,559	
La	-3,621E+04	2,156	5,705	7,861	-4,716E+04	3,084E+07	3,127	
Li	-3,834E+04	2,142	5,705	7,847	-4,927E+04	2,692E+07	3,310	
Mg	-3,851E+04	2,132	5,705	7,837	-4,943E+04	2,666E+07	3,325	
Mn	-3,651E+04	2,180	5,705	7,885	-4,750E+04	3,014E+07	3,152	
Mo	-3,655E+04	2,177	5,705	7,882	-4,753E+04	3,008E+07	3,156	
Na	-3,820E+04	2,150	5,705	7,855	-4,915E+04	2,713E+07	3,298	
Nb	-3,626E+04	2,159	5,705	7,864	-4,722E+04	3,072E+07	3,131	
P	-3,744E+04	2,293	5,705	7,998	-4,859E+04	2,791E+07	3,233	
Pb	-3,619E+04	2,133	5,705	7,838	-4,711E+04	3,099E+07	3,124	
Pd	-3,574E+04	2,173	5,705	7,878	-4,671E+04	3,172E+07	3,086	
Pt	-3,860E+04	2,170	5,705	7,875	-4,957E+04	2,637E+07	3,332	
Re	-3,609E+04	2,173	5,705	7,878	-4,706E+04	3,101E+07	3,116	
Si	-3,692E+04	2,252	5,705	7,957	-4,801E+04	2,905E+07	3,188	
Sn	-3,620E+04	2,131	5,705	7,836	-4,712E+04	3,097E+07	3,126	
Ta	-3,620E+04	2,159	5,705	7,864	-4,716E+04	3,084E+07	3,126	
Ti	-3,715E+04	2,152	5,705	7,857	-4,809E+04	2,905E+07	3,207	
V	-3,630E+04	2,191	5,705	7,896	-4,730E+04	3,051E+07	3,134	
W	-3,673E+04	2,176	5,705	7,881	-4,771E+04	2,973E+07	3,171	
Y	-3,618E+04	2,140	5,705	7,845	-4,711E+04	3,098E+07	3,124	
Zn	-3,739E+04	2,168	5,705	7,873	-4,836E+04	2,852E+07	3,229	

Table 4.4. The ordering energy values for $Zr_{67}Ni_{33}$ and $Zr_{0,67}Ni_{0,32}M_{0,01}$ systems.

M	W_{Zr-Ni} (J/mol)	w_{Zr-Ni} (J/mol)	W_{Zr-M} (J/mol)	w_{Zr-M} (J/mol)	W_{Ni-M} (J/mol)	w_{Ni-M} (J/mol)
$Zr_{67}Ni_{33}$	-2,197E+04	-1,648E+05				
Ag	-2,194E+04	-1,646E+05	1,169E+04	8,764E+04	3,222E+03	2,417E+04
Al	-2,199E+04	-1,649E+05	-2,245E+04	-1,684E+05	3,752E+03	2,814E+04
B	-2,200E+04	-1,650E+05	-9,559E+04	-7,169E+05	-2,254E+04	-1,690E+05
Ba	-2,199E+04	-1,649E+05	-4,092E+05	-3,069E+06	-4,651E+05	-3,489E+06
Bi	-2,200E+04	-1,650E+05	-4,557E+02	-3,418E+03	-5,450E+04	-4,088E+05
C	-2,202E+04	-1,651E+05	-6,029E+04	-4,522E+05	-7,209E+03	-5,407E+04
Ca	-2,198E+04	-1,649E+05	-1,065E+05	-7,990E+05	-1,054E+05	-7,902E+05
Cd	-2,195E+04	-1,647E+05	-2,517E+04	-1,887E+05	9,887E+02	7,415E+03
Co	-2,197E+04	-1,648E+05	-2,183E+04	-1,637E+05	0	0
Cr	-2,198E+04	-1,649E+05	-1,561E+04	-1,171E+05	5,624E+02	4,218E+03
Cu	-2,196E+04	-1,647E+05	-6,552E+03	-4,914E+04	2,100E+03	1,575E+04
Fe	-2,196E+04	-1,647E+05	-1,176E+04	-8,821E+04	-3,898E+02	-2,924E+03
Ga	-2,199E+04	-1,649E+05	-2,782E+04	-2,087E+05	1,251E+03	9,380E+03
Ge	-2,201E+04	-1,650E+05	-1,773E+04	-1,330E+05	1,918E+03	1,438E+04
Hf	-2,198E+04	-1,648E+05	-1,931E+02	-1,448E+03	-2,093E+04	-1,570E+05
K	-2,203E+04	-1,652E+05	-7,530E+04	-5,648E+05	-6,114E+04	-4,586E+05
La	-2,196E+04	-1,647E+05	-1,346E+03	-1,010E+04	-1,164E+04	-8,730E+04
Li	-2,198E+04	-1,648E+05	-5,061E+04	-3,796E+05	2,042E+03	1,531E+04
Mg	-2,198E+04	-1,648E+05	-2,574E+04	-1,930E+05	-8,540E+02	-6,405E+03
Mn	-2,196E+04	-1,647E+05	-1,284E+04	-9,631E+04	-6,361E+02	-4,771E+03
Mo	-2,199E+04	-1,649E+05	6,835E+02	5,126E+03	-2,760E+04	-2,070E+05
Na	-2,199E+04	-1,649E+05	-3,991E+04	-2,993E+05	-1,317E+04	-9,878E+04
Nb	-2,199E+04	-1,649E+05	1,830E+03	1,372E+04	-1,820E+04	-1,365E+05
P	-2,202E+04	-1,651E+05	-3,227E+04	-2,420E+05	9,449E+03	7,087E+04
Pb	-2,198E+04	-1,649E+05	1,461E+04	1,096E+05	-4,121E+04	-3,091E+05
Pd	-2,197E+04	-1,648E+05	7,153E+03	5,364E+04	-8,944E+03	-6,708E+04
Pt	-2,197E+04	-1,648E+05	-5,255E+04	-3,941E+05	-5,073E+03	-3,805E+04
Re	-2,202E+04	-1,651E+05	6,721E+03	5,041E+04	-1,876E+04	-1,407E+05
Si	-2,201E+04	-1,651E+05	-2,356E+04	-1,767E+05	7,314E+03	5,486E+04
Sn	-2,199E+04	-1,649E+05	-1,581E+03	-1,186E+04	-8,882E+03	-6,661E+04
Ta	-2,199E+04	-1,649E+05	1,785E+03	1,338E+04	-1,563E+04	-1,172E+05
Ti	-2,199E+04	-1,649E+05	-2,575E+04	-1,931E+05	1,161E+03	8,706E+03
V	-2,200E+04	-1,650E+05	-1,164E+04	-8,727E+04	7,848E+03	5,886E+04
W	-2,200E+04	-1,650E+05	2,694E+02	2,021E+03	-3,308E+04	-2,481E+05
Y	-2,198E+04	-1,648E+05	-2,364E+03	-1,773E+04	-7,966E+03	-5,974E+04
Zn	-2,196E+04	-1,647E+05	-3,075E+04	-2,306E+05	-2,762E+02	-2,071E+03

Table 4.5. Thermodynamic and structural data of $Zr_{67}Ni_{33}$ and $Zr_{0,67}Ni_{0,32}M_{0,01}$.

M	ΔH_{mixing} (J/mol)	S^{σ} (J/K.mol)	ΔS^{ideal} (J/K.mol)	ΔS_{mixing} (J/K.mol)	ΔG_{mixing} (J/mol)	R_c (J/s)	$\Delta\eta/\eta_o$	α_1
$Zr_{67}Ni_{33}$	-3,643E+04	2,168	5,273	7,441	-4,680E+04	3,155E+07	3,146	-0,493
Ag	-3,518E+04	2,108	5,645	7,754	-4,598E+04	3,337E+07	3,038	
Al	-3,694E+04	2,111	5,645	7,757	-4,774E+04	2,977E+07	3,189	
B	-4,123E+04	2,368	5,645	8,013	-5,239E+04	2,173E+07	3,560	
Ba	-6,769E+04	2,251	5,645	7,896	-7,869E+04	3,982E+06	5,845	
Bi	-3,730E+04	2,090	5,645	7,735	-4,808E+04	2,916E+07	3,221	
C	-3,913E+04	2,393	5,645	8,038	-5,032E+04	2,481E+07	3,378	
Ca	-4,379E+04	2,141	5,645	7,787	-5,464E+04	1,902E+07	3,781	
Cd	-3,708E+04	2,088	5,645	7,733	-4,786E+04	2,959E+07	3,202	
Co	-3,697E+04	2,166	5,645	7,812	-4,785E+04	2,948E+07	3,192	
Cr	-3,666E+04	2,167	5,645	7,812	-4,755E+04	3,006E+07	3,165	
Cu	-3,614E+04	2,156	5,645	7,802	-4,700E+04	3,115E+07	3,120	
Fe	-3,647E+04	2,170	5,645	7,815	-4,736E+04	3,043E+07	3,149	
Ga	-3,726E+04	2,121	5,645	7,767	-4,808E+04	2,911E+07	3,217	
Ge	-3,678E+04	2,170	5,645	7,816	-4,766E+04	2,983E+07	3,175	
Hf	-3,643E+04	2,087	5,645	7,732	-4,720E+04	3,088E+07	3,145	
K	-4,123E+04	2,360	5,645	8,006	-5,238E+04	2,176E+07	3,560	
La	-3,623E+04	2,109	5,645	7,755	-4,703E+04	3,118E+07	3,128	
Li	-3,836E+04	2,094	5,645	7,740	-4,914E+04	2,723E+07	3,312	
Mg	-3,720E+04	2,085	5,645	7,730	-4,797E+04	2,939E+07	3,212	
Mn	-3,653E+04	2,133	5,645	7,779	-4,736E+04	3,048E+07	3,154	
Mo	-3,656E+04	2,129	5,645	7,775	-4,739E+04	3,042E+07	3,157	
Na	-3,822E+04	2,104	5,645	7,750	-4,901E+04	2,743E+07	3,300	
Nb	-3,628E+04	2,112	5,645	7,757	-4,708E+04	3,107E+07	3,132	
P	-3,733E+04	2,247	5,645	7,892	-4,832E+04	2,847E+07	3,223	
Pb	-3,620E+04	2,087	5,645	7,732	-4,697E+04	3,134E+07	3,126	
Pd	-3,575E+04	2,126	5,645	7,771	-4,658E+04	3,208E+07	3,087	
Pt	-3,861E+04	2,123	5,645	7,768	-4,943E+04	2,667E+07	3,334	
Re	-3,610E+04	2,126	5,645	7,771	-4,692E+04	3,137E+07	3,117	
Si	-3,693E+04	2,205	5,645	7,851	-4,787E+04	2,938E+07	3,189	
Sn	-3,621E+04	2,084	5,645	7,729	-4,698E+04	3,132E+07	3,127	
Ta	-3,622E+04	2,112	5,645	7,757	-4,702E+04	3,119E+07	3,127	
Ti	-3,716E+04	2,105	5,645	7,750	-4,795E+04	2,938E+07	3,208	
V	-3,631E+04	2,144	5,645	7,789	-4,716E+04	3,086E+07	3,135	
W	-3,674E+04	2,128	5,645	7,774	-4,757E+04	3,008E+07	3,172	
Y	-3,621E+04	2,093	5,645	7,739	-4,699E+04	3,128E+07	3,127	
Zn	-3,741E+04	2,121	5,645	7,766	-4,823E+04	2,884E+07	3,230	

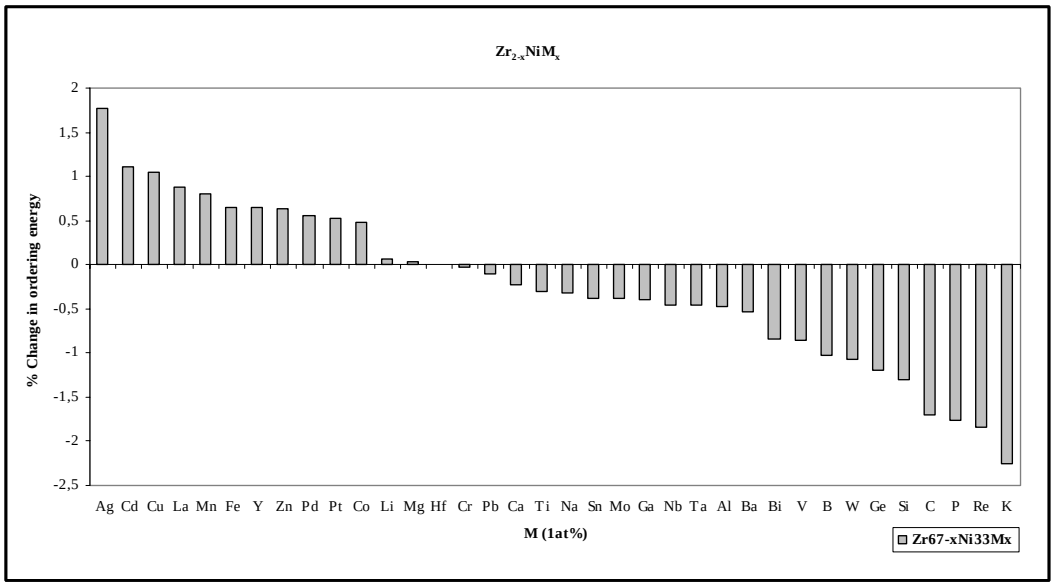

Figure 4.2. % Change in ordering energy of $Zr_{67}Ni_{33}$ intermetallic for the addition of 1 at % impurity elements (M) when 1 at % is taken from Zr ($Zr_{0,66}Ni_{0,33}M_{0,01}$system).

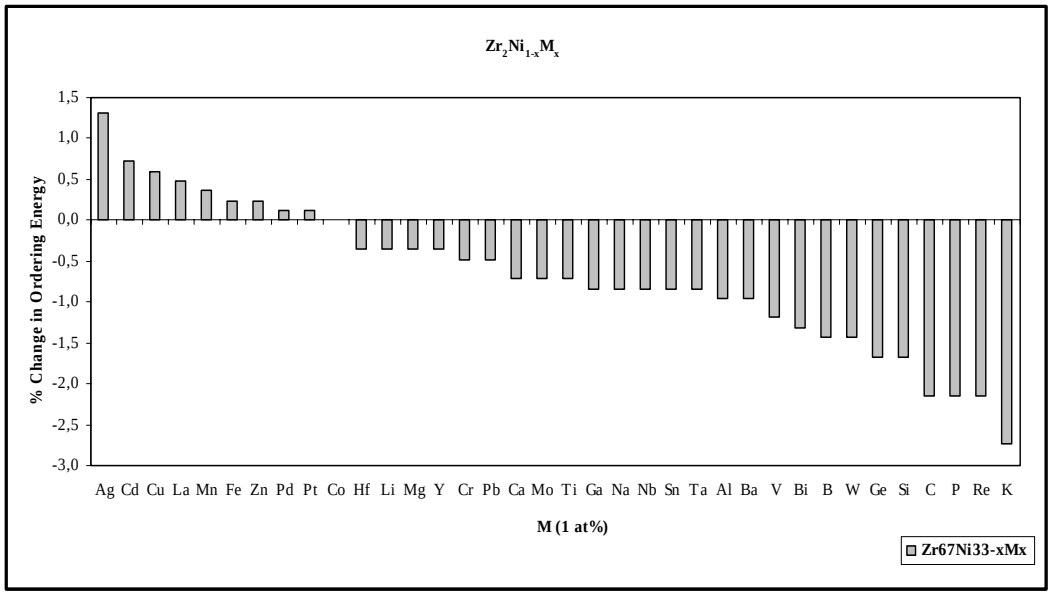

Figure 4.3. % Change in ordering energy of $Zr_{67}Ni_{33}$ intermetallic for the addition of 1 at % impurity elements (M) when 1 at % is taken from Ni ($Zr_{0,67}Ni_{0,32}M_{0,01}$system).

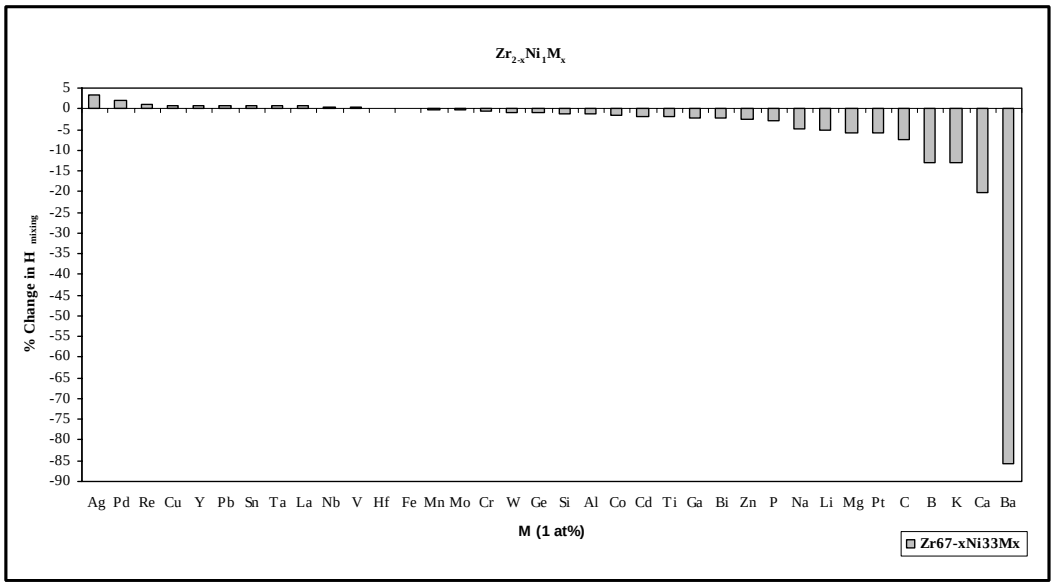

Figure 4.4. % Change in ΔH_{mixing} of $Zr_{67}Ni_{33}$ intermetallic for the addition of 1 at % impurity elements (M) when 1 at % is taken from Zr ($Zr_{0,66}Ni_{0,33}M_{0,01}$system).

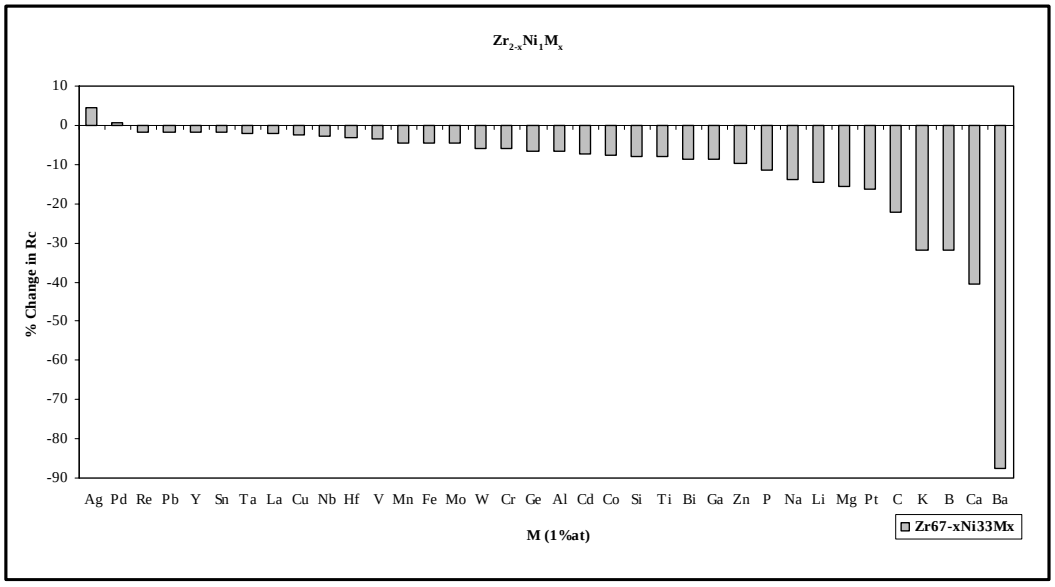

Figure 4.5. % Change in R_c of $Zr_{67}Ni_{33}$ intermetallic for the addition of 1 at % impurity elements (M) when 1 at % is taken from Zr ($Zr_{0,66}Ni_{0,33}M_{0,01}$system).

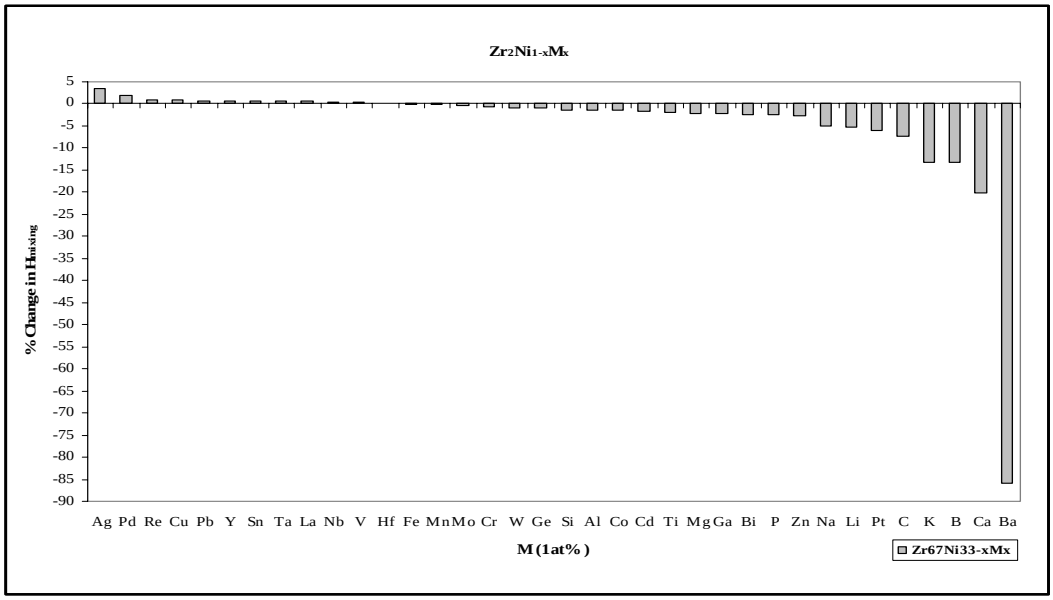

Figure 4.6. % Change in ΔH_{mixing} of $Zr_{67}Ni_{33}$ intermetallic for the addition of 1 at % impurity elements (M) when 1 at % is taken from Ni ($Zr_{0,67}Ni_{0,32}M_{0,01}$system).

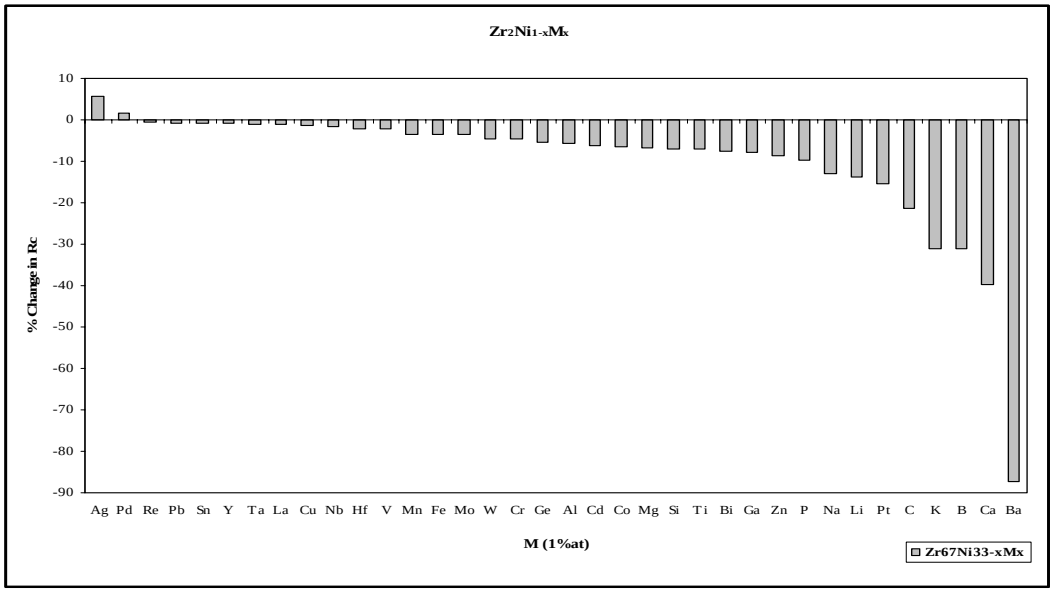

Figure 4.7. % Change in R_c of $Zr_{67}Ni_{33}$ intermetallic for the addition of 1 at % impurity elements (M) when 1 at % is taken from Ni ($Zr_{0,67}Ni_{0,32}M_{0,01}$system).

4. 4. 1. 2. $Zr_{50}Ni_{50}$ Binary System

Ordering energy of the binary $Zr_{50}Ni_{50}$ (ZrNi) system and the effects of the impurity elements on the ordering energy of the binary system were calculated. The coordination number of the amorphous $Zr_{50}Ni_{50}$ binary alloy was taken as 6.7 [85]. The melting temperature of the binary system was taken as 1533 K from Figure A.1 in Appendix A.

The ordering energy values taken from the Fortran Programs for $Zr_{1-x}NiM_x$ system for the addition of 1 at % impurity elements (M) are given in the Table B.1 in Appendix B.

Thermodynamic and structural parameters of $Zr_{1-x}NiM_x$ system, calculated for the addition of 1 at % impurity elements, are tabulated in the Table B.2. The ordering energy values taken from the Fortran Programs for $ZrNi_{1-x}M_x$ system for the addition of 1 at % impurity elements (M), are tabulated in the Table B.3. Thermodynamic and structural parameters for $ZrNi_{1-x}M_x$ system are given in the Table B.4. Figures B.1 and B.2 in Appendix B, the % change in ordering energy for the addition of 1 at % impurity elements, for $Zr_{1-x}NiM_x$ and $ZrNi_{1-x}M_x$ systems are given, respectively. Figures B.3 and B.4 indicate the % change in ΔH_{mixing} and the % change in R_c for the addition of 1 at % impurity elements for $Zr_{1-x}NiM_x$ system. Figures B.5 and B.6 indicate the % change in ΔH_{mixing} and the % change in R_c for the addition of 1 at % impurity elements for $ZrNi_{1-x}M_x$ system.

4. 4. 1. 3. $Zr_{64}Ni_{36}$ Binary System

Ordering energy of the binary $Zr_{64}Ni_{36}$ ($Zr_{16}Ni_9$) system and the effects of the impurity elements on the ordering energy of the binary system had been calculated. The coordination number of the amorphous $Zr_{16}Ni_9$ eutectic system, required for thermodynamic and structural calculations, was taken as 5.6 from the reference [86]. The melting temperature of $Zr_{16}Ni_9$ eutectic system was taken as 1283 K from Figure A.1 in Appendix A.

The ordering energy values taken from the Fortran Programs for $Zr_{16-x}Ni_9M_x$ system for the addition of 1 at % impurity elements (M) are given in the Table B.5 in Appendix B.

Thermodynamic and structural parameters of $Zr_{16-x}Ni_9M_x$ system, calculated for the addition of 1 at % impurity elements, are tabulated in the Table B.6. The ordering energy values taken from the Fortran Programs for $Zr_{16}Ni_{9-x}M_x$ system for the addition of 1 at % impurity elements (M), are tabulated in the Table B.7. Thermodynamic and structural parameters for $Zr_{16}Ni_{9-x}M_x$ system are given in the Table B.8. Figures B.7 and B.8 in Appendix B, the % change in ordering energy for the addition of 1 at % impurity elements, for $Zr_{16-x}Ni_9M_x$ and $Zr_{16}Ni_{9-x}M_x$ systems were given, respectively. Figures B.9 and B.10 indicate the % change in ΔH_{mixing} and the % change in R_c for the addition of 1 at % impurity elements for $Zr_{16-x}Ni_9M_x$ system. Figures B.11 and B.12 indicate the % change in ΔH_{mixing} and the % change in R_c for the addition of 1 at % impurity elements for $Zr_{16}Ni_{9-x}M_x$ system.

4. 4. 1. 4. $Zr_{70}Ni_{30}$ Binary System

Ordering energy of the binary $Zr_{70}Ni_{30}$ (Zr_7Ni_3) system and the effects of the impurity elements on the ordering energy of the binary systems were performed. The coordination number of the amorphous Zr_7Ni_3 binary system, required for thermodynamic and structural calculations, was taken as 7.5 [84]. The melting temperature of Zr_7Ni_3 binary system was taken as 1343 K from Figure A.1 in Appendix A.

The ordering energy values taken from the Fortran Programs for $Zr_{7-x}Ni_3M_x$ system for the addition of 1 at % impurity elements (M) are given in the Table B.9 in Appendix B.

Thermodynamic and structural parameters of $Zr_{7-x}Ni_3M_x$ system, calculated for the addition of 1 at % impurity elements, are tabulated in the Table B.10. The

ordering energy values taken from the Fortran Programs for $Zr_7Ni_{3-x}M_x$ system for the addition of 1 at % impurity elements (M), are tabulated in the Table B.11. Thermodynamic and structural parameters for $Zr_7Ni_{3-x}M_x$ system are given in the Table B.12. Figures B.13 and B.14 in Appendix B, the % change in ordering energy for the addition of 1 at % impurity elements, for $Zr_{7-x}Ni_3M_x$ and $Zr_7Ni_{3-x}M_x$ systems are given, respectively. Figures B.15 and B.16 indicate the % change in ΔH_{mixing} and the % change in R_c for the addition of 1 at % impurity elements for $Zr_{7-x}Ni_3M_x$ system. Figures B.17 and B.18 indicate the % change in ΔH_{mixing} and the % change in R_c for the addition of 1 at % impurity elements for $Zr_7Ni_{3-x}M_x$ system.

4. 4. 1. 5. $Zr_{75}Ni_{25}$ Binary System

Ordering energy of the binary $Zr_{75}Ni_{25}$ (Zr_3Ni) system and the effects of the impurity elements on the ordering energy of the binary system were determined. The coordination number of the amorphous Zr_3Ni binary system was taken as 8.6 [87]. The melting temperature of Zr_3Ni binary was taken as 1253 K from Figure A.1 in Appendix A.

The ordering energy values taken from the Fortran Programs for $Zr_{3-x}NiM_x$ system for the addition of 1 at % impurity elements (M) are given in the Table B.13 in Appendix B.

Thermodynamic and structural parameters of $Zr_{3-x}NiM_x$ system, calculated for the addition of 1 at % impurity elements, are tabulated in the Table B.14. The ordering energy values taken from the Fortran Programs for $Zr_3Ni_{1-x}M_x$ system for the addition of 1 at % impurity elements (M), are tabulated in the Table B.15. Thermodynamic and structural parameters for $Zr_3Ni_{1-x}M_x$ system are given in the Table B.16. Figures B.19 and B.20 in Appendix B, the % change in ordering energy for the addition of 1 at % impurity elements, for $Zr_{3-x}NiM_x$ and $Zr_3Ni_{1-x}M_x$ systems are given, respectively. Figures B.21 and B.22 indicate the % change in ΔH_{mixing} and the % change in R_c for the addition of 1 at % impurity elements for

$Zr_{3-x}NiM_x$ system. Figures B.23 and B.24 indicate the % change in ΔH_{mixing} and the % change in R_c for the addition of 1 at % impurity elements for $Zr_3Ni_{1-x}M_x$ system.

4. 4. 2. Results of Calculations for Zr-Fe Binary Systems

For Zr-Fe binary systems Zr_3Fe intermetallic system was studied. This system was selected for its properties and position in the Zr-Fe phase diagram, as seen in Figure A.2 in Appendix A.

4. 4. 2. 1. $Zr_{75}Fe_{25}$ Binary System

Ordering energy of the binary $Zr_{75}Fe_{25}$ (Zr_3Fe) system and the effects of the impurity elements on the ordering energy of the binary system were determined. The coordination number of the amorphous Zr_3Fe binary alloy was taken as 13.1 [88] and the melting temperature of Zr_3Fe binary was taken as 1298 K from Figure A.2 in Appendix A.

The ordering energy values taken from the Fortran Programs for $Zr_{3-x}FeM_x$ system for the addition of 1 at % impurity elements (M) are given in the Table B.17 in Appendix B.

Thermodynamic and structural parameters of $Zr_{3-x}FeM_x$ system, calculated for the addition of 1 at % impurity elements, are tabulated in the Table B.18. The ordering energy values taken from the Fortran Programs for $Zr_3Fe_{1-x}M_x$ system for the addition of 1 at % impurity elements (M), are tabulated in the Table B.19. Thermodynamic and structural parameters for $Zr_3Fe_{1-x}M_x$ system are given in the Table B.20. Figures B.25 and B.26 in Appendix B, the % change in ordering energy for the addition of 1 at % impurity elements, for $Zr_{3-x}FeM_x$ and $Zr_3Fe_{1-x}M_x$ systems are given, respectively. Figures B.27 and B.28 indicate the % change in ΔH_{mixing} and the % change in R_c for the addition of 1 at % impurity elements for $Zr_{3-x}FeM_x$ system. Figures B.29 and B.30 indicate the % change in ΔH_{mixing} and

the % change in R_c for the addition of 1 at % impurity elements for $Zr_3Fe_{1-x}M_x$ system.

4. 4. 3. Results of Calculations for Zr-Co Binary Systems

For Zr-Co binary systems Zr_3Co binary system was studied. This system was selected for its properties and position in the Zr-Co phase diagram, as seen in Figure A.3 in Appendix A.

4. 4. 3. 1. $Zr_{75}Co_{25}$ Binary System

Ordering energy of the binary $Zr_{75}Co_{25}$ (Zr_3Co) system and the effects of the impurity elements on the ordering energy of the binary system were determined. The coordination number of the amorphous Zr_3Co binary alloy was taken as 3.1 [89] and the melting temperature was taken as 1348 K from Figure A.3 in Appendix A.

The ordering energy values taken from the Fortran Programs for $Zr_{3-x}CoM_x$ system for the addition of 1 at % impurity elements (M) are given in the Table B.21 in Appendix B.

Thermodynamic and structural parameters of $Zr_{3-x}CoM_x$ system, calculated for the addition of 1 at % impurity elements, are tabulated in the Table B.22. The ordering energy values taken from the Fortran Programs for $Zr_3Co_{1-x}M_x$ system for the addition of 1 at % impurity elements (M), are tabulated in the Table B.23. Thermodynamic and structural parameters for $Zr_3Co_{1-x}M_x$ system are given in the Table B.24. Figures B.31 and B.32 in Appendix B, the % change in ordering energy for the addition of 1 at % impurity elements, for $Zr_{3-x}CoM_x$ and $Zr_3Co_{1-x}M_x$ systems are given, respectively. Figures B.33 and B.34 indicate the % change in ΔH_{mixing} and the % change in R_c for the addition of 1 at % impurity elements for $Zr_{3-x}CoM_x$ system. Figures B.35 and B.36 indicate the % change in ΔH_{mixing} and

the % change in R_c for the addition of 1 at % impurity elements for $Zr_3Co_{1-x}M_x$ system.

4. 4. 4. Results of Calculations for Zr-Al Binary Systems

For Zr-Al binary systems Zr_3Al and Zr_3Al_2 intermetallic systems were studied. These systems were selected for their properties and positions in the Zr-Al phase diagram, as seen in Figure A.4 in Appendix A.

4. 4. 4. 1. $Zr_{60}Al_{40}$ Binary System

Ordering energy of the binary $Zr_{60}Al_{40}$ (Zr_3Al_2) system and the effects of the impurity elements on the ordering energy of the binary system had been carried out. The coordination number of the amorphous Zr_3Al_2 binary alloy was taken as 8.99 [90] and the melting temperature was taken as 1773 K from Figure A.4 in Appendix A.

The ordering energy values taken from the Fortran Programs for $Zr_{3-x}Al_2M_x$ system for the addition of 1 at % impurity elements (M) are given in the Table B.25 in Appendix B.

Thermodynamic and structural parameters of $Zr_{3-x}Al_2M_x$ system, calculated for the addition of 1 at % impurity elements, are tabulated in the Table B.26. The ordering energy values taken from the Fortran Programs for $Zr_3Al_{2-x}M_x$ system for the addition of 1 at % impurity elements (M), are tabulated in the Table B.27. Thermodynamic and structural parameters for $Zr_3Al_{2-x}M_x$ system are given in the Table B.28. Figures B.37 and B.38 in Appendix B, the % change in ordering energy for the addition of 1 at % impurity elements, for $Zr_{3-x}Al_2M_x$ and $Zr_3Al_{2-x}M_x$ systems are given, respectively. Figures B.39 and B.40 indicate the % change in ΔH_{mixing} and the % change in R_c for the addition of 1 at % impurity elements for $Zr_{3-x}Al_2M_x$ system. Figures B.41 and B.42 indicate the % change in ΔH_{mixing} and

the % change in R_c for the addition of 1 at % impurity elements for $Zr_3Al_{2-x}M_x$ system.

4. 4. 4. 2. $Zr_{75}Al_{25}$ Binary System

Ordering energy of the binary $Zr_{75}Al_{25}$ (Zr_3Al) system and the effects of the impurity elements on the ordering energy of the binary system had been determined. The coordination number of the amorphous Zr_3Al binary alloy was taken as 8.99 [90] and the melting temperature was taken as 1738 K from Figure A.4 in Appendix A.

The ordering energy values taken from the Fortran Programs for $Zr_{3-x}AlM_x$ system for the addition of 1 at % impurity elements (M) are given in the Table B.29 in Appendix B.

Thermodynamic and structural parameters of $Zr_{3-x}AlM_x$ system, calculated for the addition of 1 at % impurity elements, are tabulated in the Table B.30. The ordering energy values taken from the Fortran Programs for $Zr_3Al_{1-x}M_x$ system for the addition of 1 at % impurity elements (M), are tabulated in the Table B.31. Thermodynamic and structural parameters for $Zr_3Al_{1-x}M_x$ system are given in the Table B.32. Figures B.43 and B.44 in Appendix B, the % change in ordering energy for the addition of 1 at % impurity elements, for $Zr_{3-x}AlM_x$ and $Zr_3Al_{1-x}M_x$ systems are given, respectively. Figures B.45 and B.46 indicate the % change in ΔH_{mixing} and the % change in R_c for the addition of 1 at % impurity elements for $Zr_{3-x}AlM_x$ system. Figures B.47 and B.48 indicate the % change in ΔH_{mixing} and the % change in R_c for the addition of 1 at % impurity elements for $Zr_3Al_{1-x}M_x$ system.

4. 5. Selection of Impurity Elements for Binary Systems

Numerous factors have been found to influence glass forming ability (GFA). In the Chapter 2, the thermodynamic and structural parameters, required to estimate

the GFA and to determine the suitable binary system for casting, and the formulas used to evaluate them were explained. The calculated values of these parameters for each binary system were given in Chapter 4. By using the results of above calculations, carried out for each selected intermetallic and/or eutectic Zr-based system, potential impurity elements were determined for these systems. During the determination of potential impurity elements for each system, some of the criterias, mentioned in Chapter 2, were considered.

As mentioned earlier, among the other factors, GFA of alloys depends mostly on the effects of impurity elements on ordering energy, ΔH_{mixing} and R_c values of their binary systems. During the selection of the potential impurity elements for each binary system, these elements would be predicted to satisfy the requirements of

- Resulting a decrease in the ordering energy of their binary systems.
- Resulting a decrease of ΔH_{mixing} or an increase of negative ΔH_{mixing} of their binary systems.
- Resulting a decrease in the R_c values of their binary systems.

The reasons of these requirements were explained in Chapter 2 in details. According to the above requirements, the potential impurity elements for each binary system were determined; these elements will be given in the following sections of this chapter.

4. 5. 1. Potential Impurity Elements for Zr-Ni Based Binary Systems

For Zr-Ni based binary systems, $Zr_{50}Ni_{50}$ (ZrNi), $Zr_{64}Ni_{36}$ ($Zr_{16}Ni_9$), $Zr_{67}Ni_{33}$ (Zr_2Ni), $Zr_{70}Ni_{30}$ (Zr_7Ni_3) and $Zr_{75}Ni_{25}$ (Zr_3Ni) intermetallic and/or eutectic systems were studied. According to the results of their thermodynamic and structural factors and considering the requirements of GFA, the potential impurity elements for each Zr-Ni based binary systems were determined. These potential impurity elements for each binary systems are given Table 4.6. The positions of

these potential impurity elements for each Zr-Ni based binary systems are indicated on periodic table, in Figure 4.8.

Table 4.6. Potential impurity elements for Zr-Ni based intermetallic and/or eutectic systems.

Intermetallics and/or eutectics	**Systems**	**Potential Impurity Elements**
$Zr_{50}Ni_{50}$	$Zr_{0,49}Ni_{0,50}M_{0,01}$	Transition Metals: Mo, Ti, W Metalloids: B, C Other Metals: Bi, Ga, K
	$Zr_{0,50}Ni_{0,49}M_{0,01}$	Transition Metals: Mo, Ti, W Metalloids: B, C, Ge Other Metals: Bi, Ga, K, Mg, Pb
$Zr_{64}Ni_{36}$	$Zr_{0,63}Ni_{0,36}M_{0,01}$	Transition Metals: Cr, Mo, Ti, W Metalloids: B, C, Ge, Si Other Metals: Al, Ba, Bi, Ca, Ga, Na
	$Zr_{0,64}Ni_{0,35}M_{0,01}$	Transition Metals: Ti Metalloids: B, C Other Metals: Ba, Bi, Ca, Ga, K, Li, Mg, Na
$Zr_{67}Ni_{33}$	$Zr_{0,66}Ni_{0,33}M_{0,01}$	Transition Metals: Cr, Mo, Ti, W Metalloids: B, C, Ge, Si Other Metals: Al, Ba, Bi, Ca, Ga, K, Na
	$Zr_{0,67}Ni_{0,32}M_{0,01}$	Transition Metals: Cr, Mo, Ti, W Metalloids: B, C, Ge, Si Other Metals: Al, Ba, Bi, Ca, Ga, K, Li, Mg, Na
$Zr_{70}Ni_{30}$	$Zr_{0,69}Ni_{0,30}M_{0,01}$	Transition Metals: Cr, Mo, Ti, W Metalloids: B, C, Ge, Si Other Metals: Al, Ba, Bi, Ca, Ga, K, Li, Mg, Na
	$Zr_{0,70}Ni_{0,29}M_{0,01}$	Transition Metals: Cr, Hf, Mo, Ta, Ti, V, W Metalloids: C, Si Other Metals: Al, Ba, Ca, Ga, Sn
$Zr_{75}Ni_{25}$	$Zr_{0,74}Ni_{0,25}M_{0,01}$	Transition Metals: Mo, Ti, V, W Metalloids: B, C, Ge, Si Other Metals: Al, Ba, Bi, Ca, Ga, K, Li, Mg, Na
	$Zr_{0,75}Ni_{0,25}M_{0,01}$	Transition Metals: Ti Metalloids: B, C Other Metals: Al, Ba, Ca, Ga, K, Li, Mg

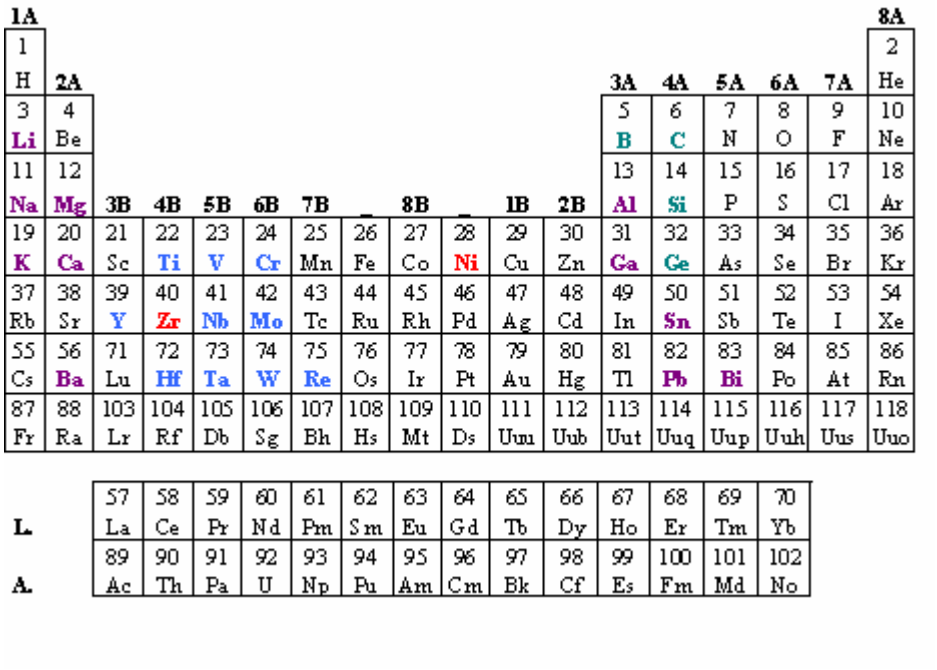

Figure 4.8. The periodic table indicates the potential impurity elements for $Zr_{50}Ni_{50}$, $Zr_{64}Ni_{36}$, $Zr_{67}Ni_{33}$, $Zr_{70}Ni_{30}$ and $Zr_{75}Ni_{25}$ intermetallic and/or eutectic based ternary systems. Red coloured elements are the elements of binary systems. Blue coloured elements are transition metals, teal coloured elements are metalloids or intermediates, violet coloured elements are metals.

4. 5. 2. Potential Impurity Elements for Zr-Fe Based Binary Systems

For Zr-Fe binary systems, Zr_3Fe intermetallic system was studied. The potential impurity elements, determined by considering the results of thermodynamic and structural parameters of $Zr_{75}Fe_{25}$ intermetallic system, are given in Table 4.7. These impurity elements, indicated on the on the periodic table to show their positions and groups, in Figure 4.9, are predicted to increase the GFA of $Zr_{75}Fe_{25}$ intermetallic system.

Table 4.7. Potential impurity elements for $Zr_{75}Fe_{25}$ intermetallic system.

Intermetallics and/or eutectics	Systems	Potential Impurity Elements
$Zr_{75}Fe_{25}$	$Zr_{0,74}Fe_{0,25}M_{0,01}$	Transition Metals: Co, Cr, Hf, Mo, Nb, Ni, Ta, Ti, W, V Metalloids: B, C, Ge, Si Other Metals: Al
	$Zr_{0,75}Fe_{0,25}M_{0,01}$	Transition Metals: Cr, Mo, Ti, W, V Metalloids: B, C Other Metals: –

	1A																8A
	1 H	2A											3A	4A	5A	6A	7A	2 He
	3 Li	4 Be											5 B	6 C	7 N	8 O	9 F	10 Ne
	11 Na	12 Mg	3B	4B	5B	6B	7B	_	8B	_	1B	2B	13 Al	14 Si	15 P	16 S	17 Cl	18 Ar
	19 K	20 Ca	21 Sc	22 Ti	23 V	24 Cr	25 Mn	26 Fe	27 Co	28 Ni	29 Cu	30 Zn	31 Ga	32 Ge	33 As	34 Se	35 Br	36 Kr
	37 Rb	38 Sr	39 Y	40 Zr	41 Nb	42 Mo	43 Tc	44 Ru	45 Rh	46 Pd	47 Ag	48 Cd	49 In	50 Sn	51 Sb	52 Te	53 I	54 Xe
	55 Cs	56 Ba	71 Lu	72 Hf	73 Ta	74 W	75 Re	76 Os	77 Ir	78 Pt	79 Au	80 Hg	81 Tl	82 Pb	83 Bi	84 Po	85 At	86 Rn
	87 Fr	88 Ra	103 Lr	104 Rf	105 Db	106 Sg	107 Bh	108 Hs	109 Mt	110 Ds	111 Uuu	112 Uub	113 Uut	114 Uuq	115 Uup	116 Uuh	117 Uus	118 Uuo
L.			57 La	58 Ce	59 Pr	60 Nd	61 Pm	62 Sm	63 Eu	64 Gd	65 Tb	66 Dy	67 Ho	68 Er	69 Tm	70 Yb		
A.			89 Ac	90 Th	91 Pa	92 U	93 Np	94 Pu	95 Am	96 Cm	97 Bk	98 Cf	99 Es	100 Fm	101 Md	102 No		

Figure 4.9. The periodic table indicates the potential impurity elements for $Zr_{75}Fe_{25}$ intermetallic based ternary systems. Red coloured elements are the elements of binary system. Blue coloured elements are transition metals, teal coloured elements are metalloids or intermediates, violet coloured element is a metal.

4. 5. 3. Potential Impurity Elements for Zr-Co Based Binary Systems

Zr_3Co intermetallic system was studied for Zr-Co binary systems. Considering the results of thermodynamic and structural factors of $Zr_{75}Co_{25}$ intermetallic

system, its potential impurity elements, given in Table 4.8, are decided to obtain high GFA in $Zr_{75}Co_{25}$ intermetallic system. These elements are shown on the periodic table to indicate their positions and groups, in Figure 4.10.

Table 4.8. Potential impurity elements for $Zr_{75}Co_{25}$ intermetallic system.

Intermetallics and/or eutectics	Systems	Potential Impurity Elements
$Zr_{75}Co_{25}$	$Zr_{0,74}Co_{0,25}M_{0,01}$	Transition Metals: Cr, Hf, Fe, Mo, Ni, Ti, W, V Metalloids: B, C, Ge, Si Other Metals: Al
	$Zr_{0,75}Co_{0,25}M_{0,01}$	Transition Metals: Cr, Hf, Fe, Mo, Ni, Ti, W, V Metalloids: B, C, Ge, Si Other Metals: Al

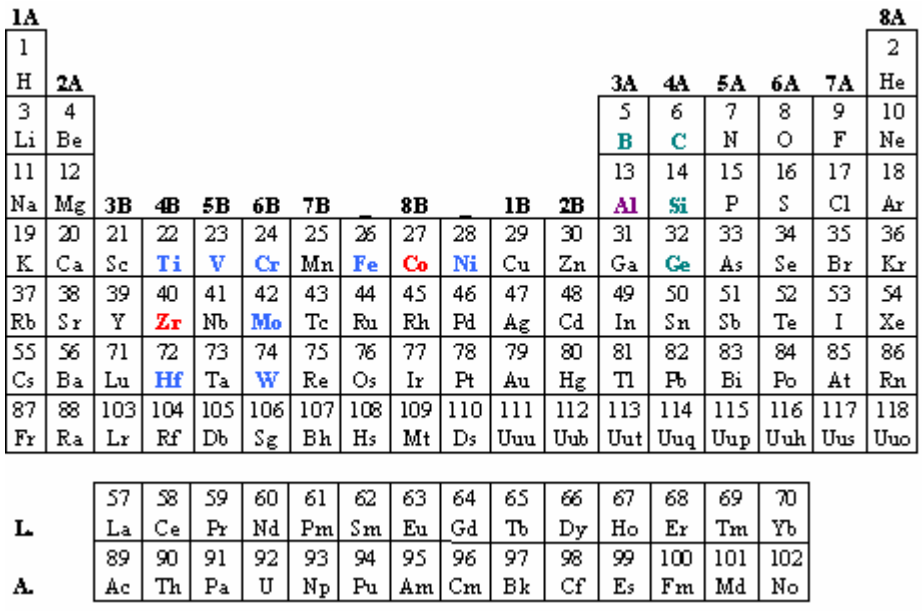

Figure 4.10. The periodic table indicates the potential impurity elements for $Zr_{75}Co_{25}$ intermetallic based ternary systems. Red coloured elements are the elements of binary system. Blue coloured elements are transition metals, teal coloured elements are metalloids or intermediates, violet coloured element is a metal.

4. 5. 4. Potential Impurity Elements for Zr-Al Based Binary Systems

For Zr-Al binary systems $Zr_{60}Al_{40}$ and $Zr_{75}Al_{25}$ intermetallic systems were studied. According to the results of thermodynamic and structural factors of $Zr_{60}Al_{40}$ and $Zr_{75}Al_{25}$ intermetallic systems, their potential impurity elements, given in Table 4.9, are decided to satisfy high GFA in these systems. The positions of these potential impurity elements for each Zr-Al based binary systems are indicated on periodic table, in Figure 4.11.

Table 4.9. Potential impurity elements for Zr-Al based intermetallic systems.

Intermetallics	Systems	Potential Impurity Elements
$Zr_{60}Al_{40}$	$Zr_{0,59}Al_{0,40}M_{0,01}$	Transition Metals: Hf, Mo, Ni, Ta, W Metalloids: B, C, Ge Other Metals: ─
	$Zr_{0,60}Al_{0,39}M_{0,01}$	Transition Metals: Mo, W Metalloids: B, C, Si Other Metals: ─
$Zr_{75}Al_{25}$	$Zr_{0,74}Al_{0,25}M_{0,01}$	Transition Metals: Co, Cr, Fe, Mo, Nb, Ni, Re, Ta, Ti, W, V Metalloids: B, C, Ge, Si Other Metals: ─
	$Zr_{0,75}Al_{0,25}M_{0,01}$	Transition Metals: ─ Metalloids: B, C, Si Other Metals: ─

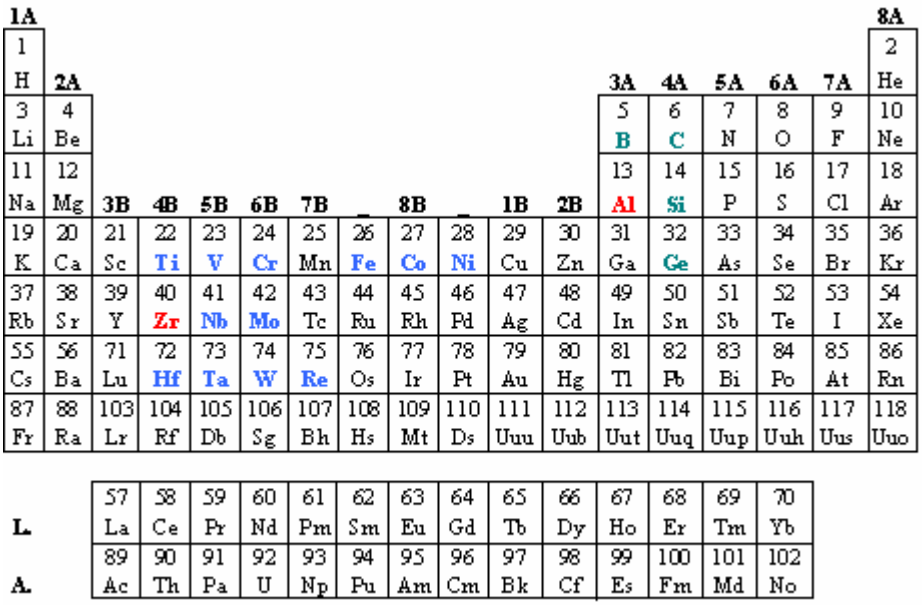

Figure 4.11. The periodic table indicates the potential impurity elements for $Zr_{60}Al_{40}$ and $Zr_{75}Al_{25}$ intermetallics based ternary systems. Red coloured elements are the elements of binary systems. Blue coloured elements are transition metals and teal coloured elements are metalloids or intermediates.

4. 6. Casting Process of $Zr_{67}Ni_{33}$ Binary Based Systems

As mentioned in Section 4.3, according to the given reasons, $Zr_{67}Ni_{33}$ intermetallic system was decided to synthesize and characterize. After the selection of $Zr_{67}Ni_{33}$ intermetallic system, the potential impurity elements, given in Table 4.6, were taken into consideration. After the elimination, Mo, W, Al and Ti metals were decided to use as potential elements for casting operation. Among these metals, as known from the literature, Al and Ti were used largely in Zr-based systems and therefore as a third dominant impurity element for ternary system, they did not preferred. Having a high melting temperature and being experimented before in Zr-based systems, made W non-preferable for being a third element in a ternary system.

Among all potential impurity elements, Mo was decided as a third element of ternary system for $Zr_{67}Ni_{33}$ based system. For quaternary alloy system, W was selected as a fourth impurity element, because of the fact that the combination of Zr, Ni, Mo and W elements did not observed in the literature survey. The five-component alloy of $Zr_{67}Ni_{33}$ intermetallic based system was decided to have constituent elements of Zr, Ni, Mo, Al and W. In the selection of impurity elements for Zr-Ni based binary system; Figure 3.1 and Figure 3.2 were considered, also. Table 4.42 indicates the percent radius difference Δr (%) and R* values for Zr and selected impurity elements (M).

Table 4.42. The Δr (%) and R* values for Zr and selected impurity elements (M).

Zr-M	**Δr (%)**	**R***
Zr-Ni	22.25	0.78
Zr-Mo	14.97	0.85
Zr-W	14.70	0.85
Zr-Al	10.66	0.89

From the Table 4.42, the Δr and R* values are in the range of preferred values, this consistency verifies the selection of right impurity elements. The determination of the composition of the constituent elements, Zr-Ni phase diagram was taken into account. The position of $Zr_{67}Ni_{33}$ intermetallic system in the phase diagram was an important factor, and during the adjustment of the composition of the constituent elements of the alloys, the proportion of atomic composition between the Zr and Ni elements in the multicomponent alloys was taken between the $Zr_{67}Ni_{33}$ intermetallic and eutectic point. It was mentioned in Chapter 2 that the closer to the eutectic composition, the higher the glass forming ability could be obtained. Therefore, the studied alloy composition was adjusted by considering the Zr-Ni binary phase diagram; Figure A.1 in Appendix, and in

all alloy systems, attention was paid if the composition of Zr and Ni constituents corresponds to the eutectic side of the $Zr_{67}Ni_{33}$ intermetallic.

Taking into account of all above factors, the $Zr_{67}Ni_{33}$ intermetallic-based systems, given in Table 3.3, were prepared and casting operation was started. Following the casting process, structural characterization of these alloys was done, these characterization methods were mentioned in Chapter 3. The casting systems, their structural characterization analysis results and glass forming ability will be given and discussed in following sections.

4. 6. 1. Structural Characterization of $Zr_{67}Ni_{33}$ Intermetallic Based Casting Systems

4. 6. 1. 1. Structural Characterization of $Zr_{67}Ni_{33}$ Intermetallic System

As a starting point of the experimental study, $Zr_{67}Ni_{33}$ intermetallic alloy system was selected and prepared for casting operation. The casting operation was carried out by centrifugal casting method into the cylindrical shaped copper mould. DSC curve of this alloy is given in Figure 4.60.

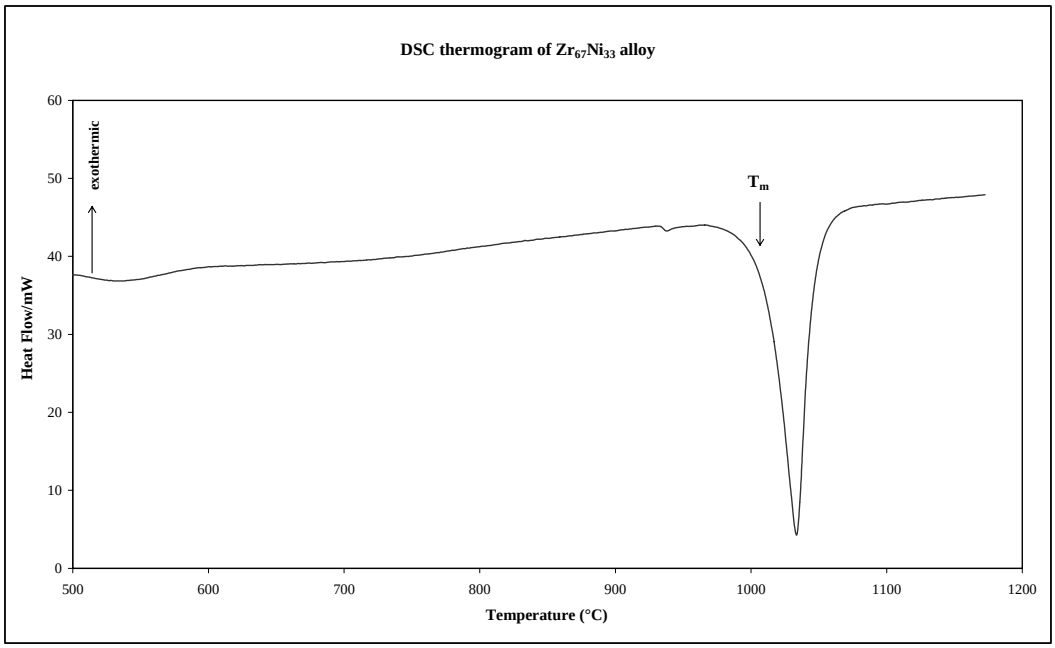

Figure 4.60. Isochronal DSC thermogram of $Zr_{67}Ni_{33}$ alloy.

From the DSC curve, one endothermic peak, indicating the melting peak of the specimen, at 1010°C, is observed. From the binary Zr-Ni phase diagram, during the solidification, Zr_2Ni intermetallic would be expected to be the first phase to solidify from the liquid. At the eutectic temperature, remaining liquid transforms to β(Zr) in Zr_2Ni cells eutectically. At eutectoid temperature, β(Zr) decomposed and all β(Zr) phase in eutectic cells transforms into α(Zr).

Microstructures examination in order to understand the GFA in $Zr_{67}Ni_{33}$ intermetallic had been done and SEM micrographs of this binary alloy are shown in Figure 4.61 (a) and (b). EDS analyses, Table 4.43, taken from the Figure 4.61 (a) and (b), and the X-ray diffraction pattern, Figure 4.62, are given. The characterized phases are mentioned on the X-ray diffraction pattern. The EDS and X-ray diffraction analysis prove the existence of Zr_2Ni and Zr phases. EDS analysis also indicates that the eutectic reaction was occurred because the composition of the formed phases are corresponding to the hypoeutectic composition.

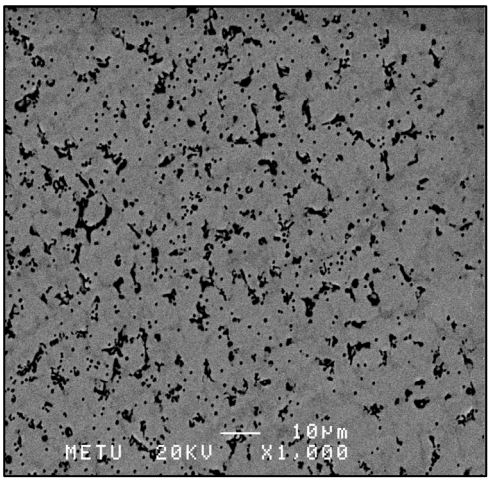

(a)

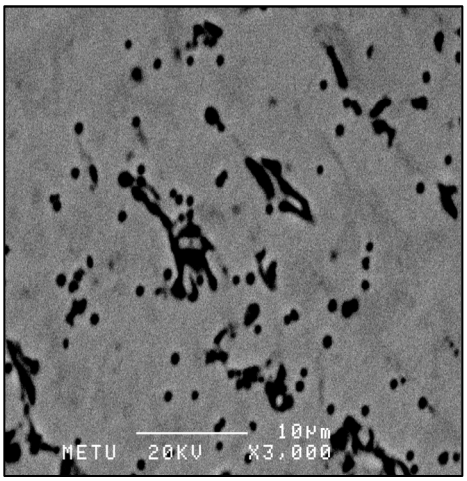

(b)

Figure 4.61. SEM images of $Zr_{67}Ni_{33}$ intermetallic alloy:

(a) Back-scattered image of the sample (x1000).

(b) Back-scattered image of the sample (x3000).

Table 4.43. EDS analyses of $Zr_{67}Ni_{33}$ intermetallic alloy.

Regions	Element	Atom %(±2.00)
Grey region	Zr	70.65
	Ni	29.35
Black Region	Zr	68.94
	Ni	31.06

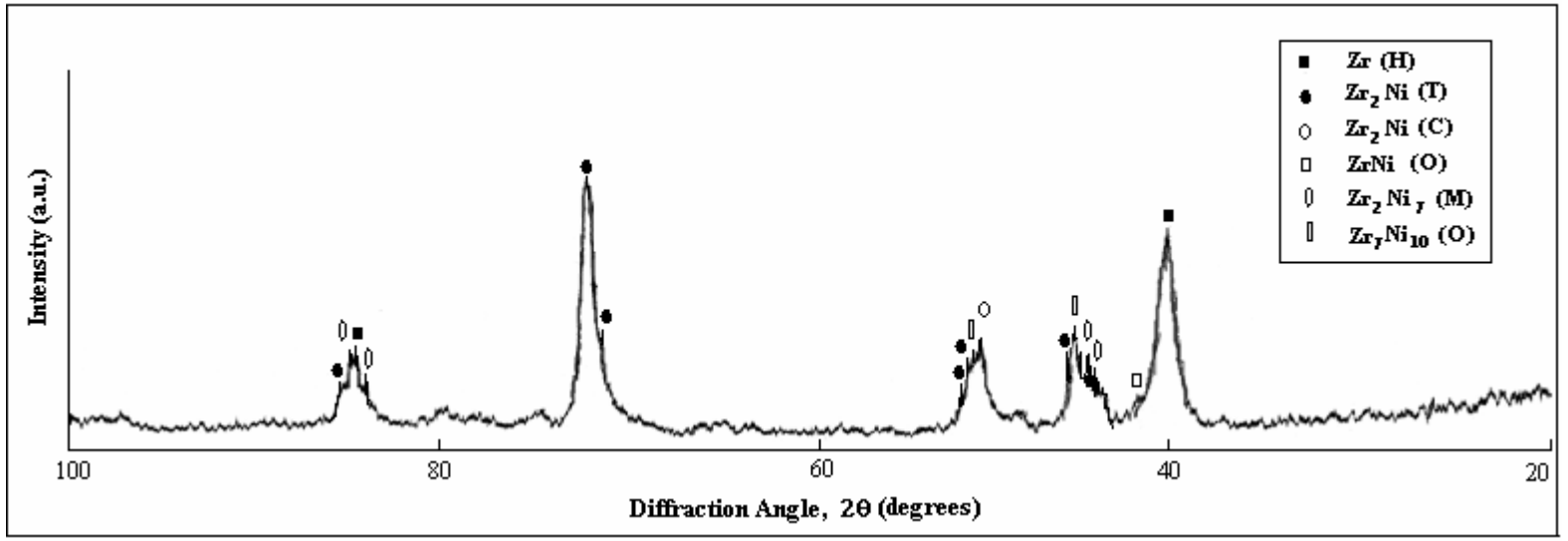

Figure 4.62. The X-ray diffraction pattern for $Zr_{67}Ni_{33}$ alloy

4. 6. 1. 2. Structural Characterization of $Zr_{60}Ni_{25}Mo_{15}$ Alloy System

After casting, $Zr_{67}Ni_{33}$ intermetallic alloy, its ternary alloy of $Zr_{60}Ni_{25}Mo_{15}$ was cast into the cylindrical shaped copper mould. The cast alloy composition corresponds to the right hand side of the $Zr_{67}Ni_{33}$ intermetallic in the Zr-Ni binary phase diagram, as mentioned before. The DSC curve of $Zr_{60}Ni_{25}Mo_{15}$ alloy is given in Figure 4.44.

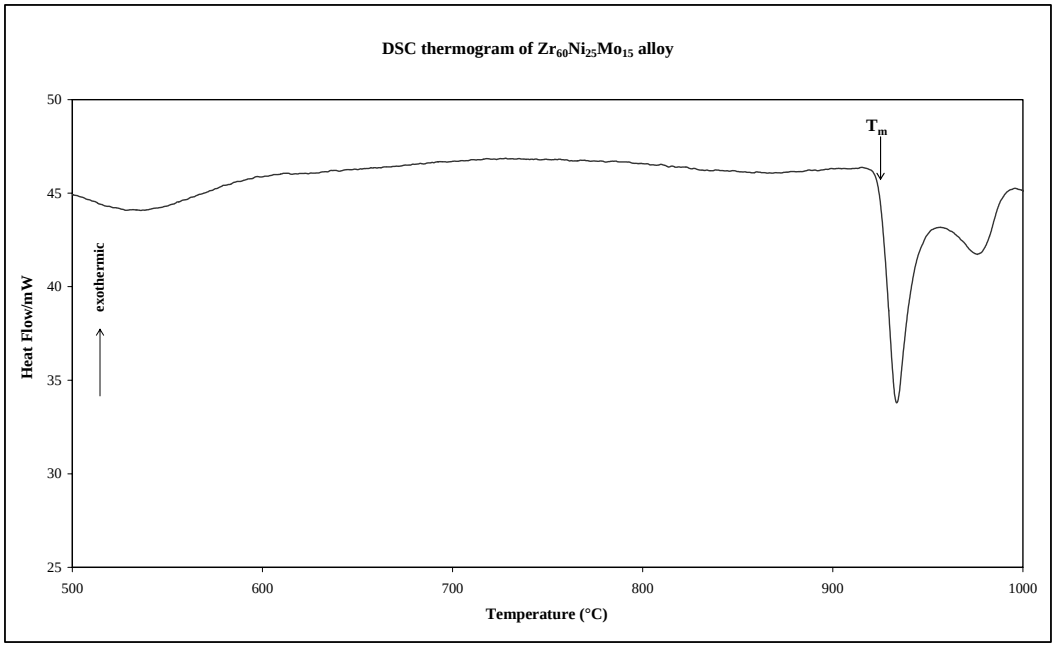

Figure 4.44. Isochronal DSC thermogram of the $Zr_{60}Ni_{25}Mo_{15}$ alloy.

From the Figure 4.44, only large endothermic peak corresponding to the melting of the alloy, at 925°C is observed. There is no evidence existing in this diagram to indicate the $Zr_{60}Ni_{25}Mo_{15}$ alloy may have an amorphous structure.

SEM and XRD analysis had been carried out also. Scanning electron micrographs of $Zr_{60}Ni_{25}Mo_{15}$ alloy, taken from general view of the sample and EDS analyses form these sections, are seen in Figure 4.63 (a) and (b) and Table 4.45. From

Figure 4.63, solidification microstructures of the sample can be understood. The difference between the solidification microstructure of $Zr_{60}Ni_{25}Mo_{15}$ alloy from that of $Zr_{67}Ni_{33}$ alloy, Figure 4.61, is caused from the addition of Mo.

From the Figure 4.63 (b), the microstructure of the near surface region of the sample is seen. From the solidification microstructure of $Zr_{60}Ni_{25}Mo_{15}$ alloy, produced under rapid cooling conditions, faceted dendritic growth morphology was observed for grey region, in which from the EDS analysis the Zr content was found to be very high and Mo was not exist. Considering the binary Zr-Ni phase diagram, this composition corresponds to the eutectic region and therefore during solidification in this region, Zr_2Ni phase would be expected. From the X-ray diffraction pattern of $Zr_{60}Ni_{25}Mo_{15}$ alloy, Figure 4.64, the existence of tetragonal and cubic Zr_2Ni phase was observed and confirmed this correspondence. Between the faceted Zr_2Ni structures, black region was observed. This region might be come from the liquid and considering the binary phase diagram of Zr-Ni, EDS analysis and XRD pattern, the forming phases could be ZrNi, Zr_2Ni, Zr_2Ni_7, Zr_7Ni_{10}, Zr_3Ni_2 phases. In the white regions in Figure 4.63 (a) and (b), faceted phases are observed in which the composition of Mo was very high. These white regions may be formed from the Mo_2Zr, $Mo_{0.93}Zr_{0.7}$ and MoNi phases considering the EDS and XRD analysis.

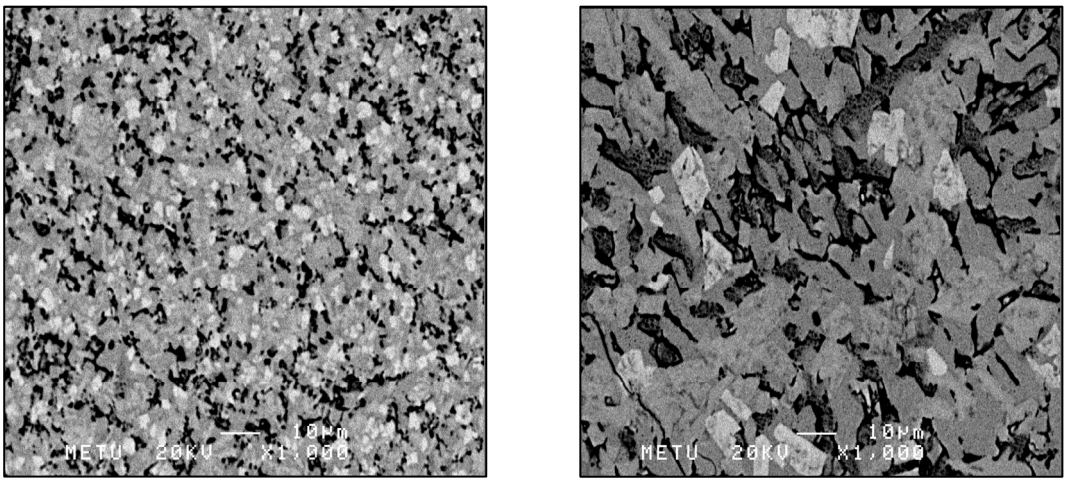

Figure 4.63. SEM images of $Zr_{60}Ni_{25}Mo_{15}$ alloy:

(a) Back-scattered image of the general view of the sample (x1000).

(b) Back-scattered image of the side region of the sample (x1000).

Table 4.45. EDS analyses of $Zr_{60}Ni_{25}Mo_{15}$ alloy.

Regions	Element	Atom %(±2.00)
White region	Zr	35.79
	Ni	3.10
	Mo	61.11
Grey Region	Zr	72.34
	Ni	27.66
	Mo	0
Black Region	Zr	57.66
	Ni	40.62
	Mo	1.71

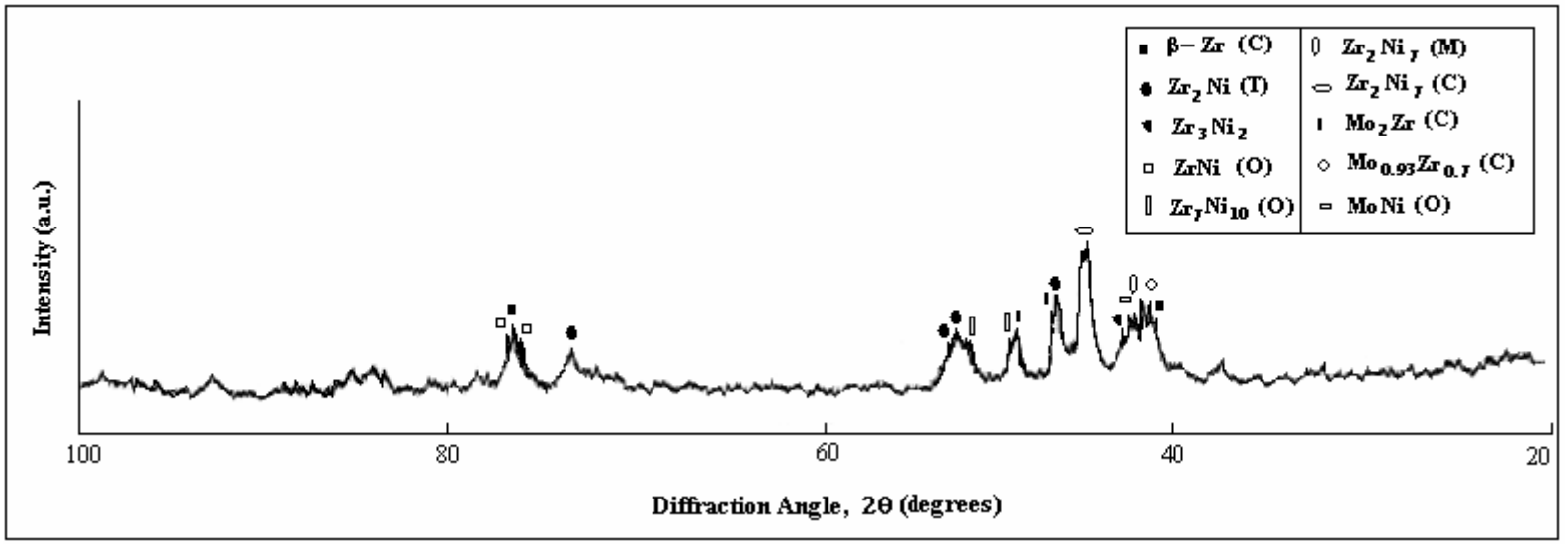

Figure 4.64. The X-ray diffraction pattern for $Zr_{60}Ni_{25}Mo_{15}$ alloy

4. 6. 1. 3. Structural Characterization of $Zr_{60}Ni_{25}Mo_{10}W_5$ Alloy System

In order to obtain the amorphous structure in the casting systems, quaternary $Zr_{60}Ni_{25}Mo_{10}W_5$ system was cast into the wedge-shaped copper mould. The reason for the prediction of amorphous structure from the wedge-shaped cast sample was explained previously. Therefore, the examinations of near-surface region of the cast sample were very important, because at this region, the mould surface and molten alloy firstly interacted to each other and the cooling rate had the highest value. The DSC curve and the temperature values obtained from this curve are given in Figure 4.65 and Table 4.46, respectively.

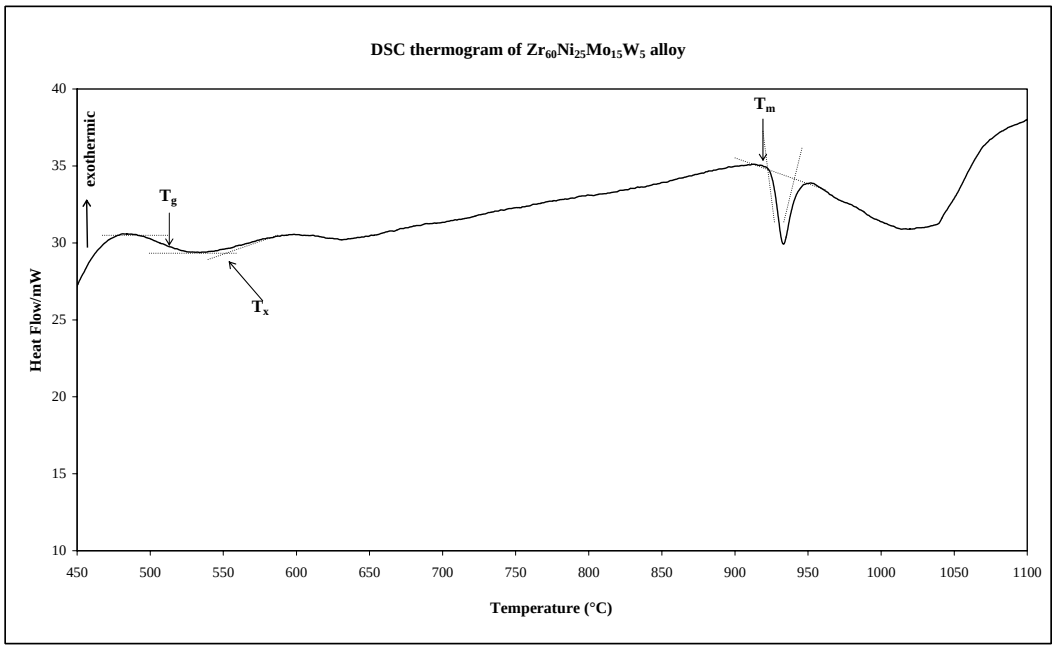

Figure 4.65. Isochronal DSC thermogram of $Zr_{60}Ni_{25}Mo_{10}W_5$ alloy.

From the Figure 4.65, endothermic peak due to the glass transition, followed by a small exothermic peak as crystallization peak are observed. Therefore, from the DSC scan of $Zr_{60}Ni_{25}Mo_{10}W_5$ alloy, the amorphous structure was expected. After this exothermic peak, another successive exothermic peak, corresponding to melting, is observed.

Table 4.46. Temperature values obtained from DSC curve for non-equilibrium wedge-shaped cast $Zr_{60}Ni_{25}Mo_{10}W_5$ alloy.

T_g (°C)	514
T_x (°C)	543
T_m (°C)	928
ΔT_x (°C)	29
T_g/T_m	0,554

SEM analysis of the wedge-shaped cast $Zr_{60}Ni_{25}Mo_{10}W_5$ alloy was performed for the thickest and thinnest sections of the sample, Figure 4.66. As mentioned before, the examinations were also done for the near-surface regions of these sections, Figure 4.67. EDS analyses that were obtained from these sections are given in Table 4.47. The X-ray diffraction pattern for wedge-shaped cast $Zr_{60}Ni_{25}Mo_{10}W_5$ alloy is given in Figure 4.68.

From the Figure 4.66, the differences between the solidification microstructures of the thin and thick regions of the $Zr_{60}Ni_{25}Mo_{10}W_5$ alloy are seen. The thinnest part of the sample has the finer microstructure than the thickest part due to the difference between the rates of cooling. The EDS and X-ray analysis give information about the phases observed after the solidification.

In Figure 4.66 and Figure 4.67, the featureless matrix is observed from the micrographs, especially from the near-surface micrographs of the sample. The existence of this featureless matrix was expected from the results of DSC and XRD analysis and proved the existence of amorphous structure in the matrix of the sample. The compositions of this matrix for the thin and thick sections are much closed to each other. In Figure 4.67 (b), in the near-surface region of the thin section of the sample, crystal clusters with the possible phases; β-Zr, Zr_2Ni, Zr_7Ni_{10} and MoNi, and 650-700 nm Zr_2Mo, MoNi, Ni_4W and $Mo_{0.93}Zr_{0.07}$ crystals embedded into this featureless matrix are observed.

The XRD analysis gave information about the phases formed during solidification. From the X-ray diffractogramme, Figure 4.68, accumulation of the peaks is observed around 43.9° and the analyzed phases confirmed the existence of tetragonal Zr_2Ni and Zr phases in the featureless matrix.

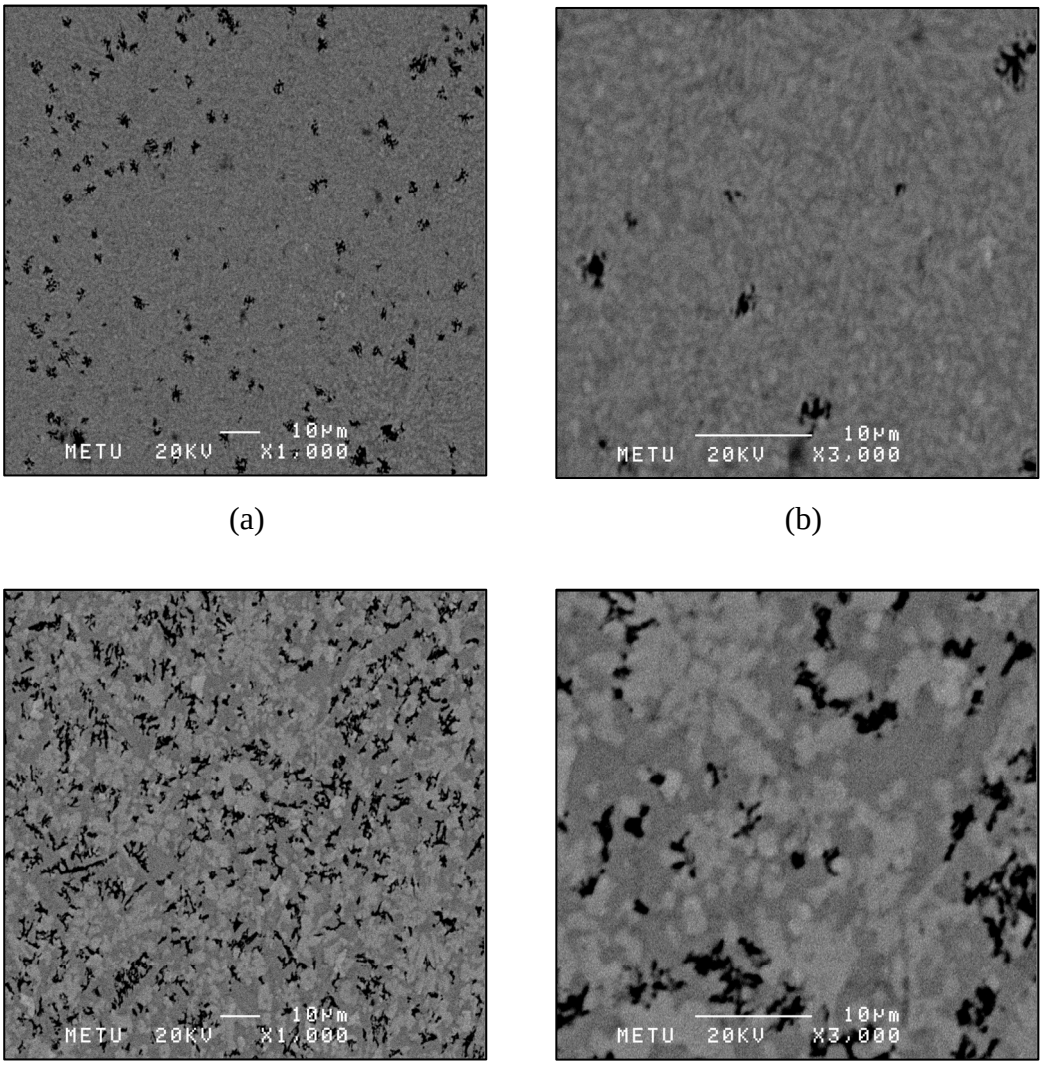

Figure 4.66. SEM images of $Zr_{60}Ni_{25}Mo_{10}W_5$ alloy:

(a) Back-scattered image of the thin section of the sample (x1000).

(b) Back-scattered image of the thin section of the sample (x3000).

(c) Back-scattered image of the thick section of the sample (x1000).

(d) Back-scattered image of the thick section of the sample (x3000).

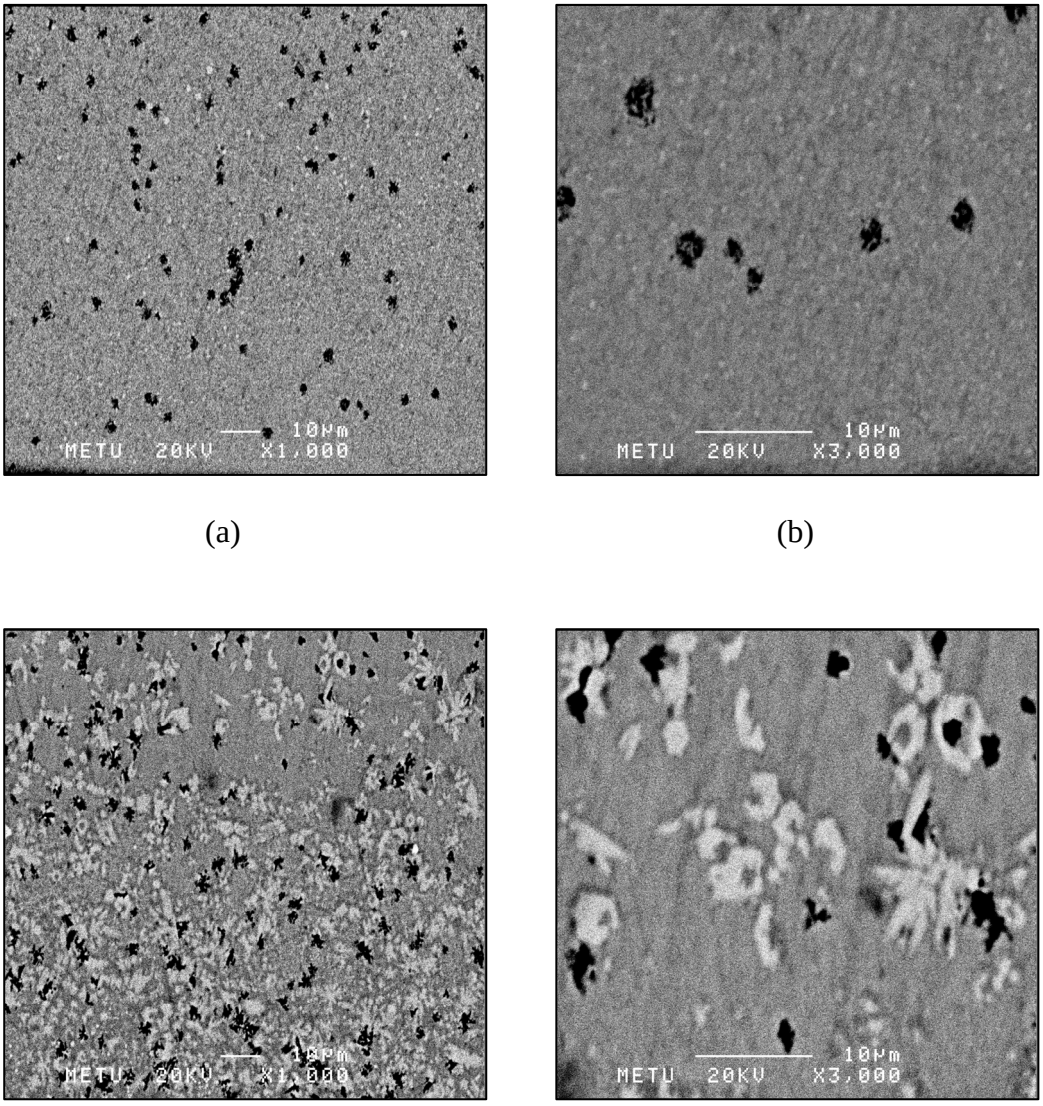

(a) (b)

(c) (d)

Figure 4.67. SEM images of $Zr_{60}Ni_{25}Mo_{10}W_5$ alloy:

(a) Back-scattered image of the near-surface region of the thin section of the sample (x1000).

(b) Back-scattered image of the near-surface region of the thin section of the sample (x3000).

(c) Back-scattered image of the thick section of the sample (x1000).

(d) Back-scattered image of the thick section of the sample (x3000).

Table 4.47. EDS analyses of $Zr_{60}Ni_{25}Mo_{10}W_5$ alloy taken from the thin and thick sections of the sample.

Thin Section	Element	Atom %(±2.00)	Thick Section	Element	Atom %(±2.00)
White region	Zr	53.59	**White region**	Zr	68.85
	Mo	32.99		Mo	21
	Ni	11.58		Ni	7.55
	W	1.84		W	2.6
Grey Region	Zr	72	**Grey Region**	Zr	66.58
	Ni	27.27		Ni	22.20
	W	0.73		Mo	10.68
	Mo	0		W	0.54
Black Region	Zr	67.40	**Black Region**	Zr	56.81
	Ni	22.98		Ni	37.57
	Mo	8.09		Mo	5.11
	W	1.53		W	0.51
Matrix of thin near-surface region	Zr	65.19	**Matrix of thick near-surface region**	Zr	64.34
	Ni	21.40		Ni	24.56
	Mo	12.48		Mo	10.16
	W	0.98		W	0.94

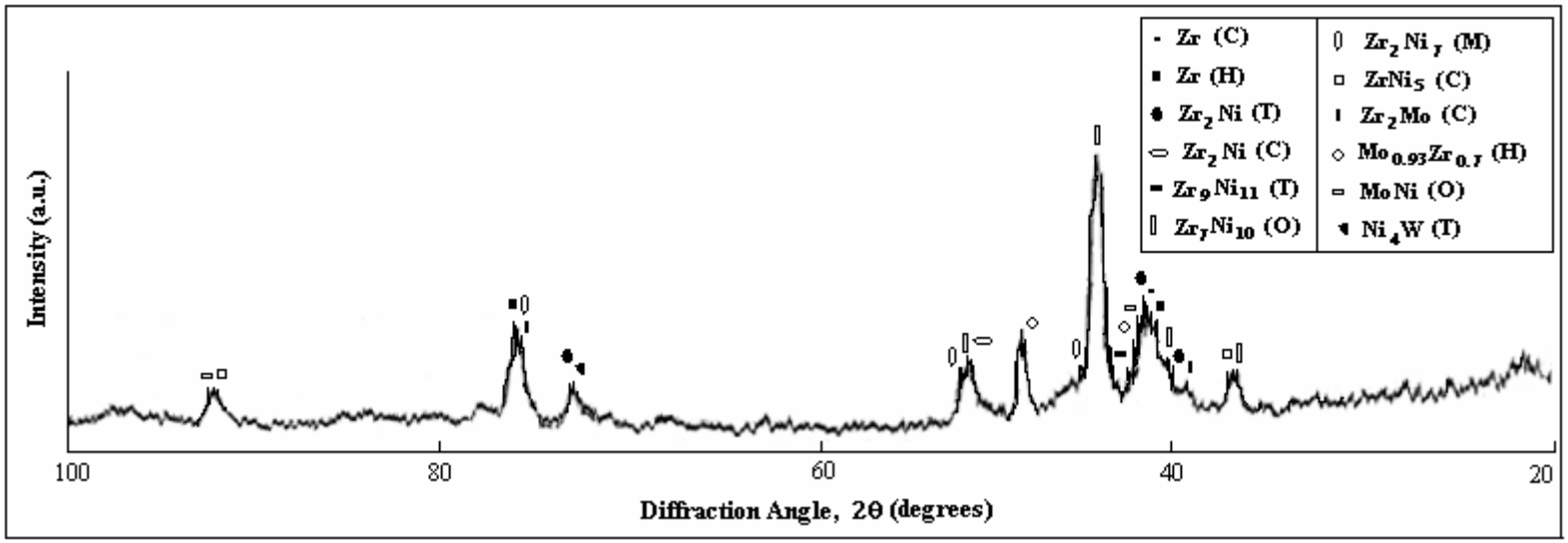

Figure 4.68. The X-ray diffraction pattern for $Zr_{60}Ni_{25}Mo_{10}W_5$ alloy

4. 6. 1. 4. Structural Characterization of $Zr_{50}Ni_{20}Al_{15}Mo_{10}W_5$ Alloy System

Similar to $Zr_{60}Ni_{25}Mo_{10}W_5$ alloy, $Zr_{50}Ni_{20}Al_{15}Mo_{10}W_5$ alloy was cast into the wedge shaped copper mould in order to obtain the amorphous structure. In addition, to understand the GFA of this alloy, the solidification behaviour was examined. For the examination, the alloy was prepared under slow cooling conditions to obtain near-equilibrium solidification microstructure. This type microstructure was compared with the wedge-shaped cast sample, which had a non-equilibrium solidification microstructure. These two samples were examined by the same characterization tests in order to make comparison.

In order to observe the cooling effect on the solidification microstructure, $Zr_{50}Ni_{20}Al_{15}Mo_{10}W_5$ alloy sample was solidified under normal cooling conditions to obtain the near-equilibrium structure. The DSC curve of near-equilibrium $Zr_{50}Ni_{20}Al_{15}Mo_{10}W_5$ alloy is given in Figure 4.69.

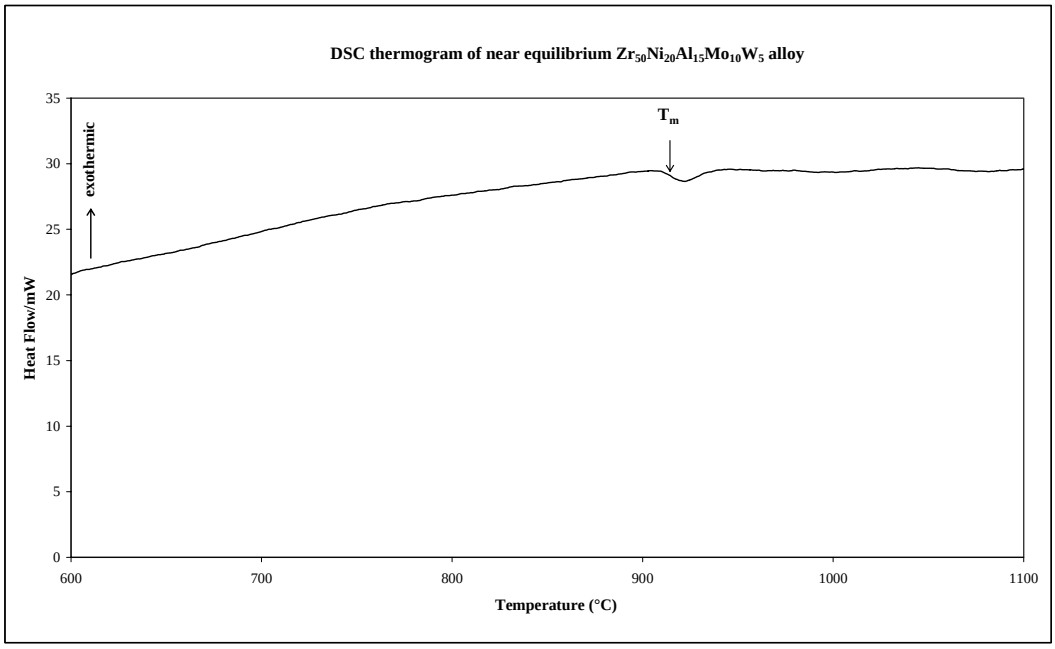

Figure 4.69. Isochronal DSC thermogram of the near-equilibrium $Zr_{50}Ni_{20}Al_{15}Mo_{10}W_5$ alloy.

The DSC curve of the near-equilibrium $Zr_{50}Ni_{20}Al_{15}Mo_{10}W_5$ alloy indicates only melting of this alloy at 910°C. This curve does not give any clue for crystallization and glass transition, as being expected for near-equilibrium structure.

The scanning electron micrographs and the EDS analysis for this near-equilibrium structure are given in Figure 4.70 and Table 4.48. As can be seen from the SEM images of the near-equilibrium structure of the $Zr_{50}Ni_{20}Al_{15}Mo_{10}W_5$ alloy, the solidification event was very complex. The black regions in the micrographs were found to have high Zr content. The composition of Mo and W content were very low in these regions. The Mo and W percent had the highest values for the white regions. The XRD analyses for these regions the phases exist in this microstructure are given in Figure 4.71.

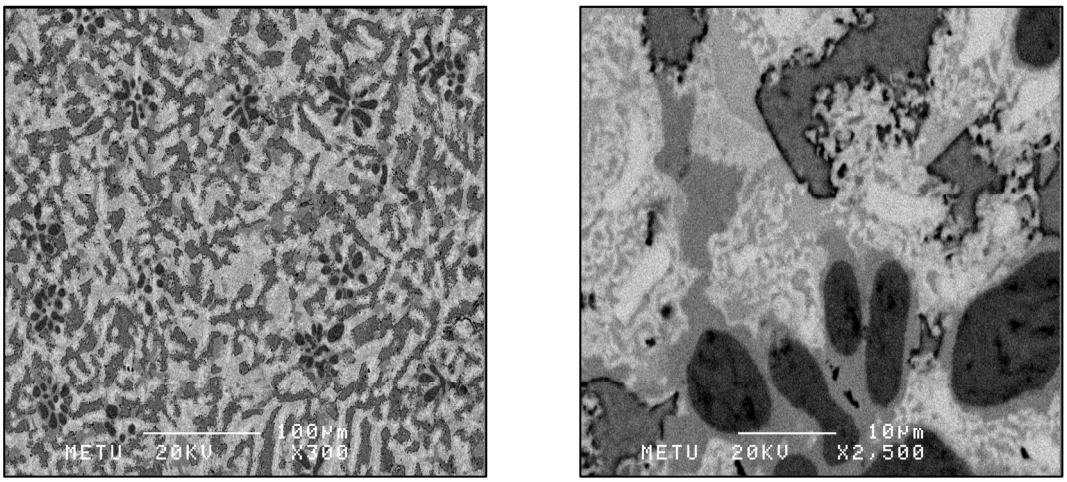

Figure 4.70. SEM images of near-equilibrium $Zr_{50}Ni_{20}Al_{15}Mo_{10}W_5$ alloy:
(a) Back-scattered image of the general view of the sample (x300).
(b) Back-scattered image of the general view of the sample (x2500).

Table 4.48. EDS analyses of near-equilibrium $Zr_{50}Ni_{20}Al_{15}Mo_{10}W_5$ alloy.

Regions	Element	Atom %(±2.00)
Black Region	Zr	92.89
	Al	5.80
	Ni	0.87
	W	0.43
	Mo	0
White region	Zr	44.65
	Mo	24.04
	Al	17.67
	Ni	11.00
	W	2.64
Light Grey Region	Zr	55.11
	Al	24.51
	Ni	18.05
	Mo	1.77
	W	0.56
Bold Grey Region	Zr	39.52
	Al	30.57
	Ni	28.73
	Mo	0.76
	W	0.42

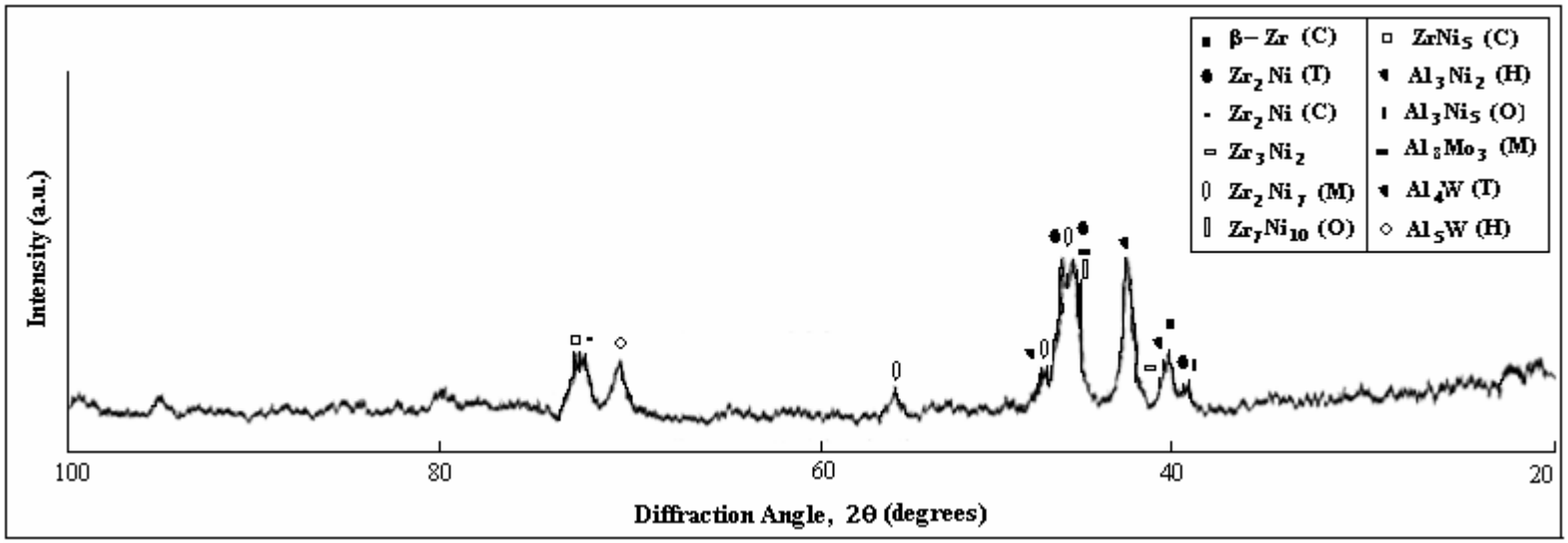

Figure 4.71. The X-ray diffraction pattern for near-equilibrium $Zr_{50}Ni_{20}Al_{15}Mo_{10}W_5$ alloy

Characterization of wedge-shaped cast $Zr_{50}Ni_{20}Al_{15}Mo_{10}W_5$ alloy was carried out also. The DSC curve and the values obtain from this curve are given in Figure 4.72 and Table 4.49, respectively.

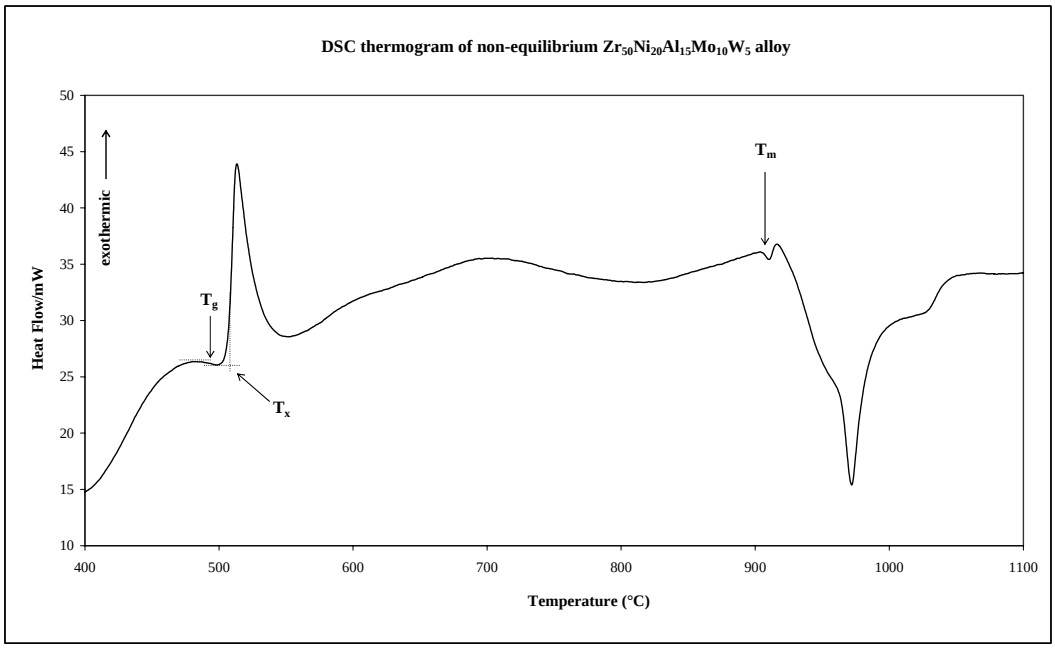

Figure 4.72. Isochronal DSC thermogram of the non-equilibrium $Zr_{50}Ni_{20}Al_{15}Mo_{10}W_5$ alloy.

The DSC curve of the wedge-shaped cast $Zr_{50}Ni_{20}Al_{15}Mo_{10}W_5$ alloy is a good example of the characteristic curve for an amorphous type structure. A small endothermic peak, giving the glass transition temperature, is followed by a successive exothermic peak which is the characteristic event of the crystallization. After crystallization, two stages melting with two endothermic peaks are observed. These peaks correspond to the peritectic and eutectic reactions. Table 4.49 indicates data obtained from this DSC curve.

Table 4.49. Temperature and enthalpy values, obtained from DSC curve, for non-equilibrium $Zr_{50}Ni_{20}Al_{15}Mo_{10}W_5$ alloy.

T_g (°C)	496
T_x (°C)	507
T_m (°C)	905
ΔT_x (°C)	11
T_g/T_m	0,548

It is seen that, T_g and T_x values are clearer to observe from the DSC curve for $Zr_{50}Ni_{20}Al_{15}Mo_{10}W_5$ alloy, Figure 4.72, than those for quaternary $Zr_{60}Ni_{25}Mo_{10}W_5$ alloy, Figure 4.65. Successive exothermic peak due to the crystallization exists for $Zr_{50}Ni_{20}Al_{15}Mo_{10}W_5$ alloy, which was not seen for $Zr_{60}Ni_{25}Mo_{10}W_5$ alloy.

SEM images of the wedge-shaped cast $Zr_{50}Ni_{20}Al_{15}Mo_{10}W_5$ alloy, taken from the thin and thick sections of the sample are given in Figure 4.73. The examination of the microstructure of the near surface regions of the thin section of the $Zr_{50}Ni_{20}Al_{15}Mo_{10}W_5$ alloy cast sample are given in Figure 4.74. EDS analyses, taken from these sections, are given in Table 4.50.

In Figure 4.73, the suppression of nucleation and growth of the phases are observed in the thinnest section of the sample. Although, the forming phases are nearly same for the thinnest and thickest sections, the finer microstructures are observed for thinnest section. From the Figure 4.74 (a) and (b), in the near-surface region of thinnest section of the wedge-shaped cast sample, the matrix microstructures are seemed to have a nearly 40-50 μm width featureless region. This featureless matrix indicated that the alloy was essentially amorphous in these sections. In this matrix, there were irregular eutectic grains and black spots exist. In the transition zone between the completely crystalline and amorphous sections, the microstructure was found to be composed of numerous crystallites embedded in an amorphous matrix. In addition to these crystallites, 3.0-3.3 μm diameter

black spots are observed in this featureless matrix. These spots might be come from the non-melting of the alloy.

The extent of the featureless matrix of the near-surface region of the thin section of the wedge-shaped cast $Zr_{50}Ni_{20}Al_{15}Mo_{10}W_5$ alloy sample, are larger than that for the quaternary $Zr_{60}Ni_{25}Mo_{10}W_5$ alloy sample. The higher amount of amorphous phase related to the featureless matrix for $Zr_{50}Ni_{20}Al_{15}Mo_{10}W_5$ alloy is seemed to be resulted from the addition of Al. The different chemical character of Group 3A element, Al from the Group 4B, 6B and 8B (transition metal group) elements, Zr, Ni, Mo and W, may cause the increase in amount of amorphous structure.

The extent and the existence of the amorphous structure were observed by the X-Ray diffraction pattern, Figure 4.75. As can be seen from this diffractogram, accumulation of phases, may be accepted as a broad single peak, are observed around 45°. The crystalline phases were tried to identify and the characterized phases were indicated by different patterns on this diffractogram. Considering the EDS and XRD analyses together, possible phases for the spot-shaped black crystals clusters formed in the featureless matrix, Figure 4.74 (b), are Zr_2Ni, Al_3Mo, Zr_7Ni_{10} and MoNi. In this SEM image, for the featureless matrix, possible phases are; Zr_2Ni Zr_2Al, MoNi, Al_3Mo, AlZr, AlNiZr, Al_4W and Al_8Mo_3.

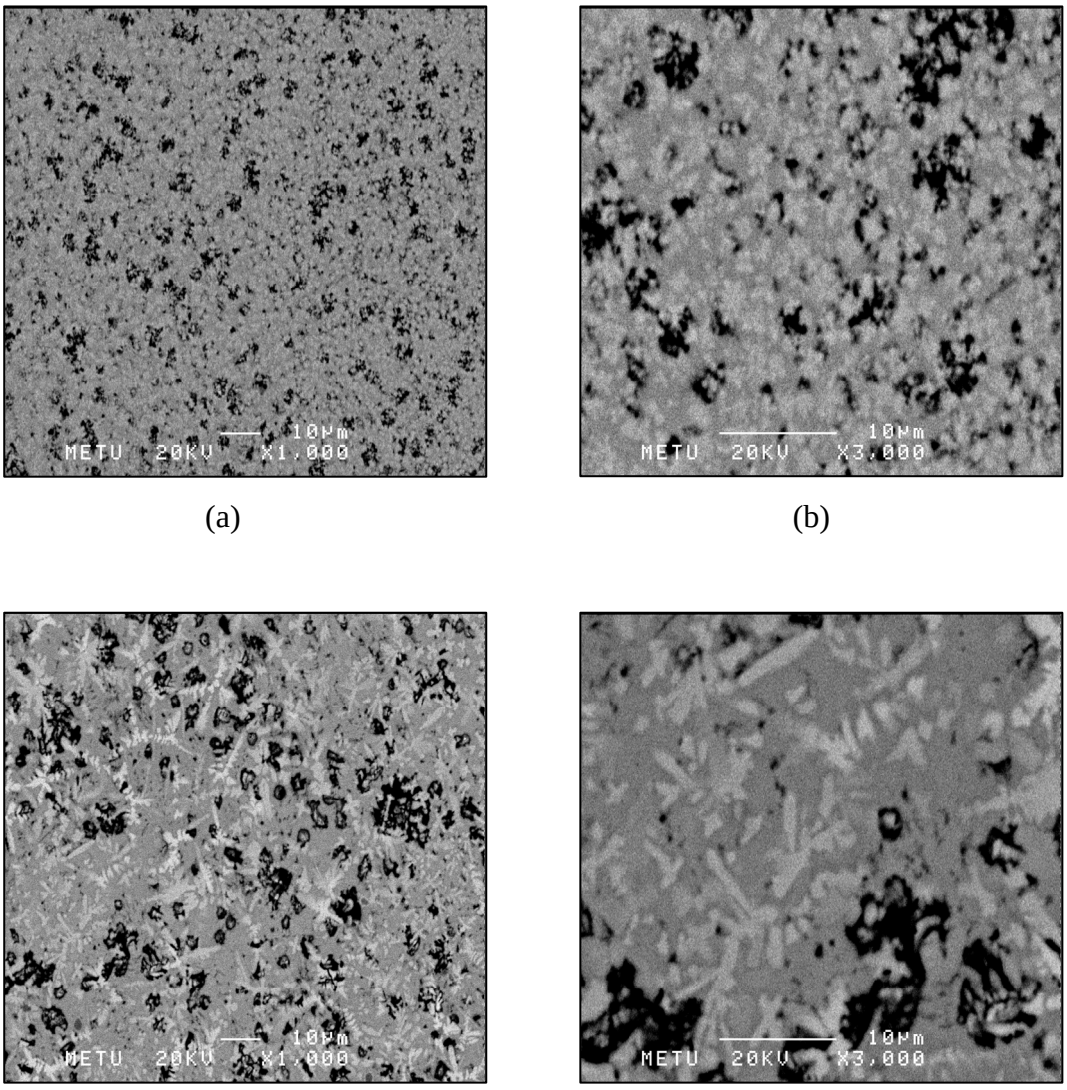

(a) (b)

(c) (d)

Figure 4.73. SEM images of non-equilibrium $Zr_{50}Ni_{20}Al_{15}Mo_{10}W_5$ alloy:

(a) Back-scattered image of thin section of the sample (x1000).

(b) Back-scattered image of thin section of the sample (x3000).

(c) Back-scattered image of thick section of the sample (x1000).

(d) Back-scattered image of thick section of the sample (x3000).

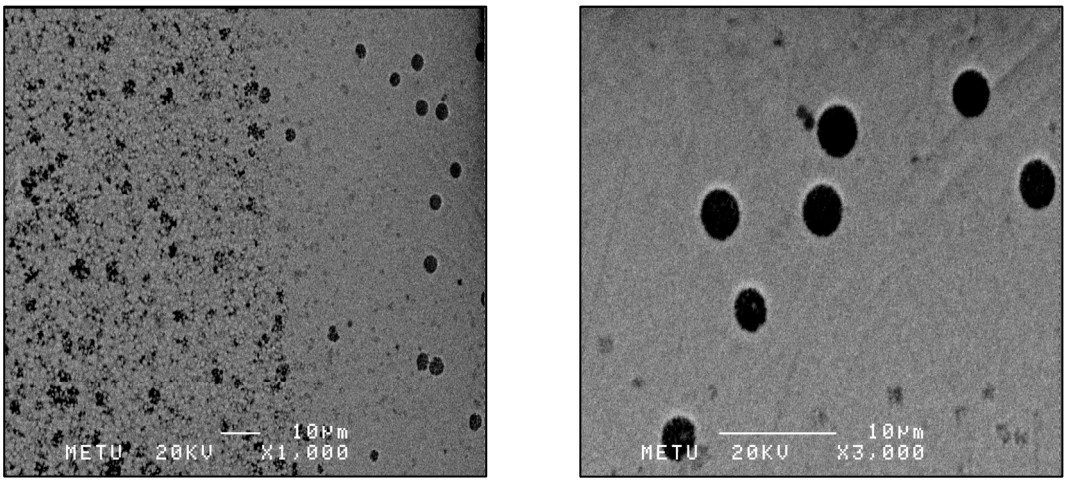

(a) (b)

Figure 4.74. SEM images of non-equilibrium $Zr_{50}Ni_{20}Al_{15}Mo_{10}W_5$ alloy:

(a) Back-scattered image of the near-surface region of the thin section of the sample (x1000).

(b) Back-scattered image of the near-surface region of the thin section of the sample (x3000).

Table 4.50. EDS analyses, taken from thin sections (Figure 4.73 (a) and 4.74 (a)) and thick sections of the sample and thick section (Figure 4.73 (c)) of non-equilibrium $Zr_{50}Ni_{20}Al_{15}Mo_{10}W_5$ alloy.

Thin Section	Element	Atom %(±2.0)	Near-surface region of thin section	Element	Atom %(±2.0)	Thick Section	Element	Atom %(±2.0)
White region	Zr	52.58	**Grey region**	Zr	54.25	**White region**	Zr	55.81
	Mo	16.32		Ni	17.26		Mo	16.79
	Al	15.36		Al	16.38		Ni	12.55
	Ni	13.57		Mo	10.80		Al	11.89
	W	2.17		W	1.30		W	2.96
Grey Region	Zr	54.78	**Black Flower**	Zr	49.49	**Grey Region**	Zr	61.21
	Ni	18.95		Mo	19.65		Ni	23.62
	Al	14.02		Ni	15.65		Al	13.06
	Mo	11.12		Al	12.93		Mo	1.66
	W	1.13		W	2.28		W	0.45
Black Region	Zr	46.13	**Black Spots**	Zr	56.71	**Black Region**	Zr	47.75
	Ni	24.81		Ni	16.14		Ni	33.28
	Mo	15.5		Al	14.12		Al	14.16
	Al	11.52		Mo	11.37		Mo	4.20
	W	2.04		W	1.66		W	0.61

In addition, effects of cooling rate on the solidification microstructures are observed when comparing Figure 4.70 with Figures 4.73 and 4.74. At nearly the same magnification, the microstructures have different character. Non-equilibrium $Zr_{50}Ni_{20}Al_{15}Mo_{10}W_5$ alloy with higher cooling rate has finer microstructure than the near-equilibrium $Zr_{50}Ni_{20}Al_{15}Mo_{10}W_5$ alloy. In addition, the suppression of nucleation and growth of crystalline phases results in the formation of featureless matrix which leads to the formation of amorphous structure.

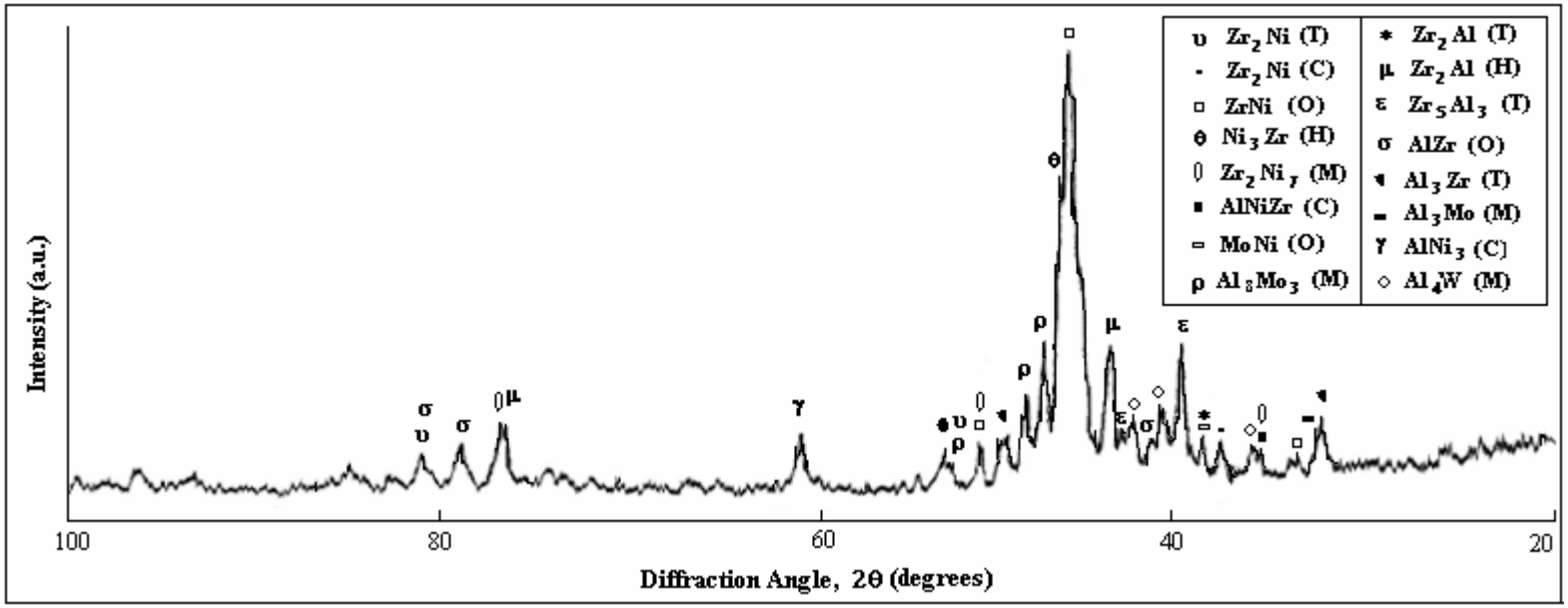

Figure 4.75. The X-ray diffraction pattern for non-equilibrium $Zr_{50}Ni_{20}Al_{15}Mo_{10}W_5$ alloy

CHAPTER 5

CONCLUSIONS

In this study, based on the semi-empirical rules and the electronic theory of alloys in pseudopotential approximation, theoretical study had been carried out in order to determine the potential impurity elements that would be predicted to increase the glass forming ability of studied Zr-based multi-component alloy systems. According to the theoretical study, including the calculations of thermodynamic and structural parameters also, Zr-Ni based systems were selected. After the determination of $Zr_{67}Ni_{33}$ intermetallic, the casting operation were started and the binary system was modified and developed by the addition of its potential impurity elements. Following the casting process, the structural characterizations of cast samples were performed. The observations and results of this study can be concluded as follows:

1. Based on the theoretical analysis, it has been found that Zr-Ni based binary systems have higher glass forming ability than Zr-Al, Zr-Fe and Zr-Co based binary systems.

2. It has been found out that commonly Al, Mo, Ti, V and W metals will be potential impurity elements in order to improve the glass forming ability of Zr-Ni based binary systems.

3. For Zr-Fe based binary systems; B, C, Co, Cr, Mo, Ti, V and W elements are determined to be potential impurity elements and are predicted to increase the glass forming tendency in these systems.

4. For Zr-Co based binary systems; Al, B, C, Co, Cr, Fe, Ge, Hf, Mo, Ni, Si, Ti, V and W elements are found as potential impurity elements and are predicted to increase the glass forming tendency in these systems.

5. For Zr-Al based binary systems; B, C, Ge, Mo, Ni, Si, Ta and W elements are found as potential impurity elements and are predicted to increase the glass forming tendency in these systems.

6. From the theoretical analysis in agreement with the literature survey, $Zr_{67}Ni_{33}$ intermetallic system has been found to have higher glass forming ability than other theoretically studied Zr-Ni based binary systems.

7. In the near-surface region of the wedge-shaped cast $Zr_{60}Ni_{25}Mo_{10}W_5$ alloy sample, featureless matrix corresponding to the amorphous structure has been observed. The presence of amorphous structure had been verified by the other structural characterization tests; DSC and XRD.

8. In the wedge-shaped cast, $Zr_{50}Ni_{20}Al_{15}Mo_{10}W_5$ alloy, nearly 40-50 μm width featureless region in the near-surface section of the sample has been seen. The extent and existence of the amorphous structure had been proved by the DSC and XRD analysis.

9. The potential impurity elements, Al, Mo and W, used in the development of $Zr_{67}Ni_{33}$ intermetallic based multi-component alloy systems, have been found to increase the glass forming ability of these systems, experimentally. This experimental result confirms the results of theoretical study.

10. It has been observed that the volume fraction of the amorphous phase is significantly increased in five-component alloy system than the quaternary alloy system. The reason of this increasing is caused from the addition of

Al. Therefore, it is understood that the addition of Al to the Zr-Ni based systems increases the glass forming ability of the systems considerably.

11. By making a comparison between the non-equilibrium and near-equilibrium $Zr_{50}Ni_{20}Al_{15}Mo_{10}W_5$ alloy, it has been proved that the cooling rate is very important factor on the microstructure of the samples for obtaining amorphous structure.

12. It has been shown that Zr-based bulk metallic amorphous alloys can be produced directly from the melt by the centrifugal casting method.

CHAPTER 6

SUGGESTIONS FOR FUTURE WORKS

In the light of observations and results obtained in this study, suggestions for future works can be summarized as follows:

- In the theoretical part of this study, four type of Zr-based binary systems were studied and for each system theoretical calculations in order to understand their glass forming ability were carried out. Among these systems, only $Zr_{67}Ni_{33}$ binary system was developed and studied in the experimental part. By using the results of these calculations and the determined potential impurity elements, other Zr-Ni, Zr-Al, Zr-Fe and Zr-Co binary systems should be studied and developed experimentally.

- It has been observed that $Zr_{67}Ni_{33}$ based multi-component systems with alloying elements; Al, Mo and W have high glass forming ability. The usage of these impurity elements in Zr-Ni based systems are not seen widely in the literature, therefore the development of Zr-Ni based systems with these alloying elements should be performed. Considering the importance of the composition effect on the glass forming ability, new $Zr_{67}Ni_{33}$ based multi-component systems with these impurity elements should be studied and produced with different compositions.

- Structural characterization and crystallization kinetics of the cast alloys can should be carried out by Transmission Electron Microscopy (TEM).

- The mechanical properties of the produced bulk amorphous alloys should be investigated and improved.

- The improvement and optimization of the processing parameters in order to obtain the desired thickness, shape and properties of the produced bulk metallic amorphous alloys should be studied.

REFERENCES

1. F. E. Luborsky, “Amorphous Metallic Alloys”, Butterworth and Co. (Publishers) Ltd., Great Britain, 1, 1983.

2. A. Inoue, “Bulk Amorphous Alloys, Preparation and Fundamental Characteristics”, Materials Science Found. 4, Trans. Tech. Publications Ltd., Switzerland, 1998.

3. O. Buchanon, MRS Bull, 27, 850-851, 2002.

4. T. R. Anantharaman, “Metallic Glasses, Production, Properties and Applications”, Trans. Tech. Publications, Switzerland, 1984.

5. W. Klement, R.H. Willens and P. Duwez, Nature, 187, 869, 1960.

6. A. Inoue, Acta Mater., 48, 279-306, 2000.

7. J. F. Löffler, Intermetallics, 11, pp. 529, 2003.

8. A. Inoue, W. L. Johnson, C. T. Liu, Bulk Metallic Glasses, MRS Symposium Proceedings, 554, Warrendale, PA, Materials Research Society, 1999.

9. A. Inoue, Acta Mater., 48, pp. 279, 2000.

10. A. Inoue, K. Amiya, Mater. Trans., JIM, 43, pp. 81, 2002.

11. A. Inoue, K. Amiya, Mater. Trans., JIM, 43, pp. 2578, 2002.

12. A. Inoue, T. Zhang, T. Masumoto, Mater. Trans. JIM, 30, pp. 965-72, 1989.

13. T. Zhang, A. Inoue, T. Masumoto, Mater. Trans. JIM, 32, pp. 1005, 1991.

14. A. Peker, WL. Johnson, Appl. Phys. Lett., 63, pp. 2342-4, 1993.

15. A. Inoue, J. S. Gook, Mater. Trans. JIM, 36, pp. 1282, 1995.

16. A. Inoue, Y. Shinohara, J. S. Gook, Mater. Trans. JIM, 36, pp. 1427, 1995.

17. A. Inoue, A. Inoue, J. S. Gook, Mater. Trans. JIM, 37, pp. 32, 1996.

18. A. Inoue, T. Zhang, T. Masumoto, Mater. Trans. JIM, 36, pp. 391, 1995.

19. W. L. Johnson, A. Peker, Mater. Sci. Forum, 35, pp. 225, 1996.

20. H. Kato, Y. Kawamura, A. Inoue, Mater. Trans. JIM, 37, pp. 70, 1996.

21. R. Doglione, S. Spriano, L. Battezzati, Nano Struct. Mater., 8, pp. 447, 1997.

22. K. H. J. Buschow, J. Phys. F. Metal Phys., 14, pp. 593, 1984.

23. S. Banerjee, R. T. Savalia, D. K. Dey, Mater. Sci. Eng., A304-306, pp. 26-33, 2001.

24. H. S. Chen, Rep. Prog. Phys., 43, pp. 355, 1980.

25. M. Harmelin, R. Calvayrac, A. Ovivy, J. Bigot, P. Burnier, M. Fayard, J. Non-Cryst. Soilds, 61/62, pp. 931, 1984.

26. L. E. Tanner, Acta Metall. Mater., 28, pp. 1805, 1980.

27. K. H. J. Buschow, Acta Metall. Mater., 31, pp. 155, 1983.

28. L. E. Tanner, in: S. Steeb, H. Warlimonts (Eds.), Preceedings of the 5th International Conference on rapidly quenched Metals, Vol. 1, Wuzburg, 1984, North Holland, Amsterdam, pp. 67, 1985.

29. G. K. Dey, S. Banerjee, Mater. Sci. Eng., 73, pp. 187, 1985.

30. S. Kavesh, in: J. J. Gillian, H. F. Leafy (Eds.), Metallic Glasses, ASM, Metals Park, OH, pp. 36, 1978.

31. G. K. Dey, Rapid Solidification of ZirconiumAlloys, Ph. D. Thesis, Banaras Hindu University, Varanasi, 1988.

32. C. Ghosh, M. Chandrashekaran, L. Delaey, Acta Metall. Mater., 37, pp. 929, 1991.

33. W. Chen, Y. Wang, J. Qiang, C. Dong, Acta Mater., 51, pp. 1899-1907, 2003.

34. G.E. Abrosimova, A. S. Aronin, Yu. V. Kirjanov, D. V. Matveev, V. V. Molokanov, I. I. Zverkova, Journal of Non-Crystalline Solids, 288, pp 121-126, 2001.

35. Min Qi, H. J. Fecht, Material Characterization, 47, pp. 215-218, 2001.

36. X. Gu, L. Q. Xing, T. C. Hufnagel, Journal of Non-Crystalline Solids, 311, pp. 77-82, 2002.

37. A. Inoue, Cang Fan, Akira Takeuchi, Mater. Trans., 40, pp. 42-51, 1999.

38. A. Inoue, "Bulk Amorphous Alloys, Practical Characteristics and Applications", Trans. Tech. Publications, Zurich, 1999.

39. V. I. P. Vintage Model Amorphous Face Golf Club Catalog, Dunlop, Tokyo, 1998.

40. R. Busch, E. Bakke, W. L. Johnson, Acta Mater., 46, 13, pp. 4725-4732, 1998.

41. O. N. Senkov, D. B. Miracle, Mater. Res. Bull., 36, pp. 2183–98, 2001.

42. O. N. Senkov, D. B. Miracle, J. Non-Cryst. Solids, 317, pp.34, 2003.

43. O. N. Senkov, D. B. Miracle, S. Rao, T. Egami, A. L. Greer, A. Inoue, S. Ranganathan, Supercooled Liquids, Glass Transition, and Bulk Metallic Glasses, MRS Proceedings, vol. 754, Warrendale, PA, pp. 59, 2003.

44. O. N. Senkov, D. B. Miracle, W. S. Sanders, Philos. Mag. A, 83, pp.2409, 2003.

45. G. M. Dougherty, Y. He, G. J. Shiflet, S. J. Poon, Scripta Metall. Mater, 30, pp.101., 1994.

46. A. R. Yavari, A. Inoue, MRS Symposium Proceedings, 554, pp. 21, 1999.

47. W. Kurz, D.J. Fisher, **"**Fundamentals of Solidification", Third Edition, Trans Tech. Publications Ltd, Switzerland, 1992.

48. R.N. Singh, F. Sommer, "Segregation and immiscibility in liquid binary alloys", Rep. Prog. Phys., 60, pp. 57-150, 1997.

49. A.R. Miedema, J. Less-Common Met., 32, pp. 117, 1973.

50. A.R. Miedema, R. Boom, F.R. de Boer, J. Less-Common Met., 41, pp. 283, 1975.

51. A.R. Miedema, J. Less-Common Met., 46, pp. 67, 1976.

52. R. Boom, F.R. de Boer, A.R. Miedema, J. Less-Common Met., 45, pp. 237, 1976.

53. R. Boom, F.R. de Boer, A.R. Miedema, J. Less-Common Met., 46, pp. 271, 1976.

54. E.A. Guggenheim, in: Mixtures, Caredon Press, Oxford, 1952.

55. F. Sommer, in: S. Steeb, H. Warlimont (Eds.), Rapidly Quenched Metals, Vol. 1, Part V, Elsevier, Amsterdam, pp. 153, 1985.

56. G.A. Mansoori, N.F. Carnahan, K.E. Starling, T.W. Leland Jr., J. Chem. Phys., 54, pp. 1523, 1971.

57. I. H. Umar, I. Yokoyama, W. H. Young, Phil. Mag., 34, pp. 535, 1976.

58. P. T. Sarjeant, R. Roy, Mater. Res. Bull., 3, pp. 265, 1968.

59. H.A. Davies, Rapid quenching and formation of metallic glasses, in: B. Cantor (Ed.), Rapidly Quenched Metals, Vol. 1, Part III, The Metal Society, pp. 1, 1978.

60. L. Battezzati, A. L. Greer, Acta Metal., 37, pp. 1791, 1989.

61. O. Akinlade, R. N. Singh, F. Sommer, Journal of Alloys & Compounds, 267, pp. 195-198, 1998.

62. A. Inoue, A. Takeuchi, Mater. Science and Eng., A304-306, pp. 446-451, 2001.

63. R.N. Singh, F. Sommer, Phys. Chem. Liq., in press, 1997.

64. R.N. Singh, N.H. March, in: J.H. Westbrook, R.L. Fleischer Eds., Intermetallic Compound-Principle and Practice, Ch. 28, Wiley, London, 1994.

65. S.M. Osman, R.N. Singh, Phys. Rev. E51, 332, 1995.

66. L. I. Yastrebov, A. A. Katsnelson, "Foundations of one electron theory of solids", English Translation, Mir Publishers, 1987.

67. J. M. Ziman, "Principles of the theory of solids", Cambridge University Press., Camridge, 1969.

68. A. O. Mekhrabov, M. V. Akdeniz, Metallurgical and Materials Transactions A, 34A, pp. 721-734, 2003.

69. A. O. Mekhrabov, M. V. Akdeniz, Chemical Eng. Comm., 190, pp. 898-910, 2003.

70. A. O. Mekhrabov, M. V. Akdeniz, Acta Materialica, 47, 7, pp. 2067-2075, 1999.

71. A. O. Mekhrabov, M. V. Akdeniz, Acta Materialica, 46, 4, pp. 1185-1192, 1998.

72. A. O. Mekhrabov, M. V. Akdeniz, M. M. Arer, Acta Materialica, 45, 3, pp. 1077-1083, 1997.

73. D. B. Miracle, O. N. Senkov, Mater. Scien. and Eng. A347, pp. 50-58, 2003.

74. K. Feldman, U. S. Pat., 3, 340, 334, 1967.

75. W. G. Hegmann, U. S. Pat., 3, 588, 951, 1971.

76. A. Inoue, T. Zhang, T. Masumoto, Mater. Trans. JIM., 31, 177**,** 1990.

77. A. Inoue, T. Zhang, T. Masumoto, J. Non-Cryst. Solids, 473, pp. 156-159, 1993.

78. A. L. Peker, W. L. Johnson, Appl. Phys. Lett., 63, pp. 2342, 1993.

79. W. L. Johnson, MRS Bull., 24, pp. 42, 1999.

80. T. Zhang, A. Inoue, T. Masumoto, Mater. Trans. JIM. 32, 1005, 1991.

81. J. Saida, M. Matsushita, A. Inoue, J. Mater. Res., 16, 28, 2001.

82. Z. Zhang, K.H. Kuo, Philos. Mag. B, 54, L83, 1986.

83. B. Yang, Philos. Mag. Lett., 57, 171, 1988.

84. J. C. de Lima, PhD Thesis, University of Paris, 1989.

85. T. Fukunaga, N. Watanable, K. Suzuki, in: Proc. Rapidly Quenched Metals 5, ed. S. Steeb and H. Warlimont, Elsevier, Amsterdam, pp. 475, 1985.

86. F. Paul, R. Frahm, Phys. Rev. B, 42, 1094-1095, 1990.

87. W. M. Kuschke, P. Lamparter and Steeb, Physica B 180 & 181, pp. 790-792, 1992.

88. H. U. Krebs, C. Michaelsen, J. Reichelt, H. A. Wagner, J. Wecker, Q.R. Zhang and H.C. Freyhardt, J. Non-Cryst. Solids 61 & 62, pp. 463-468, 1984.

89. W.Paszkowicz, J. Phys. F, to be published.

90. E. Matsubara, Y. Waseda, Mater. Trans., JIM 36, 883, 1995.

APPENDIX A

BINARY PHASE DIAGRAM DATA

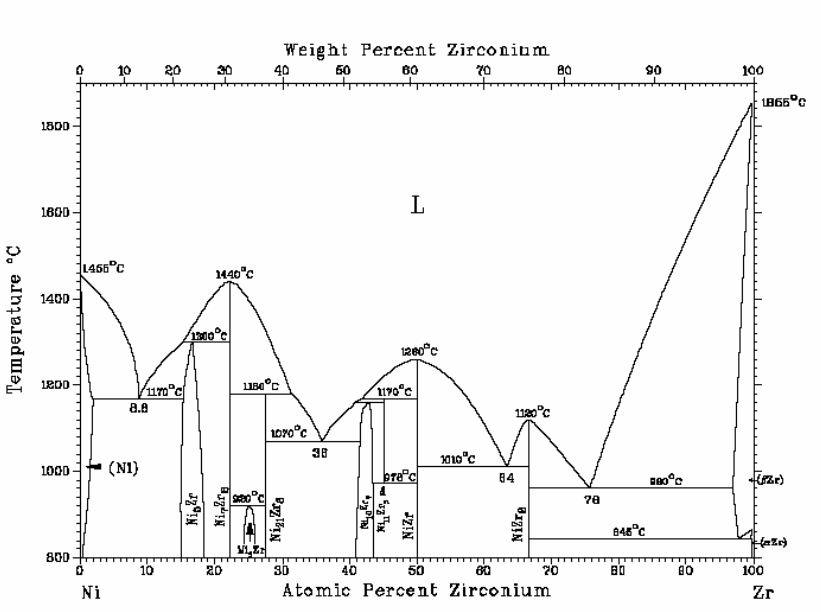

Figure A.1. The equilibrium phase diagram for Zr-Ni binary alloys

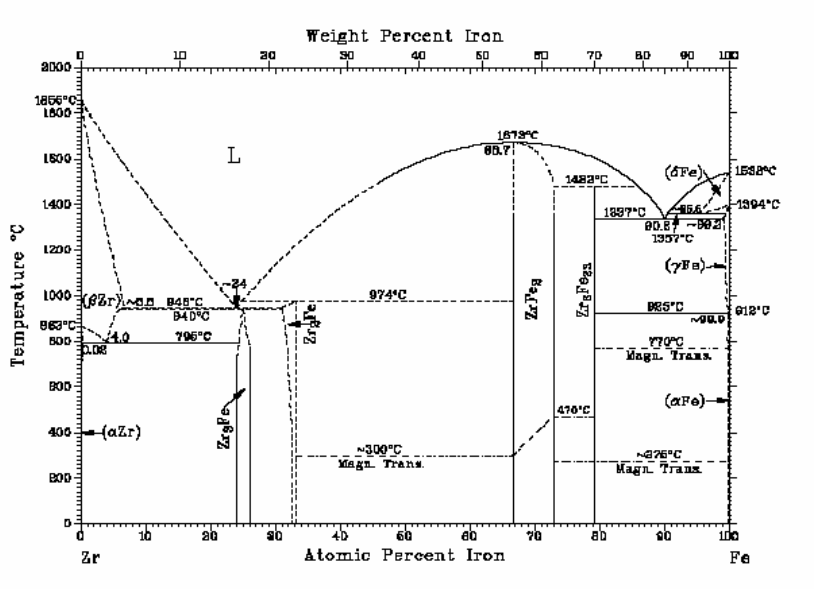

Figure A.2. The equilibrium phase diagram for Zr-Fe binary alloys

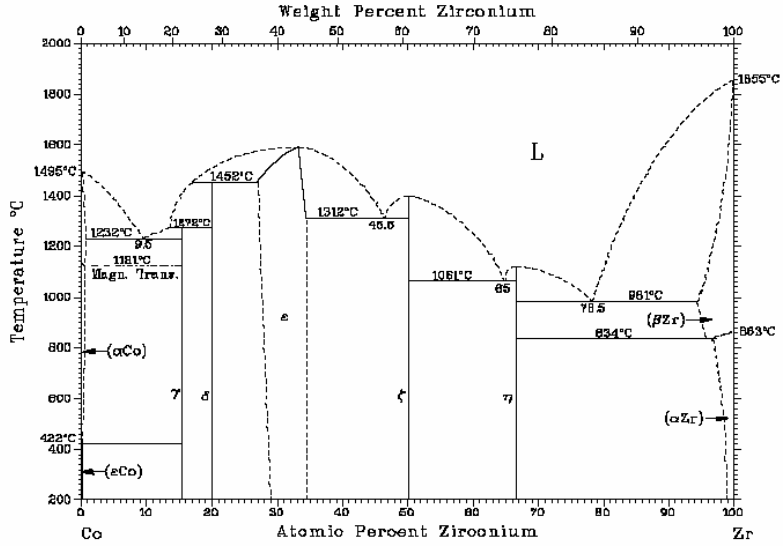

Figure A.3. The equilibrium phase diagram for Zr-Co binary alloys

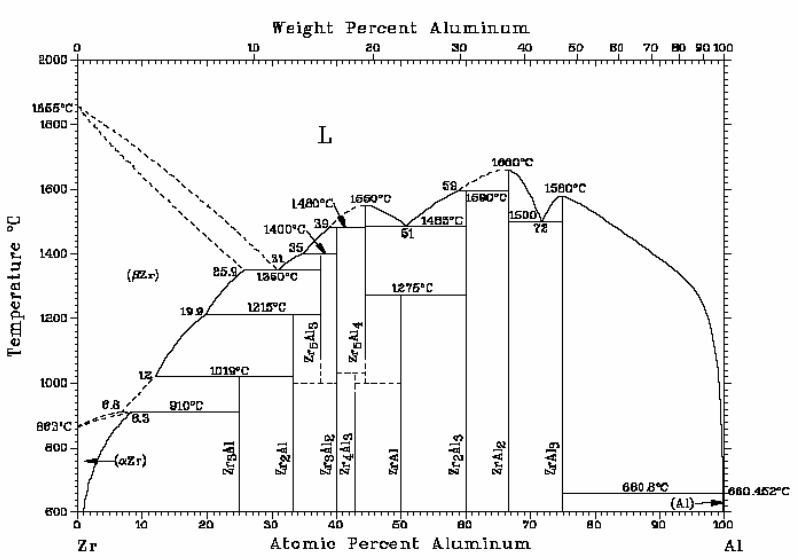

Figure A.4. The equilibrium phase diagram for Zr-Al binary alloys

APPENDIX B

CALCULATION RESULTS OF THERMODYNAMIC AND STRUCTURAL PARAMETERS DATA OF Zr-Ni, Zr-Fe, Zr-Co and Zr-Al BINARY SYSTEMS

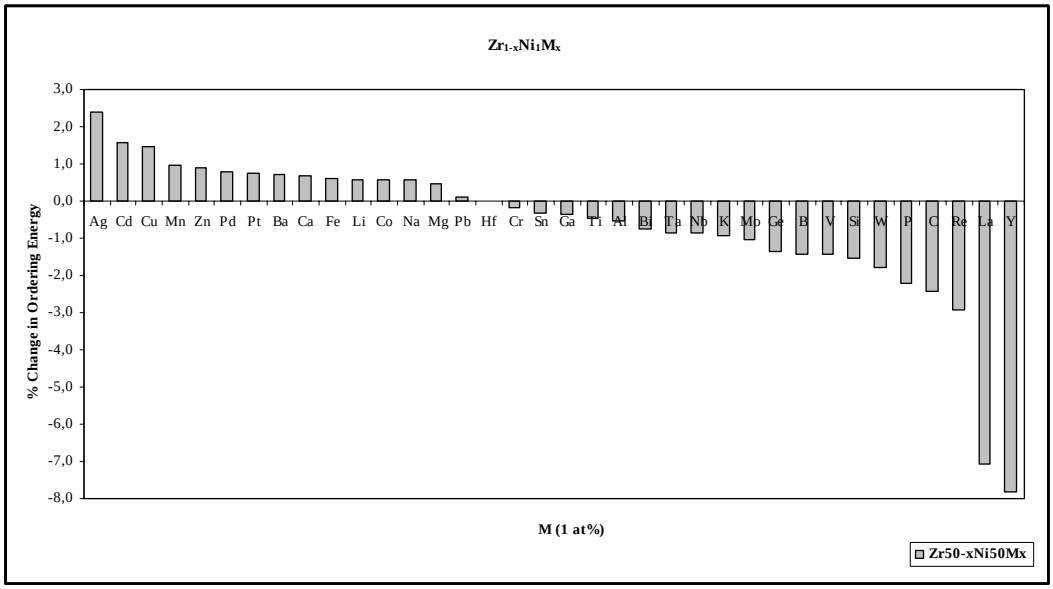

Figure B.1. % Change in ordering energy of $Zr_{50}Ni_{50}$ binary system for the addition of 1 at % impurity elements (M) when 1 at % is taken from Zr ($Zr_{0,49}Ni_{0,50}M_{0,01}$system).

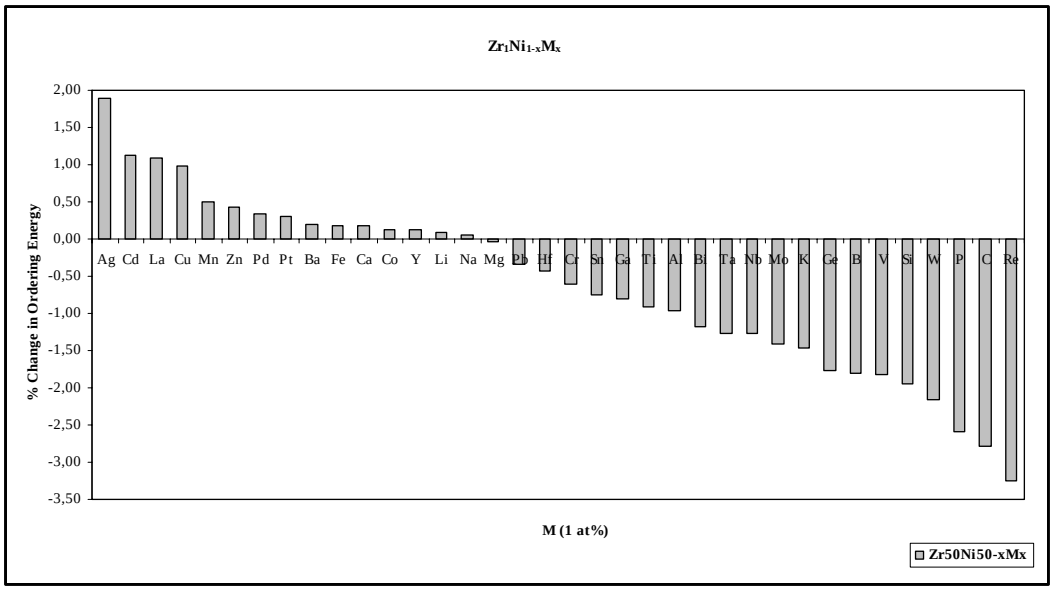

Figure B.2. % Change in ordering energy of $Zr_{50}Ni_{50}$ binary system for the addition of 1 at % impurity elements (M) when 1 at % is taken from Ni ($Zr_{0,50}Ni_{0,49}M_{0,01}$system).

Table B.1. The ordering energy values for $Zr_{50}Ni_{50}$ and $Zr_{0,49}Ni_{0,50}M_{0,01}$.

M	W_{Zr-Ni} (J/mol)	w_{Zr-Ni} (J/mol)	W_{Zr-M} (J/mol)	w_{Zr-M} (J/mol)	W_{Ni-M} (J/mol)	w_{Ni-M} (J/mol)
$Zr_{50}Ni_{50}$	-2,182E+04	-1,462E+05				
Ag	-2,177E+04	-1,459E+05	1,219E+04	8,164E+04	3,067E+03	2,055E+04
Al	-2,183E+04	-1,463E+05	-2,255E+04	-1,511E+05	3,813E+03	2,555E+04
B	-2,185E+04	-1,464E+05	-9,493E+04	-6,361E+05	-2,278E+04	-1,527E+05
Ba	-2,181E+04	-1,461E+05	-4,206E+05	-2,818E+06	-4,717E+05	-3,161E+06
Bi	-2,184E+04	-1,463E+05	2,016E+02	1,351E+03	-5,488E+04	-3,677E+05
C	-2,188E+04	-1,466E+05	-5,988E+04	-4,012E+05	-7,272E+03	-4,872E+04
Ca	-2,181E+04	-1,461E+05	-1,094E+05	-7,328E+05	-1,059E+05	-7,096E+05
Cd	-2,179E+04	-1,460E+05	-2,487E+04	-1,667E+05	9,580E+02	6,418E+03
Co	-2,181E+04	-1,461E+05	-2,167E+04	-1,452E+05	0	0
Cr	-2,183E+04	-1,462E+05	-1,566E+04	-1,049E+05	5,309E+02	3,557E+03
Cu	-2,179E+04	-1,460E+05	-6,237E+03	-4,179E+04	2,054E+03	1,376E+04
Fe	-2,181E+04	-1,461E+05	-1,163E+04	-7,793E+04	-3,786E+02	-2,537E+03
Ga	-2,183E+04	-1,463E+05	-2,760E+04	-1,849E+05	1,171E+03	7,843E+03
Ge	-2,185E+04	-1,464E+05	-1,765E+04	-1,183E+05	1,890E+03	1,266E+04
Hf	-2,182E+04	-1,462E+05	-1,721E+02	-1,153E+03	-2,094E+04	-1,403E+05
K	-2,184E+04	-1,463E+05	-7,728E+04	-5,178E+05	-6,180E+04	-4,141E+05
La	-2,198E+04	-1,473E+05	-1,264E+03	-8,469E+03	-1,175E+04	-7,870E+04
Li	-2,181E+04	-1,461E+05	-5,020E+04	-3,363E+05	2,030E+03	1,360E+04
Mg	-2,181E+04	-1,461E+05	-2,592E+04	-1,737E+05	-7,675E+02	-5,142E+03
Mn	-2,180E+04	-1,461E+05	-1,268E+04	-8,494E+04	-6,394E+02	-4,284E+03
Mo	-2,184E+04	-1,464E+05	6,553E+02	4,390E+03	-2,748E+04	-1,841E+05
Na	-2,181E+04	-1,461E+05	-4,043E+04	-2,708E+05	-1,323E+04	-8,866E+04
Nb	-2,184E+04	-1,463E+05	1,835E+03	1,229E+04	-1,787E+04	-1,197E+05
P	-2,187E+04	-1,465E+05	-3,230E+04	-2,164E+05	9,252E+03	6,199E+04
Pb	-2,182E+04	-1,462E+05	1,563E+04	1,048E+05	-4,145E+04	-2,777E+05
Pd	-2,181E+04	-1,461E+05	6,446E+03	4,319E+04	-9,163E+03	-6,139E+04
Pt	-2,181E+04	-1,461E+05	-5,189E+04	-3,477E+05	-5,310E+03	-3,558E+04
Re	-2,189E+04	-1,466E+05	6,686E+03	4,480E+04	-1,847E+04	-1,237E+05
Si	-2,186E+04	-1,464E+05	-2,362E+04	-1,582E+05	7,297E+03	4,889E+04
Sn	-2,183E+04	-1,463E+05	-1,490E+03	-9,983E+03	-8,856E+03	-5,933E+04
Ta	-2,184E+04	-1,463E+05	1,777E+03	1,191E+04	-1,536E+04	-1,029E+05
Ti	-2,183E+04	-1,463E+05	-2,555E+04	-1,712E+05	1,098E+03	7,358E+03
V	-2,185E+04	-1,464E+05	-1,164E+04	-7,799E+04	7,835E+03	5,250E+04
W	-2,186E+04	-1,465E+05	2,761E+02	1,850E+03	-3,284E+04	-2,200E+05
Y	-2,199E+04	-1,474E+05	-2,337E+03	-1,566E+04	-7,940E+03	-5,320E+04
Zn	-2,180E+04	-1,461E+05	-3,045E+04	-2,040E+05	-2,958E+02	-1,982E+03

Table B.2. Thermodynamic and structural data of $Zr_{50}Ni_{50}$ and $Zr_{0,49}Ni_{0,50}M_{0,01}$.

M	ΔH_{mixing} (J/mol)	S^{σ} (J/K.mol)	ΔS^{ideal} (J/K.mol)	ΔS_{mixing} (J/mol)	ΔG_{mixing} (J/mol)	R_c (J/s)	$\Delta\eta/\eta_o$	α_1
$Zr_{50}Ni_{50}$	-3,655E+04	2,768	5,763	8,531	-4,963E+04	3,777E+07	2,868	-1,0
Ag	-3,524E+04	2,733	6,171	8,904	-4,888E+04	3,954E+07	2,764	
Al	-3,646E+04	2,736	6,171	8,907	-5,011E+04	3,678E+07	2,860	
B	-3,974E+04	2,957	6,171	9,128	-5,373E+04	2,937E+07	3,118	
Ba	-6,509E+04	2,795	6,171	8,966	-7,884E+04	6,763E+06	5,107	
Bi	-3,764E+04	2,713	6,171	8,884	-5,126E+04	3,441E+07	2,953	
C	-3,811E+04	2,977	6,171	9,148	-5,214E+04	3,222E+07	2,990	
Ca	-4,287E+04	2,726	6,171	8,897	-5,650E+04	2,526E+07	3,363	
Cd	-3,655E+04	2,711	6,171	8,882	-5,017E+04	3,671E+07	2,868	
Co	-3,651E+04	2,786	6,171	8,957	-5,024E+04	3,639E+07	2,865	
Cr	-3,632E+04	2,787	6,171	8,958	-5,006E+04	3,680E+07	2,850	
Cu	-3,591E+04	2,778	6,171	8,949	-4,962E+04	3,776E+07	2,817	
Fe	-3,619E+04	2,790	6,171	8,960	-4,993E+04	3,707E+07	2,840	
Ga	-3,670E+04	2,745	6,171	8,916	-5,037E+04	3,620E+07	2,879	
Ge	-3,639E+04	2,790	6,171	8,961	-5,012E+04	3,664E+07	2,855	
Hf	-3,651E+04	2,710	6,171	8,880	-5,013E+04	3,680E+07	2,865	
K	-4,042E+04	2,868	6,171	9,039	-5,428E+04	2,858E+07	3,171	
La	-3,650E+04	2,708	6,171	8,879	-5,012E+04	3,682E+07	2,864	
Li	-3,738E+04	2,718	6,171	8,889	-5,101E+04	3,492E+07	2,933	
Mg	-3,668E+04	2,707	6,171	8,877	-5,029E+04	3,645E+07	2,878	
Mn	-3,622E+04	2,757	6,171	8,927	-4,991E+04	3,718E+07	2,842	
Mo	-3,674E+04	2,753	6,171	8,924	-5,042E+04	3,608E+07	2,882	
Na	-3,756E+04	2,706	6,171	8,877	-5,117E+04	3,461E+07	2,947	
Nb	-3,638E+04	2,737	6,171	8,907	-5,003E+04	3,695E+07	2,854	
P	-3,666E+04	2,856	6,171	9,027	-5,050E+04	3,572E+07	2,876	
Pb	-3,666E+04	2,699	6,171	8,870	-5,026E+04	3,653E+07	2,877	
Pd	-3,588E+04	2,750	6,171	8,920	-4,956E+04	3,797E+07	2,815	
Pt	-3,767E+04	2,747	6,171	8,917	-5,134E+04	3,419E+07	2,956	
Re	-3,631E+04	2,750	6,171	8,921	-4,999E+04	3,702E+07	2,849	
Si	-3,641E+04	2,820	6,171	8,991	-5,020E+04	3,643E+07	2,857	
Sn	-3,617E+04	2,705	6,171	8,876	-4,978E+04	3,757E+07	2,838	
Ta	-3,630E+04	2,736	6,171	8,907	-4,995E+04	3,712E+07	2,848	
Ti	-3,664E+04	2,729	6,171	8,900	-5,029E+04	3,642E+07	2,875	
V	-3,600E+04	2,766	6,171	8,937	-4,970E+04	3,762E+07	2,824	
W	-3,695E+04	2,752	6,171	8,923	-5,063E+04	3,564E+07	2,899	
Y	-3,644E+04	2,701	6,171	8,872	-5,004E+04	3,700E+07	2,859	
Zn	-3,680E+04	2,745	6,171	8,916	-5,047E+04	3,600E+07	2,887	

Table B.3. The ordering energy values for $Zr_{50}Ni_{50}$ and $Zr_{0,50}Ni_{0,49}M_{0,01}$.

M	W_{Zr-Ni} (J/mol)	w_{Zr-Ni} (J/mol)	W_{Zr-M} (J/mol)	w_{Zr-M} (J/mol)	W_{Ni-M} (J/mol)	w_{Ni-M} (J/mol)
$Zr_{50}Ni_{50}$	-2,182E+04	-1,462E+05				
Ag	-2,178E+04	-1,459E+05	1,216E+04	8,144E+04	3,076E+03	2,061E+04
Al	-2,184E+04	-1,463E+05	-2,254E+04	-1,510E+05	3,810E+03	2,553E+04
B	-2,186E+04	-1,465E+05	-9,497E+04	-6,363E+05	-2,277E+04	-1,525E+05
Ba	-2,182E+04	-1,462E+05	-4,199E+05	-2,814E+06	-4,713E+05	-3,158E+06
Bi	-2,185E+04	-1,464E+05	1,602E+02	1,073E+03	-5,486E+04	-3,676E+05
C	-2,188E+04	-1,466E+05	-5,991E+04	-4,014E+05	-7,268E+03	-4,870E+04
Ca	-2,182E+04	-1,462E+05	-1,092E+05	-7,316E+05	-1,059E+05	-7,094E+05
Cd	-2,180E+04	-1,460E+05	-2,489E+04	-1,668E+05	9,593E+02	6,427E+03
Co	-2,182E+04	-1,462E+05	-2,168E+04	-1,453E+05	0	0
Cr	-2,184E+04	-1,463E+05	-1,566E+04	-1,049E+05	5,329E+02	3,570E+03
Cu	-2,180E+04	-1,461E+05	-6,256E+03	-4,191E+04	2,057E+03	1,378E+04
Fe	-2,182E+04	-1,462E+05	-1,164E+04	-7,798E+04	-3,799E+02	-2,546E+03
Ga	-2,184E+04	-1,463E+05	-2,762E+04	-1,850E+05	1,176E+03	7,878E+03
Ge	-2,186E+04	-1,465E+05	-1,766E+04	-1,183E+05	1,891E+03	1,267E+04
Hf	-2,183E+04	-1,463E+05	-1,734E+02	-1,162E+03	-2,094E+04	-1,403E+05
K	-2,185E+04	-1,464E+05	-7,716E+04	-5,170E+05	-6,176E+04	-4,138E+05
La	-2,180E+04	-1,460E+05	-1,269E+03	-8,504E+03	-1,174E+04	-7,865E+04
Li	-2,182E+04	-1,462E+05	-5,022E+04	-3,365E+05	2,031E+03	1,361E+04
Mg	-2,182E+04	-1,462E+05	-2,591E+04	-1,736E+05	-7,727E+02	-5,177E+03
Mn	-2,181E+04	-1,461E+05	-1,269E+04	-8,501E+04	-6,388E+02	-4,280E+03
Mo	-2,185E+04	-1,464E+05	6,573E+02	4,404E+03	-2,749E+04	-1,842E+05
Na	-2,182E+04	-1,462E+05	-4,039E+04	-2,706E+05	-1,323E+04	-8,864E+04
Nb	-2,185E+04	-1,464E+05	1,835E+03	1,229E+04	-1,789E+04	-1,199E+05
P	-2,188E+04	-1,466E+05	-3,230E+04	-2,164E+05	9,265E+03	6,207E+04
Pb	-2,183E+04	-1,463E+05	1,557E+04	1,043E+05	-4,144E+04	-2,776E+05
Pd	-2,181E+04	-1,462E+05	6,491E+03	4,349E+04	-9,149E+03	-6,130E+04
Pt	-2,182E+04	-1,462E+05	-5,193E+04	-3,479E+05	-5,296E+03	-3,548E+04
Re	-2,189E+04	-1,467E+05	6,688E+03	4,481E+04	-1,848E+04	-1,238E+05
Si	-2,186E+04	-1,465E+05	-2,361E+04	-1,582E+05	7,298E+03	4,889E+04
Sn	-2,184E+04	-1,463E+05	-1,495E+03	-1,002E+04	-8,858E+03	-5,935E+04
Ta	-2,185E+04	-1,464E+05	1,778E+03	1,191E+04	-1,538E+04	-1,030E+05
Ti	-2,184E+04	-1,463E+05	-2,557E+04	-1,713E+05	1,102E+03	7,385E+03
V	-2,186E+04	-1,465E+05	-1,164E+04	-7,799E+04	7,837E+03	5,250E+04
W	-2,187E+04	-1,465E+05	2,754E+02	1,846E+03	-3,285E+04	-2,201E+05
Y	-2,182E+04	-1,462E+05	-2,339E+03	-1,567E+04	-7,941E+03	-5,320E+04
Zn	-2,181E+04	-1,461E+05	-3,047E+04	-2,042E+05	-2,945E+02	-1,973E+03

Table B.4. Thermodynamic and structural data of $Zr_{50}Ni_{50}$ and $Zr_{0,50}Ni_{0,49}M_{0,01}$.

M	ΔH_{mixing} (J/mol)	S^{σ} (J/K.mol)	ΔS^{ideal} (J/K.mol)	ΔS_{mixing} (J/mol)	ΔG_{mixing} (J/mol)	R_c (J/s)	$\Delta\eta/\eta_o$	α_1
$Zr_{50}Ni_{50}$	-3,655E+04	2,768	5,763	8,531	-4,963E+04	3,777E+07	2,868	-1,0
Ag	-3,525E+04	2,713	6,171	8,883	-4,886E+04	3,963E+07	2,765	
Al	-3,649E+04	2,715	6,171	8,886	-5,011E+04	3,683E+07	2,862	
B	-3,982E+04	2,939	6,171	9,110	-5,378E+04	2,931E+07	3,124	
Ba	-6,536E+04	2,780	6,171	8,950	-7,908E+04	6,674E+06	5,127	
Bi	-3,766E+04	2,693	6,171	8,864	-5,125E+04	3,448E+07	2,955	
C	-3,817E+04	2,960	6,171	9,130	-5,216E+04	3,220E+07	2,994	
Ca	-4,295E+04	2,708	6,171	8,879	-5,656E+04	2,520E+07	3,370	
Cd	-3,658E+04	2,690	6,171	8,861	-5,017E+04	3,675E+07	2,870	
Co	-3,654E+04	2,766	6,171	8,937	-5,024E+04	3,643E+07	2,867	
Cr	-3,635E+04	2,767	6,171	8,938	-5,005E+04	3,685E+07	2,852	
Cu	-3,593E+04	2,758	6,171	8,928	-4,962E+04	3,782E+07	2,819	
Fe	-3,622E+04	2,770	6,171	8,940	-4,992E+04	3,712E+07	2,841	
Ga	-3,674E+04	2,725	6,171	8,896	-5,037E+04	3,624E+07	2,882	
Ge	-3,641E+04	2,770	6,171	8,941	-5,012E+04	3,669E+07	2,857	
Hf	-3,653E+04	2,689	6,171	8,860	-5,011E+04	3,687E+07	2,866	
K	-4,049E+04	2,854	6,171	9,025	-5,432E+04	2,852E+07	3,176	
La	-3,621E+04	2,689	6,171	8,860	-4,979E+04	3,757E+07	2,841	
Li	-3,743E+04	2,698	6,171	8,869	-5,103E+04	3,492E+07	2,937	
Mg	-3,672E+04	2,686	6,171	8,857	-5,029E+04	3,648E+07	2,881	
Mn	-3,625E+04	2,736	6,171	8,907	-4,990E+04	3,723E+07	2,844	
Mo	-3,675E+04	2,733	6,171	8,904	-5,040E+04	3,616E+07	2,883	
Na	-3,761E+04	2,687	6,171	8,857	-5,118E+04	3,462E+07	2,950	
Nb	-3,639E+04	2,716	6,171	8,887	-5,002E+04	3,702E+07	2,855	
P	-3,669E+04	2,837	6,171	9,007	-5,050E+04	3,575E+07	2,879	
Pb	-3,667E+04	2,679	6,171	8,850	-5,024E+04	3,661E+07	2,877	
Pd	-3,589E+04	2,729	6,171	8,900	-4,954E+04	3,806E+07	2,816	
Pt	-3,772E+04	2,726	6,171	8,897	-5,136E+04	3,418E+07	2,960	
Re	-3,632E+04	2,729	6,171	8,900	-4,997E+04	3,711E+07	2,850	
Si	-3,644E+04	2,801	6,171	8,971	-5,020E+04	3,647E+07	2,859	
Sn	-3,619E+04	2,685	6,171	8,855	-4,976E+04	3,764E+07	2,839	
Ta	-3,631E+04	2,716	6,171	8,887	-4,994E+04	3,720E+07	2,849	
Ti	-3,667E+04	2,709	6,171	8,880	-5,029E+04	3,645E+07	2,877	
V	-3,602E+04	2,746	6,171	8,917	-4,969E+04	3,768E+07	2,826	
W	-3,697E+04	2,732	6,171	8,902	-5,062E+04	3,571E+07	2,900	
Y	-3,616E+04	2,682	6,171	8,852	-4,973E+04	3,773E+07	2,837	
Zn	-3,684E+04	2,724	6,171	8,895	-5,047E+04	3,603E+07	2,890	

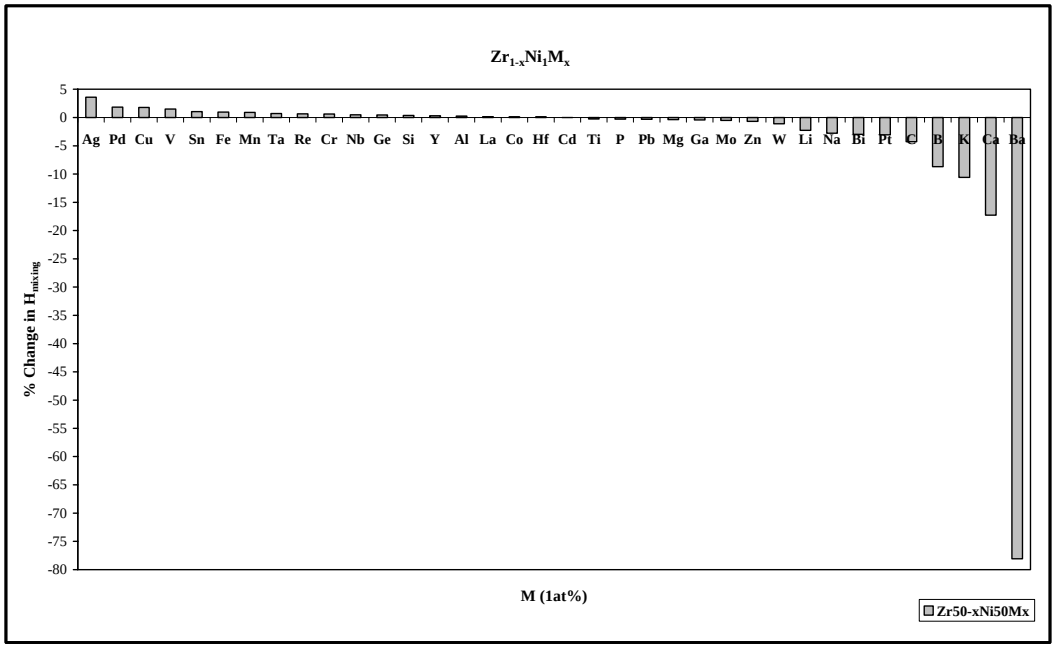

Figure B.3. % Change in ΔH_{mixing} of $Zr_{50}Ni_{50}$ binary system for the addition of 1 at % impurity elements (M) when 1 at % is taken from Zr ($Zr_{0,49}Ni_{0,50}M_{0,01}$system).

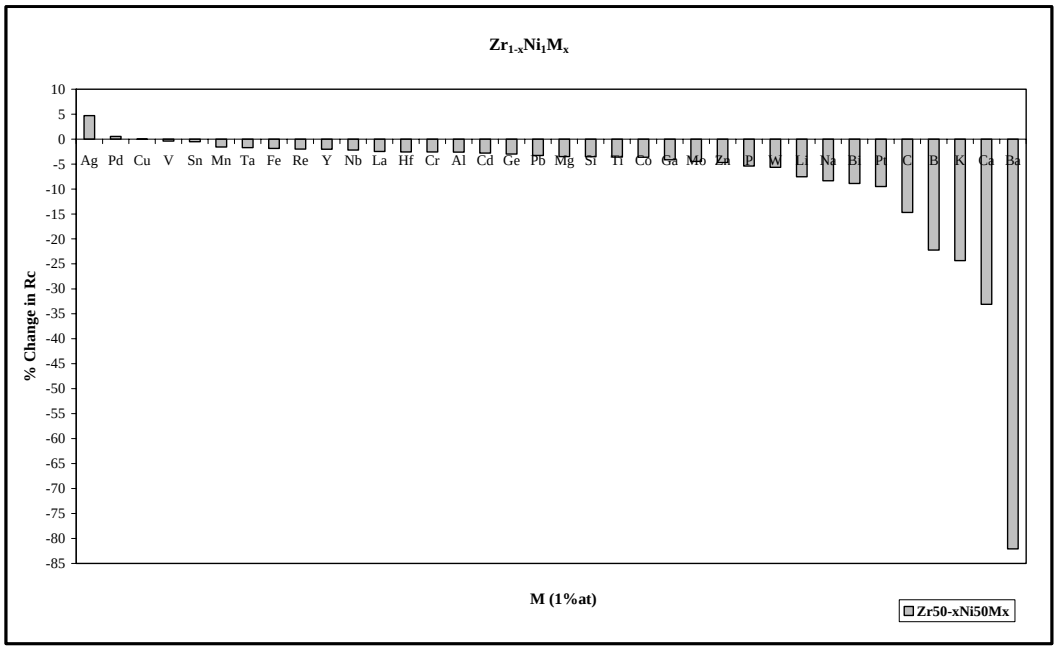

Figure B.4. % Change in R_c of $Zr_{50}Ni_{50}$ binary system for the addition of 1 at % impurity elements (M) when 1 at % is taken from Zr ($Zr_{0,49}Ni_{0,50}M_{0,01}$system).

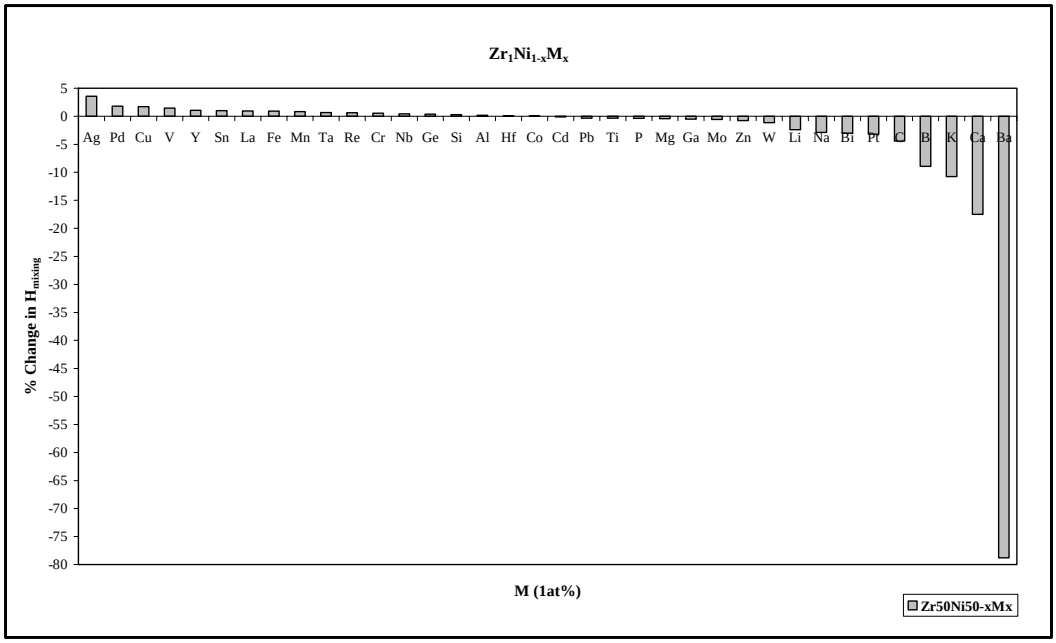

Figure B.5. % Change in ΔH_{mixing} of $Zr_{50}Ni_{50}$ binary system for the addition of 1 at % impurity elements (M) when 1 at % is taken from Ni ($Zr_{0,50}Ni_{0,49}M_{0,01}$ system).

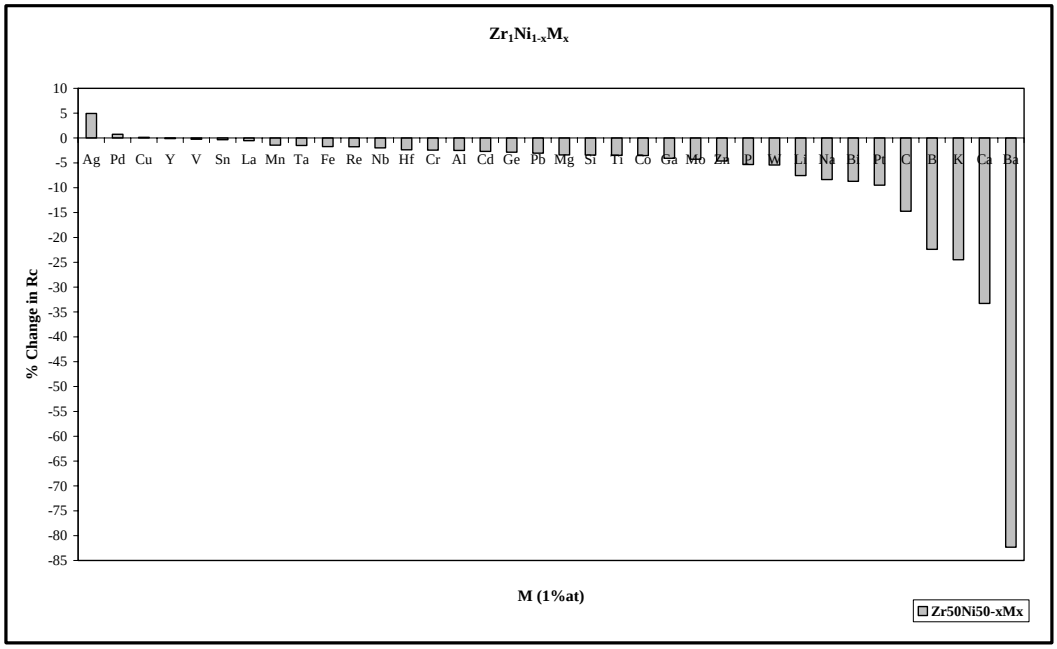

Figure B.6. % Change in R_c of $Zr_{50}Ni_{50}$ binary system for the addition of 1 at % impurity elements (M) when 1 at % is taken from Ni ($Zr_{0,50}Ni_{0,49}M_{0,01}$system).

Table B.5. The ordering energy values for $Zr_{64}Ni_{36}$ and $Zr_{0,63}Ni_{0,36}M_{0,01}$.

M	W_{Zr-Ni} (J/mol)	w_{Zr-Ni} (J/mol)	W_{Zr-M} (J/mol)	w_{Zr-M} (J/mol)	W_{Ni-M} (J/mol)	w_{Ni-M} (J/mol)
$Zr_{64}Ni_{36}$	-2,195E+04	-1,229E+05				
Ag	-2,191E+04	-1,227E+05	1,179E+04	6,601E+04	3,191E+03	1,787E+04
Al	-2,196E+04	-1,230E+05	-2,247E+04	-1,258E+05	3,764E+03	2,108E+04
B	-2,197E+04	-1,230E+05	-9,546E+04	-5,346E+05	-2,259E+04	-1,265E+05
Ba	-2,195E+04	-1,229E+05	-4,115E+05	-2,305E+06	-4,665E+05	-2,612E+06
Bi	-2,196E+04	-1,230E+05	-3,233E+02	-1,810E+03	-5,458E+04	-3,056E+05
C	-2,199E+04	-1,231E+05	-6,021E+04	-3,372E+05	-7,222E+03	-4,044E+04
Ca	-2,195E+04	-1,229E+05	-1,071E+05	-5,998E+05	-1,055E+05	-5,907E+05
Cd	-2,192E+04	-1,227E+05	-2,511E+04	-1,406E+05	9,821E+02	5,500E+03
Co	-2,193E+04	-1,228E+05	-2,180E+04	-1,221E+05	0,000E+00	0,000E+00
Cr	-2,195E+04	-1,229E+05	-1,562E+04	-8,747E+04	5,558E+02	3,113E+03
Cu	-2,192E+04	-1,228E+05	-6,487E+03	-3,633E+04	2,091E+03	1,171E+04
Fe	-2,193E+04	-1,228E+05	-1,173E+04	-6,571E+04	-3,872E+02	-2,168E+03
Ga	-2,195E+04	-1,229E+05	-2,778E+04	-1,556E+05	1,235E+03	6,915E+03
Ge	-2,197E+04	-1,230E+05	-1,772E+04	-9,922E+04	1,913E+03	1,071E+04
Hf	-2,195E+04	-1,229E+05	-1,879E+02	-1,052E+03	-2,093E+04	-1,172E+05
K	-2,199E+04	-1,232E+05	-7,570E+04	-4,239E+05	-6,128E+04	-3,432E+05
La	-2,192E+04	-1,228E+05	-1,330E+03	-7,446E+03	-1,166E+04	-6,530E+04
Li	-2,194E+04	-1,229E+05	-5,052E+04	-2,829E+05	2,039E+03	1,142E+04
Mg	-2,194E+04	-1,229E+05	-2,578E+04	-1,443E+05	-8,364E+02	-4,684E+03
Mn	-2,193E+04	-1,228E+05	-1,281E+04	-7,172E+04	-6,361E+02	-3,562E+03
Mo	-2,196E+04	-1,230E+05	6,783E+02	3,798E+03	-2,757E+04	-1,544E+05
Na	-2,195E+04	-1,229E+05	-4,001E+04	-2,241E+05	-1,318E+04	-7,383E+04
Nb	-2,196E+04	-1,230E+05	1,831E+03	1,025E+04	-1,813E+04	-1,015E+05
P	-2,199E+04	-1,231E+05	-3,227E+04	-1,807E+05	9,410E+03	5,269E+04
Pb	-2,195E+04	-1,229E+05	1,482E+04	8,299E+04	-4,126E+04	-2,311E+05
Pd	-2,193E+04	-1,228E+05	7,012E+03	3,927E+04	-8,988E+03	-5,033E+04
Pt	-2,193E+04	-1,228E+05	-5,242E+04	-2,935E+05	-5,121E+03	-2,868E+04
Re	-2,199E+04	-1,231E+05	6,714E+03	3,760E+04	-1,870E+04	-1,047E+05
Si	-2,198E+04	-1,231E+05	-2,357E+04	-1,320E+05	7,311E+03	4,094E+04
Sn	-2,195E+04	-1,229E+05	-1,562E+03	-8,748E+03	-8,876E+03	-4,970E+04
Ta	-2,196E+04	-1,230E+05	1,783E+03	9,986E+03	-1,557E+04	-8,720E+04
Ti	-2,195E+04	-1,229E+05	-2,571E+04	-1,440E+05	1,148E+03	6,427E+03
V	-2,197E+04	-1,230E+05	-1,164E+04	-6,516E+04	7,846E+03	4,394E+04
W	-2,197E+04	-1,230E+05	2,707E+02	1,516E+03	-3,303E+04	-1,850E+05
Y	-2,194E+04	-1,229E+05	-2,359E+03	-1,321E+04	-7,960E+03	-4,458E+04
Zn	-2,193E+04	-1,228E+05	-3,069E+04	-1,718E+05	-2,801E+02	-1,569E+03

Table B.6. Thermodynamic and structural data of $Zr_{64}Ni_{36}$ and $Zr_{0,63}Ni_{0,36}M_{0,01}$.

M	ΔH_{mixing} (J/mol)	S^{σ} (J/K.mol)	ΔS^{ideal} (J/K.mol)	ΔS_{mixing} (J/mol)	ΔG_{mixing} (J/mol)	R_c (J/s)	$\Delta\eta/\eta_o$	α_1
$Zr_{64}Ni_{36}$	-2,832E+04	2,306	5,433	7,739	-3,824E+04	3,869E+07	2,654	-0,562
Ag	-2,734E+04	2,290	5,861	8,151	-3,780E+04	3,995E+07	2,563	
Al	-2,860E+04	2,293	5,861	8,154	-3,907E+04	3,655E+07	2,681	
B	-3,173E+04	2,543	5,861	8,404	-4,251E+04	2,830E+07	2,974	
Ba	-5,181E+04	2,416	5,861	8,277	-6,243E+04	7,025E+06	4,856	
Bi	-2,901E+04	2,271	5,861	8,132	-3,944E+04	3,563E+07	2,719	
C	-3,019E+04	2,567	5,861	8,428	-4,101E+04	3,141E+07	2,830	
Ca	-3,378E+04	2,314	5,861	8,176	-4,427E+04	2,532E+07	3,167	
Cd	-2,871E+04	2,269	5,861	8,130	-3,914E+04	3,641E+07	2,691	
Co	-2,863E+04	2,347	5,861	8,208	-3,916E+04	3,620E+07	2,684	
Cr	-2,841E+04	2,348	5,861	8,209	-3,895E+04	3,674E+07	2,664	
Cu	-2,803E+04	2,338	5,861	8,199	-3,855E+04	3,781E+07	2,628	
Fe	-2,828E+04	2,351	5,861	8,212	-3,881E+04	3,708E+07	2,651	
Ga	-2,884E+04	2,303	5,861	8,164	-3,931E+04	3,589E+07	2,703	
Ge	-2,849E+04	2,351	5,861	8,212	-3,903E+04	3,652E+07	2,671	
Hf	-2,830E+04	2,268	5,861	8,129	-3,873E+04	3,746E+07	2,653	
K	-3,184E+04	2,517	5,861	8,378	-4,259E+04	2,819E+07	2,984	
La	-2,813E+04	2,285	5,861	8,147	-3,858E+04	3,783E+07	2,637	
Li	-2,961E+04	2,276	5,861	8,137	-4,005E+04	3,413E+07	2,776	
Mg	-2,880E+04	2,266	5,861	8,127	-3,922E+04	3,619E+07	2,699	
Mn	-2,831E+04	2,315	5,861	8,176	-3,880E+04	3,718E+07	2,654	
Mo	-2,842E+04	2,311	5,861	8,172	-3,890E+04	3,693E+07	2,664	
Na	-2,956E+04	2,281	5,861	8,142	-4,000E+04	3,424E+07	2,771	
Nb	-2,819E+04	2,294	5,861	8,155	-3,865E+04	3,762E+07	2,642	
P	-2,887E+04	2,426	5,861	8,287	-3,951E+04	3,518E+07	2,707	
Pb	-2,818E+04	2,265	5,861	8,127	-3,861E+04	3,779E+07	2,642	
Pd	-2,779E+04	2,307	5,861	8,168	-3,827E+04	3,861E+07	2,605	
Pt	-2,981E+04	2,304	5,861	8,165	-4,029E+04	3,352E+07	2,795	
Re	-2,807E+04	2,307	5,861	8,169	-3,855E+04	3,787E+07	2,631	
Si	-2,859E+04	2,385	5,861	8,246	-3,917E+04	3,608E+07	2,681	
Sn	-2,812E+04	2,265	5,861	8,126	-3,854E+04	3,797E+07	2,636	
Ta	-2,814E+04	2,293	5,861	8,154	-3,860E+04	3,776E+07	2,638	
Ti	-2,877E+04	2,286	5,861	8,148	-3,922E+04	3,616E+07	2,697	
V	-2,815E+04	2,325	5,861	8,186	-3,865E+04	3,755E+07	2,639	
W	-2,856E+04	2,310	5,861	8,171	-3,905E+04	3,656E+07	2,677	
Y	-2,811E+04	2,271	5,861	8,132	-3,855E+04	3,795E+07	2,635	
Zn	-2,894E+04	2,302	5,861	8,163	-3,942E+04	3,564E+07	2,713	

Table B.7. The ordering energy values for $Zr_{64}Ni_{36}$ and $Zr_{0,64}Ni_{0,35}M_{0,01}$.

M	W_{Zr-Ni} (J/mol)	w_{Zr-Ni} (J/mol)	W_{Zr-M} (J/mol)	w_{Zr-M} (J/mol)	W_{Ni-M} (J/mol)	w_{Ni-M} (J/mol)
$Zr_{64}Ni_{36}$	-2,195E+04	-1,229E+05				
Ag	-2,191E+04	-1,227E+05	1,176E+04	6,587E+04	3,199E+03	1,791E+04
Al	-2,197E+04	-1,230E+05	-2,247E+04	-1,258E+05	3,761E+03	2,106E+04
B	-2,198E+04	-1,231E+05	-9,549E+04	-5,347E+05	-2,257E+04	-1,264E+05
Ba	-2,196E+04	-1,230E+05	-4,110E+05	-2,301E+06	-4,661E+05	-2,610E+06
Bi	-2,197E+04	-1,230E+05	-3,574E+02	-2,001E+03	-5,456E+04	-3,055E+05
C	-2,199E+04	-1,232E+05	-6,023E+04	-3,373E+05	-7,218E+03	-4,042E+04
Ca	-2,196E+04	-1,230E+05	-1,070E+05	-5,990E+05	-1,054E+05	-5,905E+05
Cd	-2,193E+04	-1,228E+05	-2,512E+04	-1,407E+05	9,841E+02	5,511E+03
Co	-2,194E+04	-1,229E+05	-2,181E+04	-1,221E+05	0,000E+00	0,000E+00
Cr	-2,196E+04	-1,230E+05	-1,562E+04	-8,746E+04	5,571E+02	3,120E+03
Cu	-2,193E+04	-1,228E+05	-6,504E+03	-3,642E+04	2,093E+03	1,172E+04
Fe	-2,194E+04	-1,229E+05	-1,174E+04	-6,575E+04	-3,885E+02	-2,176E+03
Ga	-2,196E+04	-1,230E+05	-2,779E+04	-1,556E+05	1,239E+03	6,937E+03
Ge	-2,198E+04	-1,231E+05	-1,772E+04	-9,924E+04	1,914E+03	1,072E+04
Hf	-2,195E+04	-1,229E+05	-1,892E+02	-1,059E+03	-2,093E+04	-1,172E+05
K	-2,200E+04	-1,232E+05	-7,560E+04	-4,234E+05	-6,124E+04	-3,430E+05
La	-2,193E+04	-1,228E+05	-1,334E+03	-7,469E+03	-1,166E+04	-6,527E+04
Li	-2,195E+04	-1,229E+05	-5,055E+04	-2,831E+05	2,041E+03	1,143E+04
Mg	-2,195E+04	-1,229E+05	-2,577E+04	-1,443E+05	-8,409E+02	-4,709E+03
Mn	-2,194E+04	-1,228E+05	-1,282E+04	-7,177E+04	-6,361E+02	-3,562E+03
Mo	-2,196E+04	-1,230E+05	6,796E+02	3,806E+03	-2,758E+04	-1,544E+05
Na	-2,196E+04	-1,230E+05	-3,998E+04	-2,239E+05	-1,318E+04	-7,381E+04
Nb	-2,197E+04	-1,230E+05	1,831E+03	1,025E+04	-1,815E+04	-1,016E+05
P	-2,199E+04	-1,232E+05	-3,227E+04	-1,807E+05	9,420E+03	5,275E+04
Pb	-2,196E+04	-1,230E+05	1,477E+04	8,270E+04	-4,125E+04	-2,310E+05
Pd	-2,194E+04	-1,229E+05	7,048E+03	3,947E+04	-8,976E+03	-5,027E+04
Pt	-2,194E+04	-1,229E+05	-5,245E+04	-2,937E+05	-5,108E+03	-2,861E+04
Re	-2,200E+04	-1,232E+05	6,716E+03	3,761E+04	-1,871E+04	-1,048E+05
Si	-2,198E+04	-1,231E+05	-2,357E+04	-1,320E+05	7,312E+03	4,095E+04
Sn	-2,196E+04	-1,230E+05	-1,567E+03	-8,778E+03	-8,878E+03	-4,971E+04
Ta	-2,197E+04	-1,230E+05	1,783E+03	9,986E+03	-1,558E+04	-8,728E+04
Ti	-2,196E+04	-1,230E+05	-2,572E+04	-1,440E+05	1,152E+03	6,449E+03
V	-2,197E+04	-1,231E+05	-1,164E+04	-6,516E+04	7,846E+03	4,394E+04
W	-2,198E+04	-1,231E+05	2,701E+02	1,513E+03	-3,304E+04	-1,850E+05
Y	-2,195E+04	-1,229E+05	-2,360E+03	-1,322E+04	-7,962E+03	-4,459E+04
Zn	-2,194E+04	-1,229E+05	-3,070E+04	-1,719E+05	-2,788E+02	-1,561E+03

Table B.8. Thermodynamic and structural data $Zr_{64}Ni_{36}$ and $Zr_{0,64}Ni_{0,35}M_{0,01}$.

M	ΔH_{mixing} (J/mol)	S^{σ} (J/K.mol)	ΔS^{ideal} (J/K.mol)	ΔS_{mixing} (J/mol)	ΔG_{mixing} (J/mol)	R_c (J/s)	$\Delta\eta/\eta_o$	α_1
$Zr_{64}Ni_{36}$	-2,832E+04	2,306	5,433	7,739	-3,824E+04	3,869E+07	2,654	-0,562
Ag	-2,700E+04	2,247	5,813	8,059	-3,734E+04	4,135E+07	2,531	
Al	-2,828E+04	2,250	5,813	8,062	-3,863E+04	3,777E+07	2,651	
B	-3,143E+04	2,501	5,813	8,314	-4,210E+04	2,919E+07	2,947	
Ba	-5,142E+04	2,376	5,813	8,189	-6,192E+04	7,294E+06	4,820	
Bi	-2,865E+04	2,228	5,813	8,041	-3,896E+04	3,694E+07	2,685	
C	-2,989E+04	2,526	5,813	8,338	-4,059E+04	3,243E+07	2,802	
Ca	-3,344E+04	2,273	5,813	8,086	-4,382E+04	2,619E+07	3,135	
Cd	-2,839E+04	2,226	5,813	8,039	-3,870E+04	3,763E+07	2,661	
Co	-2,831E+04	2,304	5,813	8,117	-3,872E+04	3,742E+07	2,654	
Cr	-2,809E+04	2,305	5,813	8,117	-3,850E+04	3,799E+07	2,633	
Cu	-2,770E+04	2,294	5,813	8,107	-3,810E+04	3,910E+07	2,597	
Fe	-2,795E+04	2,308	5,813	8,120	-3,837E+04	3,835E+07	2,620	
Ga	-2,852E+04	2,259	5,813	8,072	-3,888E+04	3,709E+07	2,674	
Ge	-2,817E+04	2,308	5,813	8,121	-3,859E+04	3,776E+07	2,641	
Hf	-2,796E+04	2,225	5,813	8,038	-3,827E+04	3,879E+07	2,621	
K	-3,151E+04	2,480	5,813	8,293	-4,215E+04	2,913E+07	2,954	
La	-2,779E+04	2,244	5,813	8,056	-3,813E+04	3,914E+07	2,605	
Li	-2,931E+04	2,232	5,813	8,045	-3,963E+04	3,524E+07	2,747	
Mg	-2,848E+04	2,223	5,813	8,036	-3,879E+04	3,741E+07	2,670	
Mn	-2,799E+04	2,271	5,813	8,084	-3,836E+04	3,845E+07	2,624	
Mo	-2,807E+04	2,268	5,813	8,080	-3,843E+04	3,825E+07	2,631	
Na	-2,924E+04	2,239	5,813	8,051	-3,957E+04	3,538E+07	2,741	
Nb	-2,784E+04	2,250	5,813	8,063	-3,819E+04	3,896E+07	2,610	
P	-2,856E+04	2,383	5,813	8,196	-3,908E+04	3,634E+07	2,677	
Pb	-2,782E+04	2,223	5,813	8,036	-3,813E+04	3,918E+07	2,608	
Pd	-2,745E+04	2,264	5,813	8,077	-3,781E+04	3,998E+07	2,573	
Pt	-2,950E+04	2,261	5,813	8,074	-3,986E+04	3,461E+07	2,766	
Re	-2,772E+04	2,264	5,813	8,077	-3,808E+04	3,922E+07	2,598	
Si	-2,828E+04	2,342	5,813	8,155	-3,874E+04	3,729E+07	2,651	
Sn	-2,778E+04	2,221	5,813	8,034	-3,809E+04	3,929E+07	2,604	
Ta	-2,779E+04	2,250	5,813	8,063	-3,814E+04	3,909E+07	2,606	
Ti	-2,845E+04	2,243	5,813	8,056	-3,878E+04	3,738E+07	2,667	
V	-2,783E+04	2,282	5,813	8,095	-3,821E+04	3,883E+07	2,609	
W	-2,821E+04	2,266	5,813	8,079	-3,857E+04	3,788E+07	2,644	
Y	-2,778E+04	2,229	5,813	8,041	-3,809E+04	3,927E+07	2,604	
Zn	-2,863E+04	2,259	5,813	8,072	-3,898E+04	3,683E+07	2,684	

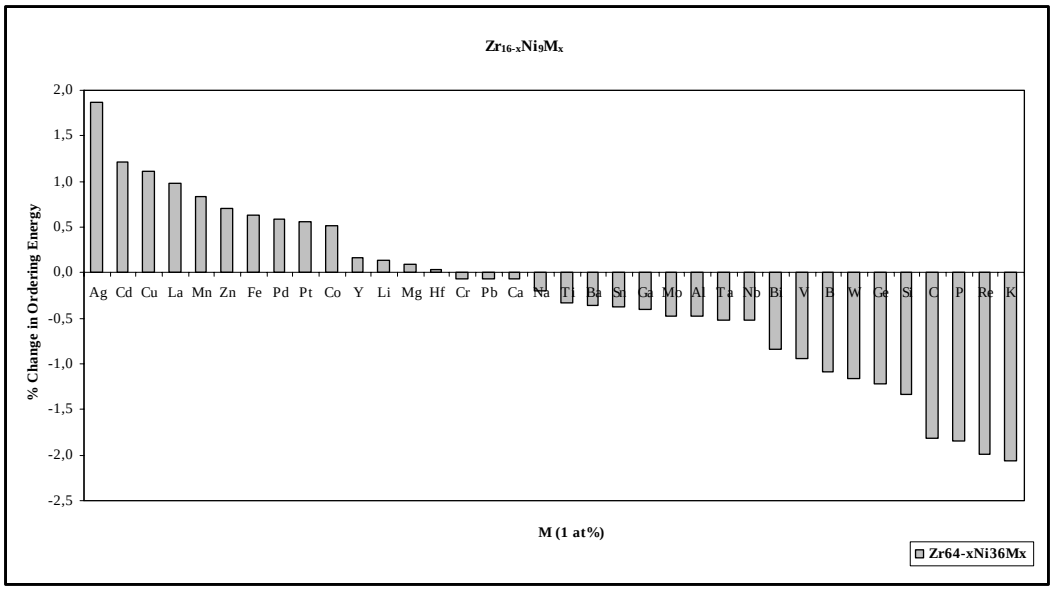

Figure B.7. % Change in ordering energy of $Zr_{64}Ni_{36}$ binary system for the addition of 1 at % impurity elements (M) when 1 at % is taken from Zr ($Zr_{0,63}Ni_{0,36}M_{0,01}$system).

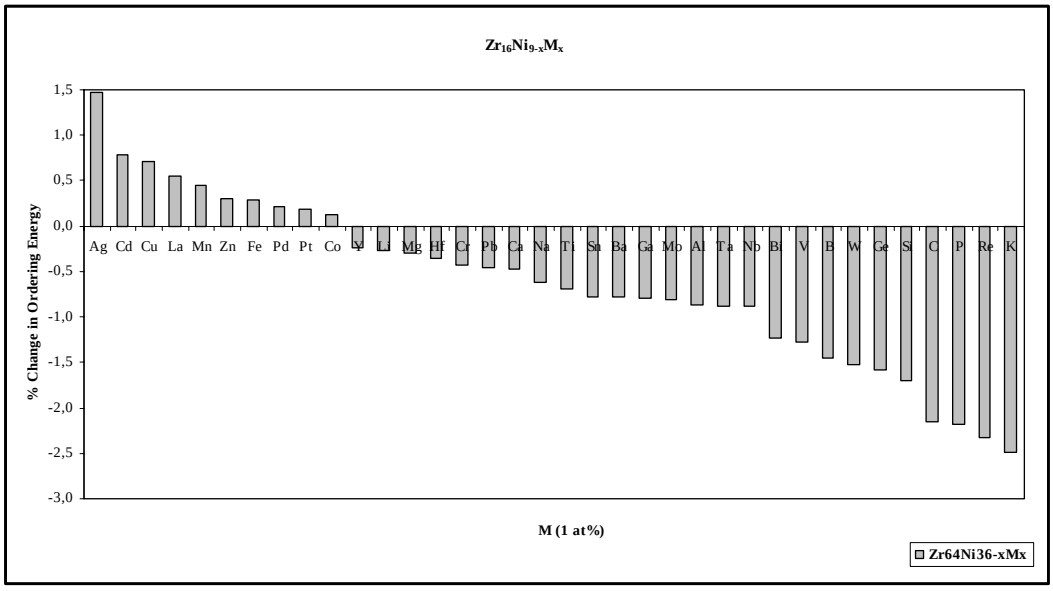

Figure B.8. % Change in ordering energy of $Zr_{64}Ni_{36}$ binary system for the addition of 1 at % impurity elements (M) when 1 at % is taken from Ni ($Zr_{0,64}Ni_{0,35}M_{0,01}$system).

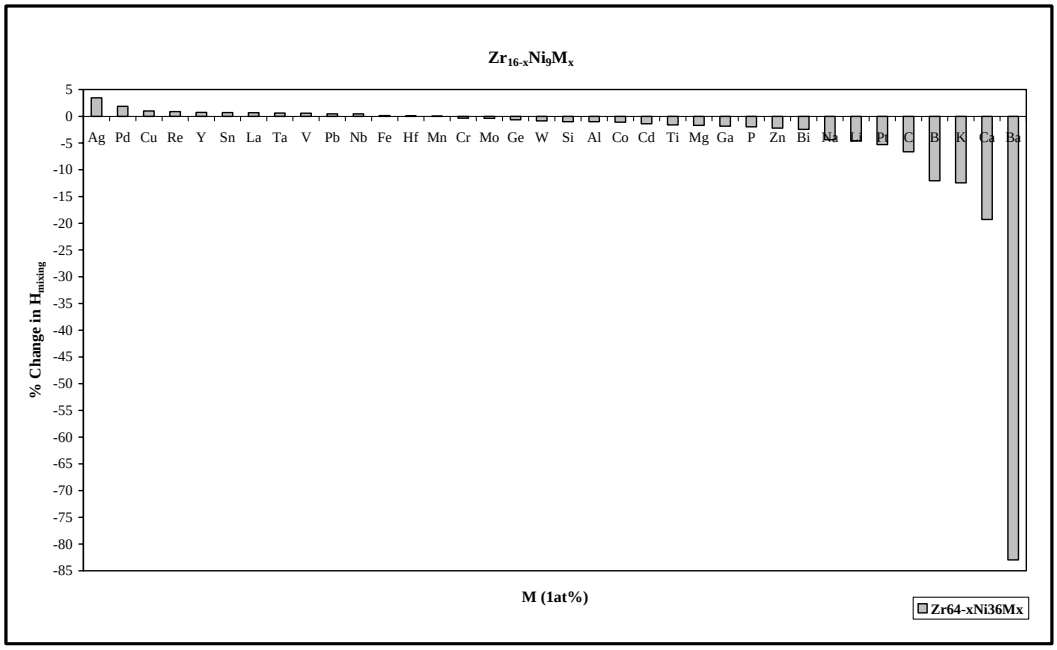

Figure B.9. % Change in ΔH_{mixing} of $Zr_{64}Ni_{36}$ binary system for the addition of 1 at % impurity elements (M) when 1 at % is taken from Zr ($Zr_{0,63}Ni_{0,36}M_{0,01}$system).

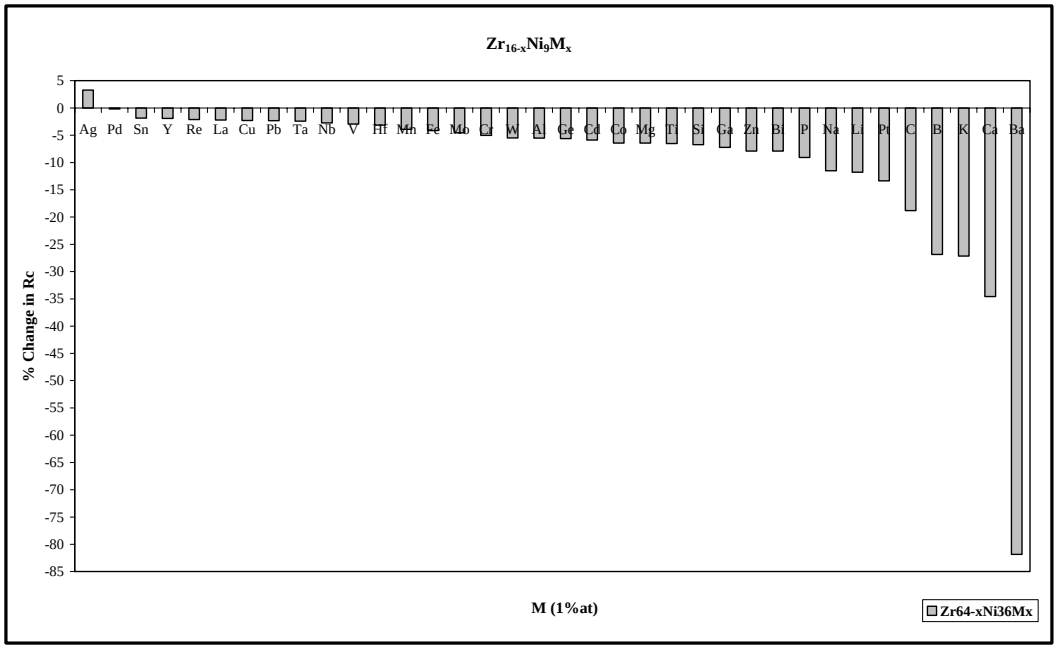

Figure B.10. % Change in R_c of $Zr_{64}Ni_{36}$ binary system for the addition of 1 at % impurity elements (M) when 1 at % is taken from Zr ($Zr_{0,63}Ni_{0,36}M_{0,01}$system).

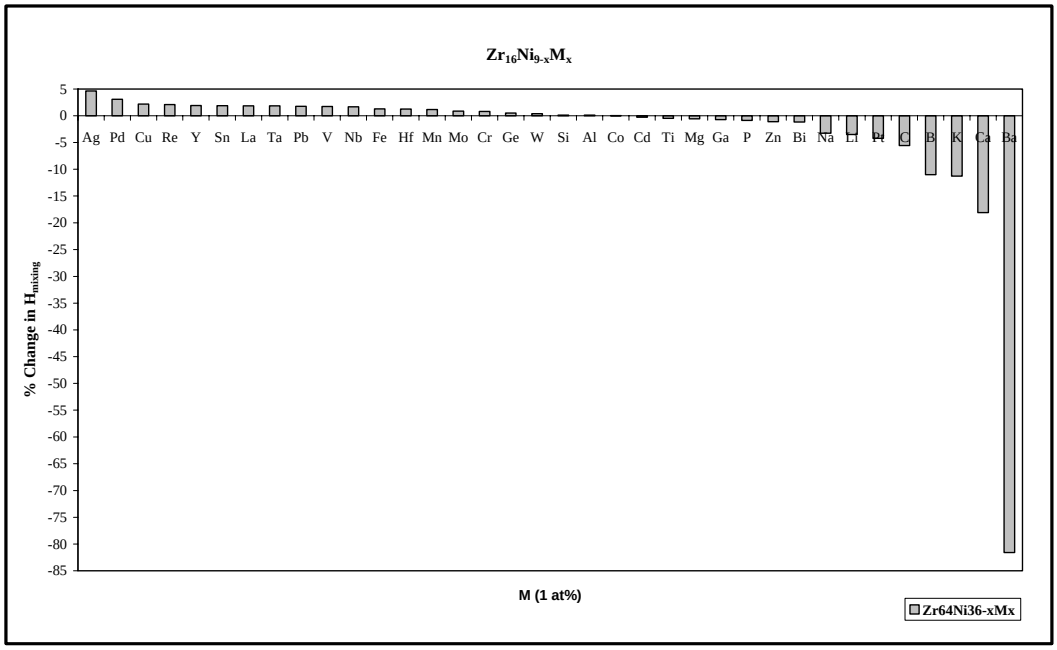

Figure B.11. % Change in ΔH_{mixing} of $Zr_{64}Ni_{36}$ binary system for the addition of 1 at % impurity elements (M) when 1 at % is taken from Ni ($Zr_{0,64}Ni_{0,35}M_{0,01}$system).

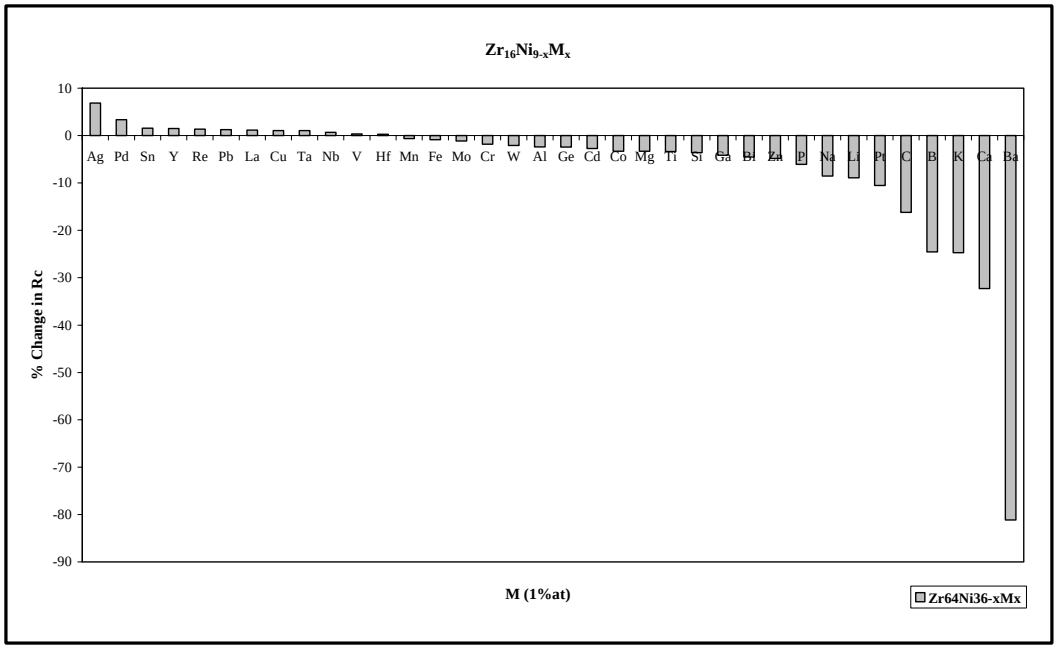

Figure B.12. % Change in R_c of $Zr_{64}Ni_{36}$ binary system for the addition of 1 at % impurity elements (M) when 1 at % is taken from Ni ($Zr_{0,64}Ni_{0,35}M_{0,01}$system).

Table B.9. The ordering energy values for $Zr_{70}Ni_{30}$ and $Zr_{0,69}Ni_{0,30}M_{0,01}$.

M	W_{Zr-Ni} (J/mol)	w_{Zr-Ni} (J/mol)	W_{Zr-M} (J/mol)	w_{Zr-M} (J/mol)	W_{Ni-M} (J/mol)	w_{Ni-M} (J/mol)
$Zr_{70}Ni_{30}$	-2,199E+03	-1,650E+05				
Ag	-2,196E+04	-1,647E+05	1,164E+04	8,730E+04	3,237E+03	2,428E+04
Al	-2,201E+04	-1,650E+05	-2,240E+04	-1,680E+05	3,746E+03	2,809E+04
B	-2,202E+04	-1,651E+05	-9,560E+04	-7,170E+05	-2,251E+04	-1,688E+05
Ba	-2,201E+04	-1,651E+05	-4,080E+05	-3,060E+06	-4,645E+05	-3,484E+06
Bi	-2,201E+04	-1,651E+05	-5,200E+02	-3,900E+03	-5,447E+04	-4,085E+05
C	-2,203E+04	-1,652E+05	-6,040E+04	-4,530E+05	-7,203E+03	-5,402E+04
Ca	-2,200E+04	-1,650E+05	-1,063E+05	-7,970E+05	-1,053E+05	-7,898E+05
Cd	-2,197E+04	-1,648E+05	-2,520E+04	-1,890E+05	9,913E+02	7,435E+03
Co	-2,198E+04	-1,649E+05	-2,187E+04	-1,640E+05	0	0
Cr	-2,200E+04	-1,650E+05	-1,560E+04	-1,170E+05	5,650E+02	4,238E+03
Cu	-2,197E+04	-1,648E+05	-6,587E+03	-4,940E+04	2,104E+03	1,578E+04
Fe	-2,198E+04	-1,649E+05	-1,177E+04	-8,830E+04	-3,911E+02	-2,933E+03
Ga	-2,200E+04	-1,650E+05	-2,787E+04	-2,090E+05	1,258E+03	9,439E+03
Ge	-2,202E+04	-1,652E+05	-1,773E+04	-1,330E+05	1,920E+03	1,440E+04
Hf	-2,199E+04	-1,650E+05	-1,947E+02	-1,460E+03	-2,093E+04	-1,570E+05
K	-2,205E+04	-1,654E+05	-7,507E+04	-5,630E+05	-6,108E+04	-4,581E+05
La	-2,198E+04	-1,648E+05	-1,360E+03	-1,020E+04	-1,163E+04	-8,723E+04
Li	-2,200E+04	-1,650E+05	-5,067E+04	-3,800E+05	2,043E+03	1,532E+04
Mg	-2,200E+04	-1,650E+05	-2,573E+04	-1,930E+05	-8,626E+02	-6,469E+03
Mn	-2,198E+04	-1,648E+05	-1,285E+04	-9,640E+04	-6,361E+02	-4,771E+03
Mo	-2,200E+04	-1,650E+05	6,867E+02	5,150E+03	-2,761E+04	-2,071E+05
Na	-2,200E+04	-1,650E+05	-3,987E+04	-2,990E+05	-1,316E+04	-9,873E+04
Nb	-2,200E+04	-1,650E+05	1,827E+03	1,370E+04	-1,823E+04	-1,368E+05
P	-2,203E+04	-1,652E+05	-3,227E+04	-2,420E+05	9,468E+03	7,101E+04
Pb	-2,200E+04	-1,650E+05	1,453E+04	1,090E+05	-4,119E+04	-3,089E+05
Pd	-2,198E+04	-1,649E+05	7,227E+03	5,420E+04	-8,923E+03	-6,692E+04
Pt	-2,198E+04	-1,649E+05	-5,267E+04	-3,950E+05	-5,050E+03	-3,787E+04
Re	-2,203E+04	-1,652E+05	6,720E+03	5,040E+04	-1,879E+04	-1,409E+05
Si	-2,202E+04	-1,652E+05	-2,360E+04	-1,770E+05	7,316E+03	5,487E+04
Sn	-2,200E+04	-1,650E+05	-1,587E+03	-1,190E+04	-8,884E+03	-6,663E+04
Ta	-2,200E+04	-1,650E+05	1,787E+03	1,340E+04	-1,565E+04	-1,174E+05
Ti	-2,200E+04	-1,650E+05	-2,573E+04	-1,930E+05	1,167E+03	8,756E+03
V	-2,201E+04	-1,651E+05	-1,164E+04	-8,730E+04	7,849E+03	5,887E+04
W	-2,202E+04	-1,651E+05	2,680E+02	2,010E+03	-3,311E+04	-2,483E+05
Y	-2,199E+04	-1,650E+05	-2,373E+03	-1,780E+04	-7,969E+03	-5,976E+04
Zn	-2,198E+04	-1,649E+05	-3,080E+04	-2,310E+05	-2,735E+02	-2,052E+03

Table B.10. Thermodynamic and structural data of $Zr_{70}Ni_{30}$ and $Zr_{0,69}Ni_{0,30}M_{0,01}$.

M	ΔH_{mixing} (J/mol)	S^{σ} (J/K.mol)	ΔS^{ideal} (J/K.mol)	ΔS_{mixing} (J/mol)	ΔG_{mixing} (J/mol)	R_c (J/s)	$\Delta\eta/\eta_o$	α_1
$Zr_{70}Ni_{30}$	-3,464E+04	2,018	5,079	7,097	-4,417E+04	3,242E+07	3,102	-0,429
Ag	-3,341E+04	2,010	5,515	7,524	-4,352E+04	3,390E+07	2,992	
Al	-3,524E+04	2,012	5,515	7,527	-4,535E+04	2,997E+07	3,156	
B	-3,964E+04	2,272	5,515	7,787	-5,010E+04	2,149E+07	3,550	
Ba	-6,574E+04	2,161	5,515	7,675	-7,605E+04	3,781E+06	5,888	
Bi	-3,543E+04	1,991	5,515	7,506	-4,551E+04	2,968E+07	3,173	
C	-3,749E+04	2,298	5,515	7,813	-4,798E+04	2,473E+07	3,357	
Ca	-4,203E+04	2,047	5,515	7,562	-5,218E+04	1,891E+07	3,764	
Cd	-3,539E+04	1,989	5,515	7,504	-4,547E+04	2,977E+07	3,170	
Co	-3,526E+04	2,068	5,515	7,582	-4,545E+04	2,969E+07	3,158	
Cr	-3,494E+04	2,068	5,515	7,583	-4,513E+04	3,033E+07	3,129	
Cu	-3,441E+04	2,058	5,515	7,573	-4,458E+04	3,149E+07	3,081	
Fe	-3,474E+04	2,071	5,515	7,586	-4,493E+04	3,073E+07	3,111	
Ga	-3,557E+04	2,022	5,515	7,537	-4,570E+04	2,926E+07	3,186	
Ge	-3,506E+04	2,072	5,515	7,587	-4,525E+04	3,007E+07	3,140	
Hf	-3,463E+04	1,988	5,515	7,503	-4,470E+04	3,134E+07	3,101	
K	-3,949E+04	2,274	5,515	7,789	-4,995E+04	2,169E+07	3,537	
La	-3,445E+04	2,013	5,515	7,528	-4,456E+04	3,159E+07	3,085	
Li	-3,672E+04	1,996	5,515	7,510	-4,681E+04	2,720E+07	3,289	
Mg	-3,550E+04	1,987	5,515	7,501	-4,557E+04	2,957E+07	3,179	
Mn	-3,480E+04	2,034	5,515	7,549	-4,494E+04	3,077E+07	3,116	
Mo	-3,474E+04	2,031	5,515	7,545	-4,488E+04	3,091E+07	3,111	
Na	-3,652E+04	2,008	5,515	7,523	-4,662E+04	2,752E+07	3,271	
Nb	-3,448E+04	2,013	5,515	7,528	-4,459E+04	3,154E+07	3,088	
P	-3,566E+04	2,149	5,515	7,664	-4,596E+04	2,856E+07	3,194	
Pb	-3,433E+04	1,989	5,515	7,504	-4,440E+04	3,198E+07	3,074	
Pd	-3,396E+04	2,027	5,515	7,542	-4,408E+04	3,260E+07	3,041	
Pt	-3,697E+04	2,024	5,515	7,539	-4,709E+04	2,665E+07	3,311	
Re	-3,428E+04	2,027	5,515	7,542	-4,441E+04	3,190E+07	3,070	
Si	-3,524E+04	2,107	5,515	7,622	-4,548E+04	2,956E+07	3,156	
Sn	-3,444E+04	1,985	5,515	7,500	-4,452E+04	3,174E+07	3,085	
Ta	-3,442E+04	2,013	5,515	7,528	-4,453E+04	3,166E+07	3,083	
Ti	-3,546E+04	2,006	5,515	7,521	-4,556E+04	2,955E+07	3,176	
V	-3,460E+04	2,045	5,515	7,560	-4,475E+04	3,114E+07	3,099	
W	-3,491E+04	2,029	5,515	7,544	-4,504E+04	3,057E+07	3,126	
Y	-3,445E+04	1,996	5,515	7,511	-4,454E+04	3,168E+07	3,085	
Zn	-3,572E+04	2,022	5,515	7,537	-4,585E+04	2,897E+07	3,199	

Table B.11. The ordering energy values for $Zr_{70}Ni_{30}$ and $Zr_{70}Ni_{0,29}M_{0,01}$.

M	W_{Zr-Ni} (J/mol)	w_{Zr-Ni} (J/mol)	W_{Zr-M} (J/mol)	w_{Zr-M} (J/mol)	W_{Ni-M} (J/mol)	w_{Ni-M} (J/mol)
$Zr_{70}Ni_{30}$	-2,199E+03	-1,650E+05				
Ag	-2,197E+04	-1,647E+05	-2,199E+04	-1,650E+05	-2,199E+04	-1,650E+05
Al	-2,201E+04	-1,651E+05	-2,185E+04	-1,639E+05	0,000E+00	0,000E+00
B	-2,202E+04	-1,652E+05	6,726E+03	5,045E+04	-1,880E+04	-1,410E+05
Ba	-2,202E+04	-1,651E+05	-6,035E+04	-4,526E+05	-7,199E+03	-5,400E+04
Bi	-2,202E+04	-1,652E+05	1,161E+04	8,710E+04	3,245E+03	2,434E+04
C	-2,204E+04	-1,653E+05	-2,521E+04	-1,891E+05	9,926E+02	7,445E+03
Ca	-2,201E+04	-1,651E+05	-5,067E+04	-3,800E+05	2,043E+03	1,532E+04
Cd	-2,198E+04	-1,649E+05	-3,983E+04	-2,987E+05	-1,316E+04	-9,872E+04
Co	-2,199E+04	-1,649E+05	-7,502E+04	-5,626E+05	-6,105E+04	-4,579E+05
Cr	-2,200E+04	-1,650E+05	-4,076E+05	-3,057E+06	-4,642E+05	-3,481E+06
Cu	-2,198E+04	-1,649E+05	-2,785E+04	-2,089E+05	1,262E+03	9,463E+03
Fe	-2,199E+04	-1,649E+05	1,447E+04	1,085E+05	-4,117E+04	-3,088E+05
Ga	-2,201E+04	-1,651E+05	-3,226E+04	-2,420E+05	9,477E+03	7,108E+04
Ge	-2,203E+04	-1,652E+05	7,253E+03	5,440E+04	-8,912E+03	-6,684E+04
Hf	-2,200E+04	-1,650E+05	-5,265E+04	-3,949E+05	-5,039E+03	-3,779E+04
K	-2,206E+04	-1,654E+05	-1,560E+04	-1,170E+05	5,669E+02	4,252E+03
La	-2,199E+04	-1,649E+05	-2,578E+04	-1,933E+05	1,170E+03	8,775E+03
Li	-2,200E+04	-1,650E+05	6,874E+02	5,156E+03	-2,762E+04	-2,071E+05
Mg	-2,200E+04	-1,650E+05	-1,287E+04	-9,649E+04	-6,361E+02	-4,771E+03
Mn	-2,199E+04	-1,649E+05	1,786E+03	1,339E+04	-1,567E+04	-1,175E+05
Mo	-2,201E+04	-1,651E+05	1,829E+03	1,372E+04	-1,825E+04	-1,369E+05
Na	-2,201E+04	-1,651E+05	-6,598E+03	-4,949E+04	2,106E+03	1,580E+04
Nb	-2,201E+04	-1,651E+05	-2,355E+04	-1,766E+05	7,317E+03	5,488E+04
P	-2,204E+04	-1,653E+05	-3,079E+04	-2,309E+05	-2,735E+02	-2,052E+03
Pb	-2,201E+04	-1,650E+05	-1,164E+04	-8,727E+04	7,850E+03	5,887E+04
Pd	-2,199E+04	-1,649E+05	2,681E+02	2,011E+03	-3,312E+04	-2,484E+05
Pt	-2,199E+04	-1,649E+05	-1,957E+02	-1,468E+03	-2,093E+04	-1,570E+05
Re	-2,204E+04	-1,653E+05	-1,775E+04	-1,331E+05	1,922E+03	1,441E+04
Si	-2,203E+04	-1,652E+05	-1,061E+05	-7,959E+05	-1,053E+05	-7,896E+05
Sn	-2,201E+04	-1,651E+05	-5,502E+02	-4,126E+03	-5,445E+04	-4,084E+05
Ta	-2,201E+04	-1,651E+05	-2,244E+04	-1,683E+05	3,743E+03	2,807E+04
Ti	-2,201E+04	-1,651E+05	-9,568E+04	-7,176E+05	-2,250E+04	-1,688E+05
V	-2,202E+04	-1,651E+05	-2,571E+04	-1,928E+05	-8,665E+02	-6,499E+03
W	-2,202E+04	-1,652E+05	-2,368E+03	-1,776E+04	-7,970E+03	-5,978E+04
Y	-2,200E+04	-1,650E+05	-1,178E+04	-8,836E+04	-3,911E+02	-2,933E+03
Zn	-2,199E+04	-1,649E+05	-1,358E+03	-1,019E+04	-1,163E+04	-8,719E+04

Table B.12. Thermodynamic and structural data of $Zr_{70}Ni_{30}$ and $Zr_{0,69}Ni_{0,30}M_{0,01}$.

M	ΔH_{mixing} (J/mol)	S^{σ} (J/K.mol)	ΔS^{ideal} (J/K.mol)	ΔS_{mixing} (J/mol)	ΔG_{mixing} (J/mol)	R_c (J/s)	$\Delta\eta/\eta_o$	α_1
$Zr_{70}Ni_{30}$	-3,464E+04	2,018	5,079	7,097	-4,417E+04	3,242E+07	3,102	-0,429
Ag	-3,508E+04	1,958	5,444	7,402	-4,502E+04	3,074E+07	3,141	
Al	-3,466E+04	1,961	5,444	7,405	-4,461E+04	3,159E+07	3,104	
B	-3,359E+04	2,223	5,444	7,666	-4,388E+04	3,270E+07	3,008	
Ba	-3,685E+04	2,113	5,444	7,557	-4,700E+04	2,668E+07	3,300	
Bi	-3,285E+04	1,940	5,444	7,384	-4,276E+04	3,579E+07	2,942	
C	-3,485E+04	2,248	5,444	7,692	-4,518E+04	2,992E+07	3,121	
Ca	-3,613E+04	1,998	5,444	7,441	-4,612E+04	2,848E+07	3,235	
Cd	-3,584E+04	1,938	5,444	7,382	-4,576E+04	2,928E+07	3,210	
Co	-3,875E+04	2,017	5,444	7,460	-4,877E+04	2,382E+07	3,470	
Cr	-6,499E+04	2,017	5,444	7,461	-7,501E+04	4,086E+06	5,821	
Cu	-3,490E+04	2,007	5,444	7,450	-4,491E+04	3,088E+07	3,126	
Fe	-3,361E+04	2,020	5,444	7,464	-4,364E+04	3,361E+07	3,010	
Ga	-3,500E+04	1,971	5,444	7,415	-4,496E+04	3,084E+07	3,134	
Ge	-3,335E+04	2,021	5,444	7,464	-4,338E+04	3,420E+07	2,987	
Hf	-3,637E+04	1,937	5,444	7,381	-4,628E+04	2,826E+07	3,257	
K	-3,439E+04	2,228	5,444	7,672	-4,469E+04	3,096E+07	3,080	
La	-3,480E+04	1,964	5,444	7,407	-4,475E+04	3,128E+07	3,117	
Li	-3,407E+04	1,944	5,444	7,388	-4,399E+04	3,296E+07	3,051	
Mg	-3,419E+04	1,935	5,444	7,379	-4,410E+04	3,273E+07	3,062	
Mn	-3,372E+04	1,983	5,444	7,427	-4,369E+04	3,355E+07	3,020	
Mo	-3,381E+04	1,979	5,444	7,423	-4,378E+04	3,337E+07	3,028	
Na	-3,382E+04	1,958	5,444	7,401	-4,376E+04	3,346E+07	3,028	
Nb	-3,459E+04	1,962	5,444	7,405	-4,453E+04	3,174E+07	3,098	
P	-3,518E+04	2,099	5,444	7,542	-4,531E+04	2,992E+07	3,150	
Pb	-3,394E+04	1,938	5,444	7,382	-4,386E+04	3,326E+07	3,040	
Pd	-3,419E+04	1,976	5,444	7,419	-4,415E+04	3,255E+07	3,062	
Pt	-3,395E+04	1,972	5,444	7,416	-4,391E+04	3,309E+07	3,040	
Re	-3,444E+04	1,976	5,444	7,419	-4,441E+04	3,199E+07	3,085	
Si	-4,140E+04	2,056	5,444	7,500	-5,147E+04	1,981E+07	3,708	
Sn	-3,472E+04	1,934	5,444	7,378	-4,463E+04	3,158E+07	3,110	
Ta	-3,461E+04	1,962	5,444	7,405	-4,455E+04	3,170E+07	3,099	
Ti	-3,902E+04	1,955	5,444	7,398	-4,896E+04	2,360E+07	3,494	
V	-3,489E+04	1,994	5,444	7,437	-4,488E+04	3,096E+07	3,125	
W	-3,383E+04	1,978	5,444	7,422	-4,379E+04	3,333E+07	3,029	
Y	-3,413E+04	1,946	5,444	7,389	-4,405E+04	3,282E+07	3,056	
Zn	-3,380E+04	1,970	5,444	7,414	-4,376E+04	3,342E+07	3,027	

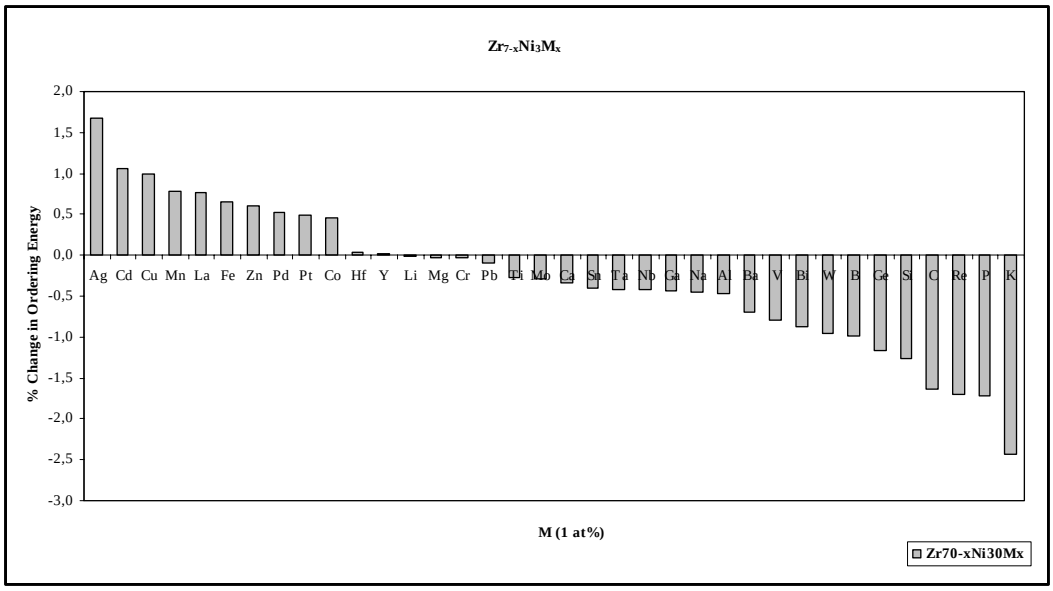

Figure B.13. % Change in ordering energy of $Zr_{70}Ni_{30}$ intermetallic for the addition of 1 at % impurity elements (M) when 1 at % is taken from Zr ($Zr_{0,69}Ni_{0,30}M_{0,01}$system).

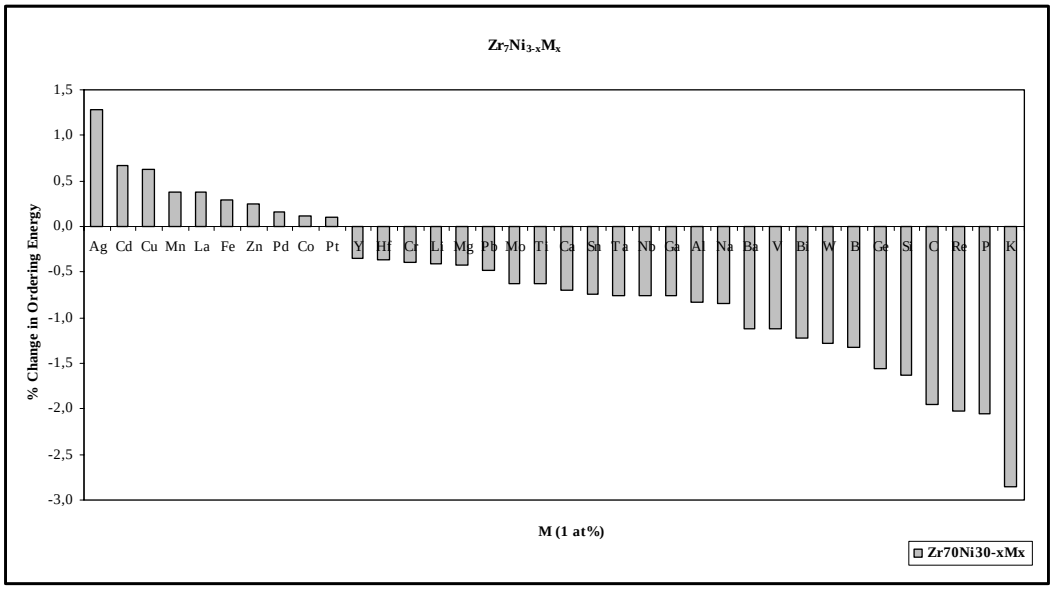

Figure B.14. % Change in ordering energy of $Zr_{70}Ni_{30}$ intermetallic for the addition of 1 at % impurity elements (M) when 1 at % is taken from Ni ($Zr_{0,70}Ni_{0,29}M_{0,01}$system).

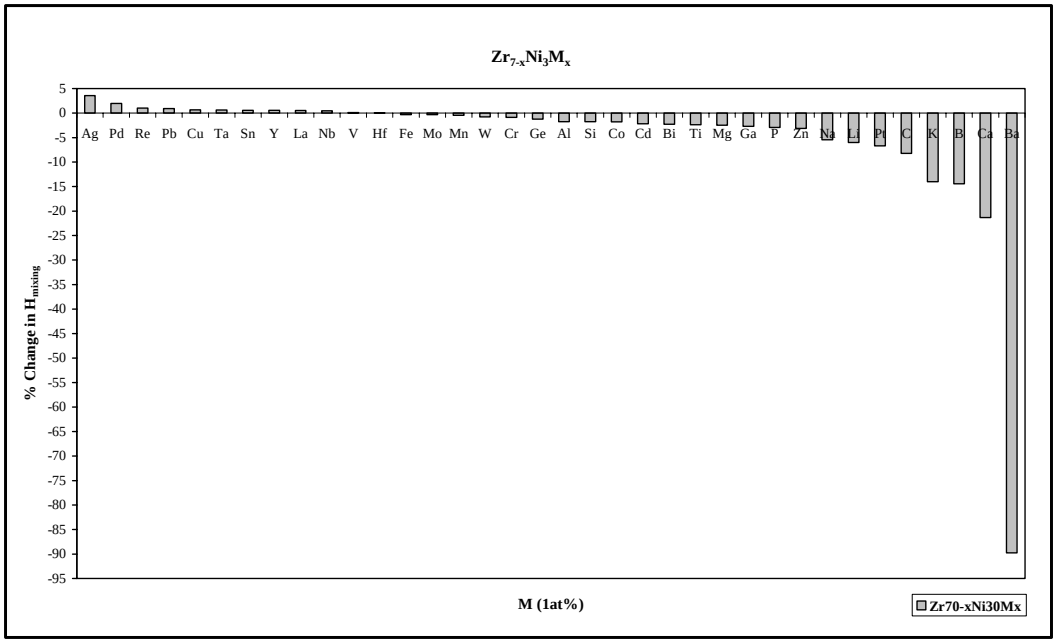

Figure B.15. % Change in ΔH_{mixing} of $Zr_{70}Ni_{30}$ intermetallic for the addition of 1 at % impurity elements (M) when 1 at % is taken from Zr ($Zr_{0,69}Ni_{0,30}M_{0,01}$system).

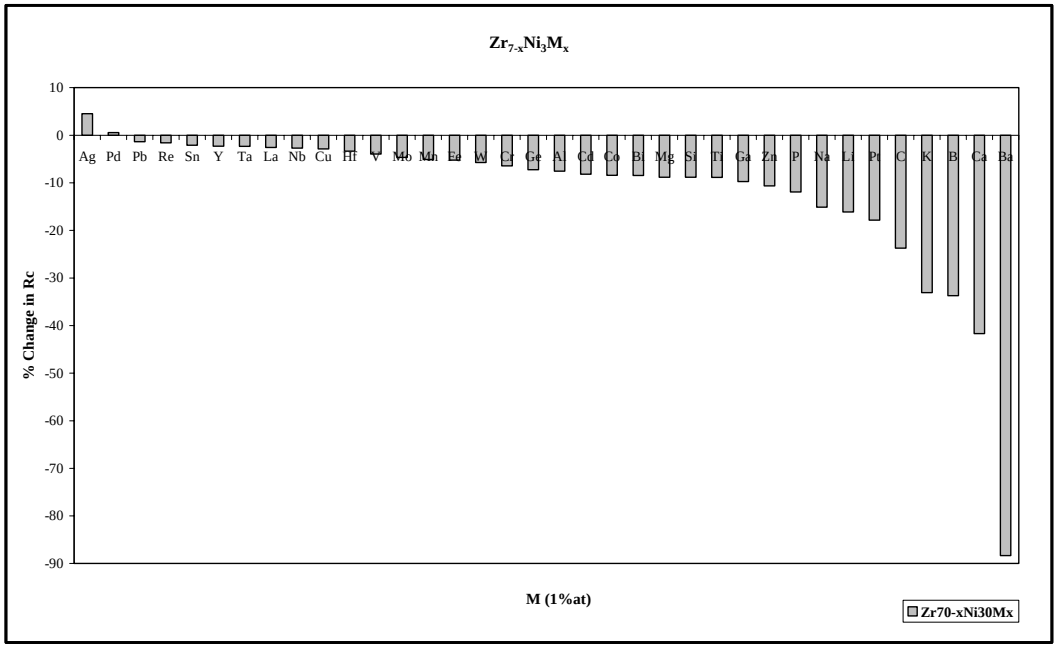

Figure B.16. % Change in R_c of $Zr_{70}Ni_{30}$ intermetallic for the addition of 1 at % impurity elements (M) when 1 at % is taken from Zr ($Zr_{0,69}Ni_{0,30}M_{0,01}$system).

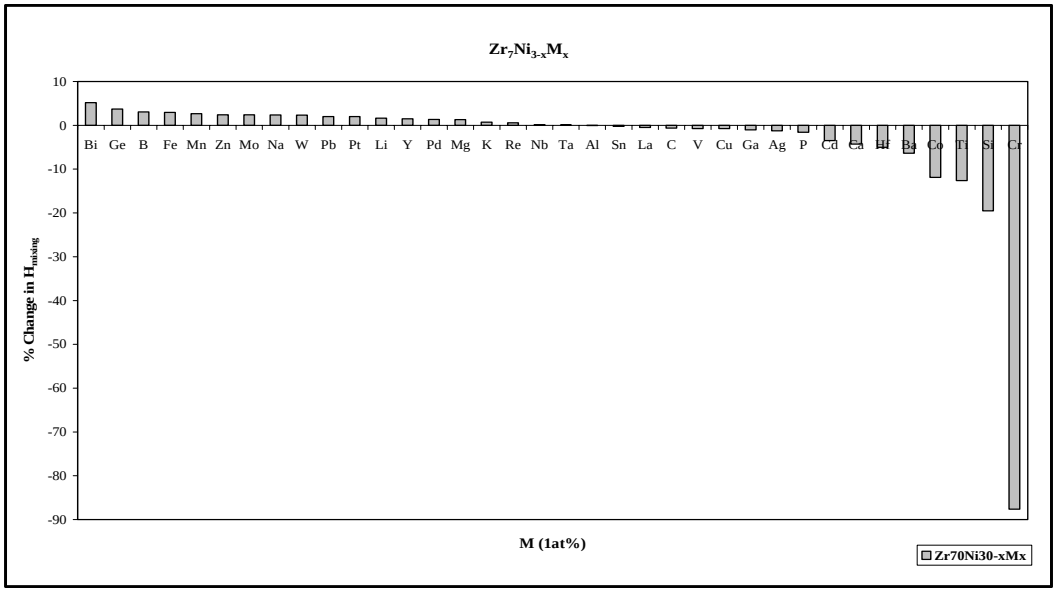

Figure B.17. % Change in ΔH_{mixing} of $Zr_{70}Ni_{30}$ intermetallic for the addition of 1 at % impurity elements (M) when 1 at % is taken from Ni ($Zr_{0,70}Ni_{0,29}M_{0,01}$system).

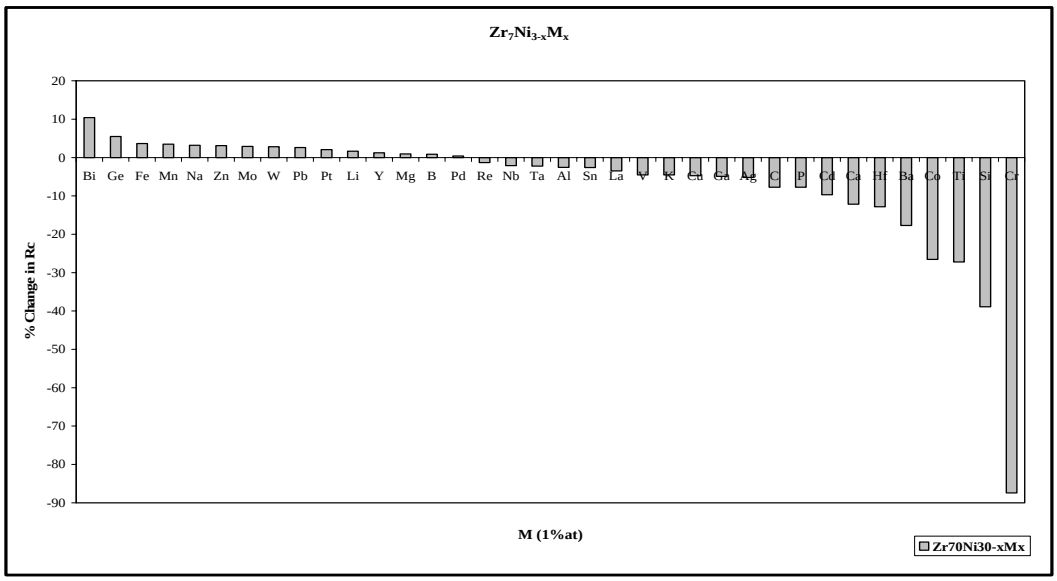

Figure B.18. % Change in R_c of $Zr_{70}Ni_{30}$ intermetallic for the addition of 1 at % impurity elements (M) when 1 at % is taken from Ni ($Zr_{0,70}Ni_{0,29}M_{0,01}$system).

Table B.13. The ordering energy values for $Zr_{75}Ni_{25}$ and $Zr_{0,74}Ni_{0,25}M_{0,01}$.

M	W_{Zr-Ni} (J/mol)	w_{Zr-Ni} (J/mol)	W_{Zr-M} (J/mol)	w_{Zr-M} (J/mol)	W_{Ni-M} (J/mol)	w_{Ni-M} (J/mol)
$Zr_{75}Ni_{25}$	-2,203E+04	-1,895E+05				
Ag	-2,200E+04	-1,892E+05	1,152E+04	9,907E+04	3,274E+03	2,815E+04
Al	-2,204E+04	-1,895E+05	-6,491E+04	-5,582E+05	-1,040E+04	-8,943E+04
B	-2,206E+04	-1,897E+05	-5,500E+04	-4,730E+05	-1,102E+04	-9,477E+04
Ba	-2,205E+04	-1,897E+05	-4,055E+05	-3,487E+06	-4,630E+05	-3,982E+06
Bi	-2,205E+04	-1,897E+05	-6,715E+02	-5,775E+03	-5,438E+04	-4,677E+05
C	-2,207E+04	-1,898E+05	-6,043E+04	-5,197E+05	-7,187E+03	-6,181E+04
Ca	-2,204E+04	-1,896E+05	-1,056E+05	-9,081E+05	-1,052E+05	-9,046E+05
Cd	-2,201E+04	-1,893E+05	-2,526E+04	-2,173E+05	9,985E+02	8,587E+03
Co	-2,202E+04	-1,894E+05	-2,188E+04	-1,882E+05	0	0
Cr	-2,203E+04	-1,895E+05	-1,560E+04	-1,341E+05	5,729E+02	4,927E+03
Cu	-2,201E+04	-1,893E+05	-6,659E+03	-5,727E+04	2,115E+03	1,819E+04
Fe	-2,202E+04	-1,894E+05	-1,181E+04	-1,015E+05	-3,937E+02	-3,386E+03
Ga	-2,204E+04	-1,896E+05	-2,789E+04	-2,399E+05	1,277E+03	1,098E+04
Ge	-2,206E+04	-1,897E+05	-1,776E+04	-1,528E+05	1,927E+03	1,657E+04
Hf	-2,203E+04	-1,895E+05	-1,997E+02	-1,717E+03	-2,093E+04	-1,800E+05
K	-2,209E+04	-1,900E+05	-7,465E+04	-6,420E+05	-6,093E+04	-5,240E+05
La	-2,202E+04	-1,894E+05	-1,373E+03	-1,181E+04	-1,161E+04	-9,981E+04
Li	-2,204E+04	-1,895E+05	-5,074E+04	-4,364E+05	2,046E+03	1,759E+04
Mg	-2,204E+04	-1,895E+05	-2,568E+04	-2,208E+05	-8,829E+02	-7,593E+03
Mn	-2,202E+04	-1,894E+05	-1,290E+04	-1,109E+05	-6,348E+02	-5,459E+03
Mo	-2,204E+04	-1,895E+05	6,927E+02	5,957E+03	-2,764E+04	-2,377E+05
Na	-2,205E+04	-1,896E+05	-3,974E+04	-3,417E+05	-1,315E+04	-1,131E+05
Nb	-2,204E+04	-1,895E+05	1,828E+03	1,572E+04	-1,831E+04	-1,575E+05
P	-2,204E+04	-1,895E+05	1,428E+04	1,228E+05	-4,113E+04	-3,537E+05
Pb	-2,204E+04	-1,895E+05	1,428E+04	1,228E+05	-4,113E+04	-3,537E+05
Pd	-2,202E+04	-1,894E+05	7,381E+03	6,347E+04	-8,872E+03	-7,630E+04
Pt	-2,202E+04	-1,894E+05	-5,277E+04	-4,538E+05	-4,995E+03	-4,296E+04
Re	-2,207E+04	-1,898E+05	6,732E+03	5,790E+04	-1,886E+04	-1,622E+05
Si	-2,206E+04	-1,897E+05	-2,354E+04	-2,025E+05	7,320E+03	6,295E+04
Sn	-2,204E+04	-1,896E+05	-1,612E+03	-1,387E+04	-8,891E+03	-7,646E+04
Ta	-2,204E+04	-1,895E+05	1,787E+03	1,537E+04	-1,572E+04	-1,352E+05
Ti	-2,204E+04	-1,895E+05	-2,581E+04	-2,220E+05	1,182E+03	1,016E+04
V	-2,205E+04	-1,896E+05	-1,164E+04	-1,001E+05	7,851E+03	6,752E+04
W	-2,205E+04	-1,896E+05	2,668E+02	2,295E+03	-3,317E+04	-2,852E+05
Y	-2,203E+04	-1,895E+05	-2,373E+03	-2,041E+04	-7,975E+03	-6,859E+04
Zn	-2,202E+04	-1,896E+05	-3,084E+04	-2,653E+05	-2,696E+02	-2,319E+03

Table B.14. Thermodynamic and structural data of $Zr_{75}Ni_{25}$ and $Zr_{0,74}Ni_{0,25}M_{0,01}$.

M	ΔH_{mixing} (J/mol)	S^{σ} (J/K.mol)	ΔS^{ideal} (J/K.mol)	ΔS_{mixing} (J/mol)	ΔG_{mixing} (J/mol)	R_c (J/s)	$\Delta\eta/\eta_o$	α_1
$Zr_{75}Ni_{25}$	-3,553E+04	1,745	4,676	6,420	-4,357E+04	2,529E+07	3,410	-0,308
Ag	-3,42E+04	1,741	5,117	6,858	-4,28E+04	2,676E+07	3,282	
Al	-3,94E+04	1,744	5,117	6,861	-4,80E+04	1,837E+07	3,784	
B	-3,88E+04	2,011	5,117	7,128	-4,78E+04	1,842E+07	3,728	
Ba	-7,09E+04	1,912	5,117	7,03	-7,97E+04	1,866E+06	6,8	
Bi	-3,63E+04	1,723	5,117	6,84	-4,49E+04	2,306E+07	3,484	
C	-3,91E+04	2,038	5,117	7,155	-4,81E+04	1,800E+07	3,754	
Ca	-4,41E+04	1,789	5,117	6,906	-5,27E+04	1,307E+07	4,229	
Cd	-3,66E+04	1,721	5,117	6,838	-4,52E+04	2,256E+07	3,514	
Co	-3,64E+04	1,8	5,117	6,917	-4,51E+04	2,259E+07	3,497	
Cr	-3,60E+04	1,8	5,117	6,918	-4,47E+04	2,324E+07	3,459	
Cu	-3,54E+04	1,79	5,117	6,907	-4,41E+04	2,436E+07	3,398	
Fe	-3,58E+04	1,804	5,117	6,921	-4,45E+04	2,364E+07	3,436	
Ga	-3,68E+04	1,754	5,117	6,871	-4,54E+04	2,212E+07	3,534	
Ge	-3,62E+04	1,804	5,117	6,921	-4,49E+04	2,298E+07	3,473	
Hf	-3,55E+04	1,721	5,117	6,838	-4,41E+04	2,441E+07	3,409	
K	-4,12E+04	2,035	5,117	7,152	-5,02E+04	1,548E+07	3,956	
La	-3,54E+04	1,752	5,117	6,869	-4,40E+04	2,455E+07	3,395	
Li	-3,83E+04	1,727	5,117	6,844	-4,68E+04	2,003E+07	3,671	
Mg	-3,67E+04	1,719	5,117	6,836	-4,53E+04	2,240E+07	3,524	
Mn	-3,59E+04	1,766	5,117	6,883	-4,45E+04	2,365E+07	3,442	
Mo	-3,56E+04	1,762	5,117	6,879	-4,42E+04	2,410E+07	3,418	
Na	-3,79E+04	1,745	5,117	6,862	-4,65E+04	2,050E+07	3,637	
Nb	-3,53E+04	1,744	5,117	6,862	-4,39E+04	2,463E+07	3,393	
P	-3,50E+04	1,884	5,117	7,001	-4,38E+04	2,468E+07	3,363	
Pb	-3,50E+04	1,724	5,117	6,841	-4,36E+04	2,525E+07	3,363	
Pd	-3,48E+04	1,758	5,117	6,875	-4,34E+04	2,563E+07	3,336	
Pt	-3,85E+04	1,755	5,117	6,872	-4,71E+04	1,958E+07	3,696	
Re	-3,51E+04	1,758	5,117	6,876	-4,37E+04	2,504E+07	3,368	
Si	-3,64E+04	1,84	5,117	6,957	-4,52E+04	2,245E+07	3,498	
Sn	-3,54E+04	1,718	5,117	6,835	-4,39E+04	2,469E+07	3,394	
Ta	-3,53E+04	1,744	5,117	6,861	-4,39E+04	2,472E+07	3,387	
Ti	-3,67E+04	1,737	5,117	6,854	-4,53E+04	2,239E+07	3,521	
V	-3,57E+04	1,777	5,117	6,894	-4,43E+04	2,398E+07	3,422	
W	-3,58E+04	1,761	5,117	6,878	-4,44E+04	2,381E+07	3,434	
Y	-3,54E+04	1,732	5,117	6,849	-4,40E+04	2,461E+07	3,396	
Zn	-3,70E+04	1,753	5,117	6,87	-4,56E+04	2,183E+07	3,552	

Table B.15. The ordering energy values for $Zr_{75}Ni_{25}$ and $Zr_{0,75}Ni_{0,24}M_{0,01}$.

M	W_{Zr-Ni} (J/mol)	w_{Zr-Ni} (J/mol)	W_{Zr-M} (J/mol)	w_{Zr-M} (J/mol)	W_{Ni-M} (J/mol)	w_{Ni-M} (J/mol)
$Zr_{75}Ni_{25}$	-2,203E+04	-1,895E+05				
Ag	-2,201E+04	-1,893E+05	1,150E+04	9,887E+04	3,280E+03	2,821E+04
Al	-2,205E+04	-1,896E+05	-6,492E+04	-5,583E+05	-1,039E+04	-8,938E+04
B	-2,206E+04	-1,897E+05	-5,501E+04	-4,731E+05	-1,102E+04	-9,475E+04
Ba	-2,206E+04	-1,897E+05	-4,050E+05	-3,483E+06	-4,627E+05	-3,979E+06
Bi	-2,206E+04	-1,897E+05	-7,004E+02	-6,024E+03	-5,436E+04	-4,675E+05
C	-2,207E+04	-1,898E+05	-6,045E+04	-5,198E+05	-7,184E+03	-6,178E+04
Ca	-2,205E+04	-1,897E+05	-1,055E+05	-9,070E+05	-1,052E+05	-9,044E+05
Cd	-2,202E+04	-1,894E+05	-2,528E+04	-2,174E+05	9,998E+02	8,598E+03
Co	-2,203E+04	-1,895E+05	-2,189E+04	-1,883E+05	0	0
Cr	-2,204E+04	-1,896E+05	-1,560E+04	-1,341E+05	5,742E+02	4,938E+03
Cu	-2,202E+04	-1,894E+05	-6,673E+03	-5,739E+04	2,117E+03	1,820E+04
Fe	-2,203E+04	-1,894E+05	-1,181E+04	-1,016E+05	-3,937E+02	-3,386E+03
Ga	-2,205E+04	-1,896E+05	-2,790E+04	-2,400E+05	1,280E+03	1,101E+04
Ge	-2,207E+04	-1,898E+05	-1,777E+04	-1,528E+05	1,928E+03	1,658E+04
Hf	-2,204E+04	-1,896E+05	-1,997E+02	-1,717E+03	-2,093E+04	-1,800E+05
K	-2,210E+04	-1,901E+05	-7,456E+04	-6,412E+05	-6,090E+04	-5,237E+05
La	-2,203E+04	-1,894E+05	-1,377E+03	-1,184E+04	-1,160E+04	-9,977E+04
Li	-2,204E+04	-1,896E+05	-5,076E+04	-4,366E+05	2,046E+03	1,759E+04
Mg	-2,204E+04	-1,896E+05	-2,567E+04	-2,208E+05	-8,868E+02	-7,627E+03
Mn	-2,202E+04	-1,894E+05	-1,291E+04	-1,110E+05	-6,348E+02	-5,459E+03
Mo	-2,204E+04	-1,896E+05	6,940E+02	5,968E+03	-2,765E+04	-2,378E+05
Na	-2,206E+04	-1,897E+05	-3,971E+04	-3,415E+05	-1,315E+04	-1,131E+05
Nb	-2,205E+04	-1,896E+05	1,828E+03	1,572E+04	-1,833E+04	-1,576E+05
P	-2,204E+04	-1,896E+05	1,423E+04	1,224E+05	-4,112E+04	-3,536E+05
Pb	-2,204E+04	-1,896E+05	1,423E+04	1,224E+05	-4,112E+04	-3,536E+05
Pd	-2,203E+04	-1,895E+05	7,411E+03	6,374E+04	-8,862E+03	-7,621E+04
Pt	-2,203E+04	-1,895E+05	-5,280E+04	-4,541E+05	-4,984E+03	-4,286E+04
Re	-2,207E+04	-1,898E+05	6,733E+03	5,791E+04	-1,888E+04	-1,623E+05
Si	-2,207E+04	-1,898E+05	-2,354E+04	-2,025E+05	7,321E+03	6,296E+04
Sn	-2,205E+04	-1,896E+05	-1,616E+03	-1,390E+04	-8,892E+03	-7,647E+04
Ta	-2,205E+04	-1,896E+05	1,787E+03	1,537E+04	-1,573E+04	-1,353E+05
Ti	-2,205E+04	-1,896E+05	-2,582E+04	-2,221E+05	1,185E+03	1,019E+04
V	-2,205E+04	-1,897E+05	-1,164E+04	-1,001E+05	7,852E+03	6,753E+04
W	-2,206E+04	-1,897E+05	2,661E+02	2,289E+03	-3,318E+04	-2,853E+05
Y	-2,204E+04	-1,896E+05	-2,375E+03	-2,042E+04	-7,977E+03	-6,860E+04
Zn	-2,203E+04	-1,894E+05	-3,086E+04	-2,654E+05	-2,683E+02	-2,307E+03

Table B.16. Thermodynamic and structural data of $Zr_{75}Ni_{25}$ and $Zr_{0,75}Ni_{0,24}M_{0,01}$.

M	ΔH_{mixing} (J/mol)	S^{σ} (J/K.mol)	ΔS^{ideal} (J/K.mol)	ΔS_{mixing} (J/mol)	ΔG_{mixing} (J/mol)	R_c (J/s)	$\Delta\eta/\eta_o$	α_1
$Zr_{75}Ni_{25}$	-3,553E+04	1,745	4,676	6,420	-4,357E+04	2,529E+07	3,410	-0,308
Ag	-3,326E+04	1,684	5,025	6,708	-4,166E+04	2,91E+07	3,192	
Al	-3,854E+04	1,687	5,025	6,711	-4,695E+04	1,99E+07	3,699	
B	-3,793E+04	1,955	5,025	6,980	-4,667E+04	2,00E+07	3,640	
Ba	-6,982E+04	1,859	5,025	6,884	-7,845E+04	2,04E+06	6,702	
Bi	-3,532E+04	1,666	5,025	6,691	-4,370E+04	2,52E+07	3,390	
C	-3,822E+04	1,982	5,025	7,007	-4,700E+04	1,95E+07	3,668	
Ca	-4,311E+04	1,733	5,025	6,758	-5,158E+04	1,42E+07	4,138	
Cd	-3,570E+04	1,664	5,025	6,689	-4,408E+04	2,45E+07	3,426	
Co	-3,552E+04	1,743	5,025	6,767	-4,400E+04	2,45E+07	3,409	
Cr	-3,511E+04	1,743	5,025	6,768	-4,359E+04	2,53E+07	3,370	
Cu	-3,448E+04	1,733	5,025	6,757	-4,294E+04	2,65E+07	3,309	
Fe	-3,487E+04	1,746	5,025	6,771	-4,335E+04	2,57E+07	3,347	
Ga	-3,591E+04	1,697	5,025	6,721	-4,433E+04	2,40E+07	3,447	
Ge	-3,526E+04	1,747	5,025	6,772	-4,375E+04	2,50E+07	3,385	
Hf	-3,456E+04	1,663	5,025	6,688	-4,294E+04	2,66E+07	3,318	
K	-4,028E+04	1,983	5,025	7,008	-4,906E+04	1,68E+07	3,866	
La	-3,443E+04	1,696	5,025	6,721	-4,285E+04	2,67E+07	3,305	
Li	-3,736E+04	1,670	5,025	6,695	-4,575E+04	2,17E+07	3,586	
Mg	-3,580E+04	1,662	5,025	6,686	-4,418E+04	2,43E+07	3,436	
Mn	-3,494E+04	1,709	5,025	6,733	-4,338E+04	2,57E+07	3,354	
Mo	-3,465E+04	1,705	5,025	6,729	-4,308E+04	2,63E+07	3,326	
Na	-3,697E+04	1,689	5,025	6,714	-4,539E+04	2,23E+07	3,549	
Nb	-3,439E+04	1,687	5,025	6,712	-4,280E+04	2,68E+07	3,301	
P	-3,406E+04	1,827	5,025	6,852	-4,264E+04	2,69E+07	3,269	
Pb	-3,406E+04	1,667	5,025	6,692	-4,244E+04	2,76E+07	3,269	
Pd	-3,381E+04	1,701	5,025	6,726	-4,224E+04	2,79E+07	3,245	
Pt	-3,761E+04	1,698	5,025	6,723	-4,604E+04	2,12E+07	3,610	
Re	-3,412E+04	1,701	5,025	6,726	-4,255E+04	2,73E+07	3,275	
Si	-3,553E+04	1,783	5,025	6,808	-4,406E+04	2,44E+07	3,410	
Sn	-3,442E+04	1,661	5,025	6,686	-4,280E+04	2,69E+07	3,304	
Ta	-3,434E+04	1,687	5,025	6,712	-4,275E+04	2,69E+07	3,296	
Ti	-3,577E+04	1,680	5,025	6,705	-4,417E+04	2,43E+07	3,433	
V	-3,473E+04	1,719	5,025	6,744	-4,318E+04	2,61E+07	3,334	
W	-3,481E+04	1,704	5,025	6,728	-4,324E+04	2,60E+07	3,342	
Y	-3,444E+04	1,676	5,025	6,701	-4,284E+04	2,68E+07	3,306	
Zn	-3,610E+04	1,696	5,025	6,720	-4,452E+04	2,37E+07	3,465	

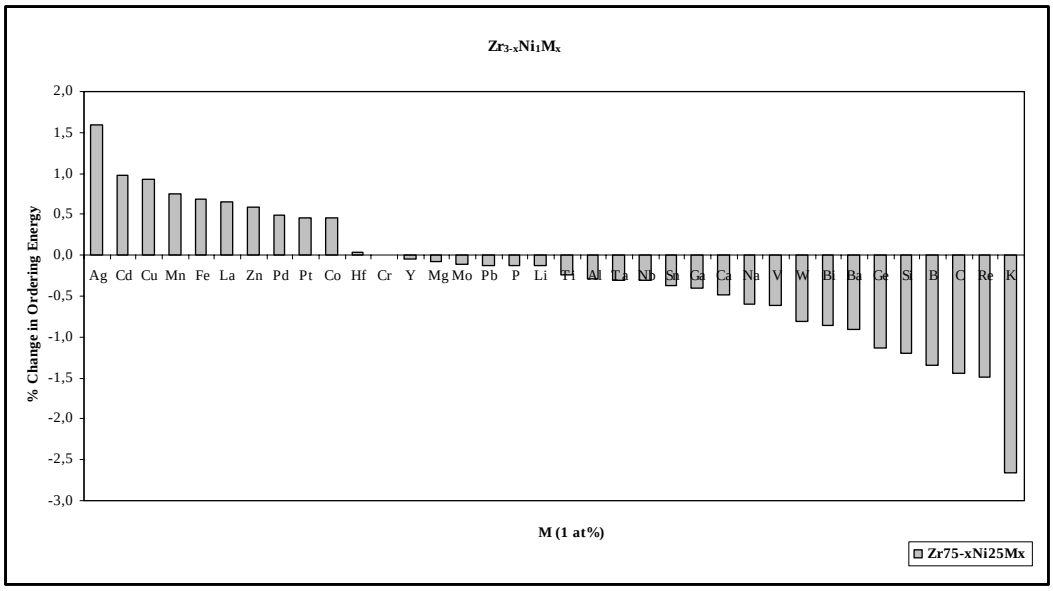

Figure B.19. % Change in ordering energy of $Zr_{75}Ni_{25}$ intermetallic for the addition of 1 at % impurity elements (M) when 1 at % is taken from Zr ($Zr_{0,74}Ni_{0,25}M_{0,01}$system).

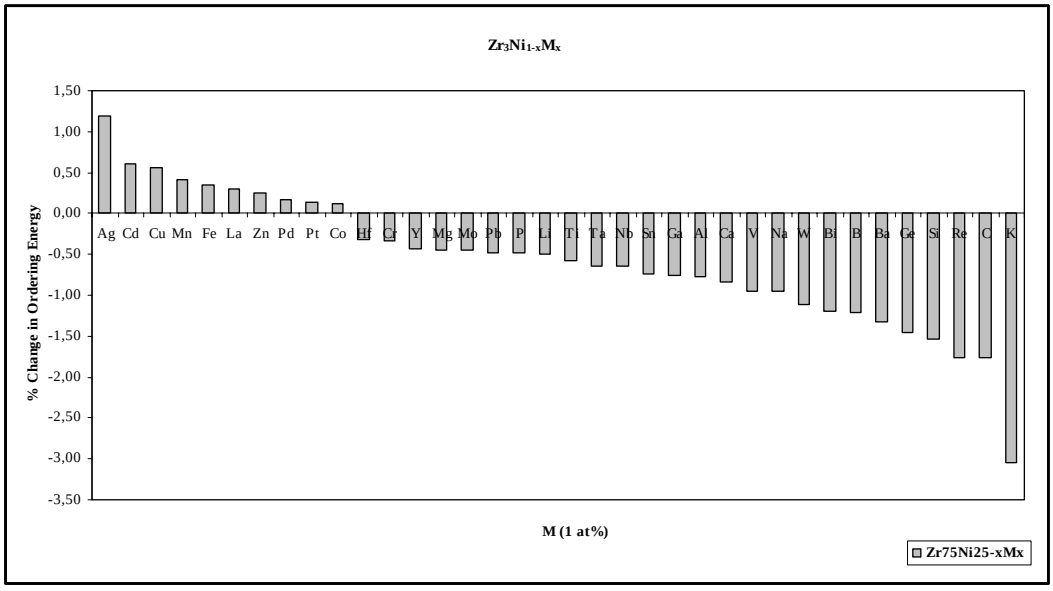

Figure B.20. % Change in ordering energy of $Zr_{75}Ni_{25}$ intermetallic for the addition of 1 at % impurity elements (M) when 1 at % is taken from Ni ($Zr_{0,75}Ni_{0,24}M_{0,01}$system).

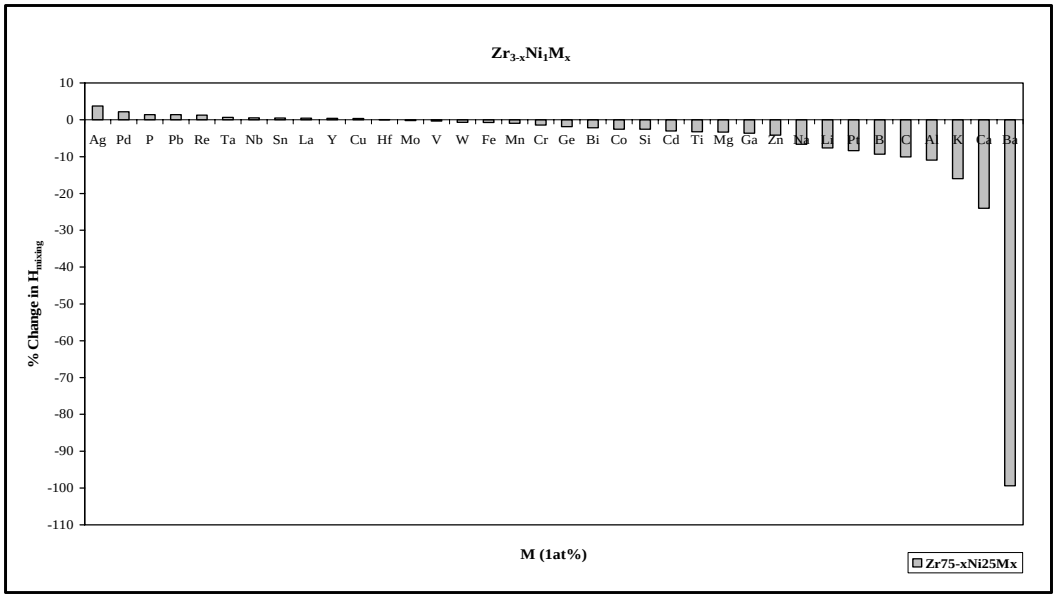

Figure B.21. % Change in ΔH_{mixing} of $Zr_{75}Ni_{25}$ intermetallic for the addition of 1 at % impurity elements (M) when 1 at % is taken from Zr ($Zr_{0,74}Ni_{0,25}M_{0,01}$system).

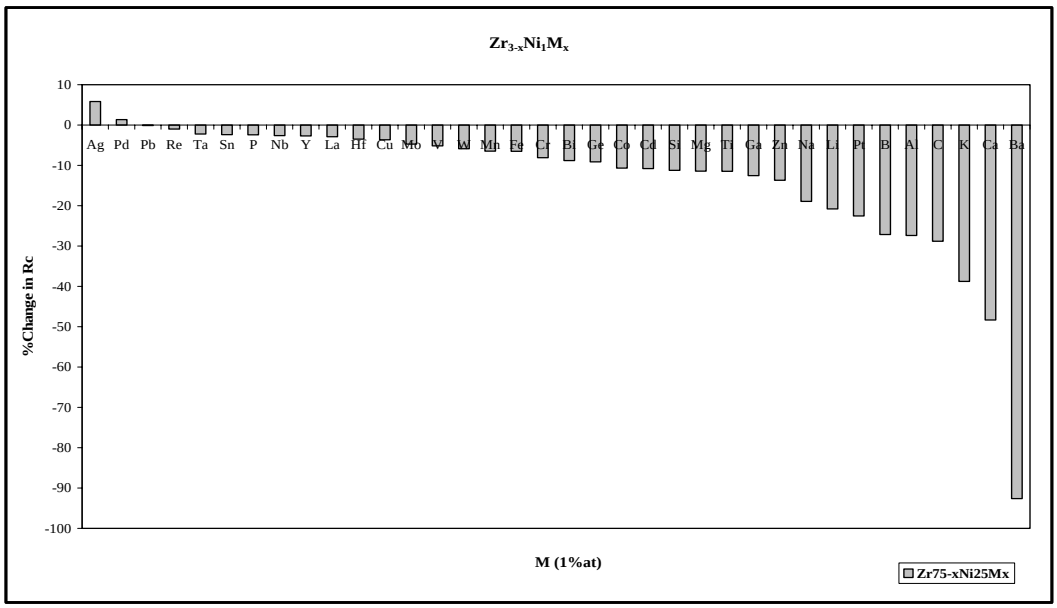

Figure B.22. % Change in R_c of $Zr_{75}Ni_{25}$ intermetallic for the addition of 1 at % impurity elements (M) when 1 at % is taken from Zr ($Zr_{0,74}Ni_{0,25}M_{0,01}$system).

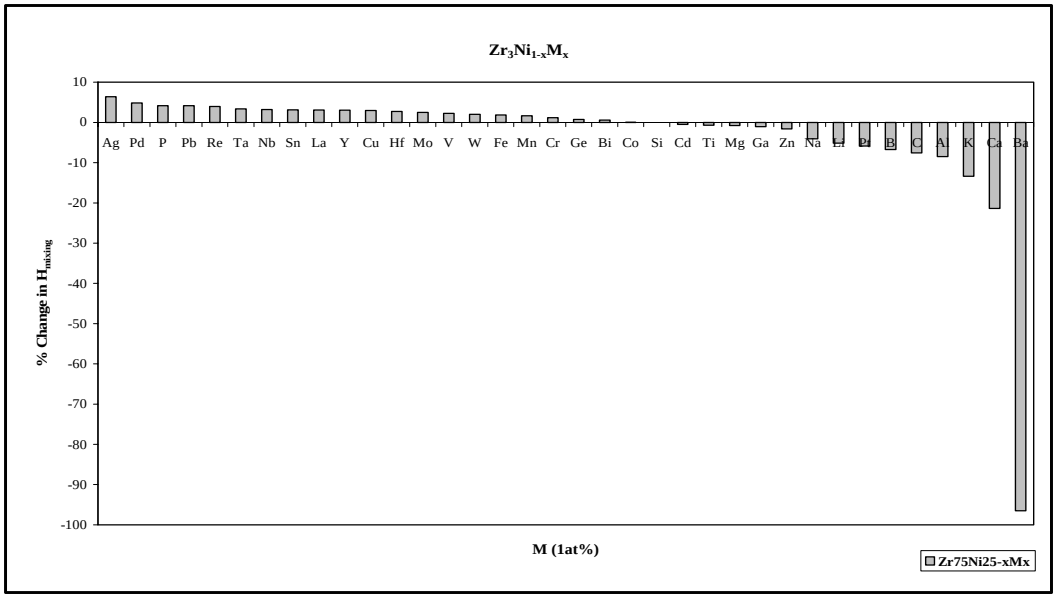

Figure B.29. % Change in ΔH_{mixing} of $Zr_{75}Ni_{25}$ intermetallic for the addition of 1 at % impurity elements (M) when 1 at % is taken from Ni ($Zr_{0,75}Ni_{0,24}M_{0,01}$system).

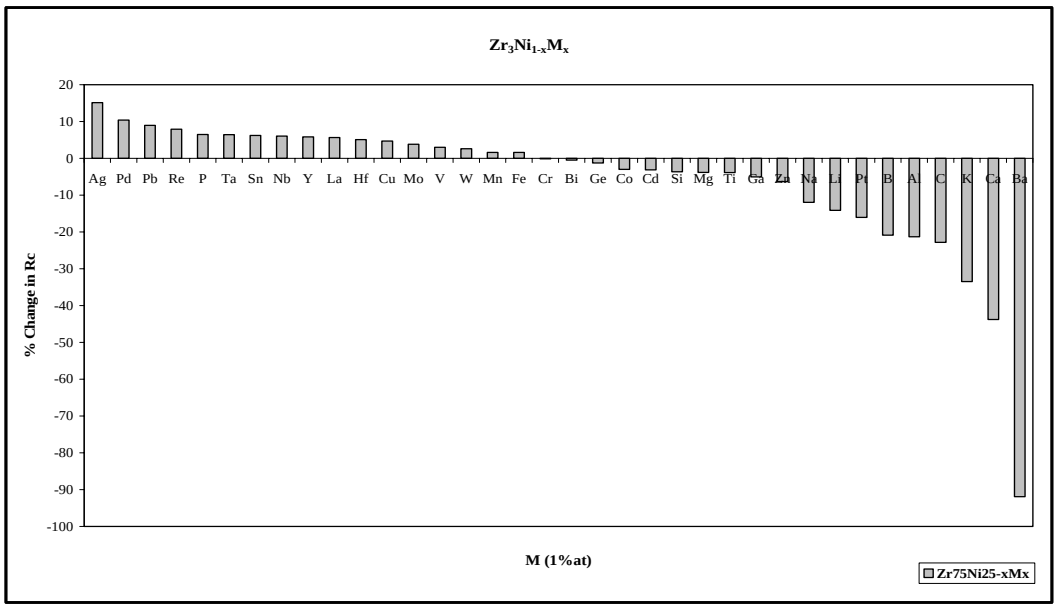

Figure B.30. % Change in R_c of $Zr_{75}Ni_{25}$ intermetallic for the addition of 1 at % impurity elements (M) when 1 at % is taken from Ni ($Zr_{0,75}Ni_{0,24}M_{0,01}$system).

Table B.17. The ordering energy values for $Zr_{75}Fe_{25}$ and $Zr_{0,74}Fe_{0,25}M_{0,01}$.

M	W_{Zr-Fe} (J/mol)	w_{Zr-Fe} (J/mol)	W_{Zr-M} (J/mol)	w_{Zr-M} (J/mol)	W_{Fe-M} (J/mol)	w_{Fe-M} (J/mol)
$Zr_{75}Fe_{25}$	-8,216E+03	-1,076E+05				
Ag	-7,973E+03	-1,044E+05	3,382E+04	4,430E+05	3,679E+03	4,819E+04
Al	-8,250E+03	-1,081E+05	-2,646E+04	-3,466E+05	5,140E+03	6,734E+04
B	-8,455E+03	-1,108E+05	-4,788E+04	-6,272E+05	-2,881E+04	-3,774E+05
Ba	-7,123E+03	-9,332E+04	-1,158E+06	-1,517E+07	-8,072E+05	-1,057E+07
Bi	-8,080E+03	-1,059E+05	4,280E+04	5,607E+05	-4,846E+04	-6,348E+05
C	-8,614E+03	-1,128E+05	-3,083E+04	-4,039E+05	-1,005E+04	-1,316E+05
Ca	-7,542E+03	-9,879E+04	-2,099E+05	-2,750E+06	-5,623E+04	-7,367E+05
Cd	-8,004E+03	-1,049E+05	-1,064E+04	-1,394E+05	1,940E+03	2,541E+04
Co	-8,237E+03	-1,079E+05	-1,624E+04	-2,127E+05	7,697E+02	1,008E+04
Cr	-8,345E+03	-1,093E+05	-2,116E+04	-2,772E+05	-1,158E+03	-1,518E+04
Cu	-8,098E+03	-1,061E+05	6,077E+03	7,961E+04	5,471E+03	7,167E+04
Ga	-8,185E+03	-1,072E+05	-1,535E+04	-2,011E+05	-1,898E+03	-2,486E+04
Ge	-8,248E+03	-1,080E+05	-1,207E+04	-1,582E+05	-2,886E+01	-3,781E+02
Hf	-8,237E+03	-1,079E+05	9,897E+02	1,297E+04	-1,469E+04	-1,925E+05
K	-6,834E+03	-8,952E+04	-3,010E+05	-3,943E+06	-1,153E+05	-1,510E+06
La	-7,782E+03	-1,019E+05	3,385E+03	4,434E+04	-1,166E+04	-1,527E+05
Li	-7,900E+03	-1,035E+05	-2,705E+04	-3,543E+05	4,040E+03	5,292E+04
Mg	-7,983E+03	-1,046E+05	-3,394E+04	-4,446E+05	8,346E+03	1,093E+05
Mn	-8,211E+03	-1,076E+05	-7,506E+03	-9,833E+04	1,571E+03	2,058E+04
Mo	-8,617E+03	-1,129E+05	1,763E+03	2,309E+04	-1,588E+04	-2,081E+05
Na	-7,549E+03	-9,890E+04	-7,058E+04	-9,246E+05	-3,489E+02	-4,570E+03
Nb	-8,452E+03	-1,107E+05	1,916E+03	2,510E+04	2,365E+02	3,098E+03
Ni	-8,242E+03	-1,080E+05	-1,628E+04	-2,133E+05	7,774E+02	1,018E+04
P	-8,384E+03	-1,098E+05	-2,657E+04	-3,480E+05	-2,885E+03	-3,779E+04
Pb	-8,070E+03	-1,057E+05	7,080E+04	9,275E+05	-3,060E+04	-4,009E+05
Pd	-8,159E+03	-1,069E+05	-3,480E+04	-4,559E+05	-1,472E+04	-1,929E+05
Pt	-8,151E+03	-1,068E+05	-1,451E+04	-1,900E+05	-1,294E+04	-1,695E+05
Re	-8,769E+03	-1,149E+05	8,539E+03	1,119E+05	-5,047E+02	-6,611E+03
Si	-8,303E+03	-1,088E+05	-2,419E+04	-3,168E+05	2,841E+03	3,722E+04
Sn	-8,143E+03	-1,067E+05	2,130E+03	2,790E+04	-4,110E+03	-5,384E+04
Ta	-8,452E+03	-1,107E+05	1,437E+03	1,883E+04	-6,662E+02	-8,728E+03
Ti	-8,342E+03	-1,093E+05	-1,304E+04	-1,708E+05	-2,119E+03	-2,775E+04
V	-8,543E+03	-1,119E+05	-9,970E+03	-1,306E+05	4,516E+03	5,916E+04
W	-8,622E+03	-1,129E+05	2,535E+03	3,321E+04	-1,427E+04	-1,870E+05
Y	-7,884E+03	-1,033E+05	-5,785E+02	-7,578E+03	-1,840E+03	-2,411E+04
Zn	-8,148E+03	-1,067E+05	-1,584E+04	-2,075E+05	-1,696E+02	-2,221E+03

Table B.18. Thermodynamic and structural data of $Zr_{75}Fe_{25}$ and $Zr_{0,74}Fe_{0,25}M_{0,01}$.

M	ΔH_{mixing} (J/mol)	S^{σ} (J/K.mol)	ΔS^{ideal} (J/K.mol)	ΔS_{mixing} (J/mol)	ΔG_{mixing} (J/mol)	R_c (J/s)	$\Delta\eta/\eta_o$	α_1
$Zr_{75}Fe_{25}$	-2,018E+04	1,790	4,676	6,466	-2,857E+04	6,225E+07	1,870	-0,333
Ag	-1,592E+04	1,786	5,117	6,903	-2,488E+04	8,047E+07	1,475	
Al	-2,239E+04	1,789	5,117	6,906	-3,136E+04	5,131E+07	2,075	
B	-2,607E+04	2,057	5,117	7,174	-3,539E+04	3,822E+07	2,416	
Ba	-1,560E+05	1,957	5,117	7,074	-1,651E+05	4,661E+03	14,451	
Bi	-1,702E+04	1,768	5,117	6,885	-2,596E+04	7,475E+07	1,577	
C	-2,419E+04	2,084	5,117	7,201	-3,354E+04	4,338E+07	2,242	
Ca	-4,047E+04	1,833	5,117	6,950	-4,949E+04	1,452E+07	3,749	
Cd	-2,037E+04	1,766	5,117	6,883	-2,930E+04	5,926E+07	1,887	
Co	-2,151E+04	1,845	5,117	6,962	-3,055E+04	5,411E+07	1,993	
Cr	-2,231E+04	1,846	5,117	6,963	-3,135E+04	5,117E+07	2,067	
Cu	-1,886E+04	1,835	5,117	6,952	-2,788E+04	6,516E+07	1,747	
Ga	-2,139E+04	1,799	5,117	6,916	-3,036E+04	5,494E+07	1,982	
Ge	-2,116E+04	1,849	5,117	6,966	-3,020E+04	5,541E+07	1,961	
Hf	-2,035E+04	1,765	5,117	6,883	-2,928E+04	5,934E+07	1,885	
K	-4,952E+04	2,079	5,117	7,196	-5,886E+04	7,470E+06	4,588	
La	-1,891E+04	1,796	5,117	6,913	-2,789E+04	6,527E+07	1,752	
Li	-2,163E+04	1,772	5,117	6,889	-3,058E+04	5,421E+07	2,005	
Mg	-2,236E+04	1,764	5,117	6,881	-3,130E+04	5,160E+07	2,072	
Mn	-2,058E+04	1,811	5,117	6,928	-2,957E+04	5,803E+07	1,907	
Mo	-2,123E+04	1,807	5,117	6,924	-3,022E+04	5,547E+07	1,967	
Na	-2,515E+04	1,790	5,117	6,907	-3,411E+04	4,236E+07	2,330	
Nb	-2,029E+04	1,790	5,117	6,907	-2,925E+04	5,938E+07	1,880	
Ni	-2,153E+04	1,847	5,117	6,964	-3,057E+04	5,403E+07	1,995	
P	-2,299E+04	1,929	5,117	7,046	-3,213E+04	4,824E+07	2,130	
Pb	-1,370E+04	1,769	5,117	6,886	-2,263E+04	9,418E+07	1,269	
Pd	-2,363E+04	1,804	5,117	6,921	-3,261E+04	4,699E+07	2,189	
Pt	-2,158E+04	1,800	5,117	6,917	-3,056E+04	5,419E+07	2,000	
Re	-2,044E+04	1,804	5,117	6,921	-2,942E+04	5,864E+07	1,894	
Si	-2,237E+04	1,886	5,117	7,003	-3,146E+04	5,066E+07	2,073	
Sn	-1,966E+04	1,763	5,117	6,880	-2,859E+04	6,226E+07	1,822	
Ta	-2,037E+04	1,789	5,117	6,906	-2,933E+04	5,907E+07	1,887	
Ti	-2,155E+04	1,782	5,117	6,899	-3,051E+04	5,446E+07	1,997	
V	-2,152E+04	1,822	5,117	6,939	-3,053E+04	5,424E+07	1,994	
W	-2,112E+04	1,806	5,117	6,923	-3,010E+04	5,593E+07	1,957	
Y	-1,922E+04	1,777	5,117	6,894	-2,817E+04	6,406E+07	1,781	
Zn	-2,129E+04	1,798	5,117	6,915	-3,026E+04	5,533E+07	1,973	

Table B.19. The ordering energy values for $Zr_{75}Fe_{25}$ and $Zr_{0,75}Fe_{0,24}M_{0,01}$.

M	W_{Zr-Fe} (J/mol)	w_{Zr-Fe} (J/mol)	W_{Zr-M} (J/mol)	w_{Zr-M} (J/mol)	W_{Fe-M} (J/mol)	w_{Fe-M} (J/mol)
$Zr_{75}Fe_{25}$	-8,216E+03	-1,076E+05				
Ag	-7,853E+03	-1,029E+05	3,382E+04	4,430E+05	3,764E+03	4,930E+04
Al	-8,130E+03	-1,065E+05	-2,636E+04	-3,453E+05	5,135E+03	6,727E+04
B	-8,334E+03	-1,092E+05	-4,811E+04	-6,303E+05	-2,885E+04	-3,779E+05
Ba	-7,009E+03	-9,181E+04	-1,157E+06	-1,515E+07	-8,087E+05	-1,059E+07
Bi	-7,963E+03	-1,043E+05	4,280E+04	5,607E+05	-4,841E+04	-6,341E+05
C	-8,491E+03	-1,112E+05	-3,082E+04	-4,038E+05	-1,008E+04	-1,321E+05
Ca	-7,424E+03	-9,726E+04	-2,096E+05	-2,745E+06	-5,706E+04	-7,475E+05
Cd	-7,887E+03	-1,033E+05	-1,064E+04	-1,394E+05	1,961E+03	2,569E+04
Co	-8,117E+03	-1,063E+05	-1,612E+04	-2,112E+05	7,697E+02	1,008E+04
Cr	-8,222E+03	-1,077E+05	-2,096E+04	-2,746E+05	-1,156E+03	-1,514E+04
Cu	-7,978E+03	-1,045E+05	6,077E+03	7,961E+04	5,505E+03	7,212E+04
Ga	-8,065E+03	-1,056E+05	-1,535E+04	-2,011E+05	-1,861E+03	-2,438E+04
Ge	-8,128E+03	-1,065E+05	-1,207E+04	-1,582E+05	-7,698E+00	-1,008E+02
Hf	-8,117E+03	-1,063E+05	9,897E+02	1,297E+04	-1,456E+04	-1,907E+05
K	-6,724E+03	-8,808E+04	-3,010E+05	-3,943E+06	-1,157E+05	-1,515E+06
La	-7,664E+03	-1,004E+05	3,385E+03	4,434E+04	-1,152E+04	-1,509E+05
Li	-7,780E+03	-1,019E+05	-2,705E+04	-3,543E+05	4,079E+03	5,344E+04
Mg	-7,863E+03	-1,030E+05	-3,394E+04	-4,446E+05	8,291E+03	1,086E+05
Mn	-8,091E+03	-1,060E+05	-7,506E+03	-9,833E+04	1,576E+03	2,064E+04
Mo	-8,494E+03	-1,113E+05	1,763E+03	2,309E+04	-1,566E+04	-2,052E+05
Na	-7,432E+03	-9,736E+04	-7,058E+04	-9,246E+05	-4,871E+02	-6,381E+03
Nb	-8,332E+03	-1,091E+05	1,916E+03	2,510E+04	3,665E+02	4,801E+03
Ni	-8,122E+03	-1,064E+05	-1,628E+04	-2,133E+05	7,774E+02	1,018E+04
P	-8,264E+03	-1,083E+05	-2,657E+04	-3,480E+05	-2,821E+03	-3,695E+04
Pb	-7,950E+03	-1,041E+05	7,080E+04	9,275E+05	-3,061E+04	-4,010E+05
Pd	-8,038E+03	-1,053E+05	-3,480E+04	-4,559E+05	-1,472E+04	-1,928E+05
Pt	-8,031E+03	-1,052E+05	-1,451E+04	-1,900E+05	-1,288E+04	-1,687E+05
Re	-8,646E+03	-1,133E+05	8,539E+03	1,119E+05	-3,080E+02	-4,035E+03
Si	-8,183E+03	-1,072E+05	-2,419E+04	-3,168E+05	2,872E+03	3,763E+04
Sn	-8,023E+03	-1,051E+05	2,130E+03	2,790E+04	-4,089E+03	-5,357E+04
Ta	-8,332E+03	-1,091E+05	1,437E+03	1,883E+04	-5,278E+02	-6,914E+03
Ti	-8,219E+03	-1,077E+05	-1,304E+04	-1,708E+05	-2,110E+03	-2,765E+04
V	-8,421E+03	-1,103E+05	-9,970E+03	-1,306E+05	4,537E+03	5,943E+04
W	-8,499E+03	-1,113E+05	2,535E+03	3,321E+04	-1,412E+04	-1,849E+05
Y	-7,767E+03	-1,017E+05	-5,785E+02	-7,578E+03	-1,720E+03	-2,253E+04
Zn	-8,028E+03	-1,052E+05	-1,584E+04	-2,075E+05	-1,617E+02	-2,118E+03

Table B.20. Thermodynamic and structural data of $Zr_{75}Fe_{25}$ and $Zr_{0,75}Fe_{0,24}M_{0,01}$.

M	ΔH_{mixing} (J/mol)	S^{σ} (J/K.mol)	ΔS^{ideal} (J/K.mol)	ΔS_{mixing} (J/mol)	ΔG_{mixing} (J/mol)	R_c (J/s)	$\Delta\eta/\eta_o$	α_1
$Zr_{75}Fe_{25}$	-2,018E+04	1,790	4,676	6,466	-2,857E+04	6,225E+07	1,870	-0,333
Ag	-1,508E+04	1,727	5,025	6,752	-2,384E+04	8,680E+07	1,397	
Al	-2,160E+04	1,730	5,025	6,755	-3,037E+04	5,514E+07	2,001	
B	-2,529E+04	2,000	5,025	7,024	-3,440E+04	4,105E+07	2,343	
Ba	-1,556E+05	1,902	5,025	6,927	-1,646E+05	4,858E+03	14,418	
Bi	-1,609E+04	1,709	5,025	6,734	-2,483E+04	8,108E+07	1,491	
C	-2,337E+04	2,026	5,025	7,051	-3,252E+04	4,672E+07	2,165	
Ca	-3,989E+04	1,776	5,025	6,801	-4,872E+04	1,537E+07	3,696	
Cd	-1,958E+04	1,708	5,025	6,732	-2,832E+04	6,365E+07	1,814	
Co	-2,070E+04	1,786	5,025	6,811	-2,954E+04	5,822E+07	1,918	
Cr	-2,148E+04	1,787	5,025	6,812	-3,032E+04	5,513E+07	1,991	
Cu	-1,804E+04	1,776	5,025	6,801	-2,687E+04	7,013E+07	1,672	
Ga	-2,058E+04	1,740	5,025	6,765	-2,936E+04	5,908E+07	1,907	
Ge	-2,035E+04	1,791	5,025	6,815	-2,920E+04	5,961E+07	1,886	
Hf	-1,950E+04	1,707	5,025	6,731	-2,824E+04	6,401E+07	1,807	
K	-4,907E+04	2,026	5,025	7,050	-5,822E+04	7,832E+06	4,547	
La	-1,810E+04	1,739	5,025	6,763	-2,688E+04	7,022E+07	1,677	
Li	-2,087E+04	1,713	5,025	6,738	-2,962E+04	5,813E+07	1,934	
Mg	-2,162E+04	1,705	5,025	6,730	-3,035E+04	5,527E+07	2,003	
Mn	-1,977E+04	1,752	5,025	6,777	-2,856E+04	6,243E+07	1,831	
Mo	-2,035E+04	1,748	5,025	6,773	-2,914E+04	5,999E+07	1,885	
Na	-2,447E+04	1,732	5,025	6,757	-3,324E+04	4,514E+07	2,268	
Nb	-1,945E+04	1,731	5,025	6,755	-2,821E+04	6,403E+07	1,802	
Ni	-2,073E+04	1,788	5,025	6,813	-2,957E+04	5,809E+07	1,921	
P	-2,218E+04	1,871	5,025	6,896	-3,114E+04	5,187E+07	2,056	
Pb	-1,275E+04	1,710	5,025	6,735	-2,149E+04	1,023E+08	1,182	
Pd	-2,284E+04	1,745	5,025	6,769	-3,162E+04	5,049E+07	2,116	
Pt	-2,077E+04	1,741	5,025	6,766	-2,955E+04	5,833E+07	1,924	
Re	-1,956E+04	1,745	5,025	6,769	-2,834E+04	6,341E+07	1,812	
Si	-2,158E+04	1,827	5,025	6,852	-3,047E+04	5,444E+07	2,000	
Sn	-1,884E+04	1,704	5,025	6,729	-2,757E+04	6,705E+07	1,745	
Ta	-1,952E+04	1,730	5,025	6,755	-2,829E+04	6,370E+07	1,809	
Ti	-2,073E+04	1,724	5,025	6,748	-2,949E+04	5,864E+07	1,921	
V	-2,069E+04	1,763	5,025	6,788	-2,950E+04	5,844E+07	1,917	
W	-2,024E+04	1,747	5,025	6,772	-2,903E+04	6,047E+07	1,875	
Y	-1,842E+04	1,719	5,025	6,744	-2,718E+04	6,886E+07	1,707	
Zn	-2,049E+04	1,739	5,025	6,764	-2,927E+04	5,947E+07	1,899	

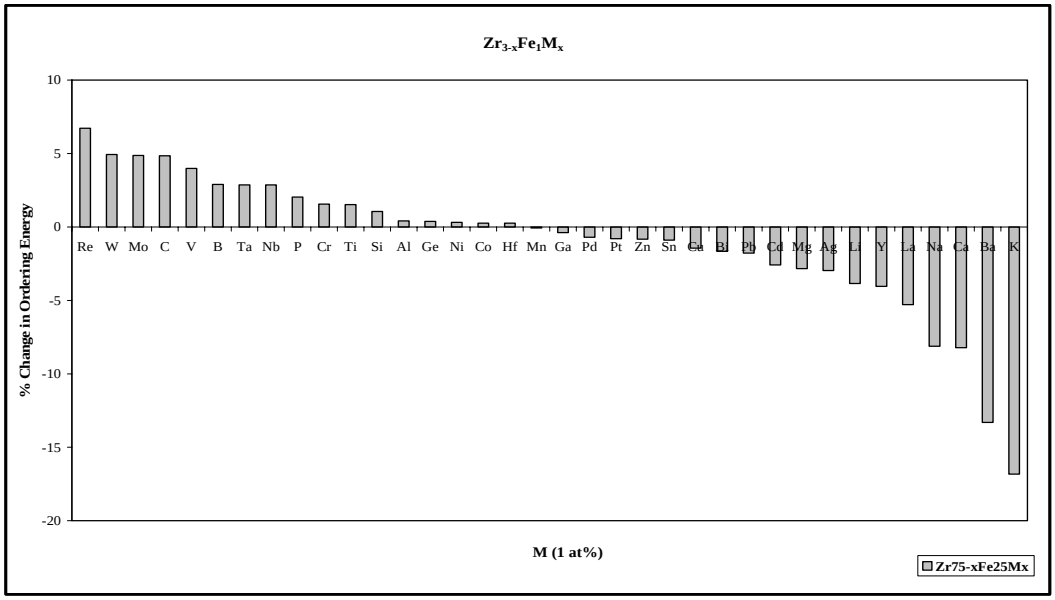

Figure B.25. % Change in ordering energy of $Zr_{75}Fe_{25}$ intermetallic for the addition of 1 at % impurity elements (M) when 1 at % is taken from Zr ($Zr_{0,74}Fe_{0,25}M_{0,01}$system).

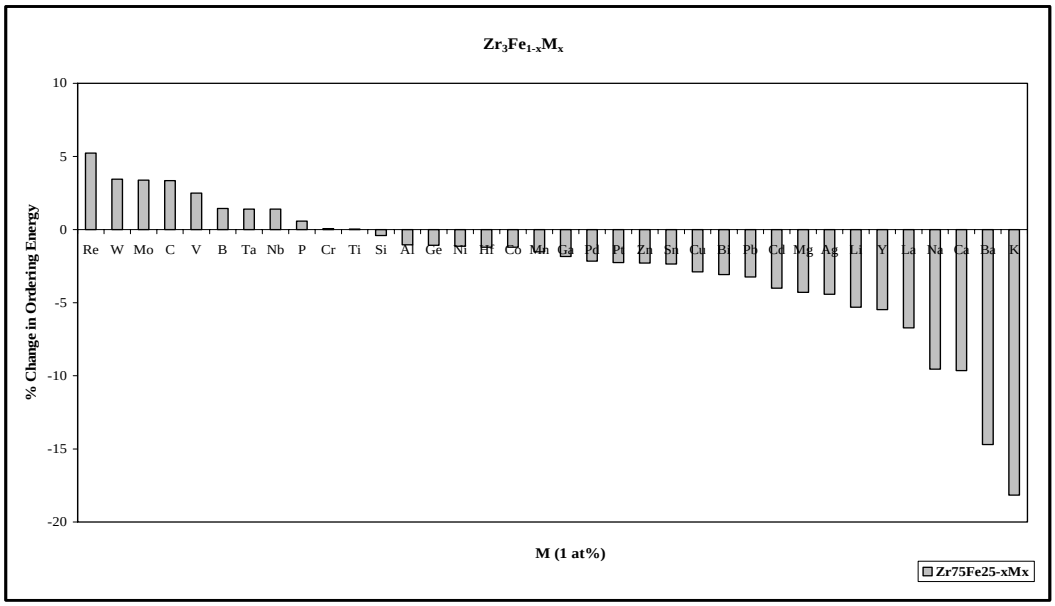

Figure B.26. % Change in ordering energy of $Zr_{75}Fe_{25}$ intermetallic system for the addition of 1 at % impurity elements (M) when 1 at % is taken from Fe ($Zr_{0,75}Fe_{0,24}M_{0,01}$system).

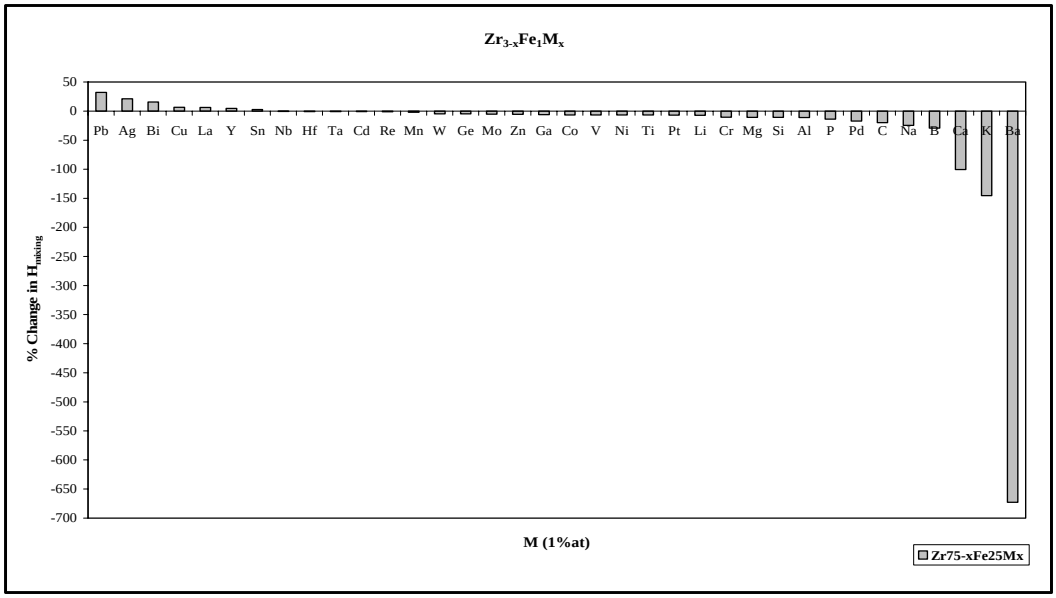

Figure B.27. % Change in ΔH_{mixing} of $Zr_{75}Fe_{25}$ intermetallic for the addition of 1 at % impurity elements (M) when 1 at % is taken from Zr ($Zr_{0,74}Fe_{0,25}M_{0,01}$system).

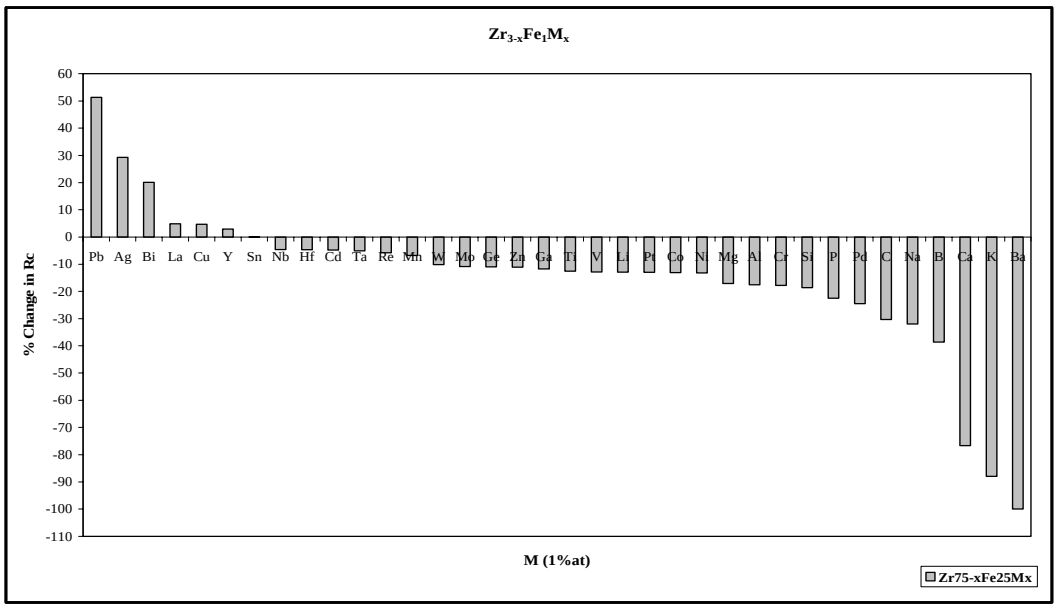

Figure B.28. % Change in R_c of $Zr_{75}Fe_{25}$ intermetallic for the addition of 1 at % impurity elements (M) when 1 at % is taken from Zr ($Zr_{0,74}Fe_{0,25}M_{0,01}$system).

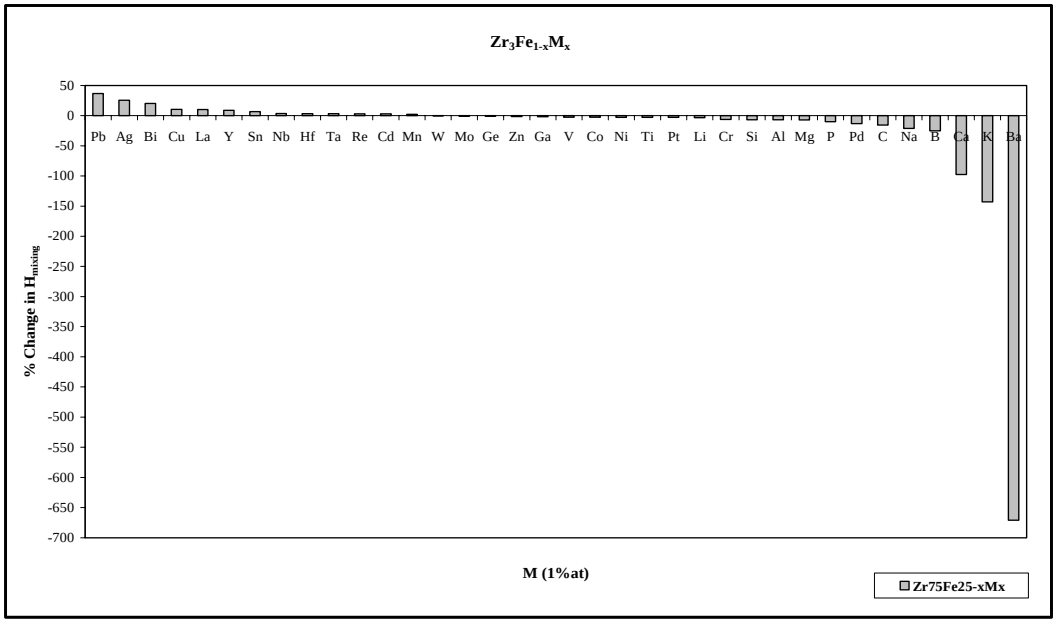

Figure B.29. % Change in ΔH_{mixing} of $Zr_{75}Fe_{25}$ binary system for the addition of 1 at % impurity elements (M) when 1 at % is taken from Fe ($Zr_{0,75}Fe_{0,24}M_{0,01}$system).

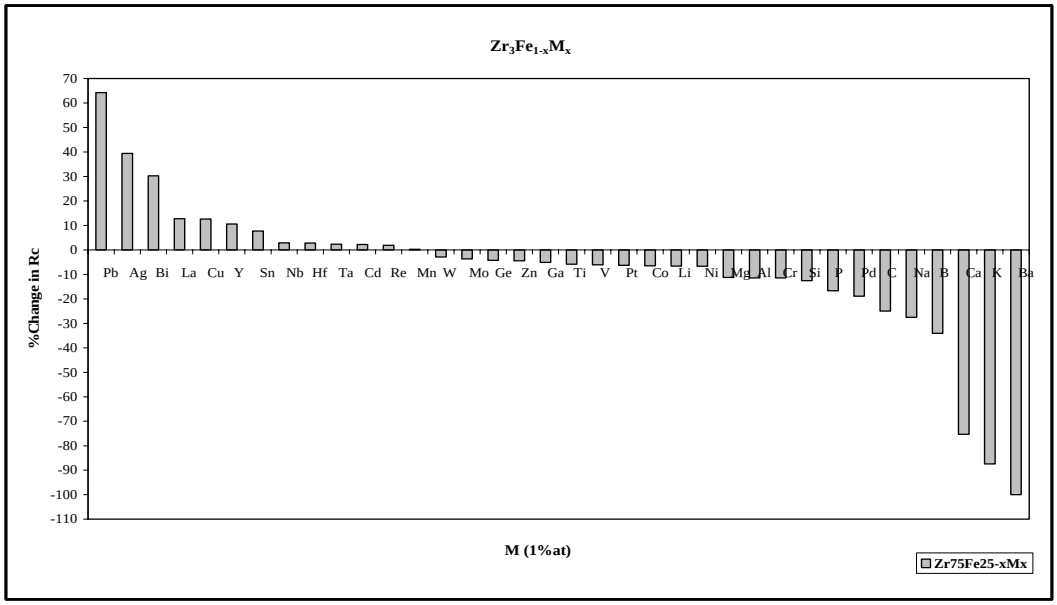

Figure B.30. % Change in R_c of $Zr_{75}Fe_{25}$ binary system for the addition of 1 at % impurity elements (M) when 1 at % is taken from Fe ($Zr_{0,75}Fe_{0,24}M_{0,01}$system).

Table B.21. The ordering energy values for $Zr_{75}Co_{25}$ and $Zr_{0,74}Co_{0,25}M_{0,01}$.

M	$W_{Zr\text{-}Co}$ (J/mol)	$w_{Zr\text{-}Co}$ (J/mol)	$W_{Zr\text{-}M}$ (J/mol)	$w_{Zr\text{-}M}$ (J/mol)	$W_{Co\text{-}M}$ (J/mol)	$W_{Co\text{-}M}$ (J/mol)
$Zr_{75}Co_{25}$	-1,905E+04	-5,906E+04				
Ag	-1,879E+04	-5,825E+04	3,508E+04	1,087E+05	-1,572E+03	-4,873E+03
Al	-1,909E+04	-5,917E+04	-2,940E+04	-9,115E+04	6,538E+03	2,027E+04
B	-1,927E+04	-5,974E+04	-8,949E+04	-2,774E+05	-3,302E+04	-1,024E+05
Ba	-1,811E+04	-5,614E+04	-1,152E+06	-3,571E+06	-9,454E+05	-2,931E+06
Bi	-1,896E+04	-5,877E+04	2,912E+04	9,026E+04	-7,208E+04	-2,234E+05
C	-1,943E+04	-6,023E+04	-5,209E+04	-1,615E+05	-6,624E+03	-2,054E+04
Ca	-1,846E+04	-5,723E+04	-1,152E+06	-3,571E+06	-1,174E+05	-3,638E+05
Cd	-1,884E+04	-5,839E+04	-1,958E+04	-6,069E+04	-1,009E+02	-3,128E+02
Cr	-1,916E+04	-5,939E+04	-1,810E+04	-5,610E+04	5,376E+02	1,667E+03
Cu	-1,891E+04	-5,862E+04	5,531E+03	1,715E+04	1,439E+03	4,460E+03
Fe	-1,914E+04	-5,933E+04	-7,862E+03	-2,437E+04	4,326E+02	1,341E+03
Ga	-1,903E+04	-5,899E+04	-2,570E+04	-7,968E+04	-1,286E+03	-3,986E+03
Ge	-1,910E+04	-5,922E+04	-1,677E+04	-5,199E+04	2,508E+03	7,775E+03
Hf	-1,907E+04	-5,912E+04	5,959E+02	1,847E+03	-2,363E+04	-7,325E+04
K	-1,789E+04	-5,545E+04	-2,710E+05	-8,400E+05	-1,405E+05	-4,356E+05
La	-1,866E+04	-5,783E+04	1,968E+03	6,100E+03	-1,758E+04	-5,449E+04
Li	-1,876E+04	-5,815E+04	-4,619E+04	-1,432E+05	2,339E+03	7,250E+03
Mg	-1,884E+04	-5,840E+04	-3,647E+04	-1,131E+05	3,749E+03	1,162E+04
Mn	-1,902E+04	-5,896E+04	-8,261E+03	-2,561E+04	-8,723E+02	-2,704E+03
Mo	-1,942E+04	-6,019E+04	1,904E+03	5,903E+03	-2,301E+04	-7,132E+04
Na	-1,847E+04	-5,724E+04	-7,238E+04	-2,244E+05	-1,467E+04	-4,549E+04
Nb	-1,927E+04	-5,973E+04	2,612E+03	8,099E+03	-7,788E+03	-2,414E+04
Ni	-1,906E+04	-5,908E+04	-1,914E+04	-5,934E+04	0	0
P	-1,924E+04	-5,964E+04	-3,733E+04	-1,157E+05	7,266E+03	2,252E+04
Pb	-1,893E+04	-5,867E+04	5,961E+04	1,848E+05	-5,338E+04	-1,655E+05
Pd	-1,898E+04	-5,883E+04	-1,264E+04	-3,918E+04	-1,800E+04	-5,581E+04
Pt	-1,897E+04	-5,882E+04	-4,090E+04	-1,268E+05	-1,515E+04	-4,696E+04
Re	-1,958E+04	-6,069E+04	1,077E+04	3,340E+04	-4,184E+03	-1,297E+04
Si	-1,915E+04	-5,938E+04	-2,920E+04	-9,052E+04	8,646E+03	2,680E+04
Sn	-1,900E+04	-5,889E+04	2,489E+03	7,714E+03	-8,501E+03	-2,635E+04
Ta	-1,927E+04	-5,973E+04	2,177E+03	6,750E+03	-6,945E+03	-2,153E+04
Ti	-1,916E+04	-5,941E+04	-2,162E+04	-6,702E+04	1,235E+03	3,827E+03
V	-1,936E+04	-6,000E+04	-8,342E+03	-2,586E+04	1,359E+04	4,214E+04
W	-1,943E+04	-6,024E+04	2,347E+03	7,277E+03	-2,573E+04	-7,976E+04
Y	-1,876E+04	-5,815E+04	-1,546E+03	-4,793E+03	-7,637E+03	-2,368E+04
Zn	-1,897E+04	-5,880E+04	-2,527E+04	-7,835E+04	-9,938E+02	-3,081E+03

Table B.22. Thermodynamic and structural data of $Zr_{75}Co_{25}$ and $Zr_{0,74}Co_{0,25}M_{0,01}$.

M	ΔH_{mixing} (J/mol)	S^{σ} (J/K.mol)	ΔS^{ideal} (J/K.mol)	ΔS_{mixing} (J/mol)	ΔG_{mixing} (J/mol)	R_c (J/s)	$\Delta\eta/\eta_o$	α_1
$Zr_{75}Co_{25}$	-1,107E+04	1,696	4,676	6,371	-1,966E+04	1,423E+08	0,988	-0,333
Ag	-9,983E+03	1,693	5,117	6,810	-1,916E+04	1,472E+08	0,891	
Al	-1,157E+04	1,696	5,117	6,813	-2,075E+04	1,323E+08	1,032	
B	-1,336E+04	1,962	5,117	7,079	-2,290E+04	1,129E+08	1,192	
Ba	-4,414E+04	1,865	5,117	6,982	-5,355E+04	1,461E+07	3,938	
Bi	-1,076E+04	1,675	5,117	6,792	-1,992E+04	1,401E+08	0,960	
C	-1,239E+04	1,989	5,117	7,106	-2,197E+04	1,201E+08	1,105	
Ca	-3,792E+04	1,741	5,117	6,858	-4,717E+04	2,254E+07	3,383	
Cd	-1,125E+04	1,673	5,117	6,790	-2,041E+04	1,356E+08	1,004	
Co	-1,140E+04	1,752	5,117	6,869	-2,066E+04	1,328E+08	1,017	
Cr	-1,071E+04	1,741	5,117	6,858	-1,995E+04	1,393E+08	0,955	
Cu	-1,115E+04	1,755	5,117	6,872	-2,042E+04	1,349E+08	0,995	
Fe	-1,151E+04	1,705	5,117	6,823	-2,071E+04	1,326E+08	1,027	
Ga	-1,132E+04	1,755	5,117	6,873	-2,058E+04	1,334E+08	1,010	
Ge	-1,111E+04	1,672	5,117	6,790	-2,026E+04	1,369E+08	0,991	
Hf	-1,756E+04	1,987	5,117	7,104	-2,714E+04	8,495E+07	1,567	
K	-1,079E+04	1,704	5,117	6,821	-1,999E+04	1,392E+08	0,963	
La	-1,180E+04	1,679	5,117	6,796	-2,096E+04	1,306E+08	1,053	
Li	-1,161E+04	1,671	5,117	6,788	-2,076E+04	1,324E+08	1,036	
Mg	-1,110E+04	1,717	5,117	6,834	-2,032E+04	1,361E+08	0,991	
Mn	-1,127E+04	1,714	5,117	6,831	-2,048E+04	1,347E+08	1,005	
Mo	-1,236E+04	1,698	5,117	6,815	-2,155E+04	1,254E+08	1,103	
Na	-1,105E+04	1,696	5,117	6,813	-2,024E+04	1,370E+08	0,986	
Nb	-1,137E+04	1,753	5,117	6,870	-2,063E+04	1,330E+08	1,014	
P	-1,183E+04	1,835	5,117	6,952	-2,120E+04	1,274E+08	1,056	
Pb	-9,900E+03	1,676	5,117	6,793	-1,906E+04	1,484E+08	0,883	
Pd	-1,131E+04	1,710	5,117	6,827	-2,052E+04	1,343E+08	1,009	
Pt	-1,194E+04	1,707	5,117	6,824	-2,114E+04	1,289E+08	1,065	
Re	-1,101E+04	1,710	5,117	6,827	-2,022E+04	1,370E+08	0,983	
Si	-1,159E+04	1,791	5,117	6,909	-2,090E+04	1,303E+08	1,034	
Sn	-1,090E+04	1,670	5,117	6,787	-2,005E+04	1,389E+08	0,973	
Ta	-1,105E+04	1,696	5,117	6,813	-2,024E+04	1,369E+08	0,986	
Ti	-1,148E+04	1,689	5,117	6,806	-2,065E+04	1,333E+08	1,024	
V	-1,119E+04	1,728	5,117	6,845	-2,041E+04	1,351E+08	0,998	
W	-1,129E+04	1,712	5,117	6,829	-2,050E+04	1,345E+08	1,007	
Y	-1,085E+04	1,684	5,117	6,802	-2,002E+04	1,390E+08	0,968	
Zn	-1,147E+04	1,705	5,117	6,822	-2,066E+04	1,331E+08	1,023	

Table B.23. The ordering energy values for $Zr_{75}Co_{25}$ and $Zr_{0,75}Co_{0,24}M_{0,01}$.

M	W_{Zr-Co} (J/mol)	w_{Zr-Co} (J/mol)	W_{Zr-M} (J/mol)	w_{Zr-M} (J/mol)	W_{Co-M} (J/mol)	W_{Co-M} (J/mol)
$Zr_{75}Co_{25}$	-1,905E+04	-5,906E+04				
Ag	-1,880E+04	-5,826E+04	3,505E+04	1,087E+05	-1,564E+03	-4,848E+03
Al	-1,909E+04	-5,917E+04	-2,940E+04	-9,113E+04	6,535E+03	2,026E+04
B	-1,927E+04	-5,975E+04	-8,953E+04	-2,776E+05	-3,301E+04	-1,023E+05
Ba	-1,812E+04	-5,617E+04	-1,151E+06	-3,569E+06	-9,452E+05	-2,930E+06
Bi	-1,896E+04	-5,879E+04	2,907E+04	9,013E+04	-7,207E+04	-2,234E+05
C	-1,943E+04	-6,023E+04	-5,211E+04	-1,615E+05	-6,624E+03	-2,054E+04
Ca	-1,847E+04	-5,726E+04	-2,221E+05	-6,884E+05	-1,174E+05	-3,639E+05
Cd	-1,884E+04	-5,841E+04	-1,959E+04	-6,074E+04	-9,828E+01	-3,047E+02
Cr	-1,916E+04	-5,939E+04	-1,808E+04	-5,606E+04	5,377E+02	1,667E+03
Cu	-1,892E+04	-5,864E+04	5,515E+03	1,710E+04	1,444E+03	4,476E+03
Fe	-1,914E+04	-5,934E+04	-7,860E+03	-2,436E+04	4,326E+02	1,341E+03
Ga	-1,903E+04	-5,900E+04	-2,572E+04	-7,972E+04	-1,281E+03	-3,970E+03
Ge	-1,911E+04	-5,923E+04	-1,677E+04	-5,200E+04	2,511E+03	7,784E+03
Hf	-1,907E+04	-5,913E+04	5,958E+02	1,847E+03	-2,363E+04	-7,324E+04
K	-1,790E+04	-5,549E+04	-2,709E+05	-8,397E+05	-1,405E+05	-4,355E+05
La	-1,866E+04	-5,785E+04	1,962E+03	6,084E+03	-1,757E+04	-5,446E+04
Li	-1,877E+04	-5,818E+04	-4,621E+04	-1,433E+05	2,341E+03	7,259E+03
Mg	-1,884E+04	-5,841E+04	-3,646E+04	-1,130E+05	3,744E+03	1,161E+04
Mn	-1,902E+04	-5,897E+04	-8,264E+03	-2,562E+04	-8,723E+02	-2,704E+03
Mo	-1,942E+04	-6,019E+04	1,904E+03	5,903E+03	-2,301E+04	-7,132E+04
Na	-1,847E+04	-5,727E+04	-7,236E+04	-2,243E+05	-1,467E+04	-4,549E+04
Nb	-1,927E+04	-5,974E+04	2,612E+03	8,099E+03	-7,798E+03	-2,418E+04
Ni	-1,906E+04	-5,908E+04	-1,914E+04	-5,935E+04	0	0
P	-1,924E+04	-5,965E+04	-3,733E+04	-1,157E+05	7,276E+03	2,256E+04
Pb	-1,893E+04	-5,869E+04	5,955E+04	1,846E+05	-5,338E+04	-1,655E+05
Pd	-1,898E+04	-5,885E+04	-1,259E+04	-3,903E+04	-1,800E+04	-5,579E+04
Pt	-1,898E+04	-5,883E+04	-4,094E+04	-1,269E+05	-1,513E+04	-4,692E+04
Re	-1,958E+04	-6,069E+04	1,078E+04	3,340E+04	-4,195E+03	-1,300E+04
Si	-1,916E+04	-5,939E+04	-2,919E+04	-9,050E+04	8,648E+03	2,681E+04
Sn	-1,900E+04	-5,890E+04	2,486E+03	7,706E+03	-8,504E+03	-2,636E+04
Ta	-1,927E+04	-5,974E+04	2,180E+03	6,758E+03	-6,950E+03	-2,155E+04
Ti	-1,917E+04	-5,942E+04	-2,162E+04	-6,703E+04	1,237E+03	3,836E+03
V	-1,936E+04	-6,000E+04	-8,326E+03	-2,581E+04	1,360E+04	4,215E+04
W	-1,943E+04	-6,025E+04	2,347E+03	7,277E+03	-2,574E+04	-7,979E+04
Y	-1,876E+04	-5,817E+04	-1,549E+03	-4,801E+03	-7,635E+03	-2,367E+04
Zn	-1,897E+04	-5,882E+04	-2,529E+04	-7,840E+04	-9,938E+02	-3,081E+03

Table B.24. Thermodynamic and structural data of $Zr_{75}Co_{25}$ and $Zr_{0,75}Co_{0,24}M_{0,01}$.

M	ΔH_{mixing} (J/mol)	S^{σ} (J/K.mol)	ΔS^{ideal} (J/K.mol)	ΔS_{mixing} (J/mol)	ΔG_{mixing} (J/mol)	R_c (J/s)	$\Delta\eta/\eta_o$	α_1
$Zr_{75}Co_{25}$	-1,107E+04	1,696	4,676	6,371	-1,966E+04	1,423E+08	0,988	-0,333
Ag	-9,684E+03	1,637	5,025	6,662	-1,866E+04	1,526E+08	0,864	
Al	-1,129E+04	1,640	5,025	6,665	-2,027E+04	1,371E+08	1,007	
B	-1,308E+04	1,908	5,025	6,933	-2,243E+04	1,169E+08	1,167	
Ba	-4,391E+04	1,814	5,025	6,838	-5,313E+04	1,506E+07	3,918	
Bi	-1,044E+04	1,620	5,025	6,644	-1,940E+04	1,455E+08	0,932	
C	-1,210E+04	1,935	5,025	6,959	-2,148E+04	1,244E+08	1,080	
Ca	-1,634E+04	1,688	5,025	6,712	-2,539E+04	9,706E+07	1,458	
Cd	-1,097E+04	1,618	5,025	6,642	-1,992E+04	1,405E+08	0,979	
Cr	-1,111E+04	1,697	5,025	6,721	-2,017E+04	1,376E+08	0,991	
Cu	-1,042E+04	1,686	5,025	6,710	-1,946E+04	1,443E+08	0,929	
Fe	-1,086E+04	1,700	5,025	6,724	-1,992E+04	1,398E+08	0,969	
Ga	-1,123E+04	1,650	5,025	6,675	-2,022E+04	1,374E+08	1,002	
Ge	-1,103E+04	1,700	5,025	6,725	-2,010E+04	1,382E+08	0,984	
Hf	-1,080E+04	1,617	5,025	6,642	-1,976E+04	1,420E+08	0,964	
K	-1,733E+04	1,938	5,025	6,962	-2,672E+04	8,762E+07	1,546	
La	-1,050E+04	1,650	5,025	6,675	-1,950E+04	1,443E+08	0,937	
Li	-1,153E+04	1,624	5,025	6,648	-2,049E+04	1,352E+08	1,029	
Mg	-1,133E+04	1,616	5,025	6,640	-2,028E+04	1,371E+08	1,011	
Mn	-1,081E+04	1,662	5,025	6,687	-1,983E+04	1,410E+08	0,965	
Mo	-1,096E+04	1,658	5,025	6,683	-1,997E+04	1,397E+08	0,978	
Na	-1,210E+04	1,643	5,025	6,668	-2,109E+04	1,298E+08	1,080	
Nb	-1,075E+04	1,641	5,025	6,665	-1,974E+04	1,421E+08	0,959	
Ni	-1,108E+04	1,698	5,025	6,722	-2,014E+04	1,378E+08	0,989	
P	-1,155E+04	1,780	5,025	6,805	-2,072E+04	1,320E+08	1,031	
Pb	-9,576E+03	1,621	5,025	6,646	-1,853E+04	1,541E+08	0,854	
Pd	-1,102E+04	1,654	5,025	6,679	-2,002E+04	1,393E+08	0,983	
Pt	-1,165E+04	1,651	5,025	6,676	-2,065E+04	1,335E+08	1,040	
Re	-1,071E+04	1,655	5,025	6,679	-1,971E+04	1,422E+08	0,955	
Si	-1,130E+04	1,736	5,025	6,761	-2,042E+04	1,350E+08	1,009	
Sn	-1,061E+04	1,615	5,025	6,639	-1,956E+04	1,440E+08	0,946	
Ta	-1,075E+04	1,640	5,025	6,665	-1,974E+04	1,420E+08	0,960	
Ti	-1,119E+04	1,634	5,025	6,658	-2,016E+04	1,381E+08	0,998	
V	-1,089E+04	1,673	5,025	6,697	-1,992E+04	1,401E+08	0,972	
W	-1,098E+04	1,657	5,025	6,681	-1,999E+04	1,396E+08	0,980	
Y	-1,056E+04	1,630	5,025	6,654	-1,953E+04	1,441E+08	0,942	
Zn	-1,118E+04	1,649	5,025	6,674	-2,018E+04	1,378E+08	0,998	

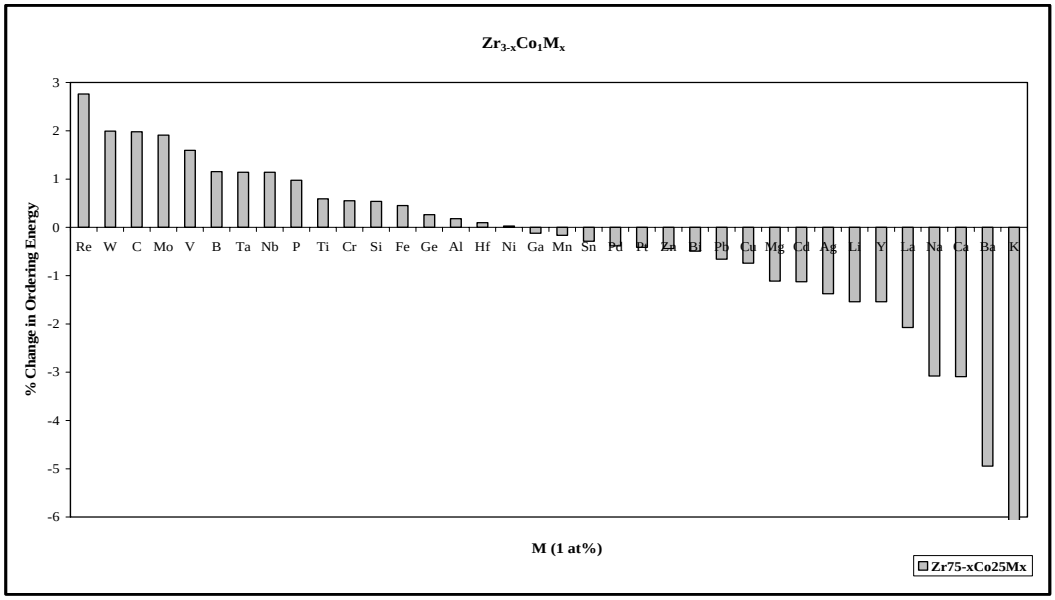

Figure B.31.% Change in ordering energy of $Zr_{75}Co_{25}$ binary system for the addition of 1 at % impurity elements (M) when 1 at % is taken from Zr ($Zr_{0,74}Co_{0,25}M_{0,01}$system).

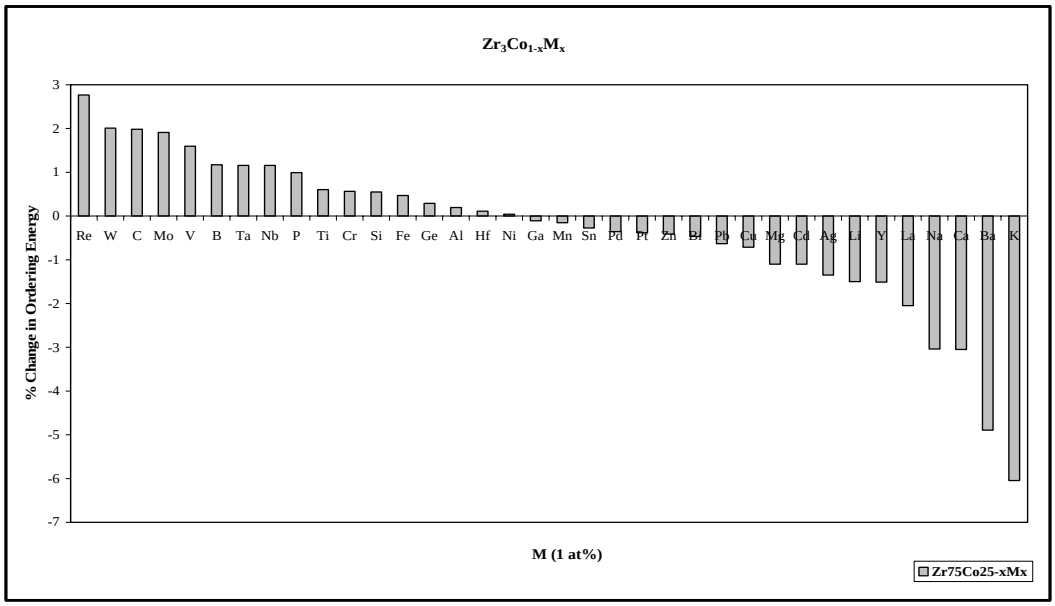

Figure B.32.% Change in ordering energy of $Zr_{75}Co_{25}$ binary system for the addition of 1 at % impurity elements (M) when 1 at % is taken from Co ($Zr_{0,75}Co_{0,24}M_{0,01}$system).

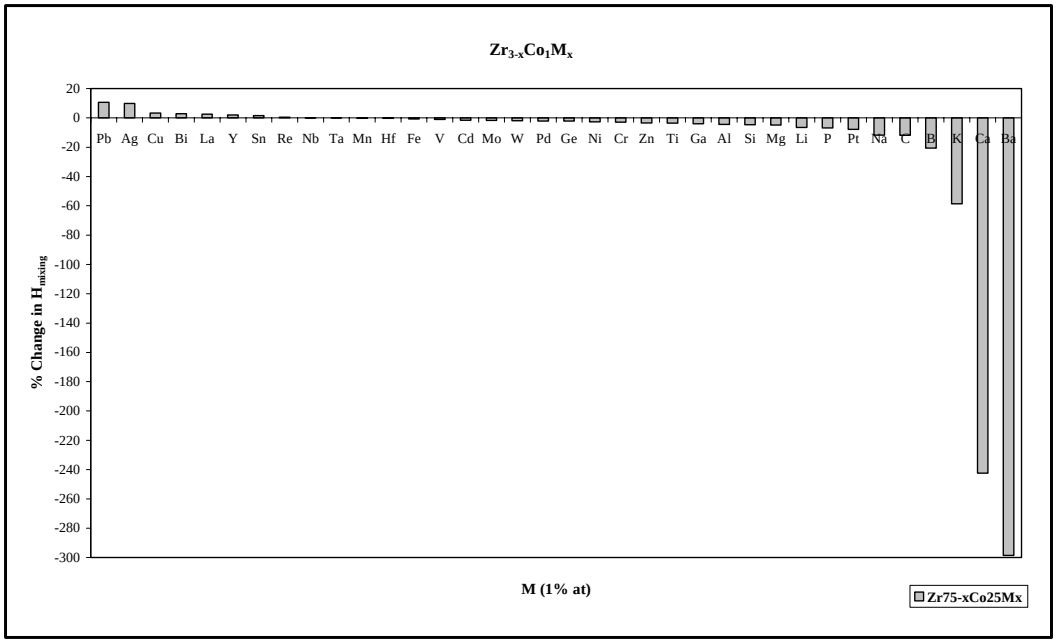

Figure B.33. % Change in ΔH_{mixing} of $Zr_{75}Co_{25}$ binary system for the addition of 1 at % impurity elements (M) when 1 at % is taken from Zr ($Zr_{0,74}Co_{0,25}M_{0,01}$system).

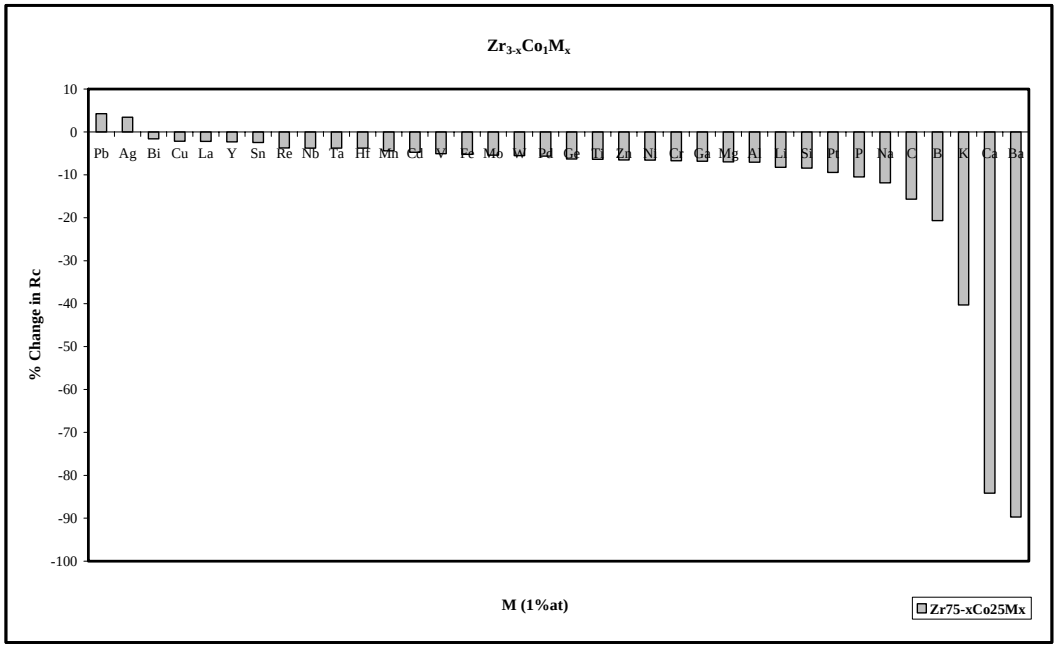

Figure B.34. % Change in R_c of $Zr_{75}Co_{25}$ binary system for the addition of 1 at % impurity elements (M) when 1 at % is taken from Zr ($Zr_{0,74}Co_{0,25}M_{0,01}$system).

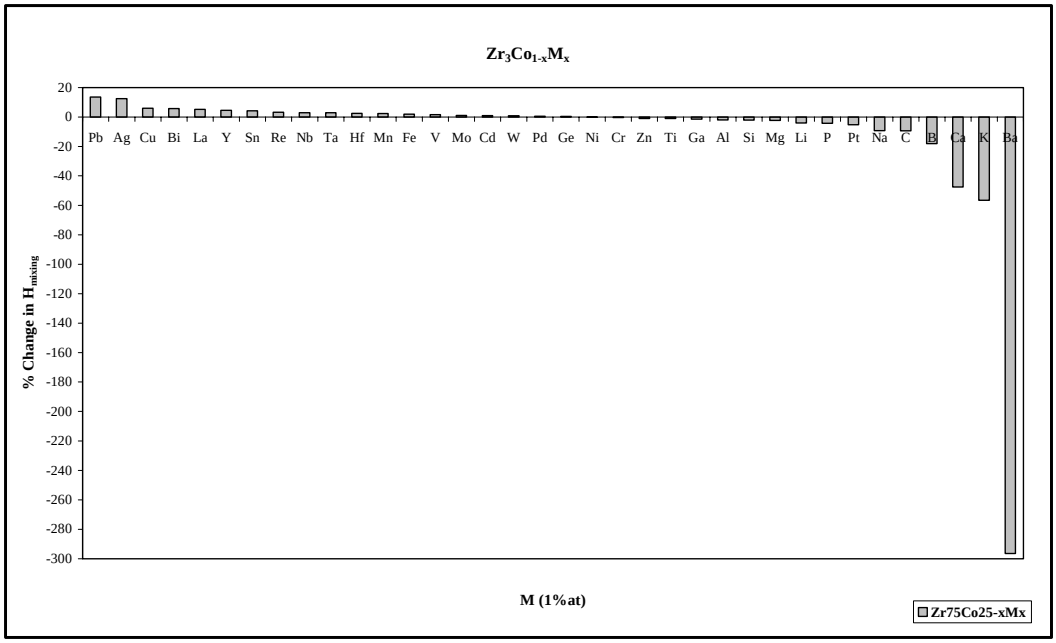

Figure B.35. % Change in ΔH_{mixing} of $Zr_{75}Co_{25}$ binary system for the addition of 1 at % impurity elements (M) when 1 at % is taken from Zr ($Zr_{0,75}Co_{0,24}M_{0,01}$system).

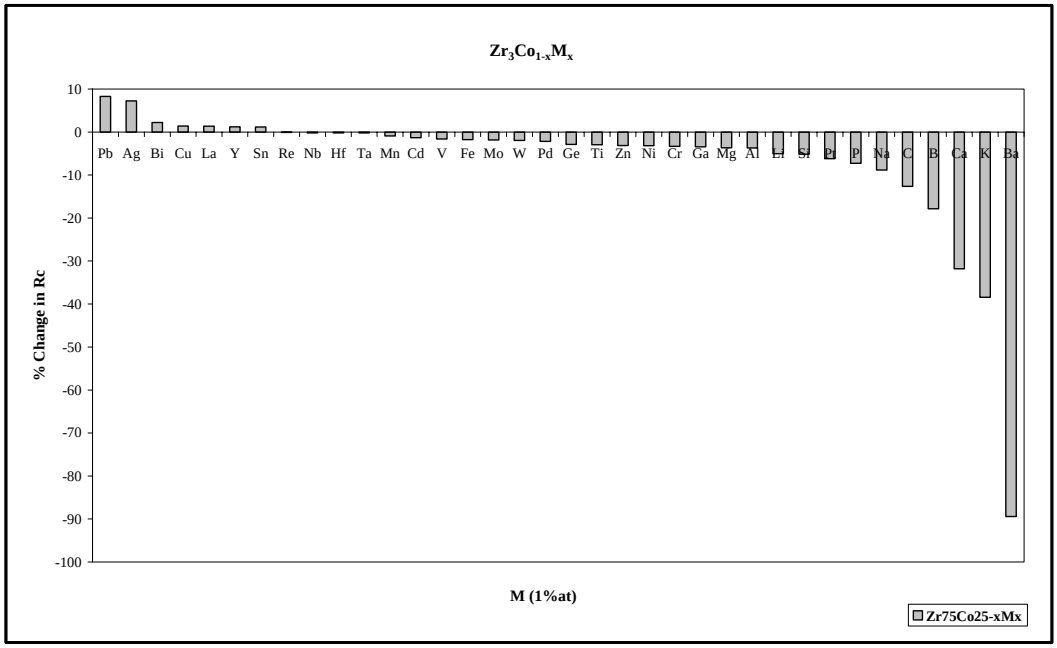

Figure B.36. % Change in R_c of $Zr_{75}Co_{25}$ binary system for the addition of 1 at % impurity elements (M) when 1 at % is taken from Zr ($Zr_{0,75}Co_{0,24}M_{0,01}$system).

Table B.25. The ordering energy values for $Zr_{60}Al_{40}$ and $Zr_{0,59}Al_{0,40}M_{0,01}$.

M	W_{Zr-Al} (J/mol)	w_{Zr-Al} (J/mol)	W_{Zr-M} (J/mol)	w_{Zr-M} (J/mol)	W_{Al-M} (J/mol)	w_{Al-M} (J/mol)
$Zr_{60}Al_{40}$	-1,695E+04	-1,524E+05				
Ag	-1,695E+04	-1,524E+05	1,640E+04	1,475E+05	1,221E+04	1,097E+05
B	-1,696E+04	-1,524E+05	-5,767E+04	-5,185E+05	-2,024E+04	-1,819E+05
Ba	-1,683E+04	-1,513E+05	-5,635E+05	-5,066E+06	-5,178E+05	-4,655E+06
Bi	-1,685E+04	-1,515E+05	1,163E+04	1,046E+05	-2,976E+04	-2,675E+05
C	-1,692E+04	-1,521E+05	-3,441E+04	-3,094E+05	-4,595E+03	-4,131E+04
Ca	-1,680E+04	-1,510E+05	-1,157E+05	-1,040E+06	-8,642E+04	-7,769E+05
Cd	-1,664E+04	-1,496E+05	-1,374E+04	-1,235E+05	2,187E+03	1,966E+04
Co	-1,632E+04	-1,467E+05	-1,277E+04	-1,148E+05	3,455E+03	3,106E+04
Cr	-1,645E+04	-1,479E+05	-1,077E+04	-9,686E+04	2,620E+03	2,355E+04
Cu	-1,693E+04	-1,522E+05	3,388E+02	3,045E+03	8,902E+03	8,003E+04
Fe	-1,688E+04	-1,518E+05	-5,774E+03	-5,190E+04	2,783E+03	2,502E+04
Ga	-1,703E+04	-1,531E+05	-1,667E+04	-1,499E+05	-1,325E+03	-1,191E+04
Ge	-1,721E+04	-1,548E+05	-1,068E+04	-9,599E+04	-8,568E+02	-7,703E+03
Hf	-1,714E+04	-1,540E+05	1,983E+02	1,783E+03	-1,653E+04	-1,486E+05
K	-1,701E+04	-1,529E+05	-1,264E+05	-1,137E+06	-7,729E+04	-6,949E+05
La	-1,701E+04	-1,529E+05	4,508E+02	4,052E+03	-9,023E+03	-8,112E+04
Li	-1,714E+04	-1,541E+05	-3,051E+04	-2,743E+05	1,354E+03	1,217E+04
Mg	-1,694E+04	-1,523E+05	-2,078E+04	-1,868E+05	-5,015E+02	-4,509E+03
Mn	-1,696E+04	-1,525E+05	-6,388E+03	-5,743E+04	3,799E+03	3,415E+04
Mo	-1,706E+04	-1,534E+05	7,340E+02	6,599E+03	-2,501E+04	-2,248E+05
Na	-1,706E+04	-1,534E+05	-3,904E+04	-3,510E+05	-9,326E+03	-8,384E+04
Nb	-1,689E+04	-1,518E+05	1,429E+03	1,285E+04	-1,606E+04	-1,444E+05
Ni	-1,699E+04	-1,527E+05	-1,284E+04	-1,154E+05	3,488E+03	3,135E+04
P	-1,691E+04	-1,521E+05	-2,220E+04	-1,996E+05	-2,745E+03	-2,468E+04
Pb	-1,710E+04	-1,538E+05	2,745E+04	2,468E+05	-1,329E+04	-1,194E+05
Pd	-1,714E+04	-1,541E+05	-3,722E+03	-3,346E+04	-1,827E+03	-1,643E+04
Pt	-1,696E+04	-1,525E+05	-2,858E+04	-2,570E+05	-5,603E+03	-5,037E+04
Re	-1,696E+04	-1,525E+05	5,515E+03	4,958E+04	-1,910E+04	-1,717E+05
Si	-1,664E+04	-1,496E+05	-1,701E+04	-1,529E+05	-3,708E+02	-3,334E+03
Sn	-1,689E+04	-1,518E+05	7,083E+02	6,367E+03	-5,117E+03	-4,600E+04
Ta	-1,706E+04	-1,534E+05	1,247E+03	1,121E+04	-1,495E+04	-1,344E+05
Ti	-1,684E+04	-1,514E+05	-1,439E+04	-1,294E+05	-7,672E+02	-6,897E+03
V	-1,692E+04	-1,521E+05	-5,753E+03	-5,172E+04	5,220E+03	4,693E+04
W	-1,700E+04	-1,529E+05	8,376E+02	7,530E+03	-2,648E+04	-2,381E+05
Y	-1,680E+04	-1,510E+05	-1,210E+03	-1,088E+04	-7,139E+03	-6,418E+04
Zn	-1,692E+04	-1,521E+05	-1,730E+04	-1,555E+05	1,788E+03	1,607E+04

Table B.26. Thermodynamic and structural data of $Zr_{60}Al_{40}$ and $Zr_{0,59}Al_{0,40}M_{0,01}$.

M	ΔH_{mixing} (J/mol)	S^{σ} (J/K.mol)	ΔS^{ideal} (J/K.mol)	ΔS_{mixing} (J/mol)	ΔG_{mixing} (J/mol)	R_c (J/s)	$\Delta\eta/\eta_o$	α_1
$Zr_{60}Al_{40}$	-3,657E+04	0,542	5,596	6,137	-4,745E+04	9,239E+07	2,481	-0,667
Ag	-3,465E+04	0,546	6,019	6,564	-4,629E+04	9,799E+07	2,351	
B	-3,976E+04	0,744	6,019	6,762	-5,175E+04	7,343E+07	2,697	
Ba	-8,422E+04	0,690	6,019	6,709	-9,612E+04	7,707E+06	5,713	
Bi	-3,620E+04	0,534	6,019	6,553	-4,782E+04	9,072E+07	2,456	
C	-3,788E+04	0,764	6,019	6,782	-4,990E+04	8,058E+07	2,570	
Ca	-4,488E+04	0,592	6,019	6,610	-5,660E+04	5,784E+07	3,045	
Cd	-3,595E+04	0,533	6,019	6,551	-4,757E+04	9,189E+07	2,439	
Co	-3,518E+04	0,588	6,019	6,606	-4,690E+04	9,480E+07	2,387	
Cr	-3,538E+04	0,588	6,019	6,607	-4,709E+04	9,385E+07	2,400	
Cu	-3,559E+04	0,580	6,019	6,599	-4,729E+04	9,296E+07	2,414	
Fe	-3,602E+04	0,590	6,019	6,609	-4,774E+04	9,080E+07	2,444	
Ga	-3,706E+04	0,555	6,019	6,573	-4,872E+04	8,657E+07	2,514	
Ge	-3,712E+04	0,591	6,019	6,609	-4,884E+04	8,588E+07	2,518	
Hf	-3,694E+04	0,532	6,019	6,551	-4,855E+04	8,740E+07	2,506	
K	-4,557E+04	0,786	6,019	6,805	-5,763E+04	5,431E+07	3,091	
La	-3,638E+04	0,562	6,019	6,580	-4,805E+04	8,952E+07	2,468	
Li	-3,794E+04	0,536	6,019	6,555	-4,956E+04	8,303E+07	2,573	
Mg	-3,707E+04	0,532	6,019	6,550	-4,868E+04	8,684E+07	2,514	
Mn	-3,618E+04	0,563	6,019	6,582	-4,785E+04	9,042E+07	2,454	
Mo	-3,706E+04	0,560	6,019	6,579	-4,872E+04	8,652E+07	2,514	
Na	-3,860E+04	0,556	6,019	6,575	-5,026E+04	8,002E+07	2,619	
Nb	-3,633E+04	0,548	6,019	6,567	-4,798E+04	8,992E+07	2,465	
Ni	-3,660E+04	0,589	6,019	6,608	-4,832E+04	8,818E+07	2,483	
P	-3,716E+04	0,649	6,019	6,668	-4,898E+04	8,497E+07	2,521	
Pb	-3,531E+04	0,538	6,019	6,557	-4,693E+04	9,487E+07	2,395	
Pd	-3,663E+04	0,558	6,019	6,577	-4,829E+04	8,843E+07	2,485	
Pt	-3,770E+04	0,556	6,019	6,574	-4,936E+04	8,379E+07	2,557	
Re	-3,639E+04	0,558	6,019	6,577	-4,805E+04	8,956E+07	2,468	
Si	-3,622E+04	0,617	6,019	6,636	-4,798E+04	8,957E+07	2,457	
Sn	-3,598E+04	0,531	6,019	6,550	-4,759E+04	9,178E+07	2,441	
Ta	-3,666E+04	0,548	6,019	6,567	-4,831E+04	8,842E+07	2,487	
Ti	-3,652E+04	0,543	6,019	6,562	-4,815E+04	8,916E+07	2,477	
V	-3,601E+04	0,571	6,019	6,590	-4,769E+04	9,113E+07	2,442	
W	-3,698E+04	0,560	6,019	6,578	-4,865E+04	8,685E+07	2,509	
Y	-3,595E+04	0,545	6,019	6,564	-4,759E+04	9,171E+07	2,439	
Zn	-3,675E+04	0,554	6,019	6,573	-4,840E+04	8,796E+07	2,493	

Table B.27. The ordering energy values for $Zr_{60}Al_{39}$ and $Zr_{0,60}Al_{0,39}M_{0,01}$.

M	W_{Zr-Al} (J/mol)	w_{Zr-Al} (J/mol)	W_{Zr-M} (J/mol)	w_{Zr-M} (J/mol)	W_{Al-M} (J/mol)	w_{Al-M} (J/mol)
$Zr_{60}Al_{40}$	-1,695E+04	-1,524E+05				
Ag	-1,682E+04	-1,512E+05	1,641E+04	1,475E+05	1,221E+04	1,098E+05
B	-1,704E+04	-1,532E+05	-5,769E+04	-5,187E+05	-2,025E+04	-1,821E+05
Ba	-1,644E+04	-1,478E+05	-5,631E+05	-5,062E+06	-5,176E+05	-4,653E+06
Bi	-1,688E+04	-1,517E+05	1,160E+04	1,043E+05	-2,975E+04	-2,675E+05
C	-1,712E+04	-1,539E+05	-3,442E+04	-3,094E+05	-4,611E+03	-4,145E+04
Ca	-1,663E+04	-1,495E+05	-1,156E+05	-1,039E+06	-8,641E+04	-7,769E+05
Cd	-1,684E+04	-1,514E+05	-1,374E+04	-1,235E+05	2,187E+03	1,966E+04
Co	-1,694E+04	-1,523E+05	-1,275E+04	-1,146E+05	3,456E+03	3,107E+04
Cr	-1,699E+04	-1,528E+05	-1,075E+04	-9,666E+04	2,621E+03	2,356E+04
Cu	-1,687E+04	-1,517E+05	3,532E+02	3,175E+03	8,906E+03	8,007E+04
Fe	-1,699E+04	-1,527E+05	-5,762E+03	-5,180E+04	2,782E+03	2,501E+04
Ga	-1,692E+04	-1,521E+05	-1,667E+04	-1,499E+05	-1,325E+03	-1,191E+04
Ge	-1,695E+04	-1,524E+05	-1,068E+04	-9,597E+04	-8,582E+02	-7,715E+03
Hf	-1,695E+04	-1,523E+05	1,982E+02	1,782E+03	-1,651E+04	-1,485E+05
K	-1,631E+04	-1,466E+05	-1,263E+05	-1,135E+06	-7,726E+04	-6,946E+05
La	-1,673E+04	-1,504E+05	4,494E+02	4,041E+03	-9,012E+03	-8,102E+04
Li	-1,678E+04	-1,509E+05	-3,051E+04	-2,742E+05	1,357E+03	1,220E+04
Mg	-1,683E+04	-1,513E+05	-2,076E+04	-1,866E+05	-5,015E+02	-4,509E+03
Mn	-1,693E+04	-1,522E+05	1,247E+03	1,121E+04	3,799E+03	3,415E+04
Mo	-1,713E+04	-1,540E+05	7,381E+02	6,635E+03	-2,497E+04	-2,245E+05
Na	-1,663E+04	-1,495E+05	-3,899E+04	-3,505E+05	-9,320E+03	-8,379E+04
Nb	-1,705E+04	-1,533E+05	1,431E+03	1,286E+04	-1,604E+04	-1,442E+05
Ni	-1,694E+04	-1,523E+05	-1,282E+04	-1,153E+05	3,488E+03	3,135E+04
P	-1,702E+04	-1,530E+05	-2,220E+04	-1,996E+05	-2,745E+03	-2,468E+04
Pb	-1,687E+04	-1,516E+05	2,741E+04	2,464E+05	-1,329E+04	-1,195E+05
Pd	-1,690E+04	-1,520E+05	-3,664E+03	-3,294E+04	-1,811E+03	-1,628E+04
Pt	-1,690E+04	-1,520E+05	-2,860E+04	-2,571E+05	-5,603E+03	-5,037E+04
Re	-1,720E+04	-1,546E+05	5,523E+03	4,965E+04	-1,907E+04	-1,714E+05
Si	-1,698E+04	-1,526E+05	-1,701E+04	-1,529E+05	-3,695E+02	-3,322E+03
Sn	-1,690E+04	-1,520E+05	7,093E+02	6,377E+03	-5,116E+03	-4,599E+04
Ta	-1,705E+04	-1,533E+05	1,247E+03	1,121E+04	-1,493E+04	-1,342E+05
Ti	-1,699E+04	-1,528E+05	-1,440E+04	-1,294E+05	-7,723E+02	-6,943E+03
V	-1,709E+04	-1,536E+05	-5,744E+03	-5,164E+04	5,216E+03	4,689E+04
W	-1,713E+04	-1,540E+05	8,416E+02	7,566E+03	-2,645E+04	-2,378E+05
Y	-1,678E+04	-1,509E+05	-1,209E+03	-1,086E+04	-7,129E+03	-6,409E+04
Zn	-1,690E+04	-1,519E+05	-1,729E+04	-1,554E+05	1,786E+03	1,606E+04

Table B.28. Thermodynamic and structural data of $Zr_{60}Al_{40}$ and $Zr_{0,60}Al_{0,39}M_{0,01}$.

M	ΔH_{mixing} (J/mol)	S^{σ} (J/K.mol)	ΔS^{ideal} (J/K.mol)	ΔS_{mixing} (J/mol)	ΔG_{mixing} (J/mol)	R_c (J/s)	$\Delta\eta/\eta_o$	α_1
$Zr_{60}Al_{40}$	-3,657E+04	0,542	5,596	6,137	-4,745E+04	9,239E+07	2,481	-0,667
Ag	-3,407E+04	0,539	5,985	6,524	-4,563E+04	1,014E+08	2,311	
B	-3,968E+04	0,741	5,985	6,725	-5,160E+04	7,400E+07	2,692	
Ba	-8,310E+04	0,687	5,985	6,672	-9,493E+04	8,188E+06	5,637	
Bi	-3,592E+04	0,528	5,985	6,512	-4,747E+04	9,239E+07	2,437	
C	-3,803E+04	0,761	5,985	6,745	-4,999E+04	8,022E+07	2,580	
Ca	-4,424E+04	0,587	5,985	6,572	-5,589E+04	6,000E+07	3,001	
Cd	-3,608E+04	0,527	5,985	6,511	-4,762E+04	9,165E+07	2,448	
Co	-3,621E+04	0,582	5,985	6,567	-4,785E+04	9,035E+07	2,456	
Cr	-3,623E+04	0,582	5,985	6,567	-4,788E+04	9,021E+07	2,458	
Cu	-3,517E+04	0,575	5,985	6,559	-4,680E+04	9,535E+07	2,386	
Fe	-3,595E+04	0,585	5,985	6,569	-4,760E+04	9,147E+07	2,439	
Ga	-3,654E+04	0,549	5,985	6,533	-4,812E+04	8,926E+07	2,479	
Ge	-3,626E+04	0,585	5,985	6,570	-4,791E+04	9,004E+07	2,460	
Hf	-3,622E+04	0,526	5,985	6,511	-4,776E+04	9,103E+07	2,457	
K	-4,383E+04	0,785	5,985	6,770	-5,584E+04	5,951E+07	2,973	
La	-3,550E+04	0,556	5,985	6,541	-4,709E+04	9,401E+07	2,408	
Li	-3,691E+04	0,530	5,985	6,515	-4,846E+04	8,783E+07	2,504	
Mg	-3,653E+04	0,525	5,985	6,510	-4,807E+04	8,959E+07	2,478	
Mn	-3,541E+04	0,557	5,985	6,542	-4,701E+04	9,440E+07	2,402	
Mo	-3,686E+04	0,554	5,985	6,539	-4,846E+04	8,772E+07	2,501	
Na	-3,741E+04	0,551	5,985	6,535	-4,899E+04	8,537E+07	2,537	
Nb	-3,635E+04	0,542	5,985	6,527	-4,792E+04	9,022E+07	2,466	
Ni	-3,621E+04	0,583	5,985	6,568	-4,786E+04	9,029E+07	2,457	
P	-3,709E+04	0,644	5,985	6,629	-4,884E+04	8,560E+07	2,516	
Pb	-3,447E+04	0,532	5,985	6,517	-4,603E+04	9,939E+07	2,338	
Pd	-3,582E+04	0,552	5,985	6,536	-4,741E+04	9,252E+07	2,430	
Pt	-3,730E+04	0,550	5,985	6,534	-4,888E+04	8,587E+07	2,530	
Re	-3,655E+04	0,552	5,985	6,536	-4,814E+04	8,915E+07	2,479	
Si	-3,664E+04	0,612	5,985	6,596	-4,834E+04	8,797E+07	2,486	
Sn	-3,570E+04	0,525	5,985	6,510	-4,724E+04	9,348E+07	2,422	
Ta	-3,632E+04	0,542	5,985	6,526	-4,789E+04	9,035E+07	2,464	
Ti	-3,655E+04	0,537	5,985	6,522	-4,812E+04	8,934E+07	2,480	
V	-3,608E+04	0,565	5,985	6,550	-4,769E+04	9,116E+07	2,447	
W	-3,691E+04	0,554	5,985	6,538	-4,851E+04	8,750E+07	2,504	
Y	-3,562E+04	0,540	5,985	6,524	-4,719E+04	9,366E+07	2,416	
Zn	-3,642E+04	0,548	5,985	6,533	-4,801E+04	8,979E+07	2,471	

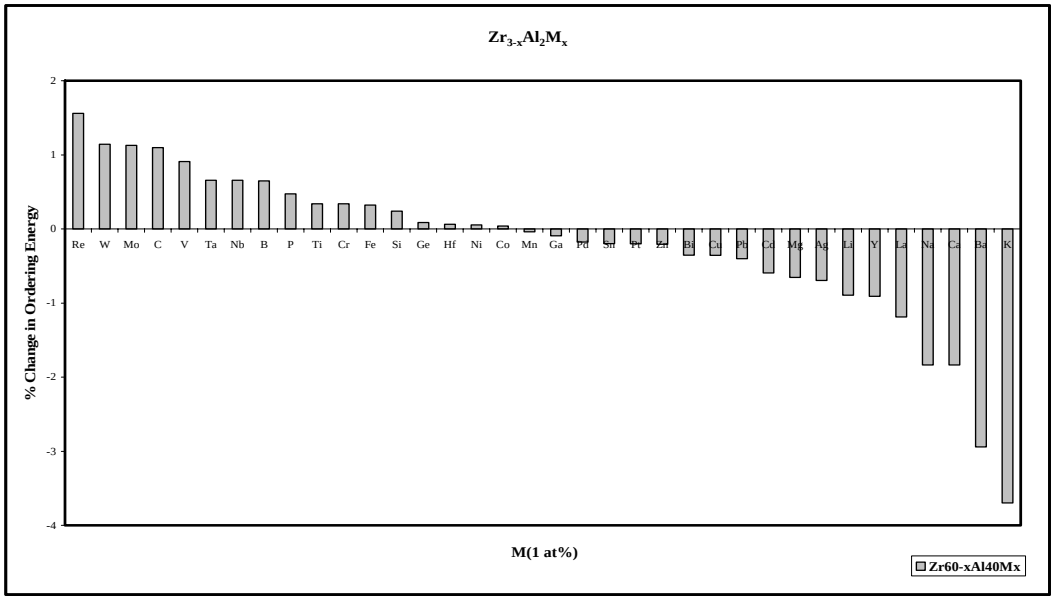

Figure B.37.% Change in ordering energy of $Zr_{60}Al_{40}$ binary system for the addition of 1 at % impurity elements (M) when 1 at % is taken from Zr ($Zr_{0,59}Al_{0,40}M_{0,01}$system).

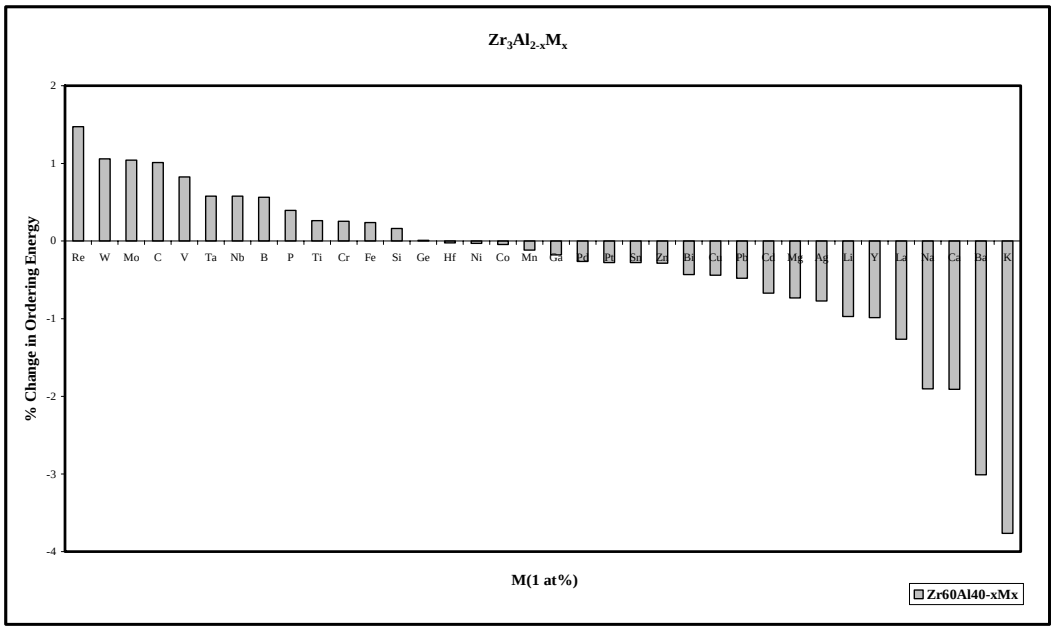

Figure B.38.% Change in ordering energy of $Zr_{60}Al_{40}$ binary system for the addition of 1 at % impurity elements (M) when 1 at % is taken from Al ($Zr_{0,60}Al_{0,39}M_{0,01}$system).

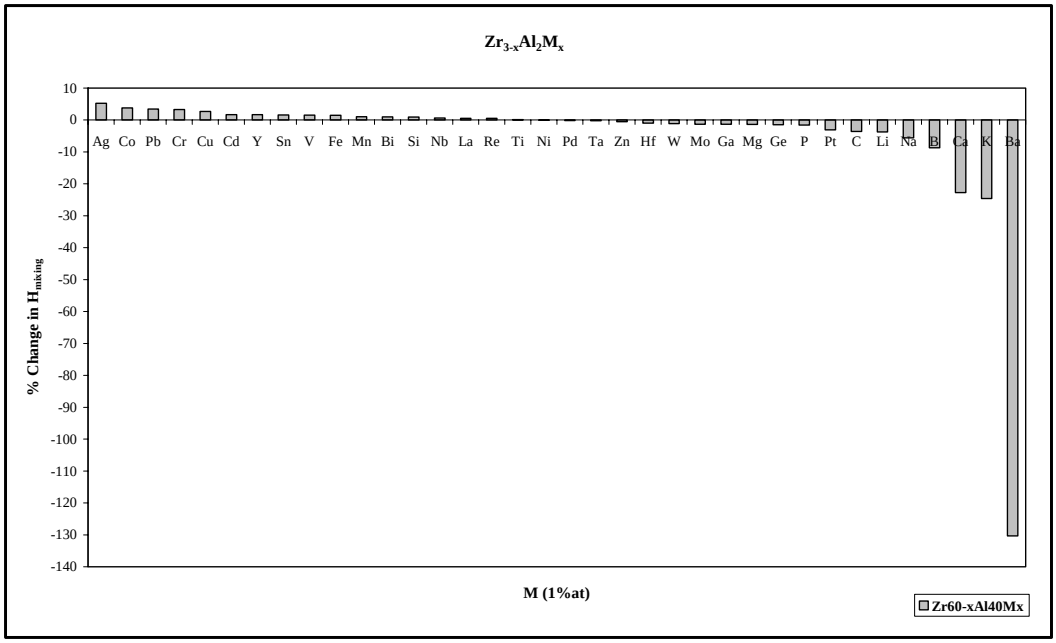

Figure B.39. % Change in ΔH_{mixing} of $Zr_{60}Al_{40}$ binary system for the addition of 1 at % impurity elements (M) when 1 at % is taken from Zr ($Zr_{0,59}Al_{0,40}M_{0,01}$system).

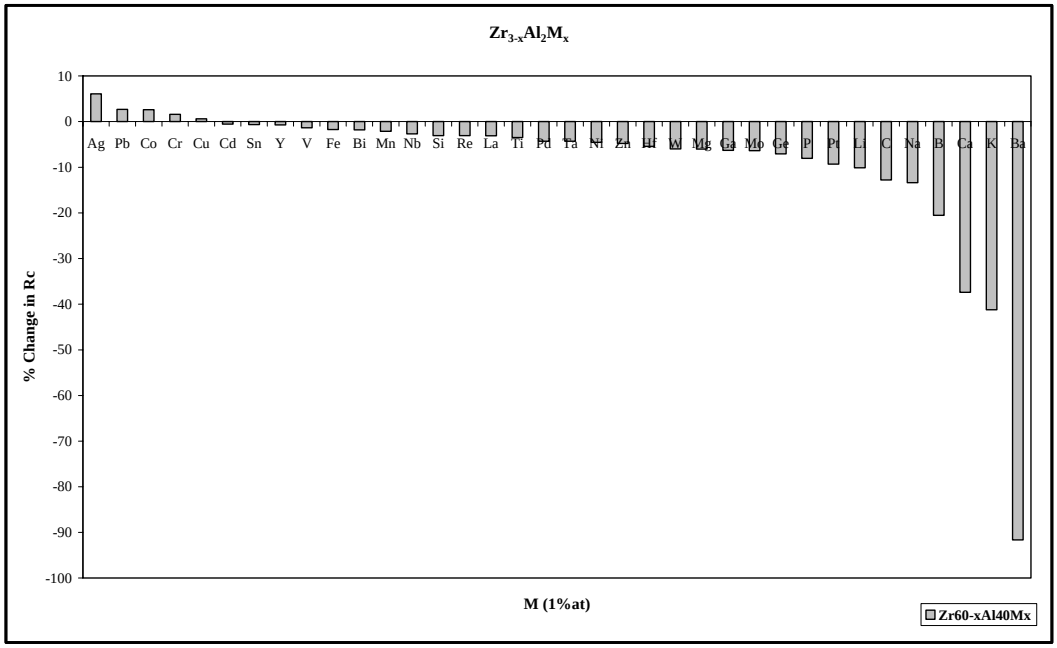

Figure B.40. % Change in R_c of $Zr_{60}Al_{40}$binary system for the addition of 1 at % impurity elements (M) when 1 at % is taken from Zr ($Zr_{0,59}Al_{0,40}M_{0,01}$system).

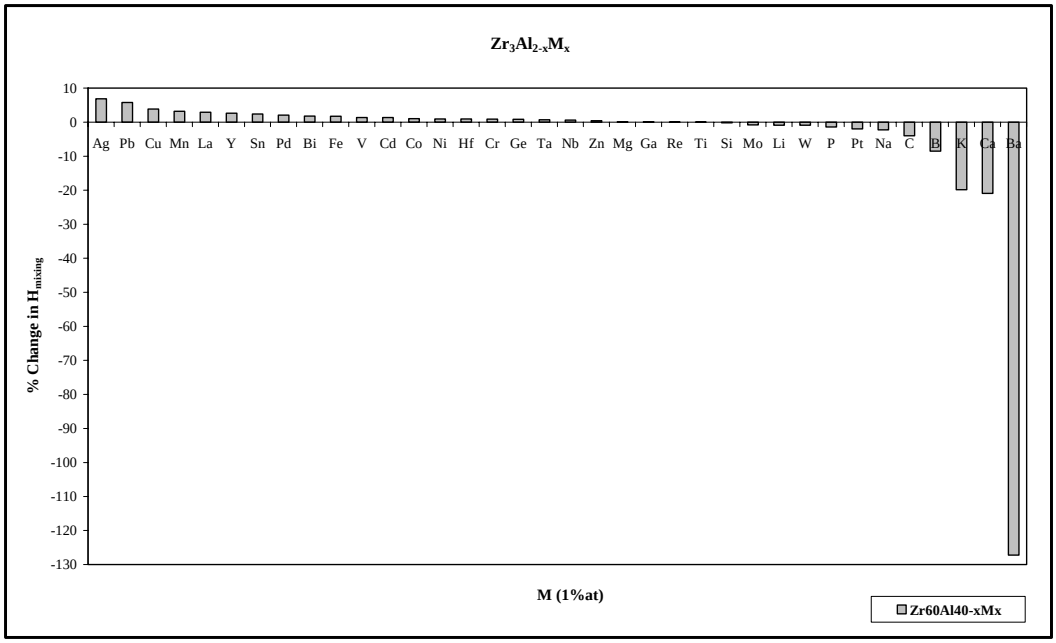

Figure B.41. % Change in ΔH_{mixing} of $Zr_{60}Al_{40}$ binary system for the addition of 1 at % impurity elements (M) when 1 at % is taken from Al ($Zr_{0,60}Al_{0,39}M_{0,01}$system).

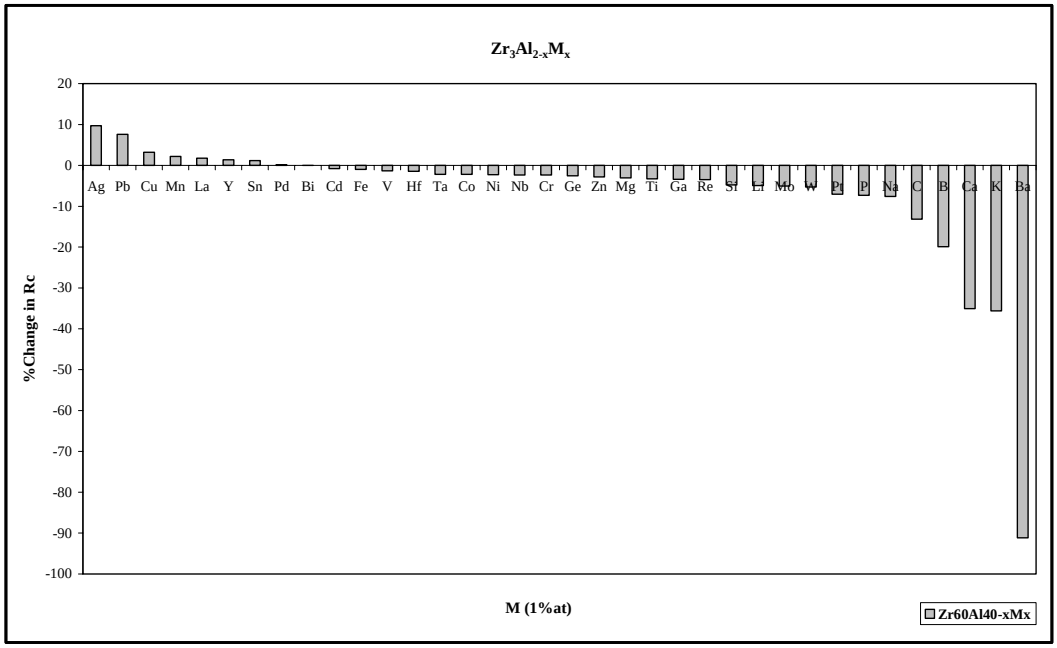

Figure B.42. % Change in R_c of $Zr_{60}Al_{40}$ binary system for the addition of 1 at % impurity elements (M) when 1 at % is taken from Al ($Zr_{0,60}Al_{0,39}M_{0,01}$system).

Table B.29. The ordering energy values for $Zr_{75}Al_{25}$ and $Zr_{0,74}Al_{0,25}M_{0,01}$.

M	W_{Zr-Al} (J/mol)	w_{Zr-Al} (J/mol)	W_{Zr-M} (J/mol)	w_{Zr-M} (J/mol)	W_{Al-M} (J/mol)	w_{Al-M} (J/mol)
$Zr_{75}Al_{25}$	-1,675E+04	-1,506E+05				
Ag	-1,664E+04	-1,496E+05	1,645E+04	1,479E+05	1,228E+04	1,104E+05
B	-1,685E+04	-1,515E+05	-5,797E+04	-5,212E+05	-2,043E+04	-1,837E+05
Ba	-1,628E+04	-1,464E+05	-5,566E+05	-5,004E+06	-5,143E+05	-4,624E+06
Bi	-1,670E+04	-1,501E+05	1,119E+04	1,006E+05	-2,965E+04	-2,666E+05
C	-1,693E+04	-1,522E+05	-3,449E+04	-3,101E+05	-4,822E+03	-4,335E+04
Ca	-1,646E+04	-1,480E+05	-1,141E+05	-1,026E+06	-8,631E+04	-7,759E+05
Cd	-1,666E+04	-1,497E+05	-1,368E+04	-1,230E+05	2,182E+03	1,962E+04
Co	-1,676E+04	-1,506E+05	-1,252E+04	-1,126E+05	3,458E+03	3,109E+04
Cr	-1,681E+04	-1,511E+05	-1,046E+04	-9,402E+04	2,643E+03	2,376E+04
Cu	-1,669E+04	-1,501E+05	5,577E+02	5,014E+03	8,957E+03	8,053E+04
Fe	-1,680E+04	-1,511E+05	-5,615E+03	-5,048E+04	2,756E+03	2,478E+04
Ga	-1,674E+04	-1,505E+05	-1,669E+04	-1,500E+05	-1,330E+03	-1,195E+04
Ge	-1,677E+04	-1,507E+05	-1,065E+04	-9,578E+04	-8,710E+02	-7,831E+03
Hf	-1,676E+04	-1,507E+05	1,876E+02	1,686E+03	-1,632E+04	-1,467E+05
K	-1,616E+04	-1,453E+05	-1,246E+05	-1,120E+06	-7,683E+04	-6,907E+05
La	-1,656E+04	-1,489E+05	4,373E+02	3,931E+03	-8,861E+03	-7,966E+04
Li	-1,661E+04	-1,493E+05	-3,039E+04	-2,732E+05	1,400E+03	1,259E+04
Mg	-1,665E+04	-1,497E+05	-2,045E+04	-1,838E+05	-5,012E+02	-4,505E+03
Mn	-1,674E+04	-1,505E+05	-6,187E+03	-5,562E+04	3,804E+03	3,420E+04
Mo	-1,693E+04	-1,522E+05	8,004E+02	7,196E+03	-2,454E+04	-2,206E+05
Na	-1,646E+04	-1,480E+05	-3,835E+04	-3,448E+05	-9,244E+03	-8,310E+04
Nb	-1,686E+04	-1,516E+05	1,445E+03	1,299E+04	-1,581E+04	-1,421E+05
Ni	-1,676E+04	-1,507E+05	-1,259E+04	-1,132E+05	3,491E+03	3,138E+04
P	-1,683E+04	-1,513E+05	-2,224E+04	-2,000E+05	-2,742E+03	-2,465E+04
Pb	-1,669E+04	-1,500E+05	2,688E+04	2,416E+05	-1,336E+04	-1,201E+05
Pd	-1,672E+04	-1,503E+05	-2,893E+03	-2,601E+04	-1,601E+03	-1,439E+04
Pt	-1,672E+04	-1,503E+05	-2,880E+04	-2,589E+05	-5,609E+03	-5,043E+04
Re	-1,700E+04	-1,529E+05	5,639E+03	5,069E+04	-1,861E+04	-1,673E+05
Si	-1,679E+04	-1,509E+05	-1,692E+04	-1,522E+05	-3,652E+02	-3,283E+03
Sn	-1,672E+04	-1,503E+05	7,221E+02	6,492E+03	-5,089E+03	-4,575E+04
Ta	-1,686E+04	-1,516E+05	1,262E+03	1,135E+04	-1,469E+04	-1,321E+05
Ti	-1,681E+04	-1,511E+05	-1,443E+04	-1,297E+05	-8,366E+02	-7,521E+03
V	-1,690E+04	-1,519E+05	-5,626E+03	-5,058E+04	5,169E+03	4,647E+04
W	-1,694E+04	-1,523E+05	8,907E+02	8,008E+03	-2,609E+04	-2,346E+05
Y	-1,661E+04	-1,493E+05	-1,195E+03	-1,075E+04	-6,998E+03	-6,291E+04
Zn	-1,672E+04	-1,503E+05	-1,718E+04	-1,545E+05	1,770E+03	1,592E+04

Table B.30. Thermodynamic and structural data of $Zr_{75}Al_{25}$ and $Zr_{0,74}Al_{0,25}M_{0,01}$.

M	ΔH_{mixing} (J/mol)	S^{σ} (J/K.mol)	ΔS^{ideal} (J/K.mol)	ΔS_{mixing} (J/mol)	ΔG_{mixing} (J/mol)	R_c (J/s)	$\Delta\eta/\eta_o$	α_1
$Zr_{75}Al_{25}$	-2,824E+04	0,402	4,676	5,078	-3,706E+04	1,422E+08	1,954	-0,333
Ag	-2,630E+04	0,412	5,117	5,529	-3,591E+04	1,509E+08	1,820	
B	-3,235E+04	0,652	5,117	5,769	-4,237E+04	1,065E+08	2,239	
Ba	-7,567E+04	0,604	5,117	5,721	-8,561E+04	1,132E+07	5,236	
Bi	-2,769E+04	0,399	5,117	5,516	-3,728E+04	1,407E+08	1,916	
C	-3,056E+04	0,676	5,117	5,793	-4,062E+04	1,165E+08	2,115	
Ca	-3,690E+04	0,477	5,117	5,595	-4,663E+04	8,621E+07	2,554	
Cd	-2,856E+04	0,398	5,117	5,515	-3,815E+04	1,345E+08	1,977	
Co	-2,862E+04	0,462	5,117	5,579	-3,832E+04	1,328E+08	1,981	
Cr	-2,859E+04	0,462	5,117	5,579	-3,828E+04	1,330E+08	1,978	
Cu	-2,753E+04	0,453	5,117	5,570	-3,721E+04	1,408E+08	1,905	
Fe	-2,826E+04	0,465	5,117	5,582	-3,796E+04	1,353E+08	1,955	
Ga	-2,898E+04	0,422	5,117	5,540	-3,860E+04	1,311E+08	2,005	
Ge	-2,861E+04	0,465	5,117	5,583	-3,832E+04	1,328E+08	1,980	
Hf	-2,823E+04	0,397	5,117	5,514	-3,782E+04	1,368E+08	1,954	
K	-3,689E+04	0,726	5,117	5,843	-4,705E+04	8,322E+07	2,553	
La	-2,772E+04	0,438	5,117	5,555	-3,737E+04	1,397E+08	1,918	
Li	-2,961E+04	0,401	5,117	5,519	-3,920E+04	1,273E+08	2,049	
Mg	-2,906E+04	0,396	5,117	5,514	-3,864E+04	1,311E+08	2,011	
Mn	-2,818E+04	0,433	5,117	5,550	-3,782E+04	1,365E+08	1,950	
Mo	-2,866E+04	0,429	5,117	5,546	-3,830E+04	1,332E+08	1,983	
Na	-3,013E+04	0,431	5,117	5,549	-3,977E+04	1,233E+08	2,085	
Nb	-2,830E+04	0,415	5,117	5,532	-3,791E+04	1,360E+08	1,958	
Ni	-2,863E+04	0,463	5,117	5,581	-3,833E+04	1,327E+08	1,981	
P	-2,953E+04	0,536	5,117	5,653	-3,936E+04	1,253E+08	2,044	
Pb	-2,627E+04	0,407	5,117	5,524	-3,587E+04	1,513E+08	1,818	
Pd	-2,804E+04	0,426	5,117	5,543	-3,768E+04	1,376E+08	1,940	
Pt	-2,985E+04	0,424	5,117	5,541	-3,948E+04	1,253E+08	2,066	
Re	-2,832E+04	0,426	5,117	5,543	-3,796E+04	1,356E+08	1,960	
Si	-2,906E+04	0,497	5,117	5,614	-3,882E+04	1,292E+08	2,011	
Sn	-2,787E+04	0,396	5,117	5,513	-3,746E+04	1,394E+08	1,929	
Ta	-2,828E+04	0,415	5,117	5,532	-3,790E+04	1,361E+08	1,957	
Ti	-2,893E+04	0,409	5,117	5,526	-3,854E+04	1,317E+08	2,002	
V	-2,836E+04	0,442	5,117	5,559	-3,803E+04	1,350E+08	1,963	
W	-2,869E+04	0,428	5,117	5,545	-3,833E+04	1,330E+08	1,986	
Y	-2,786E+04	0,417	5,117	5,534	-3,747E+04	1,391E+08	1,928	
Zn	-2,891E+04	0,422	5,117	5,539	-3,853E+04	1,316E+08	2,000	

Table B.31. The ordering energy values for $Zr_{75}Al_{25}$ and $Zr_{0,75}Al_{0,24}M_{0,01}$.

M	W_{Zr-Al} (J/mol)	w_{Zr-Al} (J/mol)	W_{Zr-M} (J/mol)	w_{Zr-M} (J/mol)	W_{Al-M} (J/mol)	w_{Al-M} (J/mol)
$Zr_{75}Al_{25}$	-1,675E+04	-1,506E+05				
Ag	-1,663E+04	-1,495E+05	1,645E+04	1,479E+05	1,228E+04	1,104E+05
B	-1,684E+04	-1,514E+05	-5,799E+04	-5,214E+05	-2,044E+04	-1,838E+05
Ba	-1,627E+04	-1,463E+05	-5,562E+05	-5,000E+06	-5,141E+05	-4,622E+06
Bi	-1,668E+04	-1,500E+05	1,116E+04	1,004E+05	-2,965E+04	-2,665E+05
C	-1,691E+04	-1,521E+05	-3,450E+04	-3,101E+05	-4,837E+03	-4,348E+04
Ca	-1,645E+04	-1,478E+05	-1,140E+05	-1,025E+06	-8,630E+04	-7,759E+05
Cd	-1,664E+04	-1,496E+05	-1,368E+04	-1,230E+05	2,182E+03	1,962E+04
Co	-1,674E+04	-1,505E+05	-1,251E+04	-1,125E+05	3,458E+03	3,109E+04
Cr	-1,679E+04	-1,510E+05	-1,044E+04	-9,385E+04	2,644E+03	2,377E+04
Cu	-1,668E+04	-1,500E+05	5,720E+02	5,142E+03	8,961E+03	8,056E+04
Fe	-1,679E+04	-1,509E+05	-5,605E+03	-5,039E+04	2,755E+03	2,476E+04
Ga	-1,672E+04	-1,503E+05	-1,669E+04	-1,500E+05	-1,330E+03	-1,195E+04
Ge	-1,675E+04	-1,506E+05	-1,065E+04	-9,576E+04	-8,724E+02	-7,843E+03
Hf	-1,675E+04	-1,506E+05	1,864E+02	1,676E+03	-1,630E+04	-1,466E+05
K	-1,615E+04	-1,452E+05	-1,245E+05	-1,119E+06	-7,680E+04	-6,904E+05
La	-1,655E+04	-1,488E+05	4,360E+02	3,919E+03	-8,852E+03	-7,958E+04
Li	-1,660E+04	-1,492E+05	-3,039E+04	-2,732E+05	1,403E+03	1,261E+04
Mg	-1,663E+04	-1,495E+05	-2,043E+04	-1,837E+05	-5,012E+02	-4,505E+03
Mn	-1,673E+04	-1,504E+05	-6,174E+03	-5,550E+04	3,805E+03	3,421E+04
Mo	-1,692E+04	-1,521E+05	8,045E+02	7,232E+03	-2,451E+04	-2,203E+05
Na	-1,645E+04	-1,479E+05	-3,831E+04	-3,444E+05	-9,238E+03	-8,305E+04
Nb	-1,685E+04	-1,514E+05	1,446E+03	1,300E+04	-1,579E+04	-1,420E+05
Ni	-1,675E+04	-1,505E+05	-1,258E+04	-1,131E+05	3,491E+03	3,138E+04
P	-1,682E+04	-1,512E+05	-2,225E+04	-2,000E+05	-2,742E+03	-2,465E+04
Pb	-1,668E+04	-1,499E+05	2,684E+04	2,413E+05	-1,337E+04	-1,202E+05
Pd	-1,671E+04	-1,502E+05	-2,841E+03	-2,554E+04	-1,587E+03	-1,426E+04
Pt	-1,671E+04	-1,502E+05	-2,881E+04	-2,590E+05	-5,609E+03	-5,043E+04
Re	-1,699E+04	-1,527E+05	5,646E+03	5,076E+04	-1,857E+04	-1,670E+05
Si	-1,678E+04	-1,508E+05	-1,692E+04	-1,521E+05	-3,652E+02	-3,283E+03
Sn	-1,671E+04	-1,502E+05	7,232E+02	6,502E+03	-5,088E+03	-4,574E+04
Ta	-1,685E+04	-1,514E+05	1,264E+03	1,136E+04	-1,467E+04	-1,319E+05
Ti	-1,679E+04	-1,510E+05	-1,443E+04	-1,297E+05	-8,406E+02	-7,557E+03
V	-1,689E+04	-1,518E+05	-5,618E+03	-5,051E+04	5,166E+03	4,644E+04
W	-1,692E+04	-1,521E+05	8,935E+02	8,032E+03	-2,607E+04	-2,343E+05
Y	-1,659E+04	-1,492E+05	-1,194E+03	-1,073E+04	-6,989E+03	-6,283E+04
Zn	-1,671E+04	-1,502E+05	-1,717E+04	-1,544E+05	1,769E+03	1,590E+04

Table B.32. Thermodynamic and structural data of $Zr_{75}Al_{25}$ and $Zr_{0,75}Al_{0,24}M_{0,01}$.

M	ΔH_{mixing} (J/mol)	S^{σ} (J/K.mol)	ΔS^{ideal} (J/K.mol)	ΔS_{mixing} (J/mol)	ΔG_{mixing} (J/mol)	R_c (J/s)	$\Delta\eta/\eta_o$	α_1
$Zr_{75}Al_{25}$	-2,824E+04	0,402	4,676	5,078	-3,706E+04	1,422E+08	1,954	-0,333
Ag	-2,553E+04	0,400	5,025	5,425	-3,496E+04	1,586E+08	1,767	
B	-3,160E+04	0,642	5,025	5,667	-4,145E+04	1,118E+08	2,187	
Ba	-7,492E+04	0,595	5,025	5,620	-8,469E+04	1,188E+07	5,185	
Bi	-2,689E+04	0,387	5,025	5,411	-3,629E+04	1,481E+08	1,861	
C	-2,980E+04	0,667	5,025	5,691	-3,969E+04	1,223E+08	2,062	
Ca	-3,616E+04	0,467	5,025	5,491	-4,571E+04	9,048E+07	2,502	
Cd	-2,781E+04	0,386	5,025	5,410	-3,721E+04	1,412E+08	1,924	
Co	-2,787E+04	0,450	5,025	5,475	-3,738E+04	1,395E+08	1,928	
Cr	-2,782E+04	0,451	5,025	5,476	-3,734E+04	1,398E+08	1,925	
Cu	-2,676E+04	0,442	5,025	5,466	-3,626E+04	1,479E+08	1,852	
Fe	-2,749E+04	0,454	5,025	5,478	-3,701E+04	1,422E+08	1,902	
Ga	-2,822E+04	0,411	5,025	5,435	-3,766E+04	1,378E+08	1,953	
Ge	-2,785E+04	0,454	5,025	5,479	-3,737E+04	1,396E+08	1,927	
Hf	-2,744E+04	0,385	5,025	5,410	-3,684E+04	1,440E+08	1,899	
K	-3,618E+04	0,719	5,025	5,744	-4,617E+04	8,715E+07	2,504	
La	-2,694E+04	0,427	5,025	5,452	-3,642E+04	1,468E+08	1,865	
Li	-2,887E+04	0,390	5,025	5,414	-3,828E+04	1,336E+08	1,998	
Mg	-2,831E+04	0,385	5,025	5,409	-3,771E+04	1,377E+08	1,959	
Mn	-2,741E+04	0,421	5,025	5,445	-3,688E+04	1,434E+08	1,897	
Mo	-2,785E+04	0,418	5,025	5,442	-3,731E+04	1,402E+08	1,928	
Na	-2,940E+04	0,420	5,025	5,445	-3,886E+04	1,294E+08	2,034	
Nb	-2,750E+04	0,403	5,025	5,428	-3,694E+04	1,431E+08	1,903	
Ni	-2,787E+04	0,452	5,025	5,477	-3,739E+04	1,394E+08	1,929	
P	-2,877E+04	0,525	5,025	5,550	-3,842E+04	1,317E+08	1,991	
Pb	-2,547E+04	0,395	5,025	5,420	-3,488E+04	1,593E+08	1,762	
Pd	-2,727E+04	0,414	5,025	5,439	-3,672E+04	1,447E+08	1,887	
Pt	-2,910E+04	0,412	5,025	5,436	-3,855E+04	1,316E+08	2,014	
Re	-2,751E+04	0,415	5,025	5,439	-3,697E+04	1,428E+08	1,904	
Si	-2,830E+04	0,486	5,025	5,511	-3,788E+04	1,357E+08	1,958	
Sn	-2,710E+04	0,384	5,025	5,409	-3,650E+04	1,466E+08	1,875	
Ta	-2,749E+04	0,403	5,025	5,427	-3,692E+04	1,432E+08	1,902	
Ti	-2,817E+04	0,397	5,025	5,422	-3,759E+04	1,384E+08	1,949	
V	-2,759E+04	0,430	5,025	5,455	-3,707E+04	1,419E+08	1,909	
W	-2,789E+04	0,417	5,025	5,441	-3,734E+04	1,400E+08	1,930	
Y	-2,708E+04	0,405	5,025	5,430	-3,652E+04	1,462E+08	1,874	
Zn	-2,815E+04	0,410	5,025	5,435	-3,760E+04	1,382E+08	1,948	

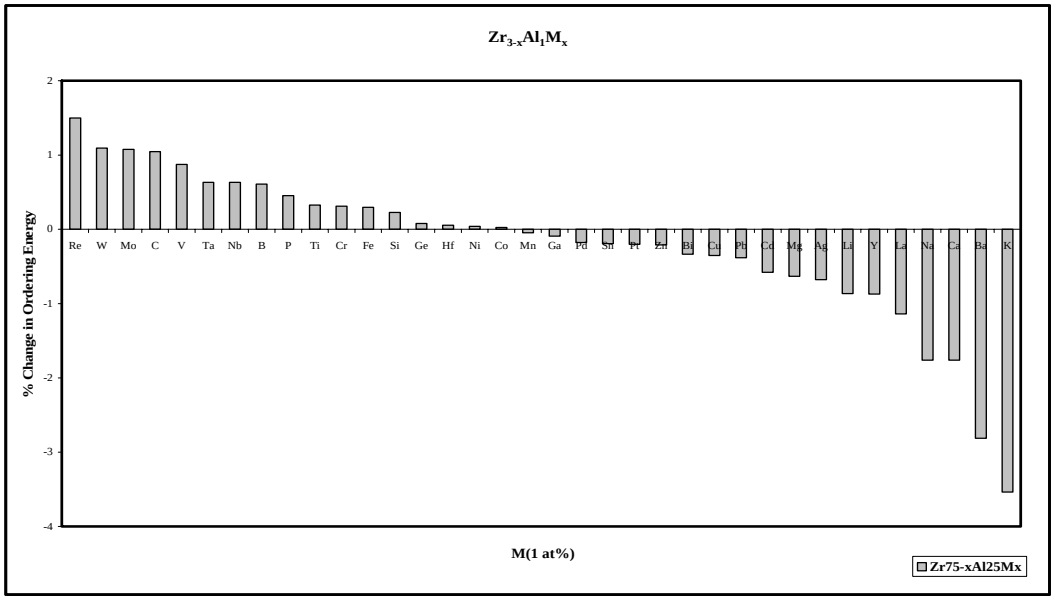

Figure B.43.% Change in ordering energy of $Zr_{75}Al_{25}$ binary system for the addition of 1 at % impurity elements (M) when 1 at % is taken from Zr ($Zr_{0,74}Al_{0,25}M_{0,01}$system).

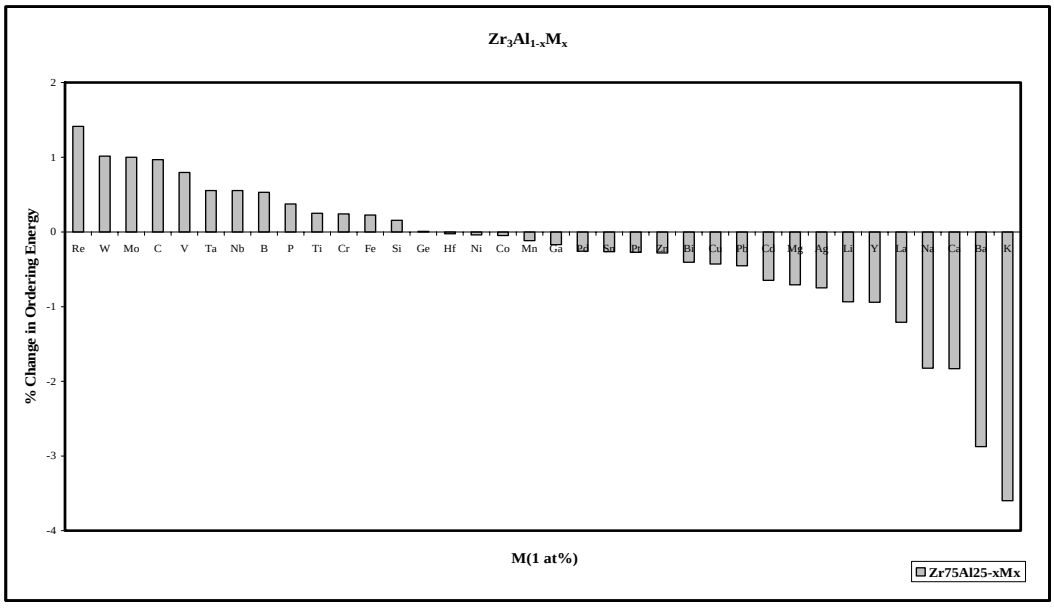

Figure B.44.% Change in ordering energy of $Zr_{75}Al_{25}$ binary system for the addition of 1 at % impurity elements (M) when 1 at % is taken from Co ($Zr_{0,75}Al_{0,24}M_{0,01}$system).

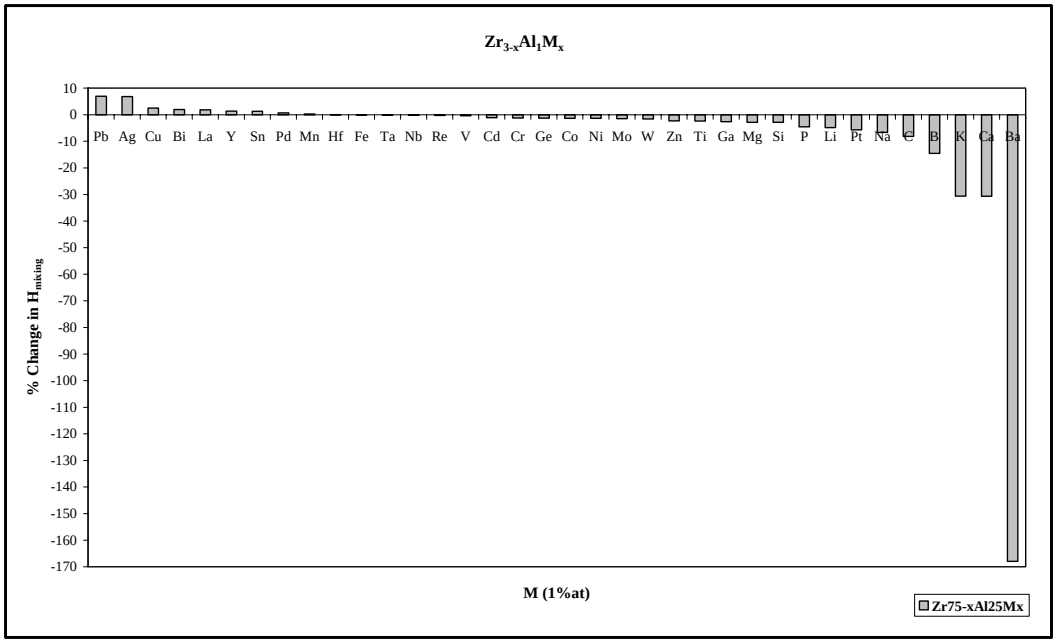

Figure B.45. % Change in ΔH_{mixing} of $Zr_{75}Al_{25}$ binary system for the addition of 1 at % impurity elements (M) when 1 at % is taken from Zr ($Zr_{0,74}Al_{0,25}M_{0,01}$system).

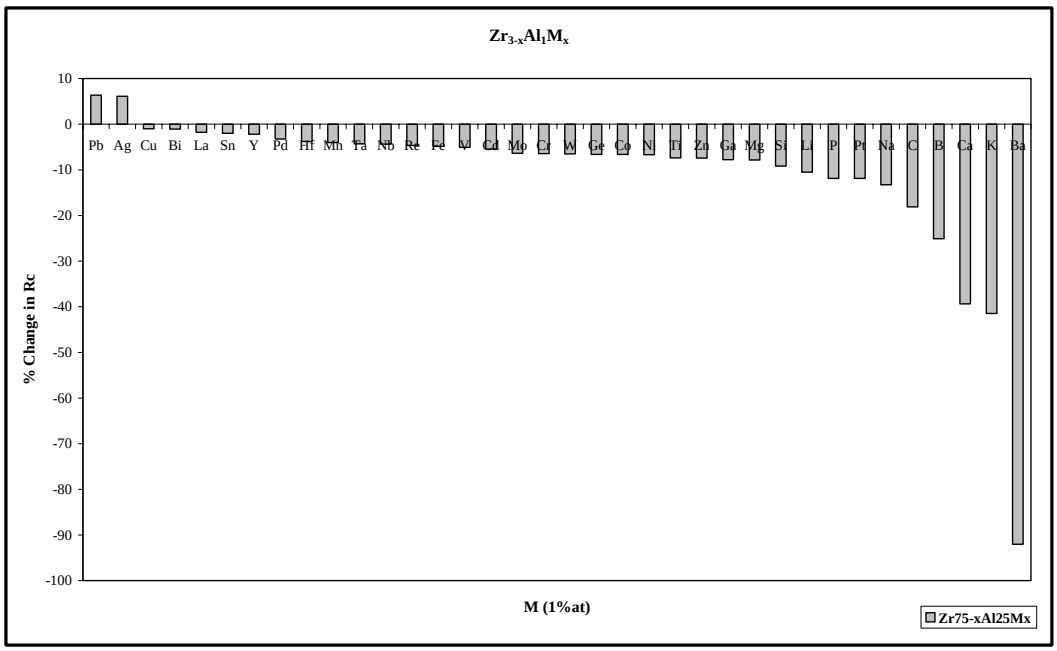

Figure B.46. % Change in R_c of $Zr_{75}Al_{25}$ binary system for the addition of 1 at % impurity elements (M) when 1 at % is taken from Zr ($Zr_{0,74}Al_{0,25}M_{0,01}$system).

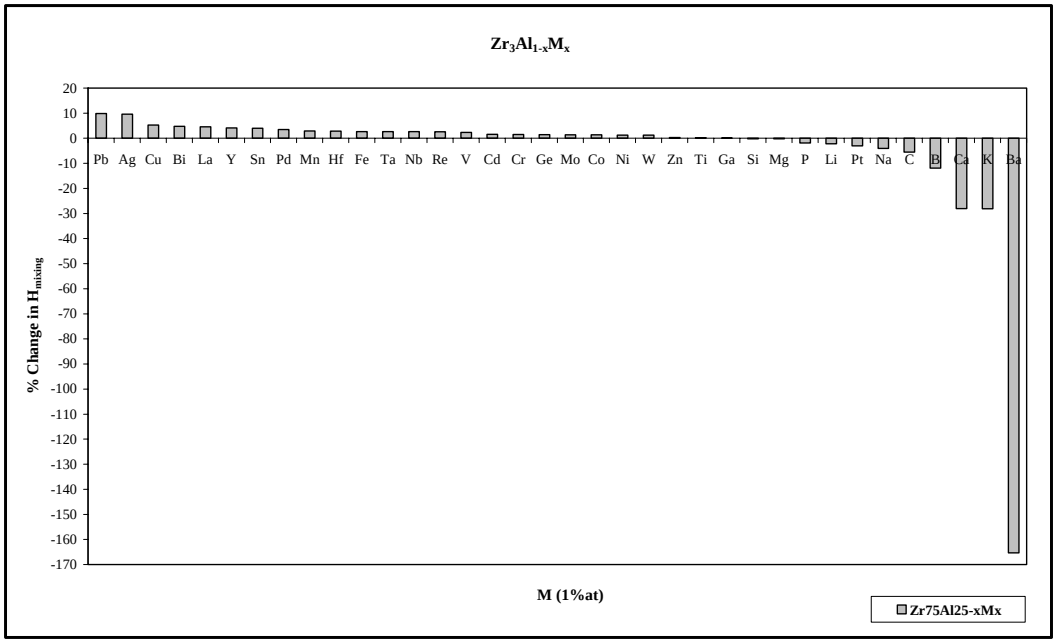

Figure B.47. % Change in ΔH_{mixing} of $Zr_{75}Al_{25}$ binary system for the addition of 1 at % impurity elements (M) when 1 at % is taken from Zr ($Zr_{0,75}Al_{0,24}M_{0,01}$system).

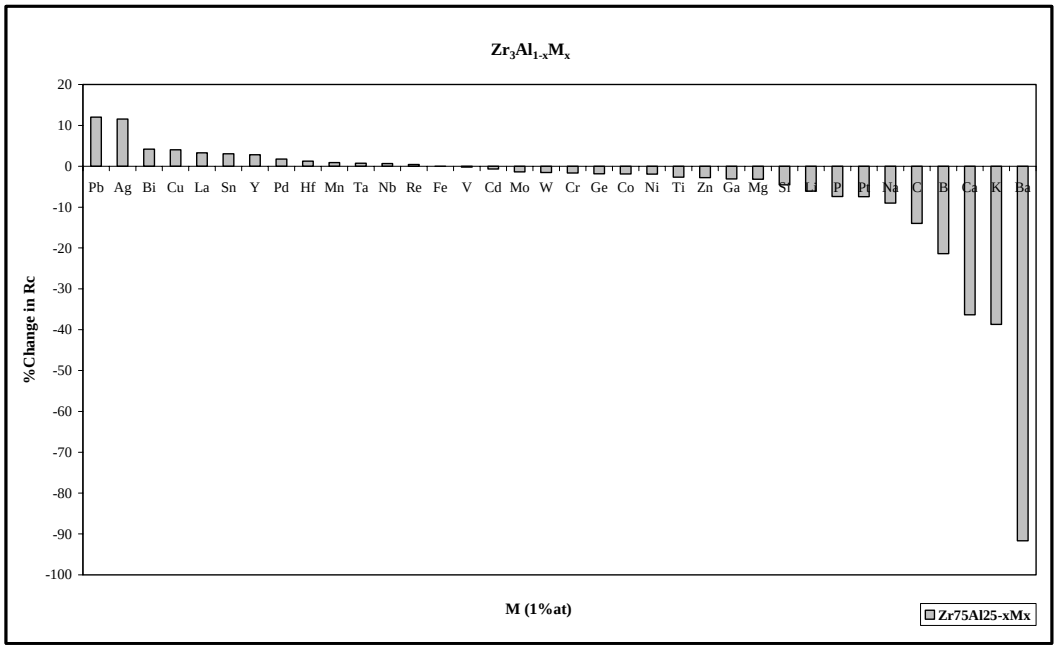

Figure B.48. % Change in R_c of $Zr_{75}Al_{25}$ binary system for the addition of 1 at % impurity elements (M) when 1 at % is taken from Zr ($Zr_{0,75}Al_{0,24}M_{0,01}$system).